AVERTISSEMENT

Ce document est le fruit d'un long travail approuvé par le jury de soutenance et mis à disposition de l'ensemble de la communauté universitaire élargie.

Il est soumis à la propriété intellectuelle de l'auteur. Ceci implique une obligation de citation et de référencement lors de l'utilisation de ce document.

D'autre part, toute contrefaçon, plagiat, reproduction illicite encourt une poursuite pénale.

Contact : ddoc-theses-contact@univ-lorraine.fr

LIENS

Code de la Propriété Intellectuelle. articles L 122. 4
Code de la Propriété Intellectuelle. articles L 335.2- L 335.10
http://www.cfcopies.com/V2/leg/leg_droi.php
http://www.culture.gouv.fr/culture/infos-pratiques/droits/protection.htm

THÈSE

pour l'obtention du titre de

DOCTEUR DE L'UNIVERSITÉ DE LORRAINE

SPÉCIALITÉ : PHYSIQUE

Présentée par :
PHILIPPE SCHEID

Investigation of light–induced ultrafast magnetization dynamics using *ab initio* methods

---

Thèse soutenue publiquement le 22/09/2020 devant le jury composé de:

M. Xavier Blase	Directeur de recherche, Institut Néel	Rapporteur
M. Brice Arnaud	Professeur, Université du Mans	Rapporteur
Mme Sangeeta Sharma	Docteur, Max–Born Institute de Berlin	Examinatrice
Mme Émilie Gaudry	Professeur, IJL, UL	Examinatrice
M. Sébastien Lebègue	Directeur de recherche, LPCT, UL	Directeur de thèse
M. Grégory Malinowski	Chargé de recherche, IJL, UL	Co–directeur de thèse
M. Stéphane Mangin	Professeur, IJL, UL	Invité

Abstract

Investigation of light–induced ultrafast magnetization dynamics using *ab initio* methods

To improve the information storage technologies, faster and more energy efficient ways of manipulating the magnetization state of the matter are researched. Within this framework, the possibility of doing so by using solely femtosecond light pulses, as suggested by the successive discoveries of the light–induced ultrafast demagnetization by Beaurepaire *et al.* in 1996, and of the so–called all–optical helicity–dependent switching by Stanciu *et al.* in 2007, is particularly attractive.
This thesis begins with a review of the current experimental and theoretical state of the art related to both of the aforementioned phenomena. This is followed by an overview of density functional theory, upon which relies most of the work reported thereafter.
The first set of results concerns the *ab initio* study of the effect of a rise in the electronic temperature on the magnetized matter properties, and more specifically Fe, Co, Ni and FePt. Indeed, as the light primarily interacts with the electrons, and due to the fact that the duration of the pulse is shorter than the coupling of the electrons with the other degrees of freedom, one can simply account for the absorbed energy by a rise of the electronic temperature. Doing so, we show that the magnetic moment carried by each atom disappears at the so–called Stoner temperature, and that this phenomenon impacts the electronic energy and specific heat, even at low electronic temperature. Then, we show that upon an increase in the electronic temperature, the interatomic Heisenberg exchange, which is responsible for the magnetic ordering, decreases. Using the atomistic Langevin Landau–Lifshitz–Gilbert equation, we demonstrate that this decrease is enough to induce a large reduction of the average magnetization by creating transversal excitations.
The second set of results regards the origin of the helicity–dependent light–induced dynamics. While the literature attributes it mainly to the inverse Faraday effect, we argue that another and novel phenomenon, which occurs during the absorption of the light, may be more suited to account for the experimental dynamics. Indeed, using the Fermi golden rule and ground state density functional theory calculations in Fe, Co, Ni and FePt, we show that, as the light is absorbed and electrons are excited, concurrently to the increase of the electronic energy, the spin–state is also changed in presence of spin–orbit coupling. This results in a difference in the value of the atomic magnetic moments, persisting even after the light is gone, as opposed to the inverse Faraday effect. Then, using real–time time–dependent density functional theory, we compute the magnetization dynamics induced by real optical and XUV femtosecond circularly polarized pulses. We show that, in both cases the dynamics is helicity–dependent and that this characteristic is largely amplified in the XUV regime involving the semi–core $3p$ states. Finally, we compare the relative role of the inverse Faraday effect and the magnetization induced during the absorption of the light and show that the latter plays a prominent role, especially after the light has gone, and in the XUV regime.

Keywords: Magnetism, *ab initio*, density functional theory, time–dependent density functional theory, ultrafast demagnetization, all–optical switching

Étude de la dynamique ultrarapide de l'aimantation induite par la lumière selon des méthodes *ab initio*

Pour améliorer les technologies de stockage de l'information, des moyens plus rapides et plus écoénergétiques de manipuler l'état de l'aimantation de la matière sont recherchés. Dans ce cadre, la possibilité de le faire en utilisant uniquement des impulsions lumineuses femtosecondes, comme le suggèrent les découvertes successives de la désaimantation ultrarapide induite par de la lumière par Beaurepaire *et al.* en 1996, et du retournement tout optique dépendant de l'hélicité par Stanciu *et al.* en 2007, est particulièrement intéressante.
Cette thèse commence par une revue de l'état actuel de l'expérimentation et de la théorie liées aux deux phénomènes susmentionnés. Ceci est suivi d'un aperçu de la théorie de la fonctionnelle de la densité, sur laquelle repose la plupart des travaux rapportés par la suite.
La première partie des résultats concerne l'étude *ab initio* de l'effet d'une élévation de la température électronique sur les propriétés de la matière aimantée, et plus précisément Ni, Co, Fe et FePt. En effet, comme la lumière interagit principalement avec les électrons, et du fait que la durée de l'impulsion est plus courte que le couplage des électrons avec les autres degrés de liberté du système, on peut simplement rendre compte de l'énergie absorbée en augmentant la température électronique. Ce faisant, nous montrons que le moment magnétique porté par chaque atome disparaît à la température dite de Stoner, et que, de manière plus générale ce phénomène impacte l'énergie électronique et la chaleur spécifique, même à basse température électronique. Ensuite, nous montrons que lors d'une augmentation de la température électronique, l'échange interatomique d'Heisenberg, responsable de l'ordre magnétique, diminue. Puis, en utilisant l'équation de Landau–Lifshitz–Gilbert atomistique, nous démontrons que cette diminution est suffisante pour induire une forte réduction de l'aimantation moyenne en créant des excitations transversales.
La deuxième partie des résultats concerne l'origine de la dépendante en l'hélicité de la dynamique induite par la lumière. Alors que la littérature l'attribue principalement à l'effet Faraday inverse, nous soutenons qu'un autre phénomène, se produisant lors de l'absorption de la lumière, peut rendre compte de la dynamique expérimentale. En effet, en utilisant la règle d'or de Fermi et des calculs utilisant la théorie de la fonctionnelle de la densité pour obtenir les états fondamentaux de Fe, Co, Ni et FePt, nous montrons que, lorsque la lumière est absorbée et que les électrons sont excités, parallèlement à l'augmentation de l'énergie électronique, le couplage spin–orbit permet la modification de l'état de spin. Il en résulte un changement de la valeur des moments magnétiques atomiques, persistant même après la disparition de la lumière, par opposition à l'effet Faraday inverse. Ensuite, en utilisant la théorie de la fonctionnelle de la densité dépendante du temps, nous calculons la dynamique de l'aimantation induite par de véritables impulsions femtosecondes polarisées circulairement dans le domaine optique et XUV. Nous montrons que, dans les deux cas, la dynamique est dépendante de l'hélicité et que cette caractéristique est largement amplifiée dans le régime XUV impliquant les états de semi–coeur $3p$. Enfin, nous comparons le rôle relatif de l'effet Faraday inverse et de l'aimantation induite lors de l'absorption de la lumière et montrons que cette dernière joue un rôle prépondérant, surtout après la disparition de la lumière et en régime XUV.

Mots-clés: magnétisme, *ab initio*, théorie de la fonctionnelle de la densité, théorie de la fonctionnelle de la densité dépendante du temps, désaimantation ultrarapide, retournement tout–optique

Acknowledgements

Ces trois dernières années furent, aussi bien humainement qu'intellectuellement, une immense période d'enrichissement et de développement. Le fruit de ce travail, ainsi que sa saveur, ne seraient pas les mêmes sans la bienveillance et le soutien dont j'ai eu le privilège de bénéficier. Ainsi, je voudrais ici exprimer ma gratitude envers nombreuses personnes qui ont contribué à rendre cette période de ma vie si épanouissante.

Je remercie tout d'abord l'ensemble des membres de mon jury ; Xavier Blase, Brice Arnaud, Sangeeta Sharma et Émilie Gaudry, qui ont accepté d'évaluer mes travaux. La richesse et la qualité des discussions scientifiques que nous avons eues lors de ma soutenance conclurent ces trois années de la plus belle des manière.

J'aimerais ensuite exprimer l'étendue de ma gratitude envers les personnes qui ont encadré ma thèse : Sébastien, la liberté, la confiance et l'expertise que tu m'as données m'ont permis de pleinement satisfaire et de développer ma curiosité pour la physique. Tu t'es constamment montré ouvert et disponible pour discuter de physique et d'autre chose, et les nombreuses opportunités de voyage que tu m'as données durant ces trois ans me laissent de magnifiques souvenirs et m'ont beaucoup enrichi. Grégory, j'ai fait ta rencontre durant les pauses déjeuner, alors que j'étais en stage, sans savoir que quelques mois plus tard tu co-encadrerais ma thèse. Cependant, c'est aussitôt que tu m'as donné ton amitié, ainsi que ce précieux garde fou survenant naturellement lors de la confrontation entre la théorie et la réalité expérimentale. Stéphane, nos séances de course à pied furent, même lorsque nous gravissions Brabois, un réel plaisir. Te laisser la primeur de l'arrivée au sommet n'était qu'une bien maigre compensation par rapport au soutien indéfectible que tu m'accordes depuis maintenant cinq ans, ainsi que les innombrables opportunités que m'a données. Celles-ci ont joué un grand rôle dans mon choix de faire une thèse, de la mener à bien et de poursuivre une carrière académique.

Durant ces trois années, j'ai également eu l'occasion de partager et de travailler avec beaucoup d'autres chercheurs. En particulier, je tiens à remercier Émilie Gaudry, que j'ai rencontrée en école d'ingénieur et qui m'a donné l'opportunité d'effectuer un « Parcours recherche ». Cela m'a mis le pied à l'étrier et a considérablement développé mon attrait pour la physique. T'avoir dans mon jury fut une belle manière de conclure mon « Odyssée de la physique » à Nancy, que tu as initiée. J'espère que nos chemins se recroiseront et nous mèneront à d'autres collaborations. Depuis mon stage de fin d'étude, j'ai également eu l'opportunité d'échanger régulièrement avec Christophe Chatelain et Daniel Malterre. Discuter avec vous fut, à chaque occasion, une source d'inspiration, et ce depuis que je vous ai connu en tant qu'enseignants en licence. Je souhaite également remercier Jon Gorchon, Julius Hohlfeld, Sébastien Petit-Watelot, Bertrand Berche, Dragi Karevski, Dario Rocca, François Dehez et Christophe Chipot, avec qui j'ai eu de nombreux et stimulant échanges, et de manière plus étendue l'ensemble des membres de l'équipe 101 et du LPCT. During my travels, I had the opportunity to meet many researcher around the world, whose work I admire. Not only they welcomed me, but they devoted a lot

of time to me, making these periods of my life as much enlightening as enjoyable. Especially, I would like to thank Vitaliy Lomakin, Marko Lubarda, Marco Menarini, Eric Fullerton, Peter Oppeneer, Marco Berritta, Marco Battiato, Hyungjun Kim, Pablo Maldonado, E.K.U. Gross, Sangeeta Sharma, and Kay Dewhurst.

Je souhaite désormais exprimer ma gratitude envers Émilie Gaudry, Stéphane Andrieu et Silvère Barrat. Me donnant votre aide et votre confiance tout au long de ce processus, vous m'avez permis de débuter l'enseignement dans les meilleurs conditions, ce qui m'y a donné goût !

Ensuite, pour leur aide précieuse vis-à-vis de l'aspect technique/informatique de ma thèse je souhaite également remercier Fabien Pascal et Francis Kosior. Vous vous êtes toujours montrés disponibles, et m'avez énormément appris.

Les nombreux aspects administratifs qui accompagnent le déroulement d'une thèse se révèlent le plus souvent ennuyant. Cependant, la gentillesse et la disponibilité de l'ensemble des hommes et des femmes qui s'occupent d'épauler les doctorants dans la réalisation de ces taches ont rendu ces dernières très agréables. Pour cela, je souhaite remercier Aurore Calmels, Isabelle Fournelle, Séverine Rollet, Christine Sartori et George Billant.

Cette période n'aurait absolument pas été la même sans l'ambiance régnant au sein des stagiaires, doctorants et postdoctorants avec qui j'ai partagé mon bureau, mes repas, et souvent mes soirées. Je pense évidemment à Alekos, Bilal, Bastien, Saber et Lamjed qui m'accompagnaient très souvent lors des pauses cafés, et parfois des parties d'échec. Je voudrais également mentionner Huyen, Kaushalya, avec qui j'ai longtemps partagé mon bureau à l'IJL. Votre humour décalé (et souvent involontaire), ainsi votre joie de vivre permanente furent un réel plaisir au quotidien. Quentin je te remercie pour les nombreuses discussions que nous avons eues à propos de la physique. Ta passion inébranlable pour ce sujet m'impressionne. Thibaud, Pierre et Alexandre, nos nombreuses nuits passées à débattre du féminisme, et de bien d'autres choses, dans une atmosphère d'écoute, de confiance et de bienveillance, furent certainement parmi les moments décisifs de cette thèse. Que vous m'ayez adopté en tant colocataire à temps partiel fut un honneur. Finalement je souhaite remercier Aurelia, Sarah, Sébastien, Dominique, Thiago, Kathleen, Miguel et Catalina. Vous compter parmi mes amis est un privilège, et j'espère que ces liens perdureront en dépit de l'inévitable accroissement de l'entropie.

Pour conclure, merci à ma famille dont l'inconditionnel soutient a rendu possible la poursuite de mes études en toute sérénité durant ces longues années.

Contents

Abstract **iii**

Acknowledgements **v**

1 Introduction **1**

2 State of the art **5**
2.1 Introduction . . . 5
2.2 Ultrafast demagnetization . . . 6
2.2.1 Early work . . . 6
2.2.2 Phenomenology of the ultrafast demagnetization . . . 8
2.2.3 Stoner and Heisenberg excitations . . . 10
2.2.4 The role of hot electrons . . . 12
2.3 Experiments exhibiting helicity–dependence . . . 20
2.3.1 All–optical switching . . . 20
2.3.1.1 The singular case of GdFeCo ferrimagnetic alloys . . . 22
2.3.1.2 From helicity–dependent to helicity–independent switching in GdFeCo . . . 24
2.3.1.3 Helicity–dependent switching in thin film metals . . . 27
2.3.2 Domain wall displacement . . . 32
2.3.3 Demagnetization . . . 36
2.3.4 Takeaways from the experiments . . . 37
2.3.4.1 Ultrafast demagnetization . . . 37
2.3.4.2 All–optical helicity–dependent switching . . . 38
2.4 Theoretical understandings . . . 39
2.4.1 2 and 3 temperature models . . . 39
2.4.1.1 General approach . . . 39
2.4.1.2 Further developments . . . 41
2.4.2 Longitudinal relaxation of the magnetization . . . 44
2.4.2.1 Elliott–Yafet spin–flip processes . . . 44
2.4.2.2 Superdiffusive spin–dependent transport . . . 48
2.4.3 Classical magnetization dynamics and transversal excitations . . . 52
2.4.3.1 Atomistic scale . . . 52
2.4.3.2 Macroscopic scale . . . 54
2.4.4 Helicity–dependent effects . . . 55
2.4.4.1 Magnetic circular dichroism and helicity–dependent switching . . . 56
2.4.4.2 The inverse Faraday effect . . . 59
2.4.5 Toward the use of real–time time–dependent density functional theory . . . 65

2.4.6 Takeaways from theory . . . 70
2.4.6.1 Ultrafast demagnetization . . . 70
2.4.6.2 Helicity–dependence . . . 71

3 Electronic structure calculations 73
3.1 The Hohenberg-Kohn theorems . . . 74
3.2 The Kohn–Sham scheme . . . 76
3.2.1 General framework . . . 76
3.2.2 Variational equations . . . 78
3.2.3 Magnetism . . . 79
3.2.4 Approximation for the exchange–correlation potential . . . 80
3.2.5 Second variational inclusion of spin–orbit coupling . . . 81
3.3 Time–dependent density functional theory . . . 82
3.3.1 One to one mapping between the density and the potential . . . 82
3.3.2 Time–dependent Kohn–Sham equations . . . 83
3.3.3 Time propagation in ELK . . . 84
3.4 Implementations . . . 85
3.4.1 Planewaves, frozen core and pseudopotentials . . . 86
3.4.2 Linear augmented plane waves . . . 88

4 *Ab initio* study of electronic temperature effects on magnetic materials properties 91
4.1 Introduction . . . 91
4.2 Theory . . . 92
4.2.1 Self-consistent calculation of electronic dependent magnetic properties . . . 92
4.2.2 Self-consistent calculation of electronic energy and specific heat . . . 92
4.2.3 Computational details . . . 93
4.3 Results and discussion . . . 94
4.3.1 Dependence of the electronic structure on the electronic temperature 94
4.3.2 Consequences of the electronic temperature on the electronic specific heat . . . 96
4.3.3 About ultrafast magnetization dynamics . . . 98
4.4 Conclusion . . . 98

5 Effects of the electronic temperature on the magnons and ultrafast demagnetization 101
5.1 Introduction . . . 101
5.2 Theory . . . 102
5.2.1 *Ab initio* calculation of the properties of magnons . . . 102
5.2.1.1 Equations of motion . . . 102
5.2.1.2 Calculation of the magnonic states and energies . . . 103
5.2.1.3 Computation of the Heisenberg exchange constants . . . 106
5.2.1.4 Computation of the Curie temperature in the mean–field approximation . . . 107
5.2.2 Stochastic atomistic Laudau–Lifshitz–Gilbert dynamics . . . 108
5.3 Results . . . 109
5.3.1 Computational details . . . 109

5.3.2 Softening of the magnon modes . . . 109
5.3.3 Reduction of the interatomic exchange . . . 110
5.3.4 Remarks on the calculation of the Curie temperature . . . 115
5.3.5 Ultrafast reduction of the magnetization caused by a quenching of the Heisenberg exchange . . . 115
5.4 Conclusion . . . 118

6 *Ab initio* theory of magnetization induced by light absorption in ferromagnets 123
6.1 Introduction . . . 123
6.2 Theory . . . 124
6.2.1 Distinction between the inverse Faraday effect and the magnetization induced by light absorption . . . 124
6.2.2 *Ab initio* computation of the absorbed magnetization . . . 125
6.3 Results . . . 126
6.3.1 Magnetization collinear with the direction of propagation of the light 126
6.3.2 Non–collinear case . . . 128
6.4 Order of magnitude of the absorbed magnetization for a realistic fluency . . 131
6.4.1 Demagnetization . . . 131
6.4.2 Helicity–dependence . . . 131
6.5 Conclusion . . . 131

7 RT–TDDFT study of helicity dependent light–induced demagnetization: from the optical regime to the XUV 133
7.1 Introduction . . . 133
7.2 Theory . . . 134
7.3 Results . . . 134
7.3.1 Longitudinal dynamics of the magnetization . . . 135
7.3.2 Origin of the difference of dynamics induced by an optical and a XUV light . . . 135
7.3.3 Magnitude of the helicity–dependence . . . 136
7.3.4 Inverse Faraday effect versus magnetization induced during light absorption . . . 138
7.4 Conclusion . . . 139

8 Conclusion 141

Bibliography 145

List of Figures

1.1 Dry magnetic compass. *Licensed under the Creative Commons Attribution-Share Alike 3.0 Unported license.* 1

2.1 Transient remanent longitudinal MOKE signal of a Ni(20 nm)/MgF2(100 nm) film for 7 mJ/cm^2 pump fluence. The signal is normalized to the signal measured in the absence of pump beam. The line is a guide to the eye. Image and caption extracted from Ref. [5]. 7

2.2 Magnetization dynamics in Ni measured using TR TMOKE over a full range of laser fluences. The highest fluence is sufficient to fully suppress the sample magnetization. The data are offset for clarity. Red curves: Fits to our microscopic model which considers the critical behavior, as well as the depth-average effects in the TR-TMOKE measurements. Inset: Fluence-dependent amplitudes of the demagnetization and recovery processes directly extracted from the TR-TMOKE results. In the TR-TMOKE results, the magnetization M and the extracted amplitudes $\langle A_1 \rangle$, $\langle A_2 \rangle$, and $\langle A_3 \rangle$ are averaged over the entire probed depth (see text). The dashed yellow line highlights the linear relation of the amplitude $\langle A_3 \rangle$ to the absorbed fluence when the fluence is above the critical fluence. Image and caption extracted from Ref. [20]. 9

2.3 (**A**) Spin-integrated photoemission spectra of Co/Cu(001) (30 ML) before (-100 fs) and after (100 fs) optical excitation. (**B**) Spin dynamics extracted from the measured spin polarization at EB = 2.3 eV. (**C** and **D**) Partial intensities of majority- and minority-spin photoemission spectra as a function of time. Lines correspond to the fits, as described in the text, whereas the arrows indicate a decrease/increase in spectral weight. Image and caption extracted from Ref. [29]. 11

2.4 (**A**) Extracted energetic shifts of the majority and minority bands as a function of time. (**B**) Modeled majority and minority spectra (top) and spin polarization (bottom), if only energetic shifts are considered, in comparison to the measured experimental data at t = 100 fs. (**C**) Extracted amount of band mirroring. The scaling prefactors A_{Maj} and B_{Maj} (blue solid and red dashed lines) that were multiplied with the unpumped ("initial") majority and minority spectra, respectively, to fit the data of the majority channel after excitation are shown. One sees that the majority channel loses spectral weight from its initial majority spectrum and gains spectral weight from the initial minority spectrum accordingly. The same was carried out for A_{Min} and B_{Min} in the minority channel (blue dashed and red solid lines). (**D**) Same as (**B**), if only band mirroring is considered. Image and caption extracted from Ref. [29]. 13

2.5 (a) Schematic representation of the multilayer structure. (b) Time evolution of the magneto-optical signal measurements for different Cu thicknesses. The laser power was adjusted to keep the maximum demagnetization constant for all samples, allowing for a normalization of the signal. Image and caption extracted from Ref. [32]. 15
2.6 (a) Schematic representation of laser excited electrons transport in magnetic heterostructures. (b) Normalized Kerr signal measured for parallel (P – diamonds) or antiparallel (AP – circles) alignment of the magnetizations. Image and caption adapted from Ref. [37]. 17
2.7 Magnetization as a function of time after pulsed laser excitation from the front (a) and from the back (b) for various thicknesses of the Ni film d_{Ni}. The insets shows the extracted demagnetization times as a function of d_{Ni}. Image and caption extracted from Ref. [36]. 19
2.8 Layer-selective magnetization dynamics in substrate/Ta(3 nm)/Fe(4 nm)-/X/Ni(5 nm)/Si_3N_4(6 nm) multilayers with different spacer layers. In (a), clear enhancement in the magnetization of the Fe layer is observed in the presence of good spin transport across the 1.7 nm Ru spacer layer. In (b) and (c), no enhancement of the magnetization of the Fe layer is observed when spin scattering spacer layers of Ta (2 nm) and W (2 nm) are used. In (d), spin currents are fully suppressed by inserting a 3 nm insulating Si_3N_4 layer. Image and caption extracted from Ref. [42]. 21
2.9 The effect of ultrashort polarized laser pulses on magnetic domains in-$Gd_{22}Fe_{74.6}Co_{3.4}$. (a) Magneto-optical image of the initial magnetic state of the sample before laser exposure. White and black areas correspond to up (M^+) and down (M^-) magnetic domains, respectively. (b) Domain pattern obtained by sweeping at low speed ($\approx$ 30 μm/s) linear (L), right-handed (σ^+), and left-handed (σ^-) circularly polarized beams across the surface of the sample, with a laser fluence of about 11.4 mJ/cm^2. The central area of the remaining spots at the end of each scan line consists of small magnetic domains, where the ratio of up to down magnetic domains is close to 1. Image and caption extracted from Ref. [6]. 22
2.10 Images of the laser spot focused onto a domain wall during the 1 kHz pulsed laser excitation with linear (L), right- (σ^+), and left–handed (σ^-) circular polarization. The images were obtained for a pulse fluence of about 11.4 mJ/cm^2. In all three cases the central region of the optically excited area is demagnetized (gray color) due to extensive heating. For circularly polarized excitation (σ^+ and σ^-) opto–magnetic switching takes place on the perimeter of the excited area, where the temperature is just below T_C. Image and caption extracted from Ref. [6]. 23
2.11 (a) and (b) Initial homogeneously magnetized state of the film with magnetizations 'up' and 'down' as represented by the circled dot and cross respectively. The light grey region represents magnetization pointing 'down' and the darker grey 'up'. (c) and (d) The film after an excitation with N (N=1, 2...5) pulses with a fluence of 2.30 mJ cm^{-2}. Each laser pulse excites the same circular region of the film and reverses the magnetization within it. The scale bar on the right corresponds to 20 μm. Image and caption extracted from Ref. [44]. 24

2.12 The magnetization evolution in $Gd_24Fe66.5Co_9.5$ after the excitation with σ^+ and σ^- circularly polarized pulses at room temperature. The domain is initially magnetized up (white domain) and down (black domain). The last column shows the final state of the domains after a few seconds. The circles show areas actually affected by pump pulses. (b) The averaged magnetization in the switched areas (5 μm) after σ^+ and σ^- laser pulses, as extracted from the images in (a) for the initial magnetization up. Image and caption extracted from Ref. [46]. 25
2.13 Switching probability P_σ as a function of the fluence at λ = 700 nm for three different polarizations. The measurements with *RC* and *LC* pulses were performed at a different time than the ones with *LP* pulses, and therefore the laser stability was different. Inset: Illustration of the switching probabilities in case of zero (solid) and nonzero (dashed) laser fluctuations using Eq. (1). F_{LC} and F_{RC} denote the switching threshold of GdFeCo for *LC* and *RC* excitation pulses, respectively. Image and caption extracted from Ref. [47]. 26
2.14 **a**, Thin-film RE–TM alloys. **b**, $[RE/TM]_N$ multilayers. **c**, Exchange-coupled $[RE/TM]_N/[RE/TM]_M$ heterostructures. **d**, SFI made of two TM layers antiferromagnetically coupled through 0.4 nm Ir interlayers. Each type of magnetic structure has shown either AO-HDS or thermal demagnetization depending on the thickness, layer structure and/or atomic concentration of the sample. Image and caption extracted from Ref. [7]. 28
2.15 Response to optical excitation for RE–TM alloys (Gd_xFeCo_{1-x}, Tb_xCo_{1-x}, Dy_xCo_{1-x}, Ho_xFeCo_{1-x}) and two types of RE–TM multilayer ([Tb/Co] and [Ho/CoFe]) as a function of the RE concentration (x). RedRed dots indicate thermal demagnetization and green stars AO–HDS. All of these alloys show perpendicular anisotropy except the two GdFeCo alloys marked IP (for in-plane anisotropy). The shaded regions correspond to alloy compositions for which T_{comp} is below room temperature. For the multilayers the RE layer thicknesses varied from 0.3 to 0.5 nm and the TM layers varied from 0.25 to 1.0 nm. Image and caption extracted from Ref. [7]. 29
2.16 Magneto-optical response in zero applied magnetic field of [Co(0.4 nm)/-Pt(0.7 nm)]$_N$ multilayer samples to various laser polarizations. (A) N = 8 repeats. (B) N =5 repeats. (C and D) N =3 repeats. For each image, the laser is circularly polarized (σ^+ or σ^-) or linear polarized (L). For (A) to (C), the laser beam was swept over a region of the sample with two perpendicularly oriented magnetic domains showing black/white contrast in the images, with a domain wall that runs vertically in the middle of each image. In (D), the laser was fixed at individual spots over a region of the sample with uniform magnetization (white contrast).The average laser intensity at different spots is indicated in the image. Image and caption extracted from Ref. [8]. 30

2.17 Magneto–optical response in zero applied magnetic field of a 15 nm FePtAgC granular film sample starting with an initially demagnetized sample. (A) Line scans for σ^+, σ^- , and linear polarized light (L). The laser beam was swept over the sample, and the magnetization pattern was subsequently imaged. (B) Images of magnetic domains written by keeping the laser spot at a fixed position on the sample. The laser was either σ^+ polarized (left column) or σ^- polarized (right column). The laser power was 677 nW. Image and caption extracted from Ref. [8]. 31
2.18 (a)–(c) Magneto-optical Kerr images obtained after exposing the sample to 600 laser pulses with a pulse duration of 1 ps, a σ^+ polarization, and laser fluences of 8.3 mJ/cm^2 (a), 9.1 mJ/cm^2 (b), and 12.3 mJ/cm^2 (c) corresponding to the lines in (d). The red and blue contrasts correspond to opposite perpendicular magnetization directions. (e)–(d) Cross section of the laser excited area for laser fluences between 4 and 18 mJ/cm^2 and various pulse durations for a laser spot diameter of 104 µm (d) and 168 µm (e). For (a)–(c), the white scale bar is 10 µm, for (d) and (e), the black bar is 50 μm. Image and caption extracted from Ref. [56]. 33
2.19 Magnetization state diagram as a function of the laser fluence, F, and the pulse duration, PD, for a circularly polarized static beam of different diameters (84 μm for triangles, 104 μm for square, and 168 μm for dots) illuminating a Co/Pt. For a given fluence, the maximum (minimum) pulse duration for which we have AO–HDS is plotted as filled (open) symbols. The inset shows a magnification of the diagram for the short pulse durations. Image and caption extracted from Ref. [56]. 33
2.20 Magneto-optical images of domain wall motion in [Co (0.4 nm)/Pt (0.7 nm)]$_{\times 3}$ and [Co (0.6 nm)/Pt (0.7 nm)]$_{\times 1}$ induced, respectively, by (a) 2-ps and (b) 40-fs laser pulses with left-circular (σ^-) and right-circular (σ^+) polarization with an energy per pulse of 0.04 and 12.5 mJ/cm^{-2}. The white star indicates the center of the beam spot, and N is the number of laser pulses. The laser beam spot is (a) placed 10 μm away from the DW within a magnetization-up (M$^+$) or -down (M$^-$) domain or (b) centered on the wall. The dotted line shows the initial position of the domain wall prior to laser exposure. Image and caption extracted from Ref. [57]. 34
2.21 (a)–(c) Magneto-optical Faraday images of a domain wall in a Pt(4.5 nm)/-Co(0.6 nm)/Pt(4.5 nm) thin film exposed to 40-fs linearly polarized (L) laser pulses with a fluence of 7 mJ/cm^2. The laser beam spot (star) is on the DW in (a) and off centered in (b) and (c). The DW moves towards the center of the beam, *i.e.*, the hottest regions, independently of the magnetization direction. (d) Normalized DWD induced by 40-fs laser pulses in Pt(4.5 nm)/Co(0.6 nm)/Pt(4.5 nm) plotted against the angle θ of the quarter-wave plate (QWP) and the degree of light ellipticity ϵ for linear polarization ϵ=0 and for circular polarization $\frac{\pi}{4}$ or -$\frac{\pi}{4}$. A maximum DW displacement of about 2 μm was obtained. The laser beam is initially centered on the DW at θ=0° and kept fixed. The fluence is set to 12.5 mJ/cm^2. Image and caption extracted from Ref. [57]. 35

2.22 Polarization dependence of the magnetization dynamics after a single 60 fs laser pulse excitation. The RCP and LCP optical pump pulses are used to excite the multilayer, which magnetization is saturated parallel $\vec{M}_{\uparrow}$ or antiparallel $\vec{M}_{\downarrow}$ to the sample normal. The magnetization dynamics for LCP laser excitation is shifted down by 0.5 for a better visual representation. Figure and caption extracted from Ref. [60]. 36
2.23 (a) Helicity-independent (ΔM) and (b) helicity-dependent (δM) magnetization change extracted from ultrafast magnetization dynamics induced by circularly polarized light. δM is proportional to the magnetic circular dichroism. Image and caption extracted from Ref. [61]. 37
2.24 (a) Experimental spin T_s and electron T_e temperatures estimated as explained in [5]. (b) Calculated spin T_s, electron T_e, and lattice T_l temperatures. Image and caption extracted from Ref. [5]. 40
2.25 **a**, Type I dynamics at T=0.5 T_C for a fictitious material (C_p=5 γ T_C) with a large spin-flip rate (R=5.0τ_{E0}^{-1}), leading to single–step demagnetization within the electron–phonon equilibration. Results for demagnetization at low (blue) and high (red) laser fluence are shown (q=0.2 and 0.8, respectively), as well as a scaled version of the low-fluence result (blue dotted). The time axis is normalized to τ_{E0}, defined as τ_E at T$\approx$ T_C. **b**, Two-step demagnetization (type II) as observed for materials with a small value of R(0.2τ_{E0}^{-1}). **c**, Generalized phase diagram, for materials with a certain relative spin-flip rate R τ_{E0} as a function of fluence q and ambient temperature T_0/T_C (see text). The curved plane (top side blue, bottom side red) separates regions of type I and type II dynamics. The opaque planes represent different materials (R τ_{E0}=5.0, 1.0 and 0.2, respectively), where green represents type I behaviour, and purple type II behaviour. Figure and caption extracted from Koopmans *et al.*[65]. 43
2.26 Normalized magnetization dynamics (a) and energy difference to equilibrium of the electronic system (b) after the optical excitation including electron-phonon scattering. Results obtained including the spin-orbit coupling contribution in the electron-phonon matrix element are labeled "with SOC-ME. Image and caption extracted from Ref. [75]. 45
2.27 Energy-resolved electron-phonon total and SF scattering rates w(E) and $w_{\uparrow\downarrow}$(E) of Ni (top), and normalized SF probability P_S(E) and approximate SF probability $P_S^{b^2}$(E) obtained from the Elliott relation (bottom). Image and caption extracted from Ref. [80]. 47
2.28 Spin-resolved DOS (filled areas) and phonon-induced spin flips (arrows) of NEQ and electron thermalized Ni. The equilibrium DOS is shown by thin lines. SF transitions are significantly different at energies above and below E_F(=0 eV). The arrow's thickness corresponds to the transition rate; its direction and length give which direction is dominant and by how much. The amount of laser-redistributed electrons has been enlarged to improve visibility. Image and caption extracted from Ref. [80]. 49

2.29 a. Calculated spatial magnetization profile of Ni at three times caused by laser excitation (at t = 0 fs). The resulting magnetization profile is given by the full curve, the initial one by the dotted curve. The magnetization profile without electric field correction is given by the dashed curve. The surface of the film is at 0 nm depth, the Ni film extends up to 15 nm depth, the remaining is the Al film. b. Computed laser-induced demagnetization in Ni. The shaded area shows where the theoretical result is expected to be (depending on the inelastic lifetime). For comparison they also show experimental XMCD data obtained by Stamm *et al.*[17]. The used time structure of the laser pulse (in a.u.) is depicted by the red solid line. Images and caption adapted from Ref. [34]. 51
2.30 Simulated demagnetization of Ni comparing classical and rescaled models with experimental data from [5]. The rescaled dynamic simulations show quantitative agreement with experiment from an atomic level model. Image and caption extracted from Ref. [91]. 54
2.31 AOS Probability as a function of temperature and MCD for N=10 pulses. Image and caption extracted from Ref. [96]. 58
2.32 Percentage of unswitched grains using a laser fluence of (a) 12 mJ/cm^2 and (b) 14 mJ/cm^2 with an inverse Faraday field modeled by a flat Gaussian for varying strengths and duration. The sides of the field are Gaussian shaped with a width of τ_l = 100 fs. Image and caption extracted from Ref. [97]. . . . 61
2.33 Second-order response for a three-level model system to the on-switching of a continuous wave external field. In the top and bottom panels, the time behaviors of a diagonal and an off-diagonal element, respectively, are displayed. The complete time behaviors are shown in panels (e) and (i) for the diagonal and off-diagonal element, respectively. The time evolutions of the density matrix elements are separated in absorption, second harmonic generation, zero-th harmonic generation, and transient behavior. Image and caption extracted from Ref. [101]. 62
2.34 Calculated total, orbital, and spin IFE $K^{IFE}(\omega)$ as function of the photon energy for several nonmagnetic metals: Cu and Au (top) and Pd and Pt (bottom). The opposite circular laser polarizations are denoted with $\sigma^{\pm}$. Image and caption extracted from Ref. [103]. 63
2.35 Calculated total, orbital, and spin inverse Faraday constant $K^{\mathrm{IFE}}(\omega)$ as function of the photon energy and laser polarizations $\sigma^{\pm}$ for ferromagnetic bcc–Fe, hcp–Co, and fcc–Ni. Image and caption extracted from Ref. [103]. 63
2.36 Calculated total, orbital, and spin IFE $K^{\mathrm{IFE}}(\omega)$ as function of the photon energy for synthetic antiferromagnetic Fe (top panels) and for ferromagnetic Fe with zero spin-orbit coupling (bottom panels). A magnification of ten is used only for the top-right panel. Image and caption extracted from Ref. [103]. 64
2.37 Top panel: **A**(t) of the laser pulse. Middle panel: relative magnetic moment. Lower panel: x-, y-, and z-projected magnetic moments per atom for a supercell of Ni. Image and caption extracted from Ref. [107]. 66

2.38 Left: Comparison of the time-dependent change of magnetic moment for 3 ML Co/Cu (001) as observed in experiment by using the second harmonic generation and by TDDFT calculations. The relative changes (normalized to values μ (t¡0) before excitation) of the total spin moment in Co/Cu(001) $\Delta\mu$ as well as of the Co contributions $\Delta\mu_{Co}$ with and without sin–orbit coupling are given. Right: Magnetic moment induced in Cu μ_{Cu} by spin transfer across the interface. Image and caption extracted from Ref. [109]. 68
2.39 Comparison between the experimentally recorded attosecond MCD trace in Ni/Pt-multilayers (blue line) and pure Ni (red) with the ab initio simulation of light-field-induced spin dynamics, including spin–orbit coupling in the multilayer (dark-green line) reveals that for the first 10 fs the demagnetization of Ni layers is entirely due to flow of majority-spin current across the material interface. Theoretical calculations without the spin–orbit interaction predict saturation of the demagnetization 15 fs after the optical excitation (light-green line). This is a clear indication that beyond this time all the demagnetization is caused by spin flips, whereas at earlier times spin dynamics is governed by OISTR, which is absent in the theoretical prediction for bulk nickel (violet line; see Fig. 2). Image and caption extracted from Ref. [110]. 69

3.1 Correspondence between external potentials v_i, associated ground states Ψ_{0,v_i} and ground state densities n_{0,v_i} in the case of non-degenerate ground states. Image extracted from [115]. 75
3.2 Schematic flow–chart for self–consistent density functional calculations. . . 79
3.3 Schematic illustration of the replacement of the all–electron wavefunction and core potential by a pseudo wavefunction. Image adapted from [123]. . . 87
3.4 The "muffin–tin" division of space into intra–atomic spheres of radius R, and interstitial regions. Image adapted from [129]. 88

4.1 Spin-polarized density of states of fcc-Ni, hcp-Co, bcc-Fe and FePt $L1_0$ for different values of the electronic temperature chosen below and above the Stoner temperature. The majority (minority) spin DOS are in orange (blue) and the value of μ, the chemical potential, is indicated by a vertical dashed line. 94
4.2 Magnetic moment per unit cell against the electronic temperature. In every compound, we observe a loss of the magnetization when the temperature is above T_S. 95
4.3 Electronic energy per unit cell against the electronic temperature for fcc-Ni, hcp-Co, bcc-Fe, FePt $L1_0$. The electronic energy obtained from TDD (TID) calculations is in blue (orange). 96
4.4 Electronic specific heat versus the electronic temperature for fcc-Ni, hcp-Co, bcc-Fe and FePt $L1_0$ computed with different approximations. 97

5.1 Side view (a)) and top view (b)) of a magnon having a wavelength λ. The red arrows represent the magnetization vectors carried by the different atomic sites. 104
5.2 Band dispersion and density of states of the magnons in fcc Ni when the electronic temperature is set to 300K (top) and 2000K (bottom). 111

5.3 Band dispersion and density of states of the magnons in fcc Co when the electronic temperature is set to 300K (top) and 3000K (bottom). 111
5.4 Band dispersion and density of states of the magnons in bcc Fe when the electronic temperature is set to 300K (top) and 3000K (bottom). 112
5.5 Bar diagram representing $N_j \times J_{ij}^{T_e}$ for j, which indexes the neighbors, in fcc Ni, fcc Co and bcc Fe. N_j is the number of neighbors of type j, *i.e.* and $J_{ij}^{T_e}$ is the Heisenberg exchange interaction between the atoms i and j. 113
5.6 Variation of the electronic energy, ΔE_e, as a function of time computed using Eq. 5.43 where r = 500 fs and $I(t)$ is a Gaussian centered at 500 fs and having a standard deviation of 60 fs. $\alpha I(t)$ is chosen such that ΔE_e peaks at 0.05, 0.10, 0.15 and 0.20 eV. 117
5.7 Electronic temperature, T_e, as a function of ΔE_e, the variation of energy in the electronic bath in fcc Ni, fcc Co and bcc Fe. 117
5.8 Electronic temperature, T_e, as a function of the time in fcc Ni, fcc Co and bcc Fe. 118
5.9 Value of $\sum_j N_j J_{ij}\,(T_e)$ in fcc Ni, fcc Co and bcc Fe as a function of the electronic temperature, where j runs over the 10 first neighbors. 119
5.10 Dynamics of the effective mean field, $\sum_j N_j J_{ij}$ produced by the absorption . 120
5.11 Dynamics of the average magnetization computed with Eq. 5.35. 121

6.1 a) Gaussian and gate profile of the intensity. b) The continuous lines represent the contribution of IFE and the MILA to the helicity–dependent part of the magnetization dynamics, $M_{\mathrm{HD}}(t)$, as well as the total dynamics as calculated with Eq. 6.1 using $\gamma_{\mathrm{IFE}} = 0.5\mu_B/at./TWcm^2$ and $\gamma_{\mathrm{MILA}} = 0.1\mu_B/fs/at./TWcm^2$, and the Gaussian profile for the intensity of the light. The dynamics represented in dashed lines is calculated using the Gate profile for the intensity. 125
6.2 Continuous lines: variation of the magnetization with respect to time induced by optical transitions in fcc Ni, hcp Co, bcc Fe and FePt $L1_0$ for circularly left and right polarized light, σ^+ and σ^-. Dashed line: difference of the variation of the magnetization induced by σ^+ and σ^- polarized light with respect to time scaled by a factor 10. 127
6.3 Joint density of states of fcc-Ni, hcp-Co, bcc-Fe and FePt $L1_0$ broken down into the different initial and final magnetic states involved, as defined in Eq. 6.6. 128
6.4 Majority (in blue) and minority (in orange) density of states of bcc Fe. The exchange splitting energy is represented by the vertical dashed lines. 129
6.5 Sketch of the induced magnetization produced by σ^+ and σ^- polarized light per unit of time for different orientations of the magnetic moments with respect to the direction of propagation of the light. The parameters α, β and γ of the fitting law defined by Eq. 6.7 are represented. 129
6.6 Markers: angle–dependent part of the magnetization induced by σ^+ and σ^- polarized photons of 1.55 eV per unit of time for different values of θ, the angle between the light propagation axis and the magnetization. Continuous lines: fit using Eq. 6.7 and the values of α, β and γ given in Tab. 6.1. 130

7.1 RT–TDDFT dynamics of the z component of the magnetization, M_z, calculated for bcc Fe, fcc Co and fcc Ni performed at 1.55 eV (a)) and in the XUV range (b)). 135
7.2 a), b) d), e): Variation of the spin and occupation resolved density of states, $\mathrm{oDOS}^{\sigma}(t = 32\mathrm{fs}) - \mathrm{oDOS}^{\sigma}(t = 0\mathrm{fs})$ in bcc Fe, induced by a σ^+ (a) and d)) and a σ^- (b) and e)) polarization of the light induced after 32 fs using an optical (a) and b)) and a XUV light (d) and e)). c), (f)): Difference of the total density of states induced by a σ^+ and a σ^- polarized light, $\mathrm{oDOS}_{\Delta\mathrm{hel.}} = \mathrm{oDOS}_{\sigma^+}(t = 32\mathrm{fs}) - \mathrm{oDOS}_{\sigma^-}(t = 32\mathrm{fs})$, after 32 fs computed at 1.55 eV (in the XUV range). The right side of d), e) and f) is magnified by a factor 10. . 137
7.3 Magnitude of the helicity–dependent dynamics over the helicity–independent one, ζ, at 1.55 eV (a)) and in the XUV range (b)) 138
7.4 Zeroth harmonic (M_{I}) and absorption (M_{F}) part of the helicity–dependent dynamics calculated with Eq. 7.6, where M_{HD} is induced by a light of 1.55 eV (a)) and in the XUVs (b)). The dashed lines in a) represent the contribution to the dynamics of the angular momentum absorption effect, calculated in Chap. 6. 140

1 Boussole magnétique aimantée. *Sous licence Creative Commons Attribution-Share Alike 3.0 Unported license.* 155

List of Tables

2.1 Here are given the *ab initio* calculated spin-flip probabilities P_S, Elliott SF probability P_S^E, demagnetization ratios D_S, and relative demagnetization fractions $\Delta M/M_0$ for laser-pumped Ni, Fe, and Co. Calculated values are given for equilibrium (low T), for thermalized electrons at a high Fermi temperature T_e, and for the nonequilibrium (NEQ) electron distribution created by femtosecond laser excitation. Computed values for the approximate Elliott SF probability P_S^E. The relative demagnetization fraction $\Delta M/M_0$, achieved by electron-phonon SF scattering, is given in % at 250 fs. Table and caption extracted from Ref. [81]. 48

2.2 Calculated values of the optical helicity-dependent laser-induced magnetization (in μ_B per atomic volume), for various metals, assuming a typical photon energy of 1.55 eV and intensity of 10 GW/cm^2. Also given is the computed optomagnetic field B_{opt}, *i.e.*, the Zeeman field needed to induce the same magnetization as the circularly polarized laser field. Table and caption extracted from Ref. [103]. 64

4.1 Calculated magnetic moment per unit cell and per atom and calculated Stoner temperature T_S for all the compounds studied here. For comparison, we added the results from 0. Gunnarsson[70]. In contrast with T_S, we also remind the experimental Curie temperature. 96

5.1 Heisenberg exchange $J_{jj}^{T_e}$ of bcc Fe, fcc Co and fcc Ni computed for the first j neighbors of a given atom i, with $j = 1...10$ at different electronic temperatures, T_e and variation of the exchange with respect to J_{ij}^{300}: $\Delta_{ij}^{T_e} = \frac{J_{ij}^{T_e} - J_{ij}^{300}}{J_{ij}^{300}}$. 114

5.2 Value of the Curie temperature, T_C, computed in the mean field approximation at different values of T_e using Eq. 5.34. For comparison, the values obtained by Halilov *et al.*[71] and by Pajda *et al.*[139] using the mean field approximation are also reported, as well as the experimental values (Exp.). . 115

6.1 Values of the parameters α, β and γ corresponding to the law Eq. 6.7 for fcc Ni, hcp Co, bcc Fe and FePt $L1_0$ for photons of 1.55eV. 131

List of Abbreviations

DFT	Density functional theory
TDDFT	Time–dependent density functional theory
RT–TDDFT	Real time time–dependent density functional theory
LDA	Localized gradient approximation
GGA	Generalized gradient approximation
OPW	Orthogonalized planewave
PAW	Projected augmented planewaves
APW	Augmented planewave
LAPW	Linear augmented planewave
T_C	Curie temperature
T_S	Stoner temperature
T_e	Electronic temperature
T_s	Temperature of the bath of the magnetic moments
T_p	Phonon, or lattice temperature
T_{comp}	Compensation temperature in ferrimagnets
2TM	Two temperature model
3TM	Three temperature model
M3TM	Microscopic three temperature model
PMA	Perpendicular magnetic anisotropy
$\sigma^{\pm}$	Left / right circular polarization of the light
π	Linear polarization of the light
AO–HDS	All–optical helicity–dependent switching
AO–HIS	All–optical helicity–independent switching
MCD	Magnetic circular dichroïsm
IFE	Inverse Faraday effect
MILA	Magnetization induced during the absorption of the light

Dedicated to Vicky and my parents.

Chapter 1

Introduction

Magnetism has, for most of our recent history, played an increasingly important role for mankind. The first traces of a scientific discussion about magnetism are attributed to Thales (625 BC to 545 BC)[1]. By the 12th century, the compass had been invented and was used to increase the accuracy of navigation. Since then, the range of practical applications using magnetism kept increasing at a faster pace, to such an extent that in this day and age most of the hardware we use in our daily lives relies in one way or another on magnetic phenomena. It is particularly the case since the advent of the computer and hard–disk drives using magnetic recording. Indeed, in the late 1980s, 99% of the information was stored using an analog format, whereas by 2007, 97% was stored digitally[2].



FIGURE 1.1: Dry magnetic compass.
Licensed under the Creative Commons Attribution-Share Alike 3.0 Unported license.

More than its omnipresence in the technological area, magnetism has presented an equally fertile ground in Physics, particularly in the domain of light–matter interaction. The effect of magnetized materials on the polarization of the light propagating through it has been known for nearly two centuries. Indeed, in 1845, Michael Faraday discovered the first experimental evidences of this phenomenon in a piece of glass containing traces of lead. He showed that, in the presence of a magnetic field, the polarization of the light was rotated by an angle that was proportional to the intensity of that field. In 1961, the reciprocal effect, called the inverse Faraday effect, was predicted by Pitaevskii[3] in non dissipative mediums. Only a few years later, experimental confirmation of a static magnetization solely induced by the light was given[4]. In the recent years, thanks to the advance of ultrafast high–intensity light sources, new regimes of light–matter interactions, in which the matter is put far away from thermodynamical equilibrium were reached. Within this framework, Beaurepaire *et al.*[5] discovered in 1996 that such a light could demagnetize a thin film of Ni in less than 1 ps, which, up to this day, remains the fastest way of influencing the magnetization state of the matter. This discovery started an intense research, both theoretical and experimental, regarding the origin of this phenomenon. This field of study got even further invigorated after the discovery of the so–called all–optical helicity–dependent switching, *i.e.* the possibility of manipulating the magnetic states of metallic magnetized thin films by using only light pulses in a ferrimagnet thin film made of gadolinium, iron and cobalt[6]. A few years later Mangin *et al.*[7] discovered the presence of the all–optical helicity–dependent switching in a wide variety of thin film alloys, where the magnetic ordering, the heterogeneity of the composition of the thin film, as

well as the type of atoms were changed without affecting its presence[7]. Notably, this type of switching can be obtained even without the presence of rare earth atoms, and more specifically in a granular media of iron and platinum which, due to its large magnetic anisotropy, is a good candidate for future information storage technologies[8].

Nevertheless, to fully harness the technological possibilities given to us by the aforementioned phenomena, their understanding is required and this thesis falls within this framework. Mostly relying on *ab initio* density functional theory, as well as its time–dependent counterpart, we will theoretically investigate multiple aspects of both the light–induced ultrafast demagnetization, as well as the helicity–dependent switching. We will see that the physics involved in their description is very broad as it includes aspects of light–matter interaction theory, nonequilibrium physics and, of course, magnetism.

Chap. 2 is dedicated to both the experimental and theoretical state of the art of the main areas of contribution of this thesis which are the ultrafast light–induced demagnetization and the all–optical helicity–dependent switching. Indeed, as it is mostly the case in physics, experiments and theory have been guiding each other and, as a consequence, one could not be understood without the other. We start this section by mentioning the early experimental results of the light–induced ultrafast demagnetization, after what the different experimental investigations of its origin are reviewed. Then, we move on to the review of the literature on the all–optical helicity–dependent switching. In this section we will argue that the understanding of the latter cannot be undertaken without knowledge about the mechanisms of the light–induced demagnetization, as both phenomena occur concurrently. A particular attention will be given in the distinction between the all–optical helicity–dependent switching, which, as aforementioned, occurs in a wide range of magnetic thin films and is one of the objects of study of this thesis, and the all–optical helicity–independent switching, whose occurrence is far more restricted and which is not examined in this manuscript. The second part of this chapter will develop the theoretical treatments of the aforementioned phenomena. After discussing the phenomenological 2 and 3 temperature models, which have been among the most profusely used models in the literature in order to rationalize both the ultrafast demagnetization and the all–optical helicity–dependent switching, we will detail the possible microscopic origin of the reduction of the magnetization. These can be divided in effects that induce a decrease of the magnetic moment carried by each atom, and effects that generate a random tilt of the latter, thus reducing the average magnetization. Then, we review the possible helicity–dependent effects, which adding up to the aforementioned ones, can possibly lead to the all–optical helicity–dependent switching are other related effects. This chapter is concluded by a summary of the current theoretical elements allowing us to rationalize the experimental results. Doing so, we highlight their shortcomings and where this thesis has contributed.

In Chap. 3 we introduce the reader to the theory on which relies most of the work in this thesis, *i.e.* density functional theory. It provides us with an exact framework allowing for a great simplification in the resolution of the many–body Schrodinger equation without, in principle, the use of any approximation. Using this, one can find the electronic density of the ground state of real materials, as well as their quantum observables, which can be expressed as functionals of the electronic density. Nevertheless, in practice one

has to rely on approximations in order for this theory to be of any practical use. These, as well as the general scheme used in this work are reviewed, and the application of the latter to magnetic material, in which this thesis is interested in, is detailed. The real–time time–dependent counterpart of this theory, used in Chap. 7 to compute the effect of circularly polarized light is then reviewed.

Chap. 4, 5, 6 and 7 report the contributions of this thesis. The first two of them focus on the behavior of the magnetization when the electronic temperature is elevated. Indeed, as extensively argued in Chap. 2, the light is primarily absorbed by the electrons, which are then considered as "hot" as compared to the other degrees of freedom of the material not interacting with the light. Within the framework of density functional theory, this can be accounted for by a change in the electronic temperature. Doing so, in Chap. 4, we found that upon an increase of the latter, a reduction of the length of the magnetic moment occurs on each atom, up to the so–called Stoner temperature varying from 3100 K to 8100 K in Fe, Co, Ni and FePt $L1_0$, where the magnetization disappears completely. However, for some compounds, the consequences of this phenomenon are noticeable on the electronic energy and specific heat even at low electronic temperature. Consequently, large deviations from the Sommerfeld approximation and from some previous work that did not take into account explicitly the dependence of the electronic structure on the electronic temperature are shown. These results are of interest in the field of laser-induced ultrafast magnetization dynamics, as they provide a more precise estimate of the electronic specific heat that enters in the aforementioned three-temperature model, and show that a longitudinal relaxation of the magnetization solely due to a rise of the electronic temperature is unlikely. In Chap. 5, we use *ab initio* density functional theory to study the effect of a rise of the electronic temperature on the states of the magnons, which are transversal magnetic excitations in periodic solids. We find that such a change in the electronic temperature results in a decrease of the eigenvalues of the magnons, which, in turn, translates in a decrease of the interatomic Heisenberg exchange. Then, using the latter and the Langevin atomistic Laudau–Lifshitz equation, we compute the dynamics of the atomic magnetic moments as a consequence of a pulse of light. We show that the increase in the electronic temperature can, indeed, account for a significant part of the demagnetization, as it lowers the magnetic order without the need for the bath of the magnons to rise in temperature, as traditionally assumed in the three–temperature model[5].

Chap. 6 and 7 examine the effect of circularly polarized light on the magnetization. In Chap. 6, we use density functional theory and the Fermi golden rule to quantitatively compute the effect of optical light absorption in ferromagnetic materials. In a first part, we differentiate this effect from the inverse Faraday effect which is traditionally invoked in the literature as being responsible for the all–optical helicity–dependent switching. Indeed, very differently from the latter, this mechanism is due to absorption and therefore remains present in the material even after the light is gone. Then, we show that, in the presence of spin-orbit coupling, optically induced transitions do not conserve the magnetization and that a systematic induced demagnetization, whose magnitude depends on both the helicity of the light and the direction of the magnetization, is observed. Before concluding, in Chap. 7, we use *ab initio* real–time time–dependent density functional theory to investigate the effect of optical and XUV circularly polarized femtosecond pulses on the magnetization dynamics of ferromagnetic materials. We show that the light always induces a reduction of the length of the magnetization, which is helicity–dependent. In

the XUV regime, were the 3p semi–core states are involved, we find a greater helicity–dependence, which persists even after the light is gone. Then, we proceed to the separation of the part of the helicity-dependent dynamics due to the absorption from the part owing to the inverse Faraday effect. Doing so, we show that the former has, overall, a greater impact on the magnetization than the latter, especially when the light is vanishing, and in the XUV regime.

Finally, in Chap. 8, we conclude by summarizing our main findings and we discuss the many possible developments that could follow this thesis.

Chapter 2

State of the art

2.1 Introduction

This chapter focuses on the review and interpretation of the existing literature on the ultrafast light–induced demagnetization as well as the light–induced helicity–dependent manipulation of the magnetization. While the work presented in this thesis brought contribution to both of these topics, the layout of this chapter is also imposed by the fact that a review of the latter cannot be conceived without an understanding the former.

We start by reporting the experimental results, beginning with the ultrafast light–induced demagnetization. This field of study appeared, concurrently to the emergence of intense femtosecond light sources, with the work of Beaurepaire *et al.*[5], who showed that a light pulse of only a few tens of femtoseconds could demagnetize a thin film of Ni in less than 1 ps. This result came as quite a surprise as it had the potential to greatly improve the speed of manipulation of the magnetic state which, as proved several years later, reaches its limits when the magnetic field has a duration of less than 2.3 ps[9]. As a consequence, an intensive search for the origin of the ultrafast demagnetization started. Many leads are currently followed by experimentalists, who are trying to disentangle the contribution of diverse magnetic excitations, as well as the role of the so–called "hot–electrons". Generated by the light, they exhibit very singular properties, such as the capability to propagate almost ballistically over several hundreds of nanometers.

A few years after the discovery of Beaurepaire *et al.*[5] came the first exhibition[10] of a light–induced polarization–dependent magnetization dynamics in the oxide $DyFeO_3$. A thorough review of these phenomena goes beyond the scope of this work and has already been undertaken by Kirilyuk *et al.*[11, 12]. On the other hand, this chapter focuses on dissipative materials, which have shown an even more drastic helicity–dependent effect, allowing for the manipulation of the magnetization by only using the light and its polarization. This phenomenon, named the all–optical helicity–dependent switching (AO–HDS), by opposition with the helicity–independent switching (AO–HIS), occurs in a wide range of different magnetic thin films[7, 8], differing both in their magnetic ordering, the heterogeneity of the structure, and the types of atoms. Notably, the AO–HDS has been observed in granular $L1_0$ FePt thin films, which, due to their high anisotropy, are very good candidates for future information storage technologies. As the ultrafast light–induced demagnetization, the AO–HDS still remains mysterious and could be the consequence of other helicity–dependent effects such as the helicity–dependent domain wall displacement and the helicity–dependent ultrafast demagnetization by which this section is concluded.

The second half of this chapter is dedicated to the theoretical aspects of the ultrafast light–induced demagnetization and the AO–HDS. It starts with the three temperature model. Initially used by Beaurepaire *et al.*[5] in order to rationalize the experimental results of magnetization dynamics in Ni, this model and its derivatives have then been used as a basis of many theoretical investigations of the ultrafast light–induced magnetization dynamics, notably together with micromagnetic calculations. Then, we detail the potential microscopic phenomena from which the ultrafast demagnetization could originate. These can be separated into two main effects on the magnetization: (1) reduction of the length of the magnetic moment carried by each atom (2) random tilt of the magnetic moment of each atom resulting in a cancellation of the average magnetization. (1) can be due to the Elliott–Yafet phenomenon, in which the electron flips its spin when scattering with a phonon, or to the ballistic propagation of hot–electrons carrying their spin angular momentum in the process. On the other hand, (2) is, as in the framework of the three temperature model, usually associated with a transfer of heat from the electrons to the magnons.

Then, we move on to the review of the possible phenomena, from which the experimentally seen helicity–dependence can arise. The first phenomenon reported is a consequence of the magnetic circular dichroism, which designates a helicity–dependent absorption of the light in magnetic materials. In this framework, while the origin of this difference is purely optical, the consequence on the magnetization dynamics is accounted for by a difference of temperature in domains featuring different magnetic orientations. This could help to stabilize the less absorbing direction of the magnetization, and therefore induce a helicity–dependent behavior. The second phenomenon, and the most invoked in the literature, is the inverse Faraday effect. Originally predicted by Pitaevskii[3] in non–dissipative and non–magnetic medium, it describes the induction of a magnetic moment in the medium where the circularly–polarized light propagates. It has later been generalized to dissipative mediums, however making this leap can lead to confusion regarding the nature of this effect, and its role in the light–induced dynamics. Therefore, after reviewing the related work, we discuss the boundaries of the inverse Faraday effect, which will allow us to differentiate it from the novel effect described in Chap. 6 of this thesis.

Finally, in the last section, we proceed to the review of the real–time time–dependent density functional theory applied to the light–induced ultrafast magnetization dynamics. This powerful method already allowed for a better understanding of the light–induced dynamics, and was even able to predict new phenomena. In this thesis, and more specifically in Chap. 7, the time–dependent density functional theory has been used to assess the contribution of different helicity–dependent effects in the real–time dynamics. However, we argue that its current limits are preventing a full description of the light–induced dynamics, especially in magnetic materials.

2.2 Ultrafast demagnetization

2.2.1 Early work

The study of light–induced ultrafast magnetization dynamics started in 1996 with the work of Beaurepaire *et al.*[5]. They pumped a polycrystalline thin film of Ni having a thickness of 22 nm with 60 fs light pulses. In order to investigate the behavior of the

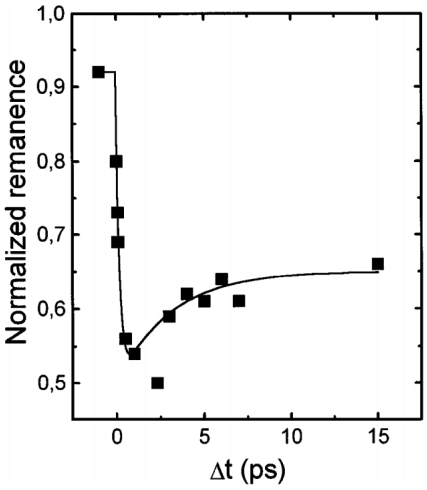


FIGURE 2.1: Transient remanent longitudinal MOKE signal of a Ni(20 nm)/MgF2(100 nm) film for 7 mJ/cm^2 pump fluence. The signal is normalized to the signal measured in the absence of pump beam. The line is a guide to the eye. Image and caption extracted from Ref. [5].

magnetization, they made use of the Kerr effect and probed the system at different delays after the pump. Fig. 2.1 shows the magneto–optical Kerr effect (MOKE) signal for a laser fluence of 7 mJ/cm^2. As this signal was thought to be proportional to the magnetization, they concluded that a rapid decrease of the magnetization resulted, as a consequence of the pump, followed by a slower recovery.

However, this proportionality between the MOKE signal and the magnetization is true at equilibrium, and the fact that this relationship stays valid during and shortly after such intense and short light pulses can be questioned. Koopmans *et al.*[13] investigated both the induced ellipticity and the rotation, and showed that, indeed, the signal they obtained was not in agreement with the proportionality hypothesis. More theoretical and experimental work followed in order to understand the relevance of the MOKE signal in the study of the light–induced ultrafast dynamics, and we refer the interested reader to the Sec. 4.4 of the review of Carva *et al.*[14]. Despite this issue, these surprising results have been reproduced using alternative techniques such as two-photon photoelectron spectroscopy[15], second harmonic generation[16] and, later, X–ray magnetic circular dichroism (XMCD)[17].

These experimental results raised a lot of questions regarding the underlying phenomena involved in the ultrafast–demagnetization. As we will discuss it further in Sec. 2.4.1, 2.4.2 and 2.4.3 from a more theoretical standpoint, the main issues are to understand where the angular momentum of the magnetization dissipates and how the light triggers this dynamics. Regarding the former question, Beaurepaire *et al.*[5] introduced a three temperature model (3TM) (see Sec. 2.4.1) to describe the flow of energy absorbed from the laser. In this model, the degrees of freedom capable of storing heat are divided into the bath of the electrons, the phonons and the magnons. While in this model, no assumption is made regarding the flows of angular momentum, it is usually assumed that, as well as the energy, the angular momentum is transferred between these baths. In this framework, the work of Stamm *et al.*[17] is of a particular relevance. Indeed, their XMCD approach allowed them to detect the total angular momentum of the electrons, *i.e.* both the orbital and the spin moment. They evidenced a decrease of 70% of the total angular

momentum, which is not compatible with a transfer from the spin to the orbital moments. As a consequence, they attributed the origin of the reduction of the angular momentum of the electron bath to a transfer to the bath of the phonons. However, in 2004, Beaurepaire *et al.*[18] showed that, as a consequence of the demagnetization, a terahertz electromagnetic field is emitted. They suggested that this phenomenon plays an important part in the angular momentum conservation.

Still on the same matter, Bigot *et al.*[19] investigated the possibility of a demagnetization due to a direct interaction of the light with the magnetization. To this end, they used a Ni thin film having a thickness of 7.5 nm and a $CoPt_3$ thin film having a thickness of 15 nm. The main novelty of their work was to use a single pulse to both excite and probe the magnetic compounds. They used 48 fs pulses sent at a repetition rate of 5 kHz at different fluences and evaluated the response of the material by looking simultaneously at the rotation and ellipticity of the transmitted light. Surprisingly, they noticed an increased change in these values, as the intensity of the light increased. As a consequence, they proved that the influence of the light on the matter occurs in less than 48 fs.

In the next section, we will introduce the phenomenology of the ultrafast demagnetization, which has been recently exhibited by You *et al.*[20]. Then, in Sec. 2.2.3 and 2.2.4 the possible physical underlying mechanisms are discussed. The origin of the ultrafast reduction of the magnetization could result from one, or a combination of a reduction of the length of the magnetic moment carried by each atom in the matter, a tilt of these vectors resulting in a lower magnetization in average and/or the propagation of spin–polarized hot electrons. The reduction of the length of the magnetization is due to the creation of Stoner excitations resulting from a decrease of the exchange splitting, while the tilt is a consequence of the creation of magnons. The possible role of both of these excitations is the object of Sec. 2.2.3. Finally, the influence of ballistic spin currents is discussed in Sec. 2.2.4.

2.2.2 Phenomenology of the ultrafast demagnetization

In this section, instead of reviewing the different experimental pieces of work that have been produced in a chronological order, we will focus on some results which will serve as a lens through which the rest will be looked at.

To begin with, the work of You *et al.*[20] is particularly relevant because they managed to clearly identify three distinct dynamics occurring during the traditional light–induced demagnetization–remagnetization experiment. To do so, they studied the response of a 400 nm thick single–crystal film of Ni subjected to pulses having a duration of 45 fs and a wavelength of 800 nm. The dynamics was probed with both the time–resolved transverse–magneto–optical Kerr effect (TR TMOKE) and the angle–resolved photo–emission (TR ARPES). The MOKE signal allowed them to access the time–dependent magnitude of the magnetization and the ARPES technique to follow the band structure dynamics, and thus, the value of the exchange splitting. Such a study had already been performed in the past[21], however, contrary to most of the literature on the topic using a two or three temperature model to describe the dynamics, You *et al.* decomposed it using a sum of two or three exponential decays, depending on the fluence of the laser:

$$m(t_d, z) = 1 + a_1(z)e^{-t_d/\tau_{demag}} - a_2(z)e^{-t_d/\tau_{recover1}} - a_3(z)e^{-t_d/\tau_{recover2}}, t_d \geq 0. \qquad (2.1)$$

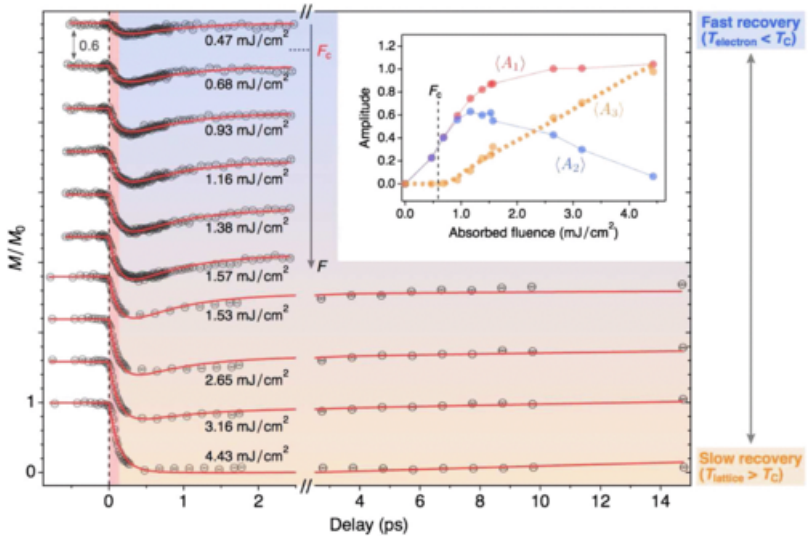


FIGURE 2.2: Magnetization dynamics in Ni measured using TR TMOKE over a full range of laser fluences. The highest fluence is sufficient to fully suppress the sample magnetization. The data are offset for clarity. Red curves: Fits to our microscopic model which considers the critical behavior, as well as the depth-average effects in the TR-TMOKE measurements. Inset: Fluence-dependent amplitudes of the demagnetization and recovery processes directly extracted from the TR-TMOKE results. In the TR-TMOKE results, the magnetization M and the extracted amplitudes $\langle A_1 \rangle$, $\langle A_2 \rangle$, and $\langle A_3 \rangle$ are averaged over the entire probed depth (see text). The dashed yellow line highlights the linear relation of the amplitude $\langle A_3 \rangle$ to the absorbed fluence when the fluence is above the critical fluence. Image and caption extracted from Ref. [20].

In this equation, $m = \frac{M}{M_0}$ is the normalized magnetization, t_d is the time delay after the pump, and z is the depth. The first decay time, τ_{demag}, corresponds to the rapid quenching of the magnetization, which the authors assumed to be due to a collapse of the exchange splitting. The two others, $\tau_{recover1}$ and $\tau_{recover2}$ are respectively the fast and slow recovery times and a_1, a_2 and a_3 are the amplitude of these different phenomena. The necessity of accounting for the depth emerges from the fact that the quantity of absorbed energy decays exponentially with it and that the TR-MOKE signal reflects the magnetization state of the bulk with a varying (and decaying with the depth) weight, as expressed by:

$$\langle M \rangle (t_d) = \frac{\int_0^\infty m(t_d, z) W(z) dz}{\int_0^\infty W(z) dz}, \tag{2.2}$$

with $W(z)$, the depth sensitivity function of the TMOKE.

The particularly interesting discovery of the authors is that, using the previously developed framework, the same value of the parameters τ_{demag}, $\tau_{recover1}$, $\tau_{recover2}$, and some proportionality constant to a_1 and a_2 allowed them to fit the MOKE signals for all the fluences. Fig. 2.2 shows the experimental data, the corresponding fitting, and, in the inset the values of $\langle A_1 \rangle$, $\langle A_2 \rangle$, and $\langle A_3 \rangle$, which are the bulk averaged values of a_1, a_2 and a_3. As the three timescales are fluence independent, the dynamics can unambiguously be decomposed into the three aforementioned phenomena.

Intriguingly, the slow recovery process only appears when the fluence reached a given value, F_c. You *et al.*, as Tengdin *et al.*[21] before them, attributed this feature to the fact that the electronic temperature, T_e, crossed the Curie temperature, T_C. However, the fact that below F_c, the average magnetization is able to relax to its original length in less than 2 ps indicates that the temperature of the lattice has not increased, which is in contradiction with the light induced heating and the fact that the electron–phonon coupling occurs in the picosecond time–scale[22].

Finally, both You *et al.*[20] and Tengdin *et al.*[21] attributed the origin of the demagnetization to a light–induced reduction of the exchange splitting, in which case the relevant ordering temperature would no longer be T_C, but rather the so–called Stoner temperature, T_S, which is significantly higher, as discussed in Chap. 4. In this context, the object of the next section is to review the experiments, which were aimed at disentangling the contribution of Stoner excitations and magnons generation in the light–induced ultrafast demagnetization.

2.2.3 Stoner and Heisenberg excitations

To this date, no consensus has been reached regarding the existence of a preponderant mechanism of the demagnetization. Interestingly, many authors using photoemission techniques leaned toward a reduction of the exchange splitting[23, 24, 21, 20], while others [25, 26, 27] argued that transverse excitations are more dominant.

In this context Turgut *et al.*[28] combined extreme UV TMOKE to probe the M edges of a 10 nm thick Co thin film to density functional theory calculation in order to disentangle the contribution of the magnons from Stoner excitations. To pump the system, they used a pulse having a duration of 40 fs while the probe was done with a pulse of 10 fs, which energy ranged from 40 eV to 72 eV. The principle of their study was to fit the experimental data by *ab initio* calculations. In these calculations, the effect of the electronic temperature was taken into account by changing the occupation of the different orbitals, as prescribed by the Fermi–Dirac distribution. Simultaneously, the Stoner excitations were artificially created by reducing the exchange splitting, and magnons by using noncollinear magnetic configurations. In these simulations, spin–orbit was taken into account and the semi–core $3p$ states, which were experimentally probed were included. By minimizing the root mean square deviation between the computed and the experimental spectrum, they could define which type of excitations were present at the peak of demagnetization (700 fs), and after 3 ps, when the magnetization recovered by 50%. Interestingly, they found that at 700 fs, the demagnetization was due to magnons at 66%, Stoner excitations at 25% and the rest to the rise of the electronic temperature. However, at 3 ps, after the decrease of T_e, an equal contribution of Stoner excitations and magnons was found.

Still on the search for the origin of the ultrafast light–induced demagnetization, Eich *et al.*[29] used the time-, spin- and angle–resolved photoelectron spectroscopy in order to study the dynamics of the valence bands of a Co thin film. The pump pulses had an energy of 1.6 eV and a duration of 74 fs, while the XUV probes had an energy of 22 eV and a duration of 33 fs. They showed that the spin polarization at a binding energy of 2.3 eV was very rapidly quenched (Fig. 2.3 (**B**)). However, as seen in Fig. 2.3 (**C**) and (**D**), they observed a clearly distinct and surprising dynamics for the majority and minority spins. While both spin states showed an increase of intensity above the Fermi energy, the majority spin intensity increased at a binding energy of 0.5 eV, where the bands are

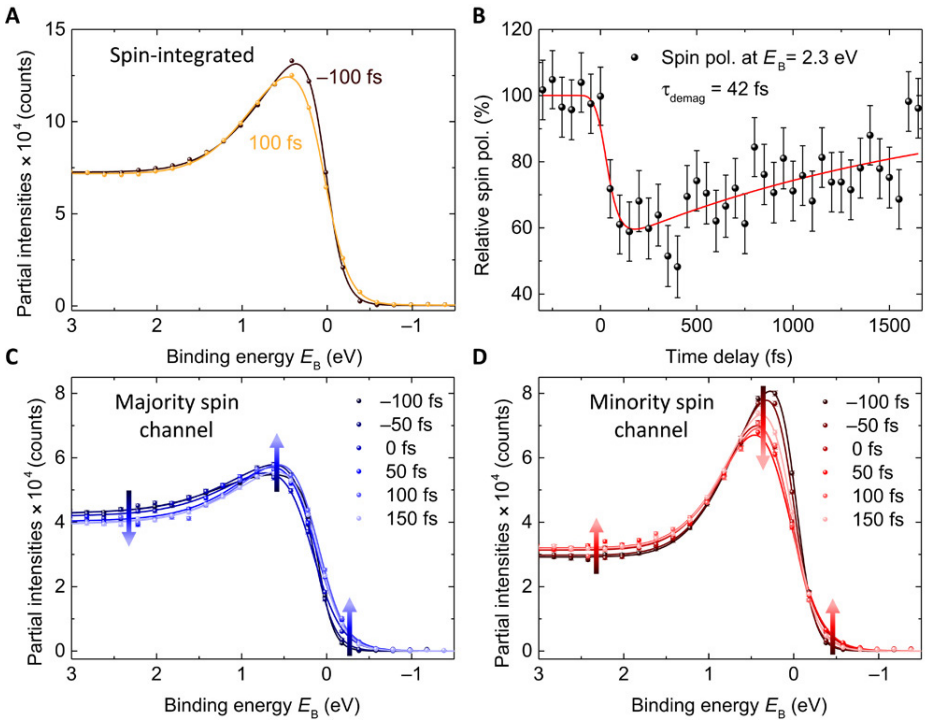


FIGURE 2.3: (**A**) Spin-integrated photoemission spectra of Co/Cu(001) (30 ML) before (-100 fs) and after (100 fs) optical excitation. (**B**) Spin dynamics extracted from the measured spin polarization at EB = 2.3 eV. (**C** and **D**) Partial intensities of majority- and minority-spin photoemission spectra as a function of time. Lines correspond to the fits, as described in the text, whereas the arrows indicate a decrease/increase in spectral weight. Image and caption extracted from Ref. [29].

localized. In a picture where the effect of the pump is to excite electrons above the Fermi energy, such a result comes as quite a surprise. Only the minority spins showed the expected decrease in intensity. Further down in binding energy, where the electrons are not impacted by the pump, their measurements exhibited the opposite behavior: The majority spin intensity decreased, while the minority increased.

To make sense of these results, Eich *et al.*[29] decomposed the unpumped (*i.e.* before the pump of the laser) signal in a background part and a peak part. To fit the background part, they used a Gaussian and a constant for the majority spins, and simply a constant for the minority spins. On the other hand, for both spin channels, the peaks were fitted with a Gaussian. Using this framework allowed them to assess if the demagnetization was Stoner–like or Heisenberg–like.

Fig. 2.4 (**A**) shows the position of the peaks representing the position of the spin up and spin down bands before and after the system had been pumped. As expected from a Stoner–like mechanism where the demagnetization results from a collapse of the exchange splitting, the majority spin band shifts upward, however, the minority band peak remains quite unchanged during the dynamics. These values are then used to change the initial positions of the peaks. Fig. 2.4 (**B**) shows that doing so at a time delay of 100 fs provides a rather weak agreement, especially regarding the spin polarization.

Next, Eich *et al.* tested the capability of transversal excitations in the fitting of the intensity obtained after 100 fs. As mentioned *supra*, such excitations correspond to magnons,

in which the magnetic moments are not ferromagnetically aligned anymore, producing a loss of the average magnetization. The consequences of such a phenomenon on the band structure is the so–called "band mirroring". Indeed, the tilt of the magnetic moment of each atom originates from a similar tilt of the spin of each electron participating in the creation of the resulting atomic moment. However, when such electronic states are projected on the initial quantization axis (giving the initial majority and minority bands) by the spin detector, they partly appear as both up and down, while the spin integrated spectral intensity is conserved. As a consequence, if the change in the average magnetization is due to transversal excitations, the intensity after the pump of the majority and the minority spins, *i.e.* "$\text{Channel}_{\text{Maj}}$" and "$\text{Channel}_{\text{Min}}$", can be written as a linear combination of the initial ones, "$\text{Spectrum}_{\text{Maj}}$" and "$\text{Spectrum}_{\text{Min}}$":

$$\text{Channel}_{\text{Maj}} = A_{\text{Maj}} \cdot \text{Spectrum}_{\text{Maj}} + B_{\text{Maj}} \cdot \text{Spectrum}_{\text{Min}} \tag{2.3}$$

and

$$\text{Channel}_{\text{Min}} = A_{\text{Min}} \cdot \text{Spectrum}_{\text{Maj}} + B_{\text{Min}} \cdot \text{Spectrum}_{\text{Min}}, \tag{2.4}$$

where the values of A_{Maj}, B_{Maj}, A_{Min} and B_{Min} represent the proportion of the initial majority and minority spectrum respectively measured in the majority and minority channels.

As seen in Fig. 2.4 (**C**), which shows the evolution of the values of A_{Maj}, B_{Maj}, A_{Min} and B_{Min}, initially A_{Maj} and B_{Maj} are equal to one and then start to decrease, while simultaneously, A_{Min} and B_{Min} are raising from 0. Furthermore, as evidenced by Fig. 2.4 (**D**), this time, the fitting of the intensity at 100 fs after the pulse, as well as the spin polarization, are in very good agreement with the experimental data. As a consequence, the authors argued that the main source of demagnetization comes from the ultrafast generation of transversal excitations, *i.e.* magnons.

These results are in apparent contradiction with previous photoemission studies[23, 24, 21, 20], which were all attributing the origin of the demagnetization to a loss of exchange–splitting. However, they also allow us to trace the origin of this disagreement. Indeed, as seen in Fig. 2.4 (**A**), the splitting between the minority and majority peaks is clearly reduced after the pulse. However, the fact that such an effect can also be due to a redistribution of the spectral weight of both spin channels induced by band mirroring, and causing the apparent shift and broadening of these peaks, has previously been omitted.

2.2.4 The role of hot electrons

The common denominator of the multiple pieces of work reviewed *supra*, is that the light is always directly interacting with the probed area. However, one could wonder if a direct interaction between photons and magnetized matter is required to obtain the ultrafast demagnetization. For instance, it was postulated by Bigot *et al.*[19] that the photon field could directly interact with the spins carried by the electrons and participate to the demagnetization through relativistic effects. On the other hand, it is now common knowledge that such a simultaneously short and high intensity pulse is capable of generating a large amount of excited electrons, also named "hot electrons". These are the result of the

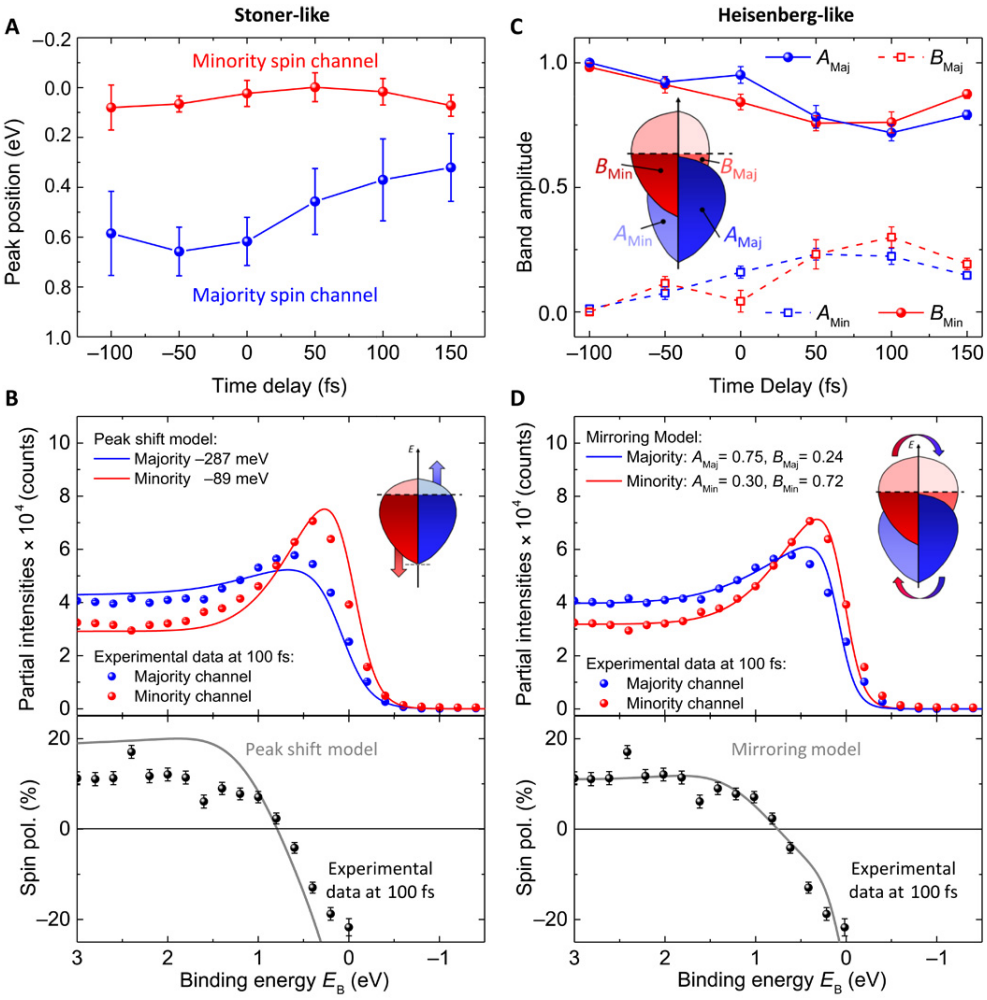


FIGURE 2.4: (**A**) Extracted energetic shifts of the majority and minority bands as a function of time. (**B**) Modeled majority and minority spectra (top) and spin polarization (bottom), if only energetic shifts are considered, in comparison to the measured experimental data at t = 100 fs. (**C**) Extracted amount of band mirroring. The scaling prefactors A_{Maj} and B_{Maj} (blue solid and red dashed lines) that were multiplied with the unpumped ("initial") majority and minority spectra, respectively, to fit the data of the majority channel after excitation are shown. One sees that the majority channel loses spectral weight from its initial majority spectrum and gains spectral weight from the initial minority spectrum accordingly. The same was carried out for A_{Min} and B_{Min} in the minority channel (blue dashed and red solid lines). (**D**) Same as (**B**), if only band mirroring is considered. Image and caption extracted from Ref. [29].

light–electrons interaction and therefore have an energy of a few eV and a velocity of approximately 1 nm/fs. This remarkable property of ultrafast transport was first evidenced by the pioneering work of Brorson *et al.*[30] in thin films of Au having multiple thicknesses. Shining a laser pulse on one side of the compound while simultaneously probing the reflectivity on the other, they showed that the delay between the pump pulse and the change in the reflectivity increased linearly. Such a phenomenon has to be differentiated from the more classical diffusion of heat, as in this case the delay would have increased as $\sqrt{\Delta t}$, where Δt is the delay. For this reason, such a transport is often referred to as ballistic. In this section, we will shortly review the role of hot electrons in the light–induced ultrafast demagnetization. First, through the prism of the transport of hot electrons, we propose an alternative interpretation of the work of You *et al.*[20]. Then, we review the effect of the presence of hot electrons on the magnetization, before finishing with their role in the transport of angular momentum. For an extensive view of this topic, we refer the interested reader to the work of Malinowski *et al.*[31].

To begin with, we would like to illustrate the possible role of the propagation of the hot electrons in the mitigation of the locally deposited laser energy. To do so, we come back to Sec. 2.2.2 where we reviewed the work of You *et al.*[20]. In this study, the authors claimed that the passage from a fast recovery regime to a slow recovery one was due to the rise of the electronic temperature over T_C. As an alternative explanation of this phenomenon, we would like to discuss the role of the propagation of hot electrons.

The authors used a very thick sample in order to minimize any effect of the interface and the substrate. However, while doing so, they simultaneously created a bigger volume in which hot electrons are able to propagate and relax. Indeed, experiments[30, 32, 33] and theory[34, 35] showed the effect of hot carriers and their capacity to rapidly propagate over long distances (at a speed of approximately 1 nm/fs), as reviewed below. As a consequence, the heating in the illuminated area is greatly reduced as the hot electrons are spreading over the whole volume. In this framework, which the authors did not mention, in the low fluence regime, *i.e.* below the critical fluence, F_C, the residual electronic temperature in the illuminated area is so quickly quenched, that almost no heat is exchanged with the phonons. As a consequence, the magnetization relaxes to its initial magnitude, *i.e.* without entering in the slow recovery regime. Such a scenario could be experimentally tested by gradually reducing the thickness of the sample, thus decreasing the volume over which the hot electrons spread. In such a condition, one would induce a transition into the second type of dynamics, involving a slower recovery. In fact, such an experiment has already been performed by Schellekens *et al.*[36] in another context, therefore, the authors did not explicitly comment on the impact of the thickness on the remagnetization dynamics. However, as seen in Fig. 2.7 (see Sec. 2.2.4), decreasing the thickness leads to the entrance in the so–called "slow recovery" regime. This experimental fact points toward the aforementioned scenario and shows the considerable role of the hot electrons.

Utilizing this fascinating property, Bergeard *et al.*[32] studied the magnetization dynamics of [Co(0.6 nm)/Pt(1.1 nm)]$_2$/Co(0.6 nm) induced only by hot electrons. To do so, they manufactured the thin films Pt(3 nm)[Co(0.6 nm)/Pt(1.1 nm)]$_2$/Co(0.6 nm)/-Cu(d)/Pt(3 nm) where d was varying from 0 to 300 nm. As seen in Fig. 2.5 (a), the sample was pumped on the side of Cu. These laser pulses had a duration of 35 fs, and were made of photons having a wavelength of 800 nm. This stack was manufactured with the aim of absorbing most of the light in the Pt layer which is situated on top of the Cu layer.

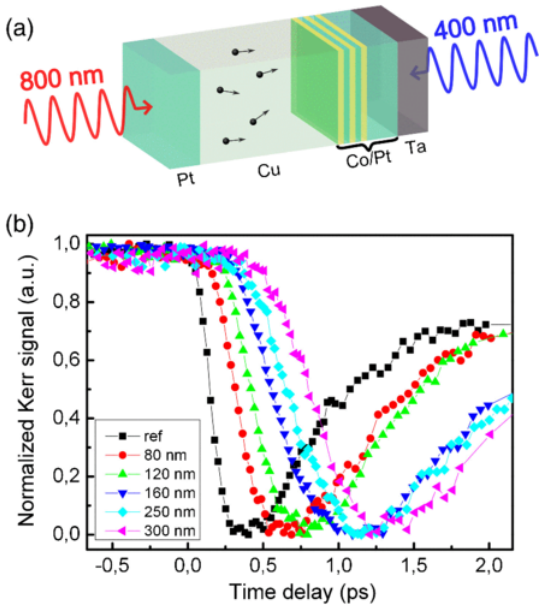


FIGURE 2.5: (a) Schematic representation of the multilayer structure. (b) Time evolution of the magneto-optical signal measurements for different Cu thicknesses. The laser power was adjusted to keep the maximum demagnetization constant for all samples, allowing for a normalization of the signal. Image and caption extracted from Ref. [32].

While Cu is far less absorptive than Pt, it confers a very long lifetime to the hot electrons coming from the Pt layer. This allows them to propagate through the Cu layer and reach the magnetized layers $[Co(0.6\ nm)/Pt(1.1\ nm)]_2/Co(0.6\ nm)$, contrary to the light. Indeed, as specified by the authors, in such a configuration the intensity of the pump at the magnetized layer is reduced by a factor 100 with d=80 nm. The dynamics of the magnetization was probed on the other side of the sample using the time resolved Kerr effect. Fig. 2.5 (b) shows the signal obtained for different thicknesses of the Cu layer. The beginning of the demagnetization occurred with a delay increasing linearly with d. This fact alone shows that: (a) as in the experiment of Brorson *et al.*[30], ballistic hot electrons (at a speed of $0.68 \cdot 10^6$ m/s in this particular case) are propagating through the Cu layer in the magnetized one. (b) The presence of hot electrons alone suffices in inducing the demagnetization in the magnetized layer. As in the initial experiment of Beaurepaire *et al.*[5], the author attributed this demagnetization to a transfer of heat from the hot electrons to the magnons, as described by the 2-3 temperature model (see Sec. 2.4.1). While the authors clearly proved that the main contribution to the demagnetization comes from a side effect of the light, *i.e.* the presence of hot carriers, the light also plays a more direct role in the demagnetization, as argued from a theoretical standpoint in Chap. 6 of this thesis.

However, and quite surprisingly, the interest of the community on the role of hot electrons in the ultrafast demagnetization has been triggered several years before the work of Bergeard *et al.*[32] by the discovery of a more subtle effect in which their role in the transport, and thus the conservation, of angular momentum was the object of interest. Indeed, it is in 2008 that the pioneering work of Malinowski *et al.*[37] showed that, along with energy, the propagation of hot electrons can also carry angular momentum and help the demagnetization of a multilayer. As seen in Fig. 2.6 (a), the authors engineered a

compound in which two identical magnetic layers of [Co (0.4 nm)/Pt(0.7 nm)]$_4$ were separated by a non magnetic third one, which was either made of Ru, a conductor, or NiO, an insulator. In both cases the thicknesses of the interlayers were chosen to obtain an antiparallel (AP) alignment as in the second sketch of Fig. 2.6 (a). To obtain the parallel (P) alignment, the authors applied a magnetic field of $\pm$ 150 mT. The ultrafast dynamics was induced and studied (using TR–MOKE) by pulses having a duration of 70 fs and a wavelength of 785 nm. Fig. 2.6 (b) shows the relative change in the Kerr rotation $\Delta\theta/\theta$, which is proportional to the change in the magnetic moment perpendicular to the thin film, starting from both an AP and a P state, and in the case of an insulator and a conductor spacer. While in the case of the insulator spacer, no difference was found in the dynamics obtained starting from the AP and the P state, there was a noticeable discrepancy in the case of the conductor spacer. Indeed, Malinowski *et al.* found that, starting from an AP configuration, the demagnetization was faster and larger. They attributed the origin of this phenomenon to the fact that light generates spin–polarized hot electrons going from each magnetized layer to the other, where their polarization is determined by the polarization of the layer in which they were created, as depicted in Fig. 2.6. As a consequence, in the AP state, hot electrons of opposite polarization are flowing in both layers, thus helping the demagnetization. However, this difference of induced demagnetization only persists for approximately 0.5 ps, duration after which both Kerr signals overlap again. This fact, along with a quasi–similar demagnetization amplitude obtained in the case of an insulator spacer indicates that the main source of the demagnetization was not produced by a local depletion of the angular momentum carried by the ballistic propagation hot electrons, but rather an ultrafast generation of transversal excitations, as argued in Chap. 5 of this thesis. Regardless, this experiment raised the attention of the community regarding the role played by hot electrons during the demagnetization.

Notably, it led Battiato *et al.*[34, 35] to develop a framework in which the main contribution to the demagnetization would be a spin–dependent ballistic superdiffusive propagation of the electrons. As reviewed in more details in Sec. 2.4.2.2, based on the fact that the lifetime of hot majority spin carriers is longer than the one of the minority carriers, Battiato *et al.* made a classical model arguing that such a discrepancy in the lifetime would be enough to induce a rapid depletion of the majority spin carriers within the exposed area. Indeed, as their propagation is favored compared to the minority hot carriers, the former are leaving the exposed area faster than the latter, which are trapped by more frequent scattering events. Soon after, experimentalists took over and started to investigate the magnitude of such a phenomenon. To this end, Melnikov *et al.*[38] used a thin film made of Au/Fe/MgO. Using a pulse having a duration of 35 fs and a wavelength of 800, they pumped the thin film from the side of the MgO, while probing the Au on the other side. Doing so, they detected an induced spin polarization in Au, which they attributed to a spin–polarized flow of hot electrons originating from the Fe layer and propagating in Au. Later, on a similar ground than the experiment of Bergeard *et al.*[32] reviewed *supra*, Eschenlohr *et al.*[39] manufactured the thin film [Au(30 nm)/Ni(15 nm)/Al]. As Bergeard *et al.* the goal was to absorb the majority of the pump in the Au layer, such that only non–polarized hot electrons would propagate to the Ni layer. However, as in the framework of Battiato *et al.*[34, 35], hot electrons having a spin aligned with the polarization of Ni would be able to propagate through the layer and reach the Al layer, while the rest of the hot electrons, which have a minority spin polarization, would scatter and be trapped in the Ni layer. A side effect of this electron–electron scattering is the so–called

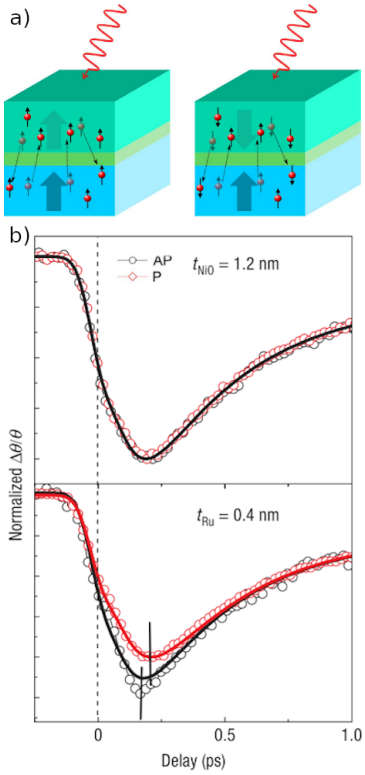


FIGURE 2.6: (a) Schematic representation of laser excited electrons transport in magnetic heterostructures. (b) Normalized Kerr signal measured for parallel (P – diamonds) or antiparallel (AP – circles) alignment of the magnetizations. Image and caption adapted from Ref. [37].

electron cascade, in which more excited electrons are generated. Among these, the ones which are majority spin polarized will be able to escape the Ni layer, further amplifying the demagnetization. According to the authors, it is the accumulation of minority spins and the simultaneous depletion of majority spins in the Ni layer which would be wholly responsible for the ultrafast demagnetization. Then, using the theory of Battiato *et al.*[34, 35], the author reproduced the observed magnetization dynamics. However, as pointed out by Khorsand *et al.*[40], a mistake made in the computation of the absorption of the light lead Eschenlohr *et al.* to strongly overestimate the absorption of the Au layer. As a consequence, a significant portion of the pump intensity reached the Ni layer.

Still on the investigation of the role of ballistic hot electrons and their spin polarization in the light–induced ultrafast demagnetization, Schellekens *et al.*[36] investigated a Ni thin film deposited on an insulating sapphire substrate in order to confine hot electrons inside the Ni film. The principle of their experiment was, as pictured in Fig. 2.7 (a), to pump the film respectively from the front and from the back, while always probing the front. Such an experiment can help disentangling the role of spin transport in the demagnetization. Indeed, if the main mechanism of the demagnetization is the propagation of spin polarized hot electrons, while in the case of a front pump and probe a classical demagnetization dynamics is expected, in the case of a front probe and a back pump the opposite behavior would have to occur, *i.e.* an increase of the magnetization should be noticed as ballistic majority spins are flowing from the back to the front. The dynamics was studied using the TR MOKE with pulses having a duration of 75 fs and a wavelength of 780 nm. The results of the front and back pulses are respectively seen in Fig. 2.7 (b) and (c). In direct contradiction with the aforementioned scenario, the authors found a rapid and similar demagnetization in both cases, occurring on a timescale of 100 fs, followed by a remagnetization on the picosecond timescale. Moreover, as seen in Fig. 2.7, even though the same laser fluence is used in every case, the maximum demagnetization decreases as the thickness of the sample increases. The author attributed this phenomenon to a decrease of the averaged absorbed light, which occurs as the thickness of the sample increases. However, the fact that the demagnetization dynamics is similar in the case of a back and a front pump means that the hot electrons redistribute homogeneously the energy deposited by the light within the sample thickness. More than the absence of any possible role of the spin current in the demagnetization in these compounds, this is a proof that, in this case, the presence of hot electrons is entirely responsible for the demagnetization. This is in accordance with the work of Bergeard *et al.*[32] and our interpretation of the work of You *et al.*[20] reviewed *supra*.

While the role of hot electrons in a single Ni layer is mostly to redistribute and homogenize the energy deposited by light, Rudolf *et al.*[41] and Turgut *et al.*[42] almost simultaneously showed a spectacular effect demonstrating the presence of spin current in a multi-layer of Ni/Ru/Fe. In Fig. 2.8 (a) can be seen the result obtained by Turgut *et al.*[42]. In their experiment, they used XUV light to probe the magnetization with the Kerr effect. This allowed them to selectively probe the magnetization of the Fe and Ni, as their M edges are respectively at ≈ 53 eV and ≈ 67 eV. In this case, the multilayer was [Ta (3 nm)/Fe (4 nm)/Ru (1.7 nm)/Ni (5 nm)] and the magnetization of the Fe layer and the Ni layer were parallel. The sample, pumped from the side of Ni, displayed a very singular dynamics as, while Ni followed the usual demagnetization pattern, the magnetization of Fe increased. Such a phenomenon is well explained by the propagation of spin polarized hot electrons from the Ni layer, to the Fe layer. To better understand this

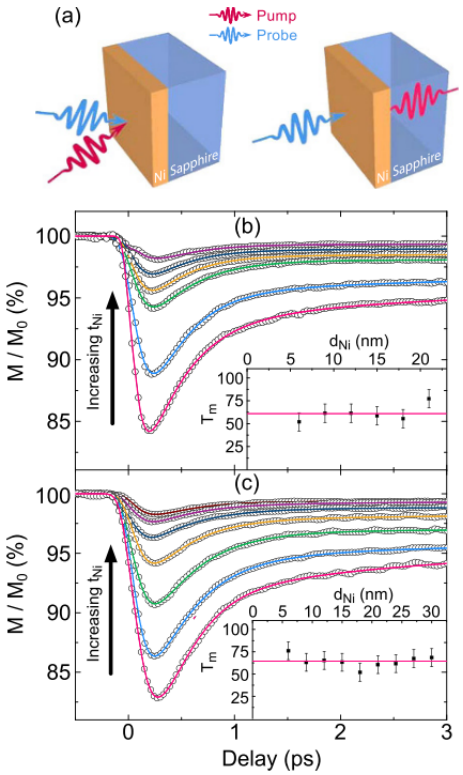


FIGURE 2.7: Magnetization as a function of time after pulsed laser excitation from the front (a) and from the back (b) for various thicknesses of the Ni film d_{Ni}. The insets shows the extracted demagnetization times as a function of d_{Ni}. Image and caption extracted from Ref. [36].

behavior, we calculated the absorption profile in the stack used by Turgut *et al.*[42]. As stated by the authors, since the energy absorbed in the Ni layer and in the Fe layer are roughly similar the question then becomes: Why would there be a dominant spin current flowing from Ni to Fe rather than the opposite, or any at all? As the authors pointed it out, the presence of the scatterer at the bottom of the stack and an insulator (Si_3N_4) at the top could induce such a behavior, as in the latter case, the electrons propagating upward are reflected, while in the former case, those propagating downward are absorbed. This could favor a downward flow. To further investigate the role of this downward spin current, Turgut *et al.* then changed the Ru spacer for Ta (2 nm), W (2 nm) and Si_3Ni_4 (3 nm). The first two mentioned serve as scatterer, *i.e.* they mostly let hot electrons flow, but they neutralize the spin polarization. As seen in Fig. 2.8 (b), (c), the magnetization of the Fe layer is now decreasing, while the magnetization of Ni is still reduced by more than half. More interestingly, in the case of the insulating spacer Fig. 2.8 (d), the magnetization of Ni is now even further reduced. This clearly indicates that while the spin polarization of hot electrons can play a role in the demagnetization, it is not the main source of magnetization loss. Another interesting point to notice is the resilience to the demagnetization of Fe relatively to Ni. While it can be imputed to the fact that Fe has a higher Curie temperature than Ni, many other factors can come into play as discussed in Chap. 5 of this thesis.

2.3 Experiments exhibiting helicity–dependence

2.3.1 All–optical switching

Two years after the discovery of a light–induced helicity–dependent magnetization dynamics in an oxide by Kimel *et al.*[10], Stanciu *et al.*[6] found that the magnetization state of a thin film made of the ferrimagnetic alloy $Gd_{22}Fe_{74.6}Co_{3.4}$ can be entirely reversed by only using a circularly polarized light. Indeed, illuminating the sample with circularly left (σ^+) or right (σ^-) polarized light pulses allowed them to deterministically select one of the two opposite magnetization states aligned along the out of plane anisotropy axis. As this final state depended on the helicity of the light and not on the initial state, this phenomenon has been named "all–optical helicity–dependent switching" (AO–HDS). In 2011, Radu *et al.*[43] showed that, in the same alloy with a different composition, a linearly polarized single light pulse can induce a full reversal of the magnetization, phenomenon, which is now known as the "all–optical helicity–independent switching" (AO–HIS) or as toggle switching.

In this section we start by reviewing these founding experimental results. Then, we mention the work that followed and allowed for a better understanding of these phenomena. We will argue that the underlying mechanisms of the AO–HDS and the AO–HIS are distinct. This fact will allow us to narrow down the focus of this chapter on the AO–HDS and other helicity–dependent effects, which have a more universal character.

In the discussion that follows, unless stated otherwise, sub 100 fs laser pulses having both a spatial and temporal Gaussian profile, and a photon energy of ≈ 1.55 eV, were used. Likewise, all the thin films were exhibiting a sufficiently large perpendicular magnetic anisotropy (PMA) to stabilize the direction of the magnetization out of the plane of the thin film.

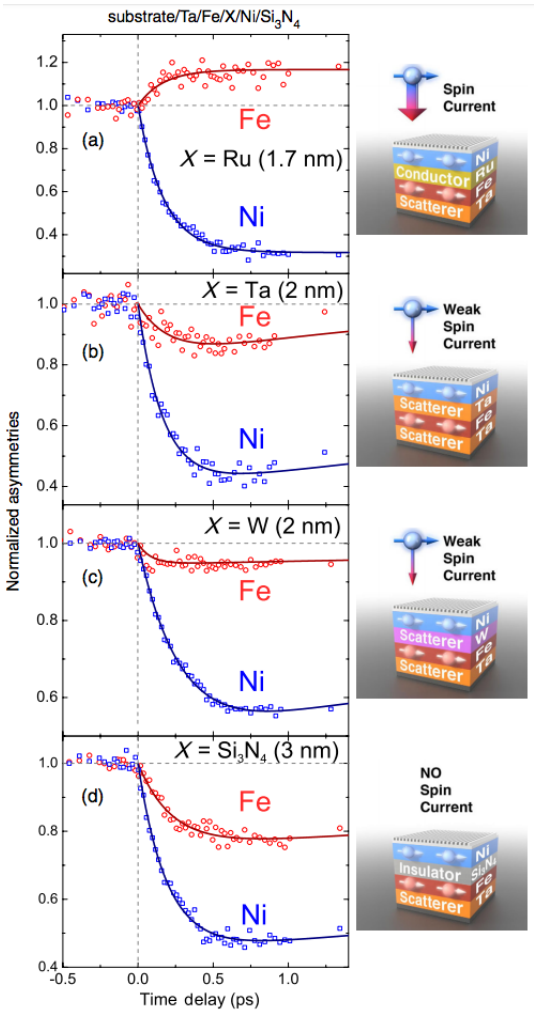


FIGURE 2.8: Layer-selective magnetization dynamics in substrate/Ta(3 nm)/Fe(4 nm)/X/Ni(5 nm)/Si_3N_4(6 nm) multilayers with different spacer layers. In (a), clear enhancement in the magnetization of the Fe layer is observed in the presence of good spin transport across the 1.7 nm Ru spacer layer. In (b) and (c), no enhancement of the magnetization of the Fe layer is observed when spin scattering spacer layers of Ta (2 nm) and W (2 nm) are used. In (d), spin currents are fully suppressed by inserting a 3 nm insulating Si_3N_4 layer. Image and caption extracted from Ref. [42].

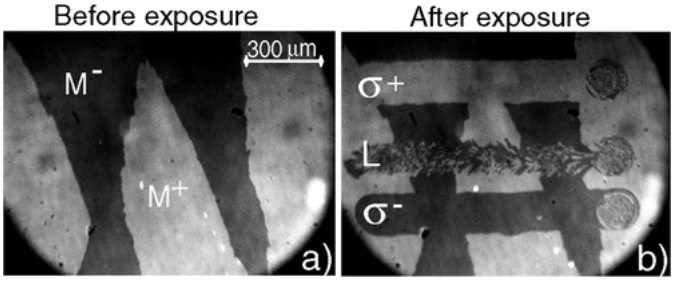


FIGURE 2.9: The effect of ultrashort polarized laser pulses on magnetic domains in $Gd_{22}Fe_{74.6}Co_{3.4}$. (a) Magneto-optical image of the initial magnetic state of the sample before laser exposure. White and black areas correspond to up (M^+) and down (M^-) magnetic domains, respectively. (b) Domain pattern obtained by sweeping at low speed ($\approx 30\ \mu$m/s) linear (L), right-handed (σ^+), and left-handed (σ^-) circularly polarized beams across the surface of the sample, with a laser fluence of about 11.4 mJ/cm^2. The central area of the remaining spots at the end of each scan line consists of small magnetic domains, where the ratio of up to down magnetic domains is close to 1. Image and caption extracted from Ref. [6].

2.3.1.1 The singular case of GdFeCo ferrimagnetic alloys

GdFeCo ferrimagnetic alloys were the first to exhibit both the AO–HDS and the AO–HIS. It is amorphous and the magnetic moments of the Fe and Co atoms are antiferromagnetically coupled to the ones of the Gd atoms. In 2007 Stanciu *et al.*[6] showed that, by sweeping a train of femtosecond laser pulses on a 30 nm thick $Gd_{22}Fe_{74.6}Co_{3.4}$ thin film, the final state of the magnetization, *i.e.* after the sweeping, was deterministically governed by the helicity of the employed light.

Fig. 2.9 shows the initial and final state of the magnetization, seen with Faraday imaging. Initially, the sample has stripes of up and down magnetic domains, revealed by their different color (light gray and dark gray). The sweeping is then done perpendicularly to these stripes, such that for all of the three polarizations of the light (σ^+, σ^- and L), its effect is seen starting from both an up and a down initial state. In Fig. 2.9 b), we see that for a σ^+ (σ^-) polarized light, the final state of the swept area is always up (down), irrespectively of the initial state. However, when the light is linearly polarized, the swept area only exhibit a multidomain state, *i.e.* it is composed of many randomly distributed and shaped up and down magnetic domains, smaller than the size of the laser beam. This experiment clearly proves the helicity–dependence of the effect. Finally, as for every polarization of the light, the laser was applied from left to right, three demagnetized spots are visible on the right of the image, at the position where the laser was turned off. It is showing that at the center of the laser, where the fluence is the highest, the final state is again, a multidomain state, even for the σ^+ and σ^- polarization. As a consequence, the switching must be occurring in a ring surrounding this multidomain area.

To further investigate this effect, Stanciu *et al.* focused the laser beam in a fixed location situated on a domain wall, as in Fig. 2.10. For each polarization of the light, the main effect is the formation of a multidomain state at the center of the illuminated area, which is revealed by the Faraday microscope as a grey color (in between the light grey and the dark grey of the up and down domains). However, in the case of the two circular polarizations, the presence of the helicity–dependent effect is noticeable inside the switching

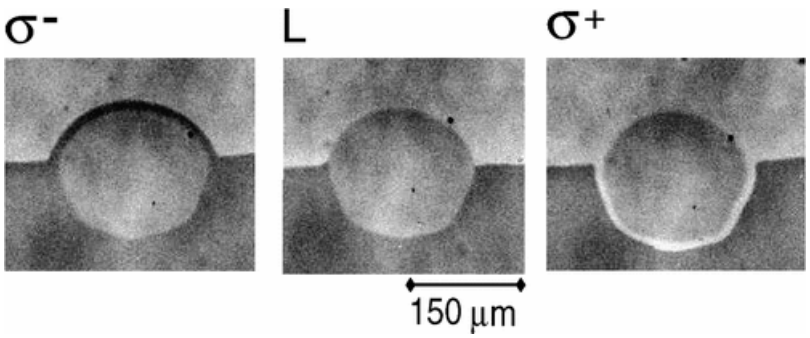


FIGURE 2.10: Images of the laser spot focused onto a domain wall during the 1 kHz pulsed laser excitation with linear (L), right- (σ^+), and left–handed (σ^-) circular polarization. The images were obtained for a pulse fluence of about 11.4 mJ/cm^2. In all three cases the central region of the optically excited area is demagnetized (gray color) due to extensive heating. For circularly polarized excitation (σ^+ and σ^-) opto–magnetic switching takes place on the perimeter of the excited area, where the temperature is just below T_C. Image and caption extracted from Ref. [6].

ring surrounding the multidomain state. This hints toward the fact that, as Stanciu *et al.* pointed it out, the helicity–dependent effect of the light may require to be thermally activated. This point will be elaborately developed later.

In 2011, Radu *et al.*[43] demonstrated the presence of a new type of light induced magnetization dynamics in a 30 nm thick $Gd_{25}Fe_{65.6}Co_{9.4}$ alloy. In this experiment, they used a single, linearly polarized light pulse in order to trigger the dynamics. They showed that such a stimulus is enough to fully reverse the magnetization of the illuminated area each time it is applied. As this effect only depends on the initial state of the magnetization and not on the polarization of the light, it has been named all–optical helicity–independent switching (AO–HIS). Using the x–ray magnetic circular dichroism (XMCD), they were able to analyze the dynamics of the Gd atoms and the Fe atoms separately. These measurements showed a very singular behavior, where the magnetization of Fe collapsed within 300 fs, while it took as long as 1.5 ps for the magnetization of Gd to do the same. Furthermore, during this dynamics, the two sublattices of Gd and Fe, initially antiferromagnetically coupled, became aligned.

Similar results have been obtained one year later by Ostler *et al.*[44] on a 20 nm thin film of $Gd_{24}Fe_{66.5}Co_{9.5}$, which is a slightly different composition than in Ref. [43]. In Fig. 2.11, they show the initial and final magnetization state after the application of one to five pulses on the same area. The light grey color corresponds to a down magnetization state and the dark grey to the opposite one. Indeed, starting from a down (up) magnetization, it illustrates that each time a pulse is applied, the reversal of the illuminated area occurs. Therefore, for an even number of pulses shone at the sample, the initial magnetization state is recovered.

Until 2017 and the work of Lalieu *et al.*[45], the AO–HIS had only been exhibited in GdFeCo ferrimagnetic alloys. They showed that such a phenomenon could also occur in Pt/Co/Gd stacks where the Pt seed layer induces PMA and the Co and Gd layers are antiferromagnetically coupled. The minimal fluence required to achieve the switching was significantly lowered due to the reduction of the Co layer thickness.

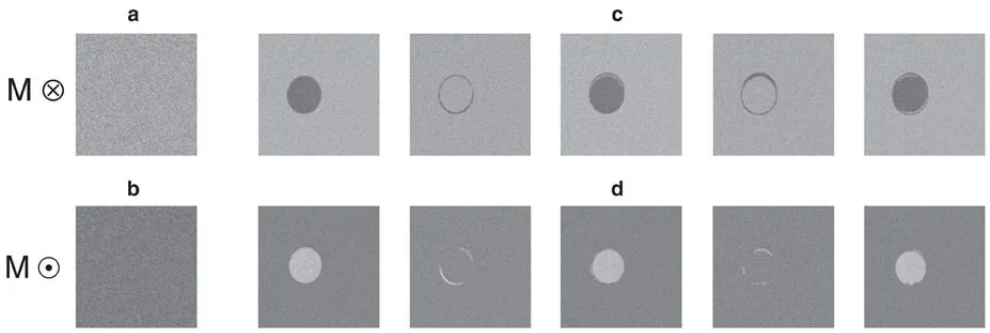


FIGURE 2.11: (a) and (b) Initial homogeneously magnetized state of the film with magnetizations 'up' and 'down' as represented by the circled dot and cross respectively. The light grey region represents magnetization pointing 'down' and the darker grey 'up'. (c) and (d) The film after an excitation with N (N=1, 2...5) pulses with a fluence of 2.30 mJ cm^{-2}. Each laser pulse excites the same circular region of the film and reverses the magnetization within it. The scale bar on the right corresponds to 20 μm. Image and caption extracted from Ref. [44].

2.3.1.2 From helicity–dependent to helicity–independent switching in GdFeCo

Following the initial discovery of AO–HDS by Stanciu *et al.*[6], Vahaplar *et al.*[46] investigated the origin of the effect on a 20 nm thin film of $Gd_{24}Fe_{66.5}Co_{9.5}$ alloy. In the experiment, seen in Fig. 2.12, they pumped the film with a single circularly polarized light pulse. In Fig. 2.12, an up magnetized state is shown as a light gray color, while a down magnetized state is represented by a dark grey color. Starting from both magnetization states, they showed that pumping the film with a σ^+ or a σ^- light pulse leads to a different final state. Indeed, when the magnetization was initially up (down), a σ^+ (σ^-) polarized light induced a switching, while a σ^- (σ^+) polarized light did not. Inspired by the discovery of Kimel *et al.*[10], their rationalization of this phenomenon relies on the fact that, due to the inverse Faraday effect (see Sec. 2.4.4.2), a circularly polarized light generates an effective magnetic field of opposite direction for σ^+ and σ^-, which would allow the light to stabilize one of the two magnetization states. However, Fig. 2.12 exhibits a final state, where the magnetization is fully reversed inside a circle, and by only a single pulse, *i.e.* much like the results of Ostler *et al.*[44] which followed several years later, rather than the AO–HDS discovered initially by Stanciu *et al.*[6].

Later on, Khorsand *et al.*[47] questioned the relevance of attributing the origin of this helicity–dependent behavior to a light induced magnetic field, as in the inverse Faraday effect since, at this time, this phenomenon had only been proved in dissipationless and non–magnetic mediums[3] (see Sec. 2.4.4.2). Instead, they argued that such a helicity–dependent phenomenon could originate from a difference of absorption between the different polarizations of the light, due to magnetic circular dichroism (MCD) (see 2.4.4.1). Pointing out the equivalence in the induced dynamics of using of a σ^+ (σ^-) polarized light on a up (down) magnetized state, they fixed the initial state to up and varied the polarization. Then, for a range of wavelengths of the light, they studied the probability of reversing this initial state as a function of the fluence and the polarization. As seen in Fig. 2.13, the switching probability as a function of the fluence for a σ^+, σ^- and a linearly polarized light differs substantially. The σ^+ (LC) polarization induces a switching

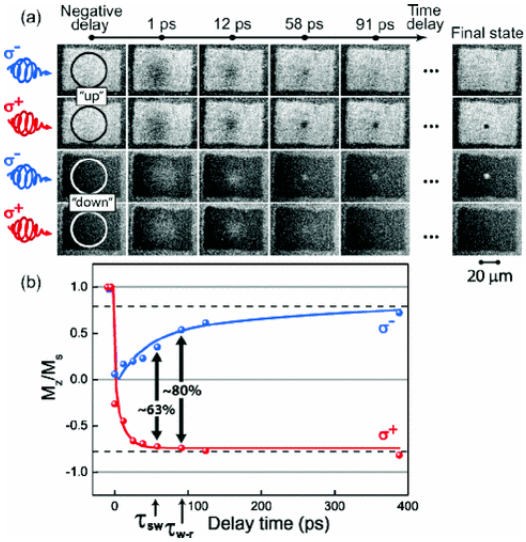


FIGURE 2.12: The magnetization evolution in $Gd_24Fe66.5Co_9.5$ after the excitation with σ^+ and σ^- circularly polarized pulses at room temperature. The domain is initially magnetized up (white domain) and down (black domain). The last column shows the final state of the domains after a few seconds. The circles show areas actually affected by pump pulses. (b) The averaged magnetization in the switched areas (5 μm) after σ^+ and σ^- laser pulses, as extracted from the images in (a) for the initial magnetization up. Image and caption extracted from Ref. [46].

as soon as the fluence reaches 3.95 mJ/cm^2. Further increasing the fluence then allows the linearly polarized light, and finally at 4.02 mJ/cm^2, the σ^- (RC) polarized light to do the same. The range of fluence where the σ^+ polarization switches the magnetization, while the opposite polarization does not, is where the helicity–dependent effect exists. They defined this window as:

$$\Delta = \frac{F_{RC} - F_{LC}}{\frac{1}{2}\left(F_{RC} + F_{LC}\right)} \tag{2.5}$$

where F_{LC} and F_{RC} are the switching thresholds for a σ^- and a σ^+ polarized light, as defined in Fig. 2.13. They found that Δ = 1.5 % for almost the whole wavelengths ranging from 500 nm to 800 nm. To relate the origin of this phenomenon to the presence of MCD, they computed the difference of absorbed energy for both polarization of the light with:

$$MCD = \frac{A_{LC} - A_{RC}}{A_{LP}} \tag{2.6}$$

where A_{LC}, A_{RC} and $A_{LP} = \frac{1}{2}$ (A_{RC} + A_{LP}) are the absorption rates of a σ^+, a σ^- and a linearly polarized light. Their experimental results indicate that $MCD \approx \Delta$ for the whole wavelengths ranging from 500 nm to 800 nm. These results demonstrate that in this case, the possibility of switching is only determined by the absorbed energy, which differs for the different polarizations of the light, rather than a direct helicity–dependent effect such as the IFE or the magnetic moment induced during the absorption of the light (see Chap. 6 and 7 of this thesis). This is further evidenced by the fact that a linear polarization of the light also induces a switching, which is not the case in the initial experiment of Stanciu

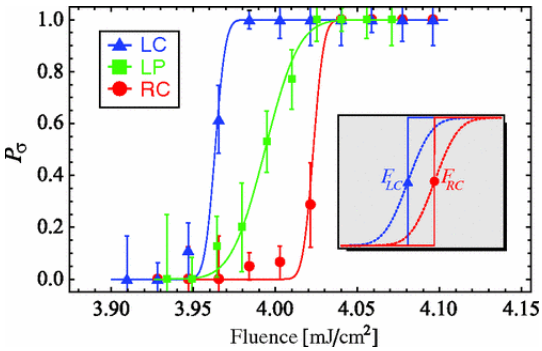


FIGURE 2.13: Switching probability P_σ as a function of the fluence at λ = 700 nm for three different polarizations. The measurements with *RC* and *LC* pulses were performed at a different time than the ones with *LP* pulses, and therefore the laser stability was different. Inset: Illustration of the switching probabilities in case of zero (solid) and nonzero (dashed) laser fluctuations using Eq. (1). F_{LC} and F_{RC} denote the switching threshold of GdFeCo for *LC* and *RC* excitation pulses, respectively. Image and caption extracted from Ref. [47].

et al.[6] shown in Fig. 2.9 b) in the case of a linearly polarized light. Therefore, as in the experiments of Radu *et al.*[43], Ostler *et al.*[44] and Lalieu *et al.*[45], Khorsand *et al.*[47] and probably Vahaplar *et al.*[46] were likely in presence AO–HIS rather than AO–HDS.

In order to disentangle the AO–HIS from the AO–HDS in GdFeCo alloys, Xu *et al.*[33] studied the film Gd_x $(FeCo)_{1-x}$ (20 nm)/Pt (Y nm) where x = 20.6% and 20.9% and Y = 5, 15, 25 nm. They sent the light pulses at a repetition of 5 kHz, and the magnetization state was seen through a microscope using the magneto–optical Kerr effect. They showed that, using a linear polarization for the light with a 5 nm Pt layer, both Gd concentrations and a fluence of 2.68 mJ/cm^2, only the typical AO–HIS behavior was present. Increasing the Pt layer thickness to 25 nm, the AO–HIS behavior is partially recovered by raising the fluence to 3.58 mJ/cm^2 and is fully present at 4.02 mJ/cm^2. Further increasing the fluence induces a multidomain state at the center of the pulse, where the intensity is the highest, which is surrounded by the ring where the AO–HIS occurs. What makes these results particularly interesting is the emergence of the AO–HDS when increasing the fluence on the same samples where the AO–HIS is seen. This demonstrates the fact that the AO–HIS and AO–HDS are occurring at different fluences and thus that the underlying causes are different.

Before concluding, a brief summary of this section may be valuable. Indeed, reviewing the main experimental results related to GdFeCo alloys, we showed that two very distinctive types of switching were exhibited. The AO–HIS is particularly puzzling because of the fact that the magnetization reversal is usually driven by a torque produced by an applied vector stimulus such as a magnetic field, an electric field or a current. However, in this case, heating alone is enough to manipulate the magnetization. This has been further evidenced by Xu *et al.*[33], by showing that the switching can be generated by hot–electron pulses and that therefore direct electron–photon interaction inside the GdFeCo is not required. Furthermore, until the recent work of Banerjee *et al.*[48], who found toggle switching in the half–metallic compensated ferrimagnetic Heusler alloy Mn_2Ru_xGa, the AO–HIS toggle switching was only achieved in the presence of Gd atoms. It is assumed

that what makes the singular behavior of Gd, such as its slow demagnetization rate, is its lack of orbital angular momentum, and thus its very low spin–orbit coupling. On the other hand, the AO–HDS has been achieved in a very wide variety of materials, as we will see shortly in Sec. 2.3.1.3.

2.3.1.3 Helicity–dependent switching in thin film metals

Before the work of Alebrand *et al.*[49], the AOS had only been evidenced in GdFeCo alloys. One particularity of these alloys is their weak PMA. While this may be one of the features which allows for the AOS to occur, it is a strong limiting factor regarding its possible applications in future information storage technologies. However, the discovery of AO–HDS in the high–anisotropy Tb_xCo_{1-x} ferrimagnetic alloys by Alebrand *et al.*[49] showed that weak PMA is not required. Indeed, replacing Gd atoms by Tb atoms, which are located on the right of Gd atoms in the periodic table allowed for a stronger PMA. They assessed the possibility of AO–HDS by sweeping the surface using long (10 ps) and short (400 fs) pulses with a wavelength of respectively 532 nm and 780 nm with a repetition rate of 5 kHz, much as in the experiment of Stanciu *et al.*[6]. Varying the composition of the thin film from x = 12% to x = 34 % they showed that AO–HDS can occur only with 23 % $<$ x $<$ 26 % when using 400 fs light pulses, and with 23 % $<$ x $<$ 30 % when using 10 ps light pulses. Interestingly, for all these concentrations of Tb, T_{comp}, the temperature at which the magnetization of the two sublattices of the ferrimagnet exactly compensate each other, is always above the room temperature. However, as the authors are pointing it out, the higher T_{comp} is, the less energy is needed to switch the magnetization. The possibility of extending the range of Tb concentration where the AO–HDS is exhibited by using longer light pulses is thought–provoking regarding the underlying mechanisms allowing for such a phenomenon, as it evidences that the helicity–dependence is stronger when the pulse lasts longer. This can be understood by the fact that, the longer the duration of the pulse, the more the material will be subjected to the rotations of the electric and magnetic field defining the circularly polarized light.

A year later, Hassdenteufel *et al.*[50] studied Tb_xFe_{x-100} alloys thin films with 19 % $<$ x $<$ 38.5 %. The light pulses, sent with a repetition rate of 250 kHz, had a duration of 100 fs and a wavelength of 800 nm. In order to test the presence of AO–HDS, they used the sweeping experiment, as Stanciu *et al.*[6]. They found that AO–HDS only occurs when 22% $<$ x $<$ 34 %. Contrary to the work of Alebrand *et al.*[49], this range of composition includes samples having a T_{comp} both above and below the room temperature, and even more surprisingly, samples without T_{comp} at all, invalidating this criterion as a requirement for the AO–HDS. They argue that instead, the relevant parameter to be considered should be the remanent magnetization, M_R. Such a criterion does not contradict the one regarding T_{comp}, as when the temperature is near T_{comp}, the macroscopic magnetization is small. The threshold fluence, at which the laser induces a multidomain state or a helicity–dependent switching decreases when M_R increases, fact that can also be seen in the work of Alebrand *et al.*[49].

Shortly after, Mangin *et al.*[7] dramatically widened our knowledge of the range of materials and structures exhibiting AO–HDS. Indeed, while previous studies focused on thin film alloys made of the rare earth (RE) antiferromagnetically coupled to transition metals (TM), they demonstrated that the AO–HDS also works in antiferromagnetically coupled RE/TM multilayers, heterostructures and even RE free synthetic ferrimagnets,

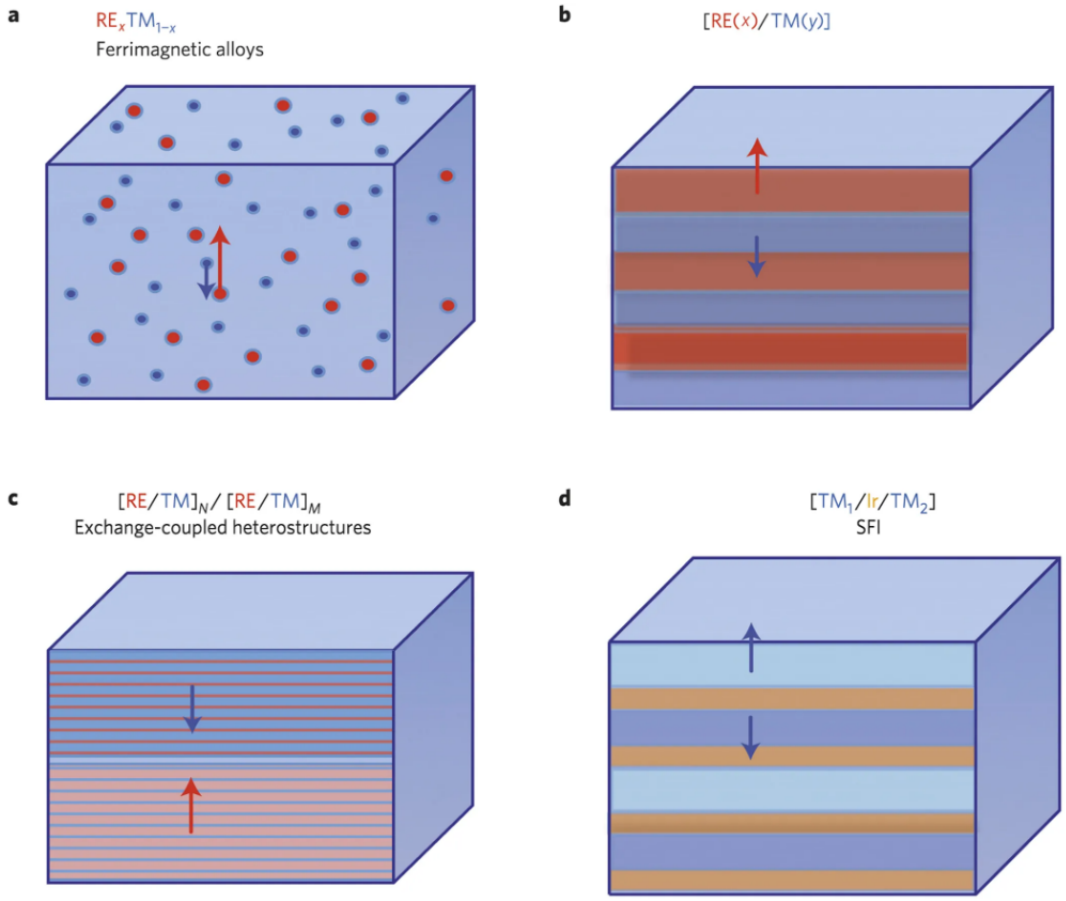


FIGURE 2.14: **a**, Thin-film RE–TM alloys. **b**, $[RE/TM]_N$ multilayers. **c**, Exchange-coupled $[RE/TM]_N/[RE/TM]_M$ heterostructures. **d**, SFI made of two TM layers antiferromagnetically coupled through 0.4 nm Ir interlayers. Each type of magnetic structure has shown either AO-HDS or thermal demagnetization depending on the thickness, layer structure and/or atomic concentration of the sample. Image and caption extracted from Ref. [7].

as shown in Fig. 2.14. Doing so, they studied more than 400 separate samples having widely different magnitudes of spin–orbit coupling, exchange coupling, magnetization and anisotropy.

As pictured by the green stars in Fig. 2.15, they observed AO–HDS in the ferrimagnetic alloys Gd_xFeCo_{1-x}, Tb_xCo_{1-x}, Dy_xCo_{1-x} and Ho_xFeCo_{1-x}, proving that this behavior is general. In agreement with the work of Alebrand *et al.*[49] when they used 400 fs pulses, Mangin *et al.* found that AO–HDS was occurring in Tb_xCo_{1-x} for 23 % $<$ x $<$ 26 %. The shaded blue area in Fig. 2.15 represents the range of composition where T_{comp} is below the room temperature. Only HoFeCo exhibits AO–HDS whereas its T_{comp} is not strictly above the room temperature.

Next, they investigated the presence of AO–HDS in antiferromagnetically–coupled multilayer structures, as depicted in Fig. 2.14 **b**. The magnetization in [Gd/Co] lied in plane as soon as the Gd thickness exceeded 1 nm, however for [Tb/Co] and [Ho/CoFe], the strong PMA allowed them to increase the thicknesses up to 3 nm. They found that AO–HDS works in these multilayers, thus proving the resilience of this phenomenon to the heterogeneity of the systems. Indeed, keeping the same average composition and

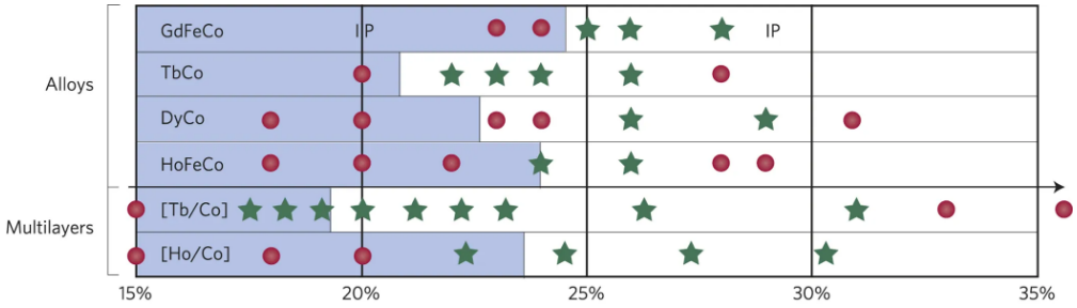


FIGURE 2.15: Response to optical excitation for RE–TM alloys (Gd_xFeCo_{1-x}, Tb_xCo_{1-x}, Dy_xCo_{1-x}, Ho_xFeCo_{1-x}) and two types of RE–TM multilayer ([Tb/Co] and [Ho/CoFe]) as a function of the RE concentration (x). RedRed dots indicate thermal demagnetization and green stars AO–HDS. All of these alloys show perpendicular anisotropy except the two GdFeCo alloys marked IP (for in-plane anisotropy). The shaded regions correspond to alloy compositions for which T_{comp} is below room temperature. For the multilayers the RE layer thicknesses varied from 0.3 to 0.5 nm and the TM layers varied from 0.25 to 1.0 nm. Image and caption extracted from Ref. [7].

thickness, the AO–HDS was exhibited both in [Tb(0.3 nm) / Co(0.3 nm)]$_{\times 42}$ and in [Tb(2.5 nm) / Co(2.5 nm)]$_{\times 5}$. Fig. 2.15 also shows the switching capability of [Tb/Co] and [Ho/Co] as a function of the RE composition. The thicknesses of the RE and TM layers varied respectively from 0.3 to 0.5 nm and from 0.25 to 1.0 nm. Surprisingly, the multilayers allowed for the presence of AO–HDS for a wider range of compositions, and even when T_{comp} was below the room temperature.

Going further on this inquiry, they tested the presence of AO–HDS in a compound made of a stack of [Tb(0.5 nm)/Co(0.45 nm)]$_N$/[Tb(0.35 nm)/Co(0.7 nm)]$_{25-N}$. Both stacks were antiferromagnetically coupled as pictured in Fig. 2.14 **c**. For $25 \leq N \leq 15$, AO–HDS was observed. A similar behavior was exhibited in [Tb(0.5 nm)/Co(0.45 nm)]$_N$/[Tb(0.35 nm)/Co(0.53 nm)]$_{25-N}$. In both cases, the authors related the location of T_{comp} near the room temperature with the presence of AO–HDS.

Last but not least, Mangin *et al.*[7] found AO–HDS in the RE–free [Co(t_1)/Ir/Co(0.4 nm)/Ni(0.6 nm)/Pt(t_2)/Co(0.4 nm)/Ir]$_N$ synthetic ferrimagnet.

Shortly after, Lambert *et al.*[8], evidenced the possibility of AO–HDS both in continuous and nanostructured ferromagnetic thin films, whereas until then, such a phenomenon had only been exhibited in ferrimagnets. They studied the response of [Co(0.4 nm)/Pt(0.7)]$_N$ multilayers with N = 3, 5 and 8. Fig. 2.16 A, B and C show the magnetization state of these samples after the laser had been swept on them. In every case, the initial configuration was made of two domains (up and down), such that the illuminated area spans both the initially up and down magnetized states for the σ^+, the σ^- and the linear (L) polarization. For N = 8, the sweeping only resulted in the formation of a multidomain state, independently of the polarization of the light. For N = 5, Lambert *et al.* also observed the formation of multidomain state, of which the sizes are larger than the ones obtained with N = 8. The helicity–dependence started to appear as, in the case of a σ^+ (σ^-) polarized light, the white (dark) domains appeared isolated on a black (white) background, whereas in the case of the linear polarization, both white and dark domains appeared at roughly the same rate. Finally, for N = 3, a full AO–HDS is evidenced, and, in the linear case, one can see the appearance of some large domains. These findings are in accordance

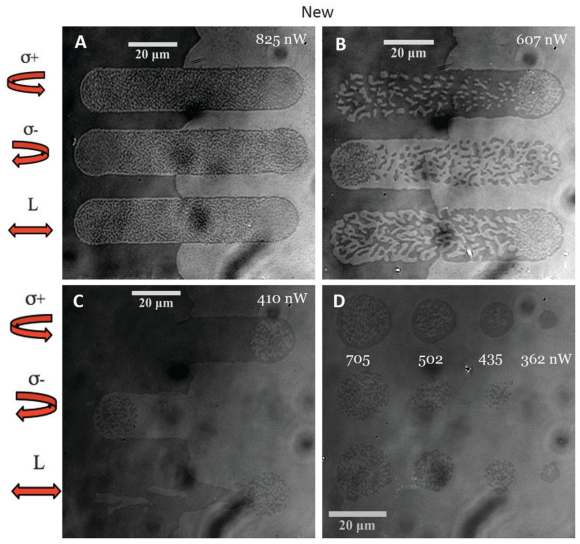


FIGURE 2.16: Magneto-optical response in zero applied magnetic field of $[Co(0.4\ nm)/Pt(0.7\ nm)]_N$ multilayer samples to various laser polarizations. (A) N = 8 repeats. (B) N =5 repeats. (C and D) N =3 repeats. For each image, the laser is circularly polarized (σ^+ or σ^-) or linear polarized (L). For (A) to (C), the laser beam was swept over a region of the sample with two perpendicularly oriented magnetic domains showing black/white contrast in the images, with a domain wall that runs vertically in the middle of each image. In (D), the laser was fixed at individual spots over a region of the sample with uniform magnetization (white contrast).The average laser intensity at different spots is indicated in the image. Image and caption extracted from Ref. [8].

with the remark of Hassdenteufel *et al.*[50], as well as the work of El Hadri *et al.*[51] regarding the fact that AO–HDS occurs when the magnetization is capable of forming large domains, as indeed, such a thing is made possible by the low remanent magnetization. Also, these results unambiguously prove that AO–HDS can occur without the presence of any T_{comp}, as already demonstrated by Hassdenteufel *et al.*[50], as the thin films used by Lambert *et al.* are ferromagnetic. In Fig. 2.16 D, the laser was maintained at a fixed location over the N = 3 thin film, where the magnetization was initially saturated in one of the two possible states. Various lasers power were used. It shows that for a σ^+ polarized light and the lowest fluence the light generated a single reversed domain, while for the other helicity, the magnetization was left unaffected. Further increasing the fluence induced a multidomain area surrounded by a ring where the magnetization was switched for σ^+, while for σ^- only a multidomain state appeared. These results are similar to those obtained in the initial work of Stanciu *et al.*[6] on GdFeCo ferrimagnetic alloys, shown in Fig. 2.9 and Fig. 2.10.

Moreover, they showed the presence of AO–HDS in $[Co(t_{Co})Pt(t_{Pt})]_N$, $[Co(t_{Co})/Pd(t_{Pd})]_N$, $[Co(t_{Co})/Pd(t_{Pd})]_N$, $[Co_xNi_{1-x}(0.6\ nm)/Pt(0.7\ nm)]_N$ and $[Co/Ni]_N$, proving the generality of this phenomenon amongst ferromagnetic thin films, as long as their thicknesses, and thus, their magnetizations are not too large. However, as pointed out by the authors, in order to have useful applications for such a technology, small magnetic grains or patterned bits having high magnetic anisotropy are necessary to allow for a lasting high–density storage of information. Some of the promising candidates for such a technology

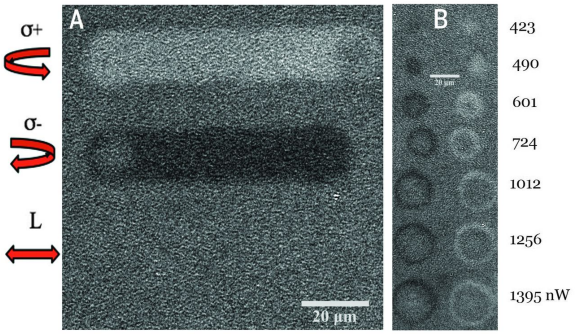


FIGURE 2.17: Magneto–optical response in zero applied magnetic field of a 15 nm FePtAgC granular film sample starting with an initially demagnetized sample. (A) Line scans for σ^+, σ^- , and linear polarized light (L). The laser beam was swept over the sample, and the magnetization pattern was subsequently imaged. (B) Images of magnetic domains written by keeping the laser spot at a fixed position on the sample. The laser was either σ^+ polarized (left column) or σ^- polarized (right column). The laser power was 677 nW. Image and caption extracted from Ref. [8].

are the FePtAgC and FePtC granular films, where the high–anisotropy FePt grains are isolated in the middle of the matrix of C atoms. Fig. 2.17 shows both the sweeping (A) and static (B) experiments on a FePtAgC film where the initial state of each grain was random, such that the overall magnetization is zero. Sweeping the surface with a σ^+ (σ^-) polarized light clearly revealed the presence of a helicity–dependent effect, as the Faraday imaging exhibited a lighter (darker) grey color than the initial one. However, they reported a saturation of only 10 to 20 % of the magnetization. Furthermore, in the case of a linearly polarized light, no change of the shade of grey was noticed, indicating that the initial randomized state had been preserved. The static experiment, Fig. 2.17 (B), also clearly revealed the presence of the AO–HDS. Indeed, at low fluence, a pure helicity–dependence appeared. Further increasing the fluence induced a switching ring where the helicity–dependent effect is effective, circling a zone where the magnetization of the grains stayed randomized. This clearly supports previous interpretations made in continuous thin films regarding the necessity of thermal activation of the AO–HDS. However, too much of a thermal activation leads to a loss of the helicity–dependent effect, thus forming the random magnetization state at the center of the laser spot, where the fluence is the highest.

The role of M_R has been further evidenced by Hassdenteufel *et al.*[52] by comparing the switching capabilities of the ferrimagnets' thin films of 16 nm $Tb_{29}Fe_{71}$ and $Tb_{34}Fe_{66}$. These compounds had a M_R of respectively 112 emu/cc and 230 emu/cc. While $Tb_{29}Fe_{71}$ exhibited switching at 300 K with a repetition rate of 10 kHz, $Tb_{34}Fe_{66}$ showed a totally different behavior. Indeed, at 300 K and with the same repetition rate, a pure thermal demagnetization was seen, however, increasing the repetition rate to 250 kHz allowed for a full recovery of AO–HDS. They imputed this phenomenon to the fact that such a repetition rate did not allow the sample to fully cool down. Therefore, the increased temperature lowered M_R, which in turn allowed for a recovery of AO–HDS. To verify this statement, they lowered the repetition rate to 10 kHz, while increasing the temperature of the sample to 345 K and 370 K. Doing so, Hassdenteufel *et al.* managed to first recover partially, and then fully the AO–HDS. Indeed, at 345 K and 370 K, the magnetization of the

$Tb_{34}Fe_{66}$ dropped down to 152 emu/cc and 106 emu/cc. Using this low remanence criterion, they explained the switching capabilities for the different composition of GdFeCo[6, 12, 53, 44, 54, 46, 55], TbFe[50] and TbCo[49] alloys used in the literature at this time. The authors also explained the appearance of switching in TbCo alloys when the duration of the pulses was increased from 400 fs to 10 ps by the fact that such a duration brings enough heat to allow for the magnetization to decrease during the pulse.

Recently, Kichin *et al.*[56] provided a detailed analysis of the effect of the pulse duration, fluence and size on the presence of AO–HDS. In their experiments, they used a Pt(0.7 nm)/Co(0.6 nm) thin film. The light was kept at the same location at all time. As seen in Fig. 2.18 (a), (b) and (c), this multilayer exhibited pure AO–HDS at a fluence of 8.3 mJ/cm^2, a AO–HDS ring surrounding a multidomain area at 9.1 mJ/cm^2 and, surprisingly, only thermal demagnetization when the fluence was further increased. The authors explained this absence of switching by the fact that, as the fluence has a Gaussian spatial profile, increasing it far away from the pure AO–HDS point reduces the surface where the fluence window is high enough to induce a switching, while at the same time low enough not to lose the helicity–dependent effect in thermal fluctuations. Indeed, upon an increase of the intensity, this surface first takes the shape of a disk and then a ring of decreasing thickness. This result can be bridged with the work of El Hadri *et al.*[51], in which they argued that the size of the laser spot should be smaller than the size of the domains in order for AO–HDS to take place. However, in this case this statement has to be nuanced, as the relevant quantity seems to be the size of the laser spot where the fluence is in the window allowing for the AO–HDS. Then, they looked at the cross section of the illuminated area for a laser spot having a diameter of 104 μm (Fig. 2.18 (d)) and 168 μm (Fig. 2.18 (e)) for different pulse durations, while increasing the fluence. For the smaller pulse diameter, they report no switching under a pulse duration of 200 fs, while for the larger diameter, AO–HDS was present even for a pulse duration of 40 fs. Fig 2.18 (d) and (e) clearly show that an increase of the pulse duration and of the pulse diameter favors the presence of AO–HDS. However, upon the increase of the duration of the pulses, an increase of the fluence is needed to recover the AO–HDS. As, for a given fluence, the increase of the duration of the pulses induces a decrease of the maximum intensity of the light, this fact suggests that reaching a threshold of intensity may be required to achieve the helicity–dependent switching.

Previous considerations about the pulse duration and the fluence are summarized in Fig. 2.19 for the case of a pulse diameter of 104 μm. The size of the window where the AO–HDS occurs increases with the pulse duration, as previously noticed by Alebrand *et al.*[49]. The fact that this increase is linear may suggest that the effect responsible for the AO–HDS also grows linearly with the fluency.

2.3.2 Domain wall displacement

Recently, a novel effect of the helicity of the light on the magnetization has been discovered by Quessab *et al.*[57]. The thin films Pt(4.5 nm)/Co(0.6 nm)/Pt(4.5 nm) and Pt(5 nm)/[Co(0.4 nm)/Pt(0.7 nm)]$_{\times 3}$/Pt(2 nm) were respectively pumped with light pulses having a duration of 40 fs and a diameter of 50 μm at a repetition rate of 5 kHz and with light pulses having a duration of 2 ps and a diameter of 45 μm at a repetition rate of 1 kHz. Using these experimental parameters, both samples exhibited AO–HDS at 0.04 mJ/cm^{-2} for Pt/[Co/Pt]$_{\times 3}$/Pt and 14.5 mJ/cm^2 for Pt/Co/Pt. The purpose of this work was to

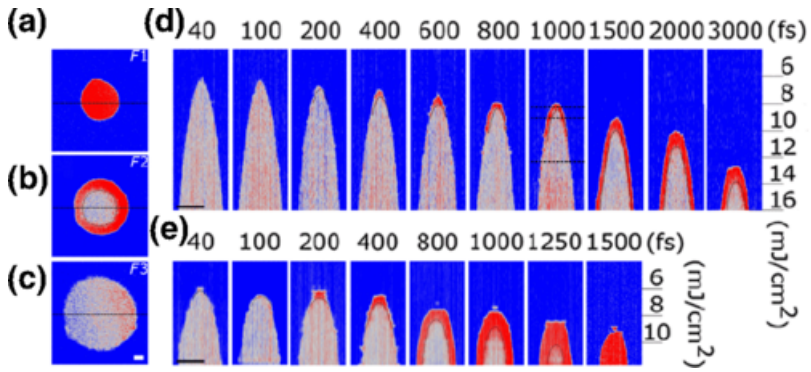


FIGURE 2.18: (a)–(c) Magneto-optical Kerr images obtained after exposing the sample to 600 laser pulses with a pulse duration of 1 ps, a σ^+ polarization, and laser fluences of 8.3 mJ/cm^2 (a), 9.1 mJ/cm^2 (b), and 12.3 mJ/cm^2 (c) corresponding to the lines in (d). The red and blue contrasts correspond to opposite perpendicular magnetization directions. (e)–(d) Cross section of the laser excited area for laser fluences between 4 and 18 mJ/cm^2 and various pulse durations for a laser spot diameter of 104 µm (d) and 168 µm (e). For (a)–(c), the white scale bar is 10 µm, for (d) and (e), the black bar is 50 μm. Image and caption extracted from Ref. [56].

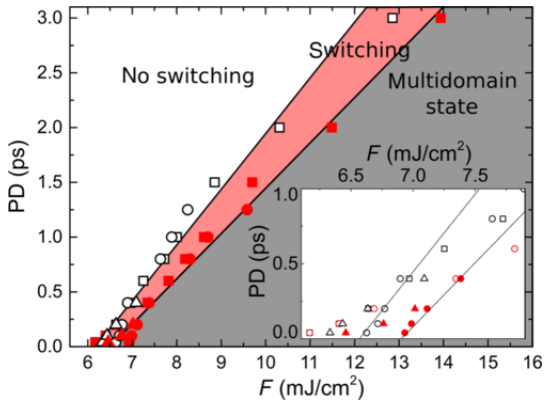


FIGURE 2.19: Magnetization state diagram as a function of the laser fluence, F, and the pulse duration, PD, for a circularly polarized static beam of different diameters (84 μm for triangles, 104 μm for square, and 168 μm for dots) illuminating a Co/Pt. For a given fluence, the maximum (minimum) pulse duration for which we have AO–HDS is plotted as filled (open) symbols. The inset shows a magnification of the diagram for the short pulse durations. Image and caption extracted from Ref. [56].

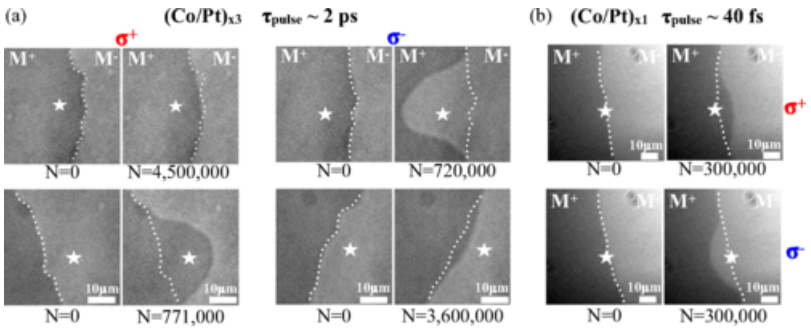


FIGURE 2.20: Magneto-optical images of domain wall motion in [Co (0.4 nm)/Pt (0.7 nm)]$_{\times 3}$ and [Co (0.6 nm)/Pt (0.7 nm)]$_{\times 1}$ induced, respectively, by (a) 2-ps and (b) 40-fs laser pulses with left-circular (σ^-) and right-circular (σ^+) polarization with an energy per pulse of 0.04 and 12.5 mJ/cm^{-2}. The white star indicates the center of the beam spot, and N is the number of laser pulses. The laser beam spot is (a) placed 10 μm away from the DW within a magnetization-up (M^+) or -down (M^-) domain or (b) centered on the wall. The dotted line shows the initial position of the domain wall prior to laser exposure. Image and caption extracted from Ref. [57].

investigate the effect of the polarization of the light on domain wall motion. To this end, a domain wall separating two large domains was initially created and the fluence was set below the previously mentioned thresholds such that any effect of the light on the magnetization was purely resulting from domain wall motions, instead of nucleation. The magnetic state was analyzed through a Faraday microscope such that the up magnetized state was represented by dark gray while the down magnetized state was represented by light gray, as seen in Fig. 2.20. To test the effect of the helicity on the domain wall motion, the center of the beam represented by a white star was alternatively focused slightly on the right and on the left of the domain wall. The Faraday images clearly show that the σ^+ (σ^-) polarization tends to propagate the M^+ (M^-) domain. Interestingly, the domain wall moved past the hottest point, located at the center of the laser spot. Fig. 2.20 shows that the same phenomenon was evidenced in the case of [Co/Pt], when the center of the beam is focused on the domain wall.

In order to gain a better understanding of this phenomenon, the authors examined the influence of a linearly polarized light on the domain wall motion. Fig. 2.21 (a), (b) and (c) show the influence of the light when the center of the beam is respectively focused on the domain wall, the left of the domain wall and the right of domain wall. In the first case, the domain wall is not moving, while in the two other cases it moves toward the center of the beam, and not past it, as in the case of the circularly polarized light. This experiment proves that a linearly polarized light purely acts as a source of heat. Indeed, as the domain wall moves toward the hottest spot[58, 59], it moves toward the center of the beam. To further investigate the role of the polarization of the light on the displacement of the domain walls, Quessab *et al.* varied the helicity from linear to σ^- to σ^+ by step of 10°, as shown in Fig. 2.21 (d) where the normalized domain wall displacement is plotted as a function of the ellipticity of the light. Initially, when the light is circularly polarized, the domain wall passes through the middle of the laser spot. Changing the ellipticity to reach a σ^- polarization simultaneously induced a motion of the domain wall away from the center of the pulse, as expected. Further increasing the angle progressively

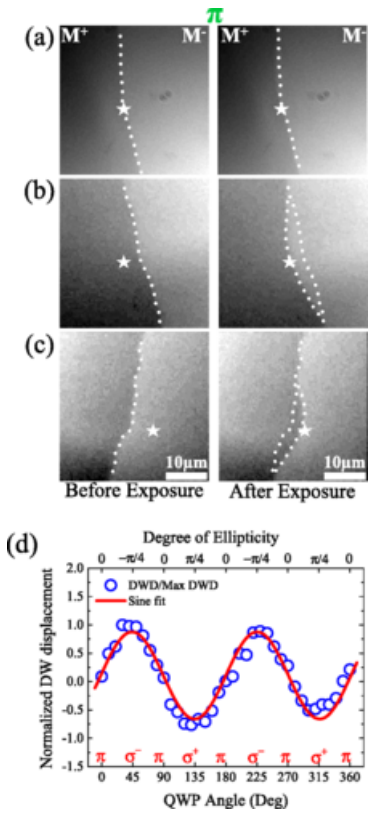


FIGURE 2.21: (a)–(c) Magneto-optical Faraday images of a domain wall in a Pt(4.5 nm)/Co(0.6 nm)/Pt(4.5 nm) thin film exposed to 40-fs linearly polarized (L) laser pulses with a fluence of 7 mJ/cm^2. The laser beam spot (star) is on the DW in (a) and off centered in (b) and (c). The DW moves towards the center of the beam, *i.e.*, the hottest regions, independently of the magnetization direction. (d) Normalized DWD induced by 40-fs laser pulses in Pt(4.5 nm)/Co(0.6 nm)/Pt(4.5 nm) plotted against the angle θ of the quarter-wave plate (QWP) and the degree of light ellipticity ϵ for linear polarization ϵ=0 and for circular polarization $\frac{\pi}{4}$ or -$\frac{\pi}{4}$. A maximum DW displacement of about 2 μm was obtained. The laser beam is initially centered on the DW at θ=0° and kept fixed. The fluence is set to 12.5 mJ/cm^2. Image and caption extracted from Ref. [57].

brings back the linear polarization of the light and, with it, the domain wall went back toward the hottest spot. From there, the increase of the angle produced a σ^+ state, and the domain wall continued its progression further away from the center of the laser spot. These experimental results clearly are the consequence of a competition between the effect of the ellipticity, which tends to favor one direction of the magnetization and the effect of the thermal gradient which brings the domain wall toward the hottest area.

In the light of these results, one can infer a part of the underlying mechanisms of the AO–HDS in continuous thin films. Indeed, the helicity–dependent effect is thermally activated. This thermal activation may allow to nucleate a reversed domain which, as a consequence of the effect of the helicity is then able to propagate away from the hottest spot and expand, thus giving birth to the AO–HDS. If the AO–HDS relies on the helicity–dependent propagation of the domain walls to occur, in the absence of AO–HDS in a

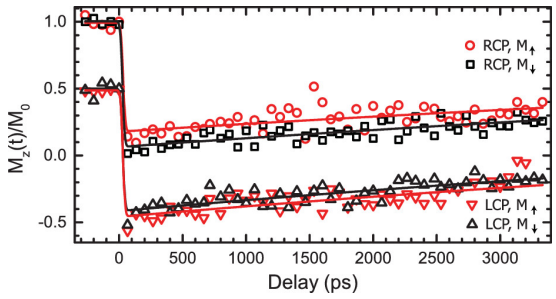


FIGURE 2.22: Polarization dependence of the magnetization dynamics after a single 60 fs laser pulse excitation. The RCP and LCP optical pump pulses are used to excite the multilayer, which magnetization is saturated parallel $\vec{M}_\uparrow$ or antiparallel $\vec{M}_\downarrow$ to the sample normal. The magnetization dynamics for LCP laser excitation is shifted down by 0.5 for a better visual representation. Figure and caption extracted from Ref. [60].

given sample, one should also not expect helicity–dependent domain wall motion. Nevertheless, such a correlation has not been tested by the authors, as they only used samples where AO–HDS was present. However, in this framework, the low magnetization remanence criterion mentioned by Hassdenteufel *et al.*[52] would be relevant as it is impacting the type and width of the domain walls, which properties may drastically impact the helicity–induced domain wall motion. Furthermore, the same remark holds for the thickness of the thin film, and thus the shape anisotropy. This fact lead El Hadri *et al.*[51] to argue that the relevant criterion is the domain size, which is the result of a compromise between the domain wall energy, evidently lowered by the presence of large domains, and the dipolar energy, favoring small domains. All of these elements may indicate another criterion related to the properties of the domain wall.

Finally, this scenario does not elucidate the origin of the light–induced torque, which the authors attribute to temperature gradients generated by the magnetic circular dichroism effect (see Sec. 2.4.4.1).

2.3.3 Demagnetization

In the search for the origin of the AO–HDS, and the helicity–dependent domain wall motion (which wasn't exhibited at that time), Tsema *et al.*[60] studied the demagnetization of the thin film $[Co(0.4\,nm)/Pt(0.7\,nm)]_{\times 3}$. To pump the system, they used a single circularly polarized pulse. Fig. 2.22 shows the induced dynamics for both helicities and initial magnetization directions. In any configuration of the light and the magnetization, the abrupt quenching of the magnetization is followed by a slower recovery. However, the amplitude of the initial quenching depends both on the helicity of the light and on the initial magnetization state. Indeed, the graph shows that for the same helicity, the amount of demagnetization is different whether the system is initially up magnetized ($M_\uparrow$) or down magnetized ($M_\downarrow$). This initial difference of demagnetization then lasts for as long as they probe the compounds, *i.e.* at least for 3000 ps. It means that, while the light only interacts with the matter during the pulse duration, the effect of the helicity can influence the magnetization dynamics for a much longer time. The authors attributed this difference in the demagnetization amplitude to the fact that, due to the MCD effect (see Sec. 2.4.4.1) the absorption depends on the polarization of the light.

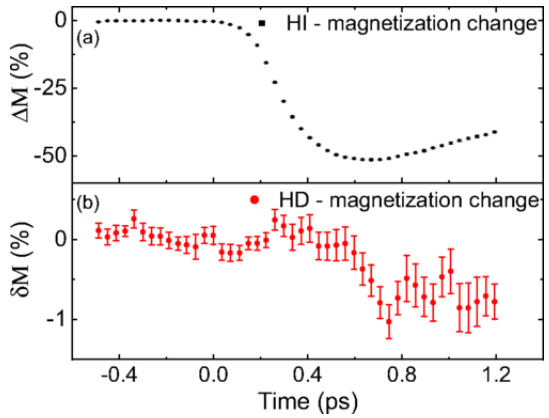


FIGURE 2.23: (a) Helicity-independent (ΔM) and (b) helicity-dependent (δM) magnetization change extracted from ultrafast magnetization dynamics induced by circularly polarized light. δM is proportional to the magnetic circular dichroism. Image and caption extracted from Ref. [61].

The same phenomenon has been exhibited in a 20 nm thick thin film of $Co_{70}Tb_{30}$ by Quessab *et al.*[61]. Fig. 2.23 (a) shows that the helicity–independent part of the magnetization, named ΔM, is quenched by 50% in the first 500 fs. Simultaneously, the authors measured a growing difference of induced demagnetization, δM, of about 1%. They correlated the sign of this difference of induced magnetization to the MCD, *i.e.* the most demagnetizing helicity is the one which is the most absorbed and, therefore, which demagnetizes the most. As this sample also presented AO–HDS and HD domain wall motion, they showed that given an initial magnetization state, the helicity which is the most absorbed switched the magnetization to the less absorbing state. Likewise, it propagated the domain wall in such a way that the less absorbing domain was expanding.

While the work of Quessab *et al.*[61] clearly links the difference of induced demagnetization to both the AO–HDS and HD domain wall motion, the fact that such a difference can only be due to MCD remains questionable. In Sec. 2.4.4.2 and Chap. 6 we discuss the possible roles of the inverse Faraday effect and the difference of induced magnetization during the absorption in the presence of this phenomenon.

2.3.4 Takeaways from the experiments

Many insights can be extracted from the overall view of all the aforementioned experimental results, some of which have, as we have seen, guided both theoretical and experimental research on this field. Here is a summary of the key takeaways from the experimental part of this review, which can be used as a prism through which both the theoretical part, as well as the rest of the results of this thesis can be looked at.

2.3.4.1 Ultrafast demagnetization

Regarding the origin of the ultrafast demagnetization, the main investigated phenomena currently are the Stoner excitations, inducing a decrease of the length of the magnetic moment on each atom, the generation of transversal excitations (magnons), reducing the average value of the magnetization, and finally the ultrafast diffusion of angular momentum out of the illuminated area by the light–induced hot electrons. While the presence

of all these phenomena have been experimentally exhibited, the most accountable for the ultrafast–demagnetization appears to be the generation of magnons. However, the mechanisms of this generation remain elusive. Notably, experiments have shown that instead of a direct light–matter interaction, the mere presence of hot–electrons is enough to induce the ultrafast demagnetization. Furthermore, the hot–electrons, behaving in the so–called "superdiffusive" way also allow for the ultrafast homogenization of the energy locally deposited by the laser.

2.3.4.2 All–optical helicity–dependent switching

The first difficulty encountered in this section was the disentanglement of the two types of light–induced switching: the all–optical helicity–independent switching and the all–optical helicity–dependent switching. The former is also named toggle switching as it occurs in only a single light pulse. Furthermore, a direct light–matter interaction is not required as this type of switching can equally be achieved by a pulse of hot–electrons. On the other hand, the helicity–dependent switching usually occurs in multiple pulses and the final state of the magnetization is purely determined by the helicity of the light. While both the AO–HIS and the AO–HDS have been found in the ferrimagnet GdFeCo, their simultaneous presence in a same thin film has been hard to evidence and it is not yet understood why a given sample is exhibiting one effect or the other. However, the AO–HIS happens at lower fluence than the AO–HDS. Indeed, the latter only occurs right below the fluency threshold at which the light induces a demagnetization. This indicates the necessity of a strong thermal activation for the AO–HDS to take place. Furthermore, unlike the AO–HIS, which has only been exhibited in GdFeCo, the AO–HDS works in many different types of heterostructures, magnetic orderings and atomic compositions.

To rationalize the presence of the AO–HDS in the different types of compounds, experimentalists are looking for some characteristics fulfilled by all the thin films exhibiting this phenomenon. As, at first, the AO–HDS had only been exhibited in ferrimagnets, it was thought that T_{comp} was the relevant quantity[8] and that its value should not be too high above T_R. Later, M_R, the remanent magnetization, was proposed and had to be low to allow for the AO–HDS[52]. This criterion covers the first one, as in the case of ferrimagnets, when the temperature is close to T_{comp}, M_R is low. Later on, El Hardri *et al.*[51] proposed that the size of the laser spot should be smaller than the size of the magnetic domains. However, this criterion is also partially contained in the low M_R requirement, as the lower the remanent magnetization, the larger the domains.

The helicity–dependent domain wall motion provided us with a potential mechanism leading to the emergence of AO–HDS. Indeed, once a multidomain state is created at the center of the beam, where the fluence is the highest, the domains having the right direction could be expanded by the light, thus creating the *switching ring* surrounding the demagnetization area. In such a context, the properties of the domain walls could play an important role in the effectiveness of the light–induced propagation. This can be bridged with the low M_R criteria, as a lower M_R leads to thinner domain walls.

Finally, the AO–HDS appears to be a cumulative process as, contrary to the AO–HIS, it occurs in multiple pulses and seems to be more efficient for longer lasting pulses.

2.4 Theoretical understandings

To this day there is no consensus, and even less a unified theory of the light–induced magnetization dynamics. Indeed, exactly solving such a problem is a rather daunting task, as it would require us to solve the many–body Schrödinger equation in order to compute the full dynamics of the system subjected to a femtosecond light pulse, taking into account both the electrons, the nucleus and the magnons, while accounting for the openness of the system. While real–time time–dependent density functional theory provides a rigorous framework to do that, such a task is, at the moment, far out of reach. As a consequence, many phenomenological models are used to rationalize the whole dynamics.

The first part of this theoretical review will be focused on models related to the light–induced ultrafast demagnetization. They can be roughly divided in effects inducing a longitudinal relaxation of the magnetic moments and effects inducing transversal fluctuations. As argued extensively in Sec. 2.3, the presence of these excitations seems to be necessary for the appearance of helicity–depend effects. The latter will be the object of the second part of this theoretical review. The main candidates currently thought of in the literature are the magnetic circular dichroism, inducing an absorption which depends on the magnetization state, and the inverse Faraday effect, usually seen as a light–induced optomagnetic field.

2.4.1 2 and 3 temperature models

2.4.1.1 General approach

In order to understand both the ultrafast light–induced demagnetization, as well as the possible emergence of AO–HDS, which, as argued in Sec. 2.3.1.3 is thermally activated, the most fundamental and widely used frameworks are the 2 and 3 temperature models (2 and 3TM). These are usually invoked to describe the flow of energy, primarily absorbed by the electrons during the light-matter interaction. The TM models rely on the separation of the different degrees of freedom into three distinct baths: the electrons, the phonons and, in the case of the 3TM, the spins. Here, by spin we designate the magnetic moment localized on each atom. This phenomenological approach, before being used in the description of laser–driven ultrafast dynamics by Beaurepaire *et al.*[5], was first introduced to describe the light–induced dynamics in non–magnetic metals (see Anisimov *et al.*[62] and references therein). Assuming the existence of a thermal distribution at every time (hypothesis that has later been relaxed by Maldonado *et al.*[22]), as well as heat transfer, one can write the following coupled differential equations for the dynamics of the laser–deposited heat:

$$\begin{aligned} C_e \frac{dT_e}{dt} &= -G_{e-l}(T_e - T_l) + P(t) - \frac{(T_e - T_{room})}{\tau_{th}} \\ C_l \frac{dT_l}{dt} &= G_{g-l}(T_e - T_l) \\ C_s \frac{T_s}{dt} &= G_{s-e}(T_e - T_s) \end{aligned} \tag{2.7}$$

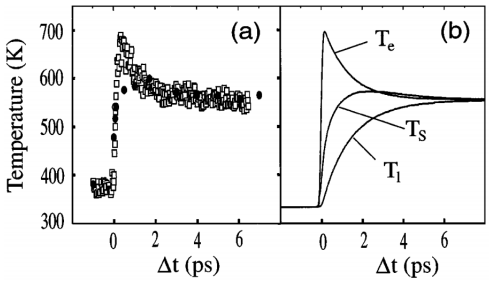


FIGURE 2.24: (a) Experimental spin T_s and electron T_e temperatures estimated as explained in [5]. (b) Calculated spin T_s, electron T_e, and lattice T_l temperatures. Image and caption extracted from Ref. [5].

where C_e, C_l and C_s are respectively the electronic, the lattice and the spin specific heats, G_{el}, G_{es} and G_{sl} are the electron–lattice, electron–spin and spin–lattice interaction, considered as independent of the temperature and $P(t)$ is the laser power. The last term of the first equation represents the heat sink, which is bringing the system back to equilibrium with the room temperature, T_{room}, at a rate given by τ_{th}. The laser power is usually assumed to take a Gaussian shape:

$$P(t) = I_0 F e^{-\left(\frac{t-t_0}{\tau_l}\right)^2} \tag{2.8}$$

Within this framework, and neglecting the heat sink, the temperature dynamics obtained by Beaurepaire *et al.*[5] is shown in Fig. 2.24.

While the agreement between experiments and the 3TM is good, many notes of caution are warranted. Indeed, for the calculation of C_l, the Debye approximation is usually made. In the case of Ni, which is studied by Beaurepaire *et al.*, it leads to an error of 5% in the range of temperature considered. As for C_e, the Sommerfeld approximation is always invoked, *i.e.* $C_e = \gamma T_e$. However, this approximation is only valid at a low electronic temperature, which is not the case here. As a consequence, instead of using the standard value of γ in the case of Ni, Beaurepaire *et al.* had to increase it to better fit their experimental results. Later on, in the work of Lin *et al.*[63], the Sommerfeld approximation has been relaxed. Nevertheless, the authors found that the electronic specific heat was below the one given by the Sommerfeld approximation. However, in their work, Lin *et al.* did not self consistently let the electronic states relax accordingly to the change in the electronic temperature, *i.e.* they used the rigid band approximation. In Chap. 4 of this thesis, we went beyond this approximation and showed that, especially in the case of Ni, the Sommerfeld approximation is wrong, even at low temperature, and leads to a strong undervaluation. This work has also other implications on the possible role of a collapse of the exchange splitting as the origin of the ultrafast demagnetization. Regarding C_s, Beaurepaire *et al.*[5] calculated its value by subtracting the contribution of the phonons and the electrons to the total specific heat of Nickel experimentally obtained. In the fitting of the experimental results, the different coupling values, G_x were taken as parameters. Fig. 2.24 (b) shows the dynamics for the three baths. As the light is absorbed by the electrons, the electronic temperature raised very rapidly. Then, the electronic bath started to exchange heat with the spin bath, and in a less intense fashion with the lattice bath, diminishing its temperature in the process. From this, the magnitude of the magnetization is computed using the M(T) curve at equilibrium, where the temperature is given by T_s.

This is valid under the assumption that the spin bath thermalizes faster than the change in the temperature to which it is subjected and that the Heisenberg exchange is not evolving during and after the pulse. However, as we will discuss it in Chap. 5 of this thesis, these assumptions have some limitations.

Overall, in this approach many unknowns serve as fitting parameters. While in the case of Beaurepaire *et al.*[5], the experimental value of the total specific heat was used in order to access the magnetization specific heat, it is very often also taken as a free parameter[56], and crude approximations are made in order to obtain the value of the electronic specific heat (Sommerfeld approximation). However, the widespread use of the 2TM and 3TM in the literature may come from the fact that, having many freely varying parameters, it can fit almost any dynamics. On the downside, this is also severely hindering its predictive capabilities.

2.4.1.2 Further developments

As already mentioned in Sec. 2.2.1, a particularly puzzling question regards the conservation of angular momentum during the light–induced ultrafast demagnetization. One possibility, recently backed up by the work of Dornes *et al.*[64] is, that, along with a transfer of energy, angular momentum is also passed from the bath of the electrons to the bath of the phonons.

It is in this context that Koopmans *et al.*[65] developed the so–called microscopic three temperature model (M3TM). In this model, the demagnetization rate is mediated through Elliott-Yafet scattering events. As described in more detail in Sec. 2.4.2.1, in this process, the spin of an electron flips while scattering with a phonon, and the difference of angular momentum due to the spin–flip is supposed to be transferred to the phonon. To develop a model relying on this phenomenon, they considered localized spins, which sites are indexed by j and which magnetization are given by the operator $S_{z,j}$ in a Fermi sea of spinless electrons. The spin bath obeys the Boltzmann statistics and is described by two–level systems having an exchange splitting $\langle S \rangle = \dfrac{\Delta_{ex}}{2k_B T_C}$ where $\langle S \rangle$ is the average magnetization and Δ_{ex} is the exchange splitting. In this model, the magnetization dynamics is simply given by:

$$\frac{dm}{dt} = Rm\frac{T_p}{T_C}\left(1 - m\coth\left(\frac{mT_C}{T_e}\right)\right) \tag{2.9}$$

where $m(t) = \frac{M(t)}{M_S}$, T_p is the phonon temperature, T_C is the Curie temperature and R is a material specific prefactor which accordingly scales the demagnetization rate. It is proportional to $a_{sf}T_C^2/\mu_{at}$, where μ_{at} is the atomic magnetic moment and a_{sf} is the probability of a spin–flip event due to a scattering with a phonon. This equation is used in combination with the differential equations for T_e and T_p as expressed in Eq. 2.7. In this regard, while the authors refer to this model as a 3TM, it is in fact a 2TM model where the dynamics of the average magnetization is computed using Eq. 2.9. In fact, Eq. 2.9 can be viewed as a more sophisticated way of calculating the magnetization dynamics than from the more simpler Bloch–type equation:

$$\frac{dM(t)}{dt} = -\frac{M(t) - M_0(T_e(t))}{\tau}, \tag{2.10}$$

as used in, *e.g.*[66, 67]. However, in such a framework, the role of the magnetic moments as a heat reservoir is missing, which at least has the convenience of reducing the number of required parameters to fit (the magnetic moments specific heat in this case). In Eq. 2.10, τ is the magnetization relaxation time, which, in the case of the model of Koopmans *et al.*[65] is given a microscopical origin, as it depends on the rate of Elliot–Yafet spin–flip events and on the value of the magnetization at equilibrium at a given temperature, which corresponds to the electronic one. In order to fit their experimental data, the authors took the coupling between electrons and phonons as a fitting parameter. Strangely, instead of using the Debye approximation for the value of the specific heat of the phonons, C_p, it was also treated as a fitting parameter and the same is true for γ, which serves in the computation of the electronic specific heat in the Sommerfeld approximation. However, while the values of C_p and G_{e-l} were given by the authors, the value of γ, which could have served as a test of the relevance of this particular model, is lacking.

Fig. 2.25 shows the principal features of this model. It predicts two distinct types of dynamics for the magnetization. In the first type, Fig. 2.25 **a**, the demagnetization produced by the raise of T_e occurs faster than the equilibration of the temperatures of the phonons and the electrons. Therefore, when the equilibration is finally completed, a quick recovery of the magnetization is seen. The second regime, seen in Fig. 2.25 **b**, occurs when the demagnetization rate is slower, such that the increase of T_e does not last long enough to allow the magnetization to drop below its equilibrium value after equilibration of the phonon and the electron baths. In this case, instead of a recovery, the magnetization continues to decrease after the initial drop. In Fig. 2.25, the transition from the first type to the second type of dynamics is shown as a function of q, the fluence, T_0/T_C, the ratio between the ambient temperature and the Curie one, and $R\tau_{E0}$, where τ_{E0} is the electron–phonon equilibration timescale. Upon an increase of R (which can be caused by an increase of a_{sf}), the dynamics evolves from a type II to a type I, as the rate of demagnetization increases, as seen Eq. 2.9. On the contrary, increasing the fluence or the initial energy will produce a transition from a type I to a type II dynamics as, after the laser deposited energy and equilibration, the system is close to its Curie temperature.

While this model has been able to fit multiple experiments[65, 68], the values they found for the Elliott–Yafet spin flip probabilities are very high compared to others (see Sec. 2.4.2.1) and, as in the case of the conventional 3TM, the many fitting parameters severely reduce its predictive capabilities.

Last but not least, experimental[69] as well as theoretical[70, 71, 72] results show that the quenching of the magnetization due to a longitudinal relaxation occurs at quite higher temperatures than by creating magnons. As discussed in more detail in Chap. 4, the critical temperature in the former case is the Stoner temperature, T_S, while in the later one it is T_C. As a consequence, the transition from an ordered magnetized state to a paramagnetic state as seen experimentally at thermal equilibrium mainly happens due to transversal fluctuations. However, in the model of Koopmans, what mediates the demagnetization are the Elliott–Yafet spin–flips, which are inducing a longitudinal reduction of the magnetization. Nevertheless, in their model, T_C appears as a parameter, whereas if only longitudinal excitations are involved the relevant critical temperature is T_S. On a final note, as discussed in the experimental part of this review (see Sec. 2.2.3), the origin of the demagnetization is likely to be mainly due to transversal excitations (magnons).

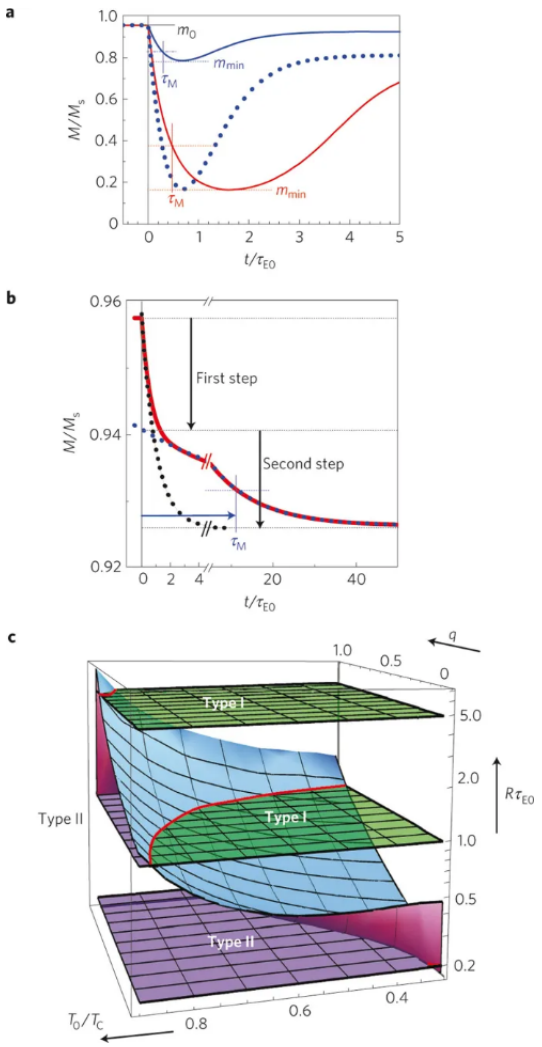


FIGURE 2.25: **a**, Type I dynamics at T=0.5 T_C for a fictitious material (C_p=5 γ T_C) with a large spin-flip rate (R=5.0τ_{E0}^{-1}), leading to single–step demagnetization within the electron–phonon equilibration. Results for demagnetization at low (blue) and high (red) laser fluence are shown (q=0.2 and 0.8, respectively), as well as a scaled version of the low-fluence result (blue dotted). The time axis is normalized to τ_{E0}, defined as τ_E at T$\approx$ T_C. **b**, Two-step demagnetization (type II) as observed for materials with a small value of R(0.2τ_{E0}^{-1}). **c**, Generalized phase diagram, for materials with a certain relative spin-flip rate R τ_{E0} as a function of fluence q and ambient temperature T_0/T_C (see text). The curved plane (top side blue, bottom side red) separates regions of type I and type II dynamics. The opaque planes represent different materials (R τ_{E0}=5.0, 1.0 and 0.2, respectively), where green represents type I behaviour, and purple type II behaviour. Figure and caption extracted from Koopmans *et al.*[65].

2.4.2 Longitudinal relaxation of the magnetization

2.4.2.1 Elliott–Yafet spin–flip processes

In 1954 Elliott [73] evidenced that, in the presence of "spin–mixing", consequence of the presence of spin–orbit coupling, electron–phonon scattering events can lead to a change of the spin state of the electron, even though the matrix elements of the scattering are spin diagonal. Later, Yafet[74] showed that the presence of spin–orbit also allows non spin–diagonal transitions.

In the following, we place ourselves in the framework of density functional theory applied to periodic systems. Therefore, the states are fully indexed by their wavevector, $\boldsymbol{k}$, their band index, n, and, in the absence of spin–orbit coupling their spin state, σ, which can be $\uparrow$ or $\downarrow$. In such a case, the electron–phonon matrix elements, $g^{\nu\sigma\sigma'}_{\boldsymbol{k}n\boldsymbol{k}'n'}(\boldsymbol{q})$ are written as

$$g^{\nu\sigma\sigma'}_{\boldsymbol{k}n\boldsymbol{k}'n'}(\boldsymbol{q}) = \left| \boldsymbol{u}_{\boldsymbol{q}\nu} \cdot \langle \Psi^{\sigma}_{\boldsymbol{k}n} | \nabla_{\boldsymbol{R}} V | \Psi^{\sigma'}_{\boldsymbol{k}'n'} \rangle \right|^2 . \tag{2.11}$$

.

In Eq. 2.11, $\boldsymbol{q}$ is the wavevector of the created or annihilated phonon, ν is its band index, $\boldsymbol{k}$ and $\boldsymbol{k}'$ are the wavevectors of the initial and final electronic state satisfying the relation $\boldsymbol{q} = \boldsymbol{k}' - \boldsymbol{k}$, n and n' are the bands of the involved electronic states, $\boldsymbol{u}_{\boldsymbol{q}\nu}$ is the displacement vector of the nucleus and $\nabla_{\boldsymbol{R}} V$ is the Hamiltonian of the electron–phonon interaction. It is made of the gradient with respect to the displacement of atoms, $\nabla_{\boldsymbol{R}}$, of the total potential, V, felt by the electrons. In the work of Essert *et al.*[75], they used the Boltzmann equation in order to compute the dynamics of the occupation of the electrons induced by both the electron–phonon scattering and the electron–photon scattering:

$$\frac{\partial}{\partial t} f_{\boldsymbol{k}n} = \frac{\partial}{\partial t} f_{\boldsymbol{k}n} \bigg|_{e-phonons} + \frac{\partial}{\partial t} f_{\boldsymbol{k}n} \bigg|_{e-photons} \tag{2.12}$$

where $f_{\boldsymbol{k}n}$ is the occupation of the Bloch orbital indexed by $\boldsymbol{k}$ and n the band index.

The electron–photon scattering matrix elements were computed using the dipolar approximation and the electron–phonon scattering matrix elements, $g^{\nu\sigma\sigma'}_{\boldsymbol{k}n\boldsymbol{k}'n'}(\boldsymbol{q})$, were computed with and without including the spin–orbit coupling in the potential V. The light pulse had a fluence of 4 mJ/cm^2 and a Gaussian temporal shape having a full width half minimum of 50 fs and a photon energy of 1.55 eV. In order to propagate Eq. 2.12, the authors extracted all the required quantities (among which are the electron–phonon and photon scattering matrix elements) from density functional theory, using the augmented spherical wave method[76] in the atomic sphere approximation. Note that these quantities were then kept constant during the dynamics, *i.e.* changes in the band structure (as *e.g.* in the exchange splitting), as well as in the scattering matrix elements were neglected. Fig. 2.26 shows the dynamics of the magnetization expectation value, neglecting the orbital angular momentum, as well as the electronic energy. In the case of Ni, it is computed with and without the contribution of the spin–orbit coupling in $g^{\nu\sigma\sigma'}_{\boldsymbol{k}n\boldsymbol{k}'n'}(\boldsymbol{q})$. In both cases, the magnetization drops rapidly by 5%. However, after this sudden drop, the magnetization recovers and even increases above its initial value. This may be due to the fact that, as electron–electron scattering is not taken into account, the electrons do not thermalize. Therefore, the dynamics obtained after the thermalization time ($\approx 300fs$[77, 78, 79, 23]) cannot be correct. In the case of Fe a lesser decrease of about 3% is observed and the

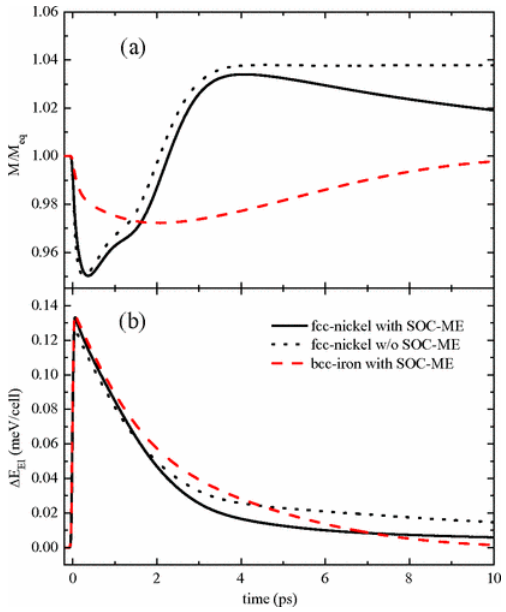


FIGURE 2.26: Normalized magnetization dynamics (a) and energy difference to equilibrium of the electronic system (b) after the optical excitation including electron-phonon scattering. Results obtained including the spin-orbit coupling contribution in the electron-phonon matrix element are labeled "with SOC-ME. Image and caption extracted from Ref. [75].

recovery is slower. Interestingly, however, as seen in Fig. 2.26 (b), the absorbed energy is transferred to the phonon bath at the same rate for both compounds.

Furthermore, Fig. 2.26 shows that the presence of the spin–orbit in the calculation of $g^{\nu\sigma\sigma'}_{\boldsymbol{k}n\boldsymbol{k}'n'}(\boldsymbol{q})$ (the so–called Yafet contribution) does not significantly impact the dynamics, especially in the early stages at which the fast demagnetization occurs. However, it is important to recall that while the spin–orbit coupling is neglected in the calculation of the scattering matrix elements, it was included in the Hamiltonian during the computation of the ground state and that it has consequences on the Bloch states. Indeed, in the presence of spin–orbit coupling, the spin is not a good quantum number anymore and the states are a superposition of spin up and spin down. Such states can be written as:

$$\begin{aligned}\Psi^{\Uparrow}_{\boldsymbol{k}n}(\boldsymbol{r}) &= \left(a^{\Uparrow}_{\boldsymbol{k}n}(\boldsymbol{r})\,|\uparrow\rangle + b^{\Uparrow}_{\boldsymbol{k}n}(\boldsymbol{r})\,|\downarrow\rangle\right) e^{i\boldsymbol{k}\cdot\boldsymbol{r}} \\ \Psi^{\Downarrow}_{\boldsymbol{k}n}(\boldsymbol{r}) &= \left(b^{\Downarrow}_{\boldsymbol{k}n}(\boldsymbol{r})\,|\uparrow\rangle + a^{\Downarrow}_{\boldsymbol{k}n}(\boldsymbol{r})\,|\downarrow\rangle\right) e^{i\boldsymbol{k}\cdot\boldsymbol{r}}\end{aligned} \tag{2.13}$$

As indicated by $\Uparrow$ or $\Downarrow$, even though the magnetization state is not correctly defined by the spin anymore, as the spin–orbit is generally weak with respect to the other elements of the Hamiltonian, the states are "almost" up or down, *i.e.* $\langle\Psi^{\Uparrow}_{\boldsymbol{k}n}|\uparrow\rangle\langle\uparrow|\Psi^{\Uparrow}_{\boldsymbol{k}n}\rangle >> \langle\Psi^{\Uparrow}_{\boldsymbol{k}n}|\downarrow\rangle\langle\downarrow|\Psi^{\Uparrow}_{\boldsymbol{k}n}\rangle$ and $\langle\Psi^{\Downarrow}_{\boldsymbol{k}n}|\uparrow\rangle\langle\uparrow|\Psi^{\Downarrow}_{\boldsymbol{k}n}\rangle << \langle\Psi^{\Downarrow}_{\boldsymbol{k}n}|\downarrow\rangle\langle\downarrow|\Psi^{\Downarrow}_{\boldsymbol{k}n}\rangle$. To refer to these new magnetization labels (*i.e.* $\Uparrow$ and $\Downarrow$), we use $\tilde{\sigma}$. In this framework, Eq. 2.11 can be rewritten as:

$$g^{\nu\tilde{\sigma}\tilde{\sigma}'}_{\boldsymbol{k}n\boldsymbol{k}'n'}(\boldsymbol{q}) = \left|\boldsymbol{u}_{\boldsymbol{q}\nu}\cdot\langle\Psi^{\tilde{\sigma}}_{\boldsymbol{k}n}|\,\nabla_{\boldsymbol{R}}V\,|\Psi^{\tilde{\sigma}'}_{\boldsymbol{k}'n'}\rangle\right|^2. \tag{2.14}$$

.

While in the absence of spin–orbit coupling, $g^{\nu\sigma\sigma'}_{\boldsymbol{k}n\boldsymbol{k}'n'}(\boldsymbol{q}) = 0$ when $\sigma \neq \sigma'$, $g^{\nu\tilde{\sigma}\tilde{\sigma}'}_{\boldsymbol{k}n\boldsymbol{k}'n'} \geq 0$ when $\tilde{\sigma} \neq \tilde{\sigma}'$. Furthermore, the fact that the dynamics does not change when including the spin–orbit coupling in $g^{\nu\tilde{\sigma}\tilde{\sigma}'}_{\boldsymbol{k}n\boldsymbol{k}'n'}$ means that most of the spin–flips are a consequence of the spin mixing, rather than the Yafet contribution.

Almost simultaneously, Carva *et al.*[80] published their investigation of the contribution of the Elliott–Yafet scattering mechanism. Their analysis rested on their generalization of the energy– and spin–dependent Eliashberg function. Its purpose is to "count" the number of available electron–phonon scattering events available in the whole Brillouin zone at a given electronic energy E, and a phonon frequency Ω, where each transition is weighted by the electron–phonon scattering matrix element $g^{\nu\tilde{\sigma}\tilde{\sigma}'}_{\boldsymbol{k}n\boldsymbol{k}'n'}(\boldsymbol{q})$. It writes as:

$$\alpha^2_{\tilde{\sigma}\tilde{\sigma}'}F(E,\Omega) = \frac{1}{2M\left|\Omega\right|}\sum_{\nu nn'}\int_{\mathrm{BZ}} d\boldsymbol{k}d\boldsymbol{k}' g^{\nu\tilde{\sigma}\tilde{\sigma}'}_{\boldsymbol{k}n\boldsymbol{k}'n'}(\boldsymbol{q})\delta(\omega_{\boldsymbol{q}\nu} - |\Omega|)\delta(E^{\tilde{\sigma}}_{\boldsymbol{k}n} - E)\delta(E^{\tilde{\sigma}'}_{\boldsymbol{k}'n'} - E^{\tilde{\sigma}}_{\boldsymbol{k}n} - \hbar\Omega) \tag{2.15}$$

In this equation, $E^{\tilde{\sigma}}_{\boldsymbol{k}n}$ is the eigenenergy of the state $|\Psi^{\tilde{\sigma}}_{\boldsymbol{k}n}\rangle$ and $\omega_{\boldsymbol{q}\nu}$ is the frequency of the phonon of wavevector $\boldsymbol{q}$ and band ν. Note that Ω can be negative in case of phonon absorption processes.

If one weights Eq. 2.15 by $N(\Omega)$, the occupation of the phonon states of energy Ω and integrates it with respect to the phonon energy, the following spin–resolved transition rate $w_{\tilde{\sigma}\tilde{\sigma}'}$ is obtained under some approximations mentioned in [80, 81]:

$$w_{\tilde{\sigma}\tilde{\sigma}'}(E) = \int_0^\infty d\Omega\alpha^2_{\tilde{\sigma}\tilde{\sigma}'}F(E,\Omega)\left[1 + 2N(\Omega)\right] \tag{2.16}$$

Further weighting $w_{\tilde{\sigma}\tilde{\sigma}'}(E)$ by the occupation of the initial electronic state, $f_{\tilde{\sigma}}(E)$, and the final state, $f_{\tilde{\sigma}'}(E)$, and integrating with respect to the electronic energy E produces the spin–resolved transition rate:

$$S_{\tilde{\sigma}\tilde{\sigma}'} = \int w_{\tilde{\sigma}\tilde{\sigma}'}(E)f_{\tilde{\sigma}}(E)\left[1 - f_{\tilde{\sigma}'}(E)\right]dE. \tag{2.17}$$

From Eq. 2.17 is defined the spin–flip probability of an electron during an electron–phonon scattering event:

$$P_S = \frac{(S_{\Uparrow\Downarrow} + S_{\Downarrow\Uparrow})}{\sum_{\tilde{\sigma}\tilde{\sigma}'} S_{\tilde{\sigma}\tilde{\sigma}'}} \tag{2.18}$$

As pointed out by Carva *et al.*[80], P_S is the quantity which is used by Koopmans *et al.*[65] in the microscopic 3TM model (see Sec. 2.4.1.2) in order to justify the transfer of angular momentum from the bath of the electrons to the bath of the phonons. However, Eq. 2.18 measures the total number of spin–flips while the relevant quantity should be what Carva *et al.* call the demagnetization ratio:

$$D_S = \frac{(S_{\Uparrow\Downarrow} - S_{\Downarrow\Uparrow})}{\sum_{\tilde{\sigma}\tilde{\sigma}'} S_{\tilde{\sigma}\tilde{\sigma}'}} \tag{2.19}$$

A widely used approximation for P_S is the one made by Elliott[73]. It writes as:

$$P^E_S = p\left\langle b^2\right\rangle, \tag{2.20}$$

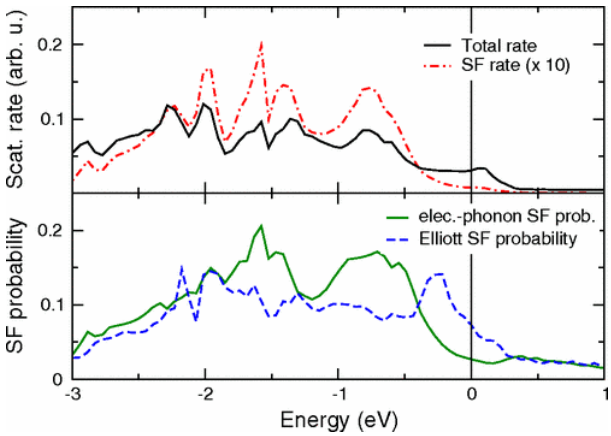


FIGURE 2.27: Energy-resolved electron-phonon total and SF scattering rates w(E) and $w_{\uparrow\downarrow}$(E) of Ni (top), and normalized SF probability P_S(E) and approximate SF probability $P_S^{b^2}$(E) obtained from the Elliott relation (bottom). Image and caption extracted from Ref. [80].

where p is a material dependent constant which has been shown to vary between 1 and 10[82, 83] and $\langle b^2 \rangle$ is the average spin–mixing calculated using:

$$\langle b^2 \rangle = \sum_{\tilde{\sigma},n} \int d\boldsymbol{k} |b^{\tilde{\sigma}}_{\boldsymbol{k}n}|^2 \tilde{\delta}(E^{\tilde{\sigma}}_{\boldsymbol{k}n} - E_F). \tag{2.21}$$

In Eq. 2.21, $\tilde{\delta}$ is a Dirac distribution smeared in order to take the electronic temperature into account.

As Essert *et al.*[75], all the electron–phonon scattering matrix elements, as well as the eigenvalues were obtained from *ab initio* density functional theory, but instead of using the augmented spherical wave method in the atomic sphere approximation, Carva *et al.* used the full–potential linear augmented plane wave method as implemented in the Elk code. Fig. 2.27 (top) shows the energy resolved scattering rate occurring without spin–flip, $w(E)$, and the one occurring with a spin–flip, $w_{\Uparrow\Downarrow}(E)$. In Fig. 2.27 (bottom), the energy resolved spin–flip probability, $P_S(E)$, as well as the spin–flip probability calculated within the approximation of Elliott, $P_S^E(E)$ using $p = 4$, are plotted. It shows that the Elliott approximation fails to capture the details of the spin–flips induced by electron–phonon scattering, especially near the Fermi energy, E_F. The authors attributed this discrepancy to the fact that, as the Elliott approximation is derived in a paramagnetic metal, the occupation of the minority and majority states are the same, whether, as seen on Fig. 2.28, it is not the case in the presence of exchange–splitting and such a fact is accounted for in Eq. 2.17. This highlights the role of the occupation of the different states in the intensity of the observed spin–flip scattering, as discussed below.

Tab. 2.1 shows the calculated values for P_S^E, P_S, D_S and $\Delta M/M_0$ extracted from Ref. [81]. Overall, P_S^E always overestimates P_S and, as expected, D_S is smaller than P_S and drastically increases in the case of a non–thermal electronic distribution. As depicted in Fig. 2.28, the underlying reason for this phenomenon is, that in the case of a thermal electronic distribution, spin–flips from $\Uparrow$ to $\Downarrow$ occurring near E_F are compensated by the opposite process below E_F, while it is not necessarily the case if the distribution is non–thermal. However, it is important to note that, very differently from the work of Essert *et al.*[75], the occupation here is approximated, *i.e.* it is chosen to depend only on the energy

	P_S^E	P_S	D_S	$\Delta M/M_0$
Ni (low T)	0.07	0.04	0	0
Ni ($T_e = 3000K$)	0.11	0.07	0.003	3.1
Ni (NEQ)	0.12	0.09	0.025	16.7
Fe (low T)	0.068	0.04	0	0
Fe ($T_e = 3000K$)	0.13	0.09	0.008	4.5
Fe (NEQ)	0.14	0.07	0.030	11.4
Co (low T)	0.06	0.010	0	0
Co ($T_e = 3000K$)	0.095	0.017	0.002	0.9
Co (NEQ)	0.105	0.022	0.010	2.3

TABLE 2.1: Here are given the *ab initio* calculated spin-flip probabilities P_S, Elliott SF probability P_S^E, demagnetization ratios D_S, and relative demagnetization fractions $\Delta M/M_0$ for laser-pumped Ni, Fe, and Co. Calculated values are given for equilibrium (low T), for thermalized electrons at a high Fermi temperature T_e, and for the nonequilibrium (NEQ) electron distribution created by femtosecond laser excitation. Computed values for the approximate Elliott SF probability P_S^E. The relative demagnetization fraction $\Delta M/M_0$, achieved by electron-phonon SF scattering, is given in % at 250 fs. Table and caption extracted from Ref. [81].

and on the magnetization state. As a consequence, Carva *et al.*[80, 81] can only account for an excited state where all the electrons at the same energy and the same magnetization state have the same occupation. However, in the case of an optical excitation such a condition does not hold true, as the intensity of the electron–photon scattering depends on the location in the Brillouin zone as well. In this approximation Carva *et al.* computed a demagnetization of 16.7 % in Ni, 11.4 % in Fe and 2.3 % in Co for a non–equilibrium electronic distribution. Consequently, and as Essert *et al.*[75], they concluded that the demagnetization rate was too slow to fully explain the ultrafast demagnetization seen experimentally.

2.4.2.2 Superdiffusive spin–dependent transport

In 2010, Battiato *et al.*[34], triggered by the appealing experimental result from Malinowski *et al.*[37] (see Sec. 2.2.4), proposed a model relying on a spin–dependent transport of laser–excited electrons to explain the ultrafast demagnetization.

Because the size of the laser spot is typically several orders of magnitude larger than the mean free path of the electrons, *i.e.* a few tens of μm versus a few tens of nm, only the spatial component perpendicular to the surface was kept (z in this case). Moreover, on the assumption that each excited electron propagates with an isotropic angular probability density, the authors expressed the probability $\phi(z, t|z_0, t_0)$ of finding an electron initially at z_0 at a time t_0 at z at a time t. ϕ also supposes that electrons are propagating in straight lines until they scatter, and have a life time, $\tau(\sigma, E, z)$, which depends respectively on the spin, the energy and z because of the existence of several layers.

To account for the light–induced electronic excitations, the authors defined $S^{ext}(\sigma, E, z, t)$, which represents the number of electrons per unit of volume and time which are being excited. It depends on both the structure of the compound (through z) and the laser

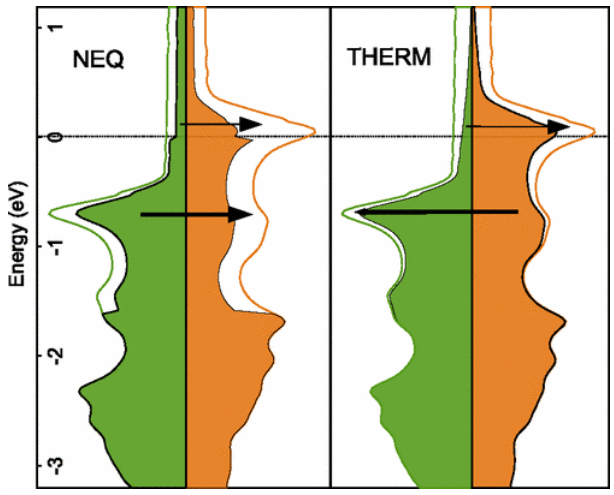


FIGURE 2.28: Spin-resolved DOS (filled areas) and phonon-induced spin flips (arrows) of NEQ and electron thermalized Ni. The equilibrium DOS is shown by thin lines. SF transitions are significantly different at energies above and below E_F(=0 eV). The arrow's thickness corresponds to the transition rate; its direction and length give which direction is dominant and by how much. The amount of laser-redistributed electrons has been enlarged to improve visibility. Image and caption extracted from Ref. [80].

(through t and E). From both $S^{ext}(\sigma, E, z, t)$ and $\phi(z, t|z_0, t_0)$, it is possible to compute the current density $\Phi(z, t)$:

$$\Phi(z,t) = \int_{-\infty}^{\infty} dz_0 \int_{-\infty}^{t} dt_0 S^{ext}(z_0, t_0)\phi(z, t|z_0, t_0), \tag{2.22}$$

which is a sum over all the values of t_0 and z_0, representing when and where the electrons are created, weighted by the probability of finding them at the position z at a time t.

The continuity equation for the density $n^{[1]}(\sigma, E, z, t)$ of *first–generation* electrons, *i.e.* electrons excited directly from photon–electron scattering events, writes as:

$$\frac{\partial n^{[1]}}{\partial t} + \frac{n^{[1]}}{\tau} = -\frac{\partial \hat{\phi} S^{ext}}{\partial z} + S^{ext} \tag{2.23}$$

where the operator $\hat{\phi}$ is defined by $\hat{\phi}S^{ext} = \Phi$, $\frac{n^{[1]}}{\tau}$ accounts for the decaying number of first–generation electrons, due to scattering processes and $-\frac{\partial \hat{\phi} S^{ext}}{\partial z}$ is the divergence of the current density. Electrons leaving the first–generation fill the second one. Their source term can be calculated as:

$$S^{[2]}(\sigma, E, z, t) = \sum_{\sigma'} \int p(\sigma, \sigma', E, E', z) \frac{n^{[1]}(\sigma', E', z, t)}{\tau(\sigma', E', z)} dE'. \tag{2.24}$$

In Eq. 2.24, $p(\sigma, \sigma', E, E', z)$ is the probability of transition of an electron having an energy E' and a spin σ' to a state having an energy and spin E and σ. Notice that while

this formalism allows for spin–flip scattering, such a phenomenon is not accounted for in the work of Battiato *et al.*[34].

The continuity equation which holds for $S^{[2]}(\sigma, E, z, t)$ is similar to Eq. 2.23:

$$\frac{\partial n^{[2]}}{\partial t} + \frac{n^{[2]}}{\tau} = -\frac{\partial \hat{\phi} S^{[2]}}{\partial z} + S^{[2]} \tag{2.25}$$

Iterating this procedure will generate a set of coupled continuity equations for all the generations of electrons.

Battiato *et al.*[34] then stressed that the obtained dynamics is different in the case of a purely ballistic regime and in the case of a purely diffusive regime. Indeed, in the latter, the variance of the displacement distribution, $\sigma^2(t)$, evolves as t, whether in the former, one would find that $\sigma^2(t) \propto t^2$[84]. However, in this particular dynamics, both contributions exist and are accounted for. Indeed, for small values of t with respect to the electronic lifetime, one would find a ballistic regime, while for larger values of t a shift toward a diffusive dynamics would occur. In order to emphasize this point, they called such a dynamics "superdiffusive".

The main issue addressed by Battiato *et al.* was regarding the capability of such a singular dynamics to induce a demagnetization, solely due to a depletion of majority spins diffusing away from the illuminated area faster than the minority spins. However, to correctly characterize such a dynamics, $\tau(\sigma, E, z)$ has to be fully defined. To this end, the energy and spin–dependent lifetime were extracted from *ab initio* GW calculations[85, 86].

Fig. 2.29 a. shows the evolution of the magnetic profile of a [Ni (15 nm) / Al (35 nm)] thin film during and after a 60 fs laser pulse, as calculated by Battiato *et al.*. As the light–matter interaction is assumed to be spin conserving, the total magnetic moment is constant during the dynamics. However, due to the spin–dependent lifetime, the majority spins are leaving the film, while the minority ones, slower, remain. As a consequence, the magnetization near the surface rapidly decreased, while on the other side, near the Al layer, it remained almost unchanged during the first 90 fs, and weakly reduced after 300 fs. Simultaneously, a magnetic polarization started to appear in the Al layer. Fig. 2.29 b. presents the evolution of the average magnetization in Ni as, according to Battiato *et al.*, the probe is equally sensitive to the magnetization throughout the thickness of the sample. Furthermore, this average was convoluted by a Gaussian having a full width at half maximum of 100 fs to account for the fact that the probe effectively produces a time averaged value of the magnetization, rather than providing an instantaneous value. The shaded area corresponds to the magnetization dynamics calculated with two different extrapolations of the lifetimes. Overall, the agreement between experiment and theory is quite satisfactory. More details about this theory and the numerical implementation are discussed in Ref. [87].

While, as seen in Fig. 2.29 b., such a model is able to fit the ultrafast demagnetization obtained by Stamm *et al.*[17] in Ni, and has been shown to successfully reproduce other experimental results, such as the work of Eschenlohr *et al.*[39] or the ultrafast magnetization enhancement in metallic multilayers [41], several notes of caution are warranted.

First, Khorsand *et al.*[40] showed that the calculation of absorption in Ref. [39] was largely overestimated in Au (90 % of the incident energy of the light, versus 2.8% as calculated by Khorsand *et al.*[40]). Despite this drastic difference in the absorption profile

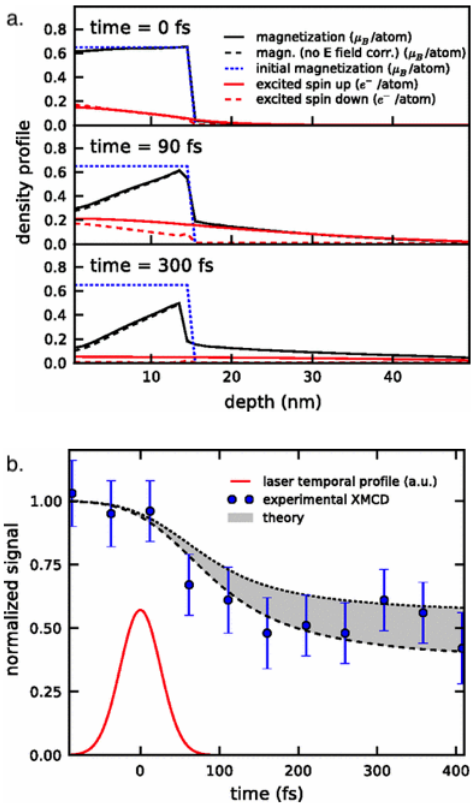


FIGURE 2.29: a. Calculated spatial magnetization profile of Ni at three times caused by laser excitation (at t = 0 fs). The resulting magnetization profile is given by the full curve, the initial one by the dotted curve. The magnetization profile without electric field correction is given by the dashed curve. The surface of the film is at 0 nm depth, the Ni film extends up to 15 nm depth, the remaining is the Al film. b. Computed laser-induced demagnetization in Ni. The shaded area shows where the theoretical result is expected to be (depending on the inelastic lifetime). For comparison they also show experimental XMCD data obtained by Stamm *et al.*[17]. The used time structure of the laser pulse (in a.u.) is depicted by the red solid line. Images and caption adapted from Ref. [34].

uniquely defining S^{ext}, the authors still managed to reproduce the magnetization dynamics. This may indicate that, while this model definitely brought attention to the fact that hot–electrons could play a role in the ultrafast demagnetization, its value is less predictive than descriptive.

Moreover, Schellekens *et al.*[36], who, as reviewed in Sec. 2.2.4, blocked the propagation of hot electrons outside a magnetic layer by surrounding it with insulators, showed that demagnetization still occurs. However, according to the model of Battiato *et al.*[34], which conserves the total angular momentum of the electron bath, in such a case any demagnetization would be impossible. Furthermore, Schellekens *et al.*[36] reported no difference in the dynamics when pumping from the front or the back of the sample. This is in contradiction with the magnetization profile obtained in Fig. 2.29 a..

Another discrepancy with some of the experimental results comes from the fact that, if the demagnetization would be purely due to spin–polarized hot–electrons, only a longitudinal relaxation of the magnetization of each atomic magnetic moment would be seen due to the depletion of majority electrons. Such a dynamics contradicts the work of Carva *et al.*[14] and Eich *et al.*[29] who have shown that most of the demagnetization comes from transversal excitations, as reviewed in Sec. 2.2.4. However, this longitudinal relaxation has to be differentiated from Stoner excitations, which are the consequence of spin–flips and, unlike the work of Battiato *et al.*, are therefore not conserving the spin angular momentum of the electron bath.

Lastly, the hypothesis of conservation of the total angular momentum in the electron bath has recently been disproved by Dornes *et al.*[64], who showed that 80 % of the angular momentum is dissipated in the phonon bath on a timescale of 200 fs, which corresponds to the duration of the demagnetization.

2.4.3 Classical magnetization dynamics and transversal excitations

2.4.3.1 Atomistic scale

In the atomic description of the magnetization dynamics, each atom carries a magnetic moment whose dynamics is described by the Landau-Lifshitz-Gilbert equation. An extensive review of this topic has already been written in 2014 by Evans *et al.*[88]. In this section, we will briefly recall the principal equations, followed by a report of the work directly related the topic of light–induced ultrafast demagnetization.

The dynamics of an atomic magnetic moment, i, is governed by the Laudau–Lifshitz–Gilbert equation of motion:

$$\frac{\partial \mathbf{S}_i}{\partial t} = -\frac{\gamma}{(1+\lambda^2)\mu_S}\left[\mathbf{S}_i \times \mathbf{H}^i_{\text{eff}} + \lambda \mathbf{S}_i \times \left(\mathbf{S}_i \times \mathbf{H}^i_{\text{eff}}\right)\right] \tag{2.26}$$

In this equation, $\mathbf{S}_i$ is a unit vector pointing in the direction of the magnetic moment of the atom on the site i, $\mathbf{H}^i_{\text{eff}}$ is the effective field felt by the atom i, μ_S is the modulus of its magnetization, γ is the gyromagnetic ratio of the electrons and λ is the microscopic damping. As each element of the right–hand side brings a contribution perpendicular to the direction of $\mathbf{S}_i$, this equation conserves the norm of the atomic magnetic moments. The first term accounts for the Larmor precession of the magnetization, while the second is a dissipative contribution which tends to align the magnetic moment with the existing field. $\mathbf{H}^i_{\text{eff}}$ is derived from the spin Hamiltonian:

$$\mathbf{H}^i_{\text{eff}} = -\frac{1}{\mu_S}\frac{\partial \mathcal{H}}{\partial \mathbf{S}_i}, \tag{2.27}$$

where $\mathcal{H}$ typically accounts for the exchange, the anisotropy, the dipolar field and any external field.

However, using Eq. 2.26 and Eq. 2.27 does not produce a thermal distribution of the magnetization as fluctuations are not accounted for. To remedy this issue and fulfill the fluctuation–dissipation theorem, Brown[89] developed a Langevin dynamics, which assumes that thermal fluctuations can be represented as a Gaussian white noise term. In this framework, the instantaneous thermal field present on the atomic site i expressed as:

$$\mathbf{H}^i_{\text{th}} = \mathbf{\Gamma}(t)\sqrt{\frac{2\lambda k_B T \mu_S}{\gamma \Delta t}}, \tag{2.28}$$

is added to $\mathbf{H}^i_{\text{eff}}$ in Eq. 2.26. In Eq. 2.28, $\mathbf{\Gamma}(t)$ is a three–dimensional Gaussian distribution with a mean of zero, k_B is the Boltzmann constant, Δt is the time–step and T is the temperature at which the system is supposed to be. As it will soon be argued, the definition of the latter quantity is rather ambiguous.

As discussed in depth in Sec. 2.2.3, the most likely mechanisms for the ultrafast demagnetization are the generation of transversal magnetic excitations and Stoner excitations. It is not fully understood yet how these excitations are emerging from the light–matter interaction on such a short timescale. In this context, the Langevin atomistic LLG dynamics can provide some insights, as it is the simplest description accounting only for transversal excitations. Kazantseva *et al.*[90] used this method coupled to a two temperature model accounting for the bath of the electrons and the phonons in order to study the light–induced demagnetization. Before going further into the description of the dynamics, it is mandatory to mention the implications of the lack of a bath for the magnetic moments. First, it means that a non–neglectable part of the specific heat of the system, whose contribution is especially important near the Langevin ferromagnetic–paramagnetic phase transition, is neglected. Second, and as a direct consequence of the first implication, the total energy is not conserved for the entire system, *i.e.* the magnetic moments, the electrons and the phonons, but only for the electron–phonon system. Looking more carefully at the amplitude of the changes in the total energy could be a good way to assess the validity of this approximation. Third, as no temperature is defined for the bath of the magnetic moments, it is considered here that they instantly react to the electronic temperature, *i.e.* in Eq. 2.28, $T = T_e$. However, this choice seems rather arbitrary as the bath of the phonons could equally have been chosen, or for this matter, any linear combination of the two. It means that in this framework, the magnetic moments only react to the change of the temperature, without having any constraint on the conservation of energy, and that, in fact, there is no transfer of energy between the electrons and the phonons included in the 2TM and the magnons. Kazantseva *et al.* found out that, even though the changes in the electronic temperature are instantly "felt" by the bath of the magnetic moments, changes in the magnetization are only as fast as the rate at which the increase of the thermal fluctuations affects the system. According to the fluctuation dissipation theorem, this rate is proportional to the damping, λ. As a consequence, even though the electronic system is raised above the Curie temperature during a brief period, the system does not necessarily have the time to fully demagnetize.

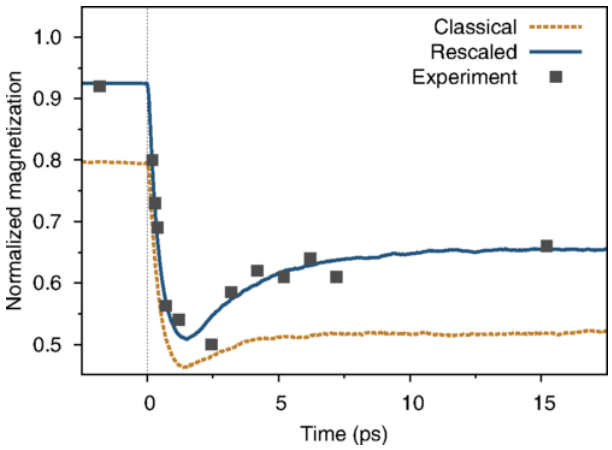


FIGURE 2.30: Simulated demagnetization of Ni comparing classical and rescaled models with experimental data from [5]. The rescaled dynamic simulations show quantitative agreement with experiment from an atomic level model. Image and caption extracted from Ref. [91].

Later on, Evans *et al.*[91] showed that using the same framework as Kazantseva *et al.*, it was possible to fit the light–induced demagnetization of Ni if a rescaling was applied to the temperature such as:

$$\frac{T_{\text{sim}}}{T_{\text{c}}} = \left(\frac{T_{\text{exp}}}{T_{\text{c}}}\right)^{\alpha} \tag{2.29}$$

Where T_{sim} is the temperature used in Eq. 2.28, for the calculation of the amplitude of the fluctuations. α was obtained from the fit of the experimental static temperature–dependent magnetization. Interestingly, this scaling factor, which has been obtained from static measurements, greatly improved the fitting of the light–induced dynamics in case of Ni, as seen in Fig. 2.30.

Before concluding this section, it is mandatory to mention that even though, as discussed in Sec. 2.2.3, the main origin of the ultrafast light–induced demagnetization is the generation of magnons, other phenomena inducing a longitudinal relaxation of the magnetic moment may be involved. As it is presented here, the atomistic LLG equation does not account for such excitations, as the length of the magnetic moment carried by each atom is considered constant during the dynamics. As it has been discussed in Sec. 2.4.2.1, and will be in Chap. 6, such an excitation can be induced by electron–phonon scattering events through the Elliott-Yafet mechanism and by light absorption. The latter is of a primary interest in the understanding of the AO–HDS, as this contribution can be helicity–dependent and lasts even after the light is gone. The inclusion of a longitudinal relaxation term could be though of as in the Laudau–Lifshitz–Bloch equation reviewed in the next section.

2.4.3.2 Macroscopic scale

To circumvent the limitations of size imposed by the computationally intensive atomistic LLG approach, a micromagnetic theory, in which the magnetization is now described as a continuum can be used. While it allows for a dramatic increase of the size of the systems, it fails to describe correctly the temperature effects[92]. This is mainly due to the fact

that each finite element holds a temperature–independent magnetic moment acting as a macro-spin. As a consequence, every material acts as a superparamagnet.

To remedy the drawbacks of the micromagnetic (*i.e.* finite element) LLG, Garanin *et al.*[93] derived from the Fokker-Planck equation a Landau-Lifshitz-Bloch (LLB) equation. The LLB equation adds the longitudinal degree of freedom to the dynamics, which allows each of the finite elements to change its magnetization length according to the temperature. However, the equation developed by Garanin did not include the effects of thermal fluctuations, whose presence is of primary importance to model the effects of temperature, as discussed in Sec. 2.4.3.1. In 2012, Evan *et al.*[94] derived a stochastic LLB equation giving a magnetization distribution consistent with the Boltzmann one. It writes as:

$$\frac{d\boldsymbol{m}}{dt} = -\gamma\left[\boldsymbol{m}\times\boldsymbol{H}_{eff}\right] - \frac{\gamma\alpha_{\parallel}}{\boldsymbol{m}^2}\left(\boldsymbol{m}\cdot\boldsymbol{H}_{eff}\right)\boldsymbol{m} - \frac{\gamma\alpha_{\perp}}{\boldsymbol{m}^2}\left[\boldsymbol{m}\times\left(\boldsymbol{m}\times\left(\boldsymbol{H}_{eff}+\boldsymbol{\zeta}_{\perp}\right)\right]+\boldsymbol{\zeta}_{\parallel}\right. \tag{2.30}$$

with $\boldsymbol{m} = \frac{\boldsymbol{M}}{M_e(0)}$, the normalized magnetic moment of a finite element, $M_e(T)$ the finite element magnetic module at the temperature T, $M_e(0) = M_s$ its maximum value when T = 0 K and $\boldsymbol{M}$ the instantaneous magnetic moment of the finite element.

In Eq. 2.30, in addition to the perpendicular damping term proportional to $\alpha_{\perp}$ and playing the same role in the LLB equation than α in the LLG equation, a second parallel damping term, proportional to $\alpha_{\parallel}$ appears. It describes how fast changes in the electron temperature will reflect on the finite element magnetization length.

Using this approach, a perpendicular $\boldsymbol{\zeta}_{i,\perp}(t,r)$ and parallel $\boldsymbol{\zeta}_{i,\parallel}(t,r)$ thermal field appear. They must satisfy the following constraints:

$$\left\langle \boldsymbol{\zeta}_{i,\perp}(t,r)\boldsymbol{\zeta}_{j,\perp}(t',r')\right\rangle = \frac{2k_BT\left(\alpha_{\perp}-\alpha_{\parallel}\right)}{|\gamma|\,M_sV\alpha_{\perp}^2}\delta_{ij}\delta(t-t')\delta(r-r') \tag{2.31a}$$

$$\left\langle \boldsymbol{\zeta}_{i,\parallel}(t,r)\boldsymbol{\zeta}_{j,\parallel}(t',r')\right\rangle = \frac{2\,|\gamma|\,k_BT}{M_sV}\alpha_{\parallel}\delta_{ij}\delta(t-t')\delta(r-r') \tag{2.31b}$$

In this derivation, $\boldsymbol{\zeta}_{i,\parallel}(t,r)$ is an additive noise, *i.e.* it is not added inside the second term of the right–hand side of Eq. 2.30, as it is the case for the perpendicular noise, added in the third term.

Using this framework and a two temperature model, Mendil *et al.*[95] reproduced the experimental magnetization induced during and after a femtosecond laser pulse in FePt. Still in the case of FePt, and before the derivation of Evan, Kazantseva *et al.*[90] extracted all the relevant parameters needed in the LLB equation from atomistic LLG simulations.

2.4.4 Helicity–dependent effects

The heart of this section is to review the different possible helicity–dependent effects from which could arise the helicity–dependent all-optical switching. First, we will discuss the role of the helicity–dependent absorption coming from the magnetic circular dichroism. Even though its origin lies in an optical effect, the driving mechanism of the switching is purely thermal. On the contrary, the inverse Faraday effect is purely optical and is usually considered as a light–induced helicity–dependent magnetic field. However, it is not clear

if this effect should also be considered as an induced magnetization. Finally, a second purely optical helicity–dependent effect, which is one of the novelties of this thesis, will be described in Chap. 6.

2.4.4.1 Magnetic circular dichroism and helicity–dependent switching

The purpose of this section is to review the work relating the magnetic circular dichroism to the helicity–dependent switching. Indeed, Gorchon *et al.*[96], as well as Ellis *et al.*[97] presented numerical evidences showing that a difference of absorption between the two opposite magnetic states could lead to a helicity–dependent switching purely due to the simultaneously induced difference of thermal fluctuations. However, before reviewing the aforementioned work, we will briefly recall the origin of the helicity–dependent absorption emanating from the properties of the dielectric tensor of magnetic materials.

In order to understand the roots of the magnetic circular dichroism (MCD), we consider a homogeneous material holding a permanent magnetization along the z axis. Its dielectric tensor takes the following form:

$$\varepsilon(\omega) = \begin{pmatrix} \varepsilon_{11}(\omega) & \varepsilon_{12}(\omega) & 0 \\ -\varepsilon_{12}(\omega) & \varepsilon_{11}(\omega) & 0 \\ 0 & 0 & \varepsilon_{11}(\omega) \end{pmatrix} \tag{2.32}$$

Where the out of diagonal elements arise from a "Lorentz force" caused by the presence of both magnetic moments and spin–orbit coupling. The dielectric tensor, Eq. 2.32, is diagonal in the circularly polarized basis:

$$\boldsymbol{u}_{\pm} = \frac{1}{\sqrt{2}} \left(\boldsymbol{u}_x \pm i \boldsymbol{u}_y \right) \tag{2.33}$$

and the diagonal elements write as $\varepsilon_{\pm} = \varepsilon_{11} \pm i\varepsilon_{12}$. As a consequence, the propagation of a σ^+ and a σ^- polarized light along the z axis will be different, as evidenced by the real and imaginary part of the complex optical index $\tilde{n}_{\pm} = n_{\pm} + ik_{\pm}$ writing as:

$$n_{\pm}(\omega) = \sqrt{\frac{|\varepsilon_{\pm}(\omega)| + \mathrm{Re}\left[\varepsilon_{\pm}(\omega)\right]}{2}} \tag{2.34}$$

and:

$$k_{\pm}(\omega) = \sqrt{\frac{|\varepsilon_{\pm}(\omega)| - \mathrm{Re}\left[\varepsilon_{\pm}(\omega)\right]}{2}}. \tag{2.35}$$

The helicity–dependence of $k_{\pm}$ is of a particular interest, as it induces an helicity–dependent absorption coefficient:

$$A_{\pm}(\omega) = \frac{2\omega k_{\pm}(\omega)}{c} \tag{2.36}$$

From Eq. 2.36, one can compute the MCD as $\mathrm{MCD} = \frac{2(A_+ - A_-)}{A_+ + A_-}$. As we will see shortly, the order of magnitude of this MCD effect is typically of $\approx 1\%$. Before moving on to the description of the reason such a phenomenon can induce a switching, it is necessary to recall that upon time reversal, both the magnetization direction and the helicity of the light is reversed. As a consequence, the absorption of a σ^+ (resp. σ^-) polarized light by

an up (resp. down) state is the same as the absorption of a σ^- (resp. σ^+) polarized light by a down (resp. up) state. This fact is particularly relevant in the case of the experimental configuration, in which the AO–HDS is occurring as, of course, for a given light pulse, the polarization is either σ^+ or σ^-. However, for a given polarization of the light, the magnetic domains will absorb differently whether their magnetization is up or down.

To investigate the possibility of such an absorption difference to induce a helicity–dependent switching, Gorchon *et al.*[96] represented a magnetic material by an array of N_x by N_y macrospins, all having a strong out of plane anisotropy and being totally uncoupled, as both the dipolar field and the exchange interaction was ignored. Contrary to the precessional dynamics described by the LLG and LLB equations developed in Sec. 2.4.3, each macrospin could only be in an up–state or a down–state. To compute the probability of switching from one state to the other due to the effect of thermal fluctuation, Gorchon *et al.*[96] used the Néel–Brown formula[89]:

$$\tau_{ab}(T) = \tau_0 e^{\frac{E_{ab}(T)}{k_B T}} \tag{2.37}$$

where τ_{ab} is the characteristic hopping time from a state a to a state b, τ_0 is the attempt time, T is the temperature of the cell and $E_{ab} = K(T)V$ is the energy barrier where V is the volume of the macrospin and $K(T)$ is the temperature–dependent energy density of the anisotropy, which decreases as T increases. The physics contained in this formula is that the higher the temperature, the more the system will hope from a state a to a state b. Knowing τ_{ab}, the probability of going from the state a to the state b, P_{ab}, as well as the probability of staying on the state a are given by:

$$\begin{aligned} P_{ab} &= \frac{1}{2}\left[1 - e^{-\frac{t_{\text{hot}}}{\tau_{ab}(T_0+\Delta T)}}\right] \\ P_{aa} &= 1 - P_{ab} \end{aligned} \tag{2.38}$$

where T_0 is the initial temperature and ΔT represents the increase of temperature induced by the light–matter interaction. However, due to the helicity–dependence of the absorption described *supra*, the temperature at which the macrospins are heated depends on their state. It is given by $T_{hot/cold} = T_0 + (1 \pm \frac{MCD}{2})\Delta T$. As a consequence, $P_{ab} \neq P_{ba}$ and, in the case where the state a absorbs more than the state b, $P_{ab} > P_{ba}$. Such a fact can lead to a deterministic switching as, for an infinite number of pulses, the authors found that the probability of obtaining the b state is given by $\frac{P_{ab}}{P_{ab}+P_{ba}}$.

In their case study, Gorchon *et al.*[96] considered a granular thin–film of FePt–C–$L1_0$ where gains of 5 nm to 7 nm are contained in a matrix of C and are therefore not correlated by exchange interactions. This justifies the aforementioned macrospin approximation. All the relevant parameters of the simulation were either obtained or fitted from experiments. The temperature profile was considered to be steplike and lasted 1 ns. Fig. 2.31 shows the probability of obtaining a switching after 10 pulses, as a function of both the MCD and the temperature increase. It reveals that, in agreement with experiments, this mechanism requires a strong thermal activation, as the deterministic switching is only obtained when the temperature approaches T_c. Moreover, increasing the value of the MCD improves the efficiency, as the window of temperature at which the deterministic switching occurs widens. The authors used Kerr rotation and Kerr ellipticity measurements in Refs. [98, 99] to compute the experimental value of MCD for a light having a wavelength of 810

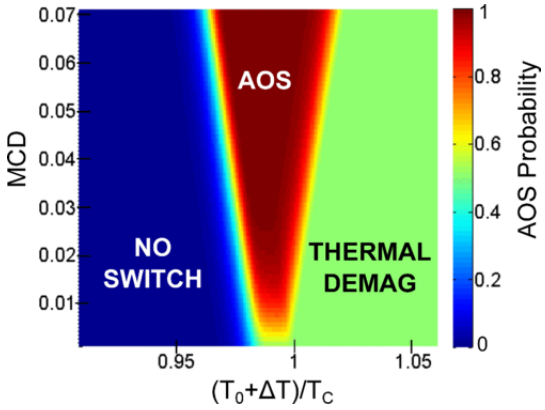


FIGURE 2.31: AOS Probability as a function of temperature and MCD for N=10 pulses. Image and caption extracted from Ref. [96].

nm. They found a value of 5.8%, for which, as seen Fig. 2.31 deterministic switching can indeed occur.

Soon after Gorchon *et al.*, Ellis *et al.*[97] arrived at nearly as the same conclusion using the same framework. To compute the grain temperature, instead of using a steplike profile, they relied on a 2TM model and the electronic temperature was attributed to the magnetic moments. As Gorchon *et al.*, they obtained a switching toward the less absorptive state but, in their case, without reaching any saturation. Finally, and as argued by Gorchon *et al.*, the fact that the dipolar field has been neglected can lead to a strong overestimation of the switching as, in the presence of such a field a fully saturated film is harder to obtain and to maintain during the cooling process.

While in the work of Gorchon *et al.* and Ellis *et al.* reviewed *supra*, MCD has been held responsible for the helicity–dependent switching of macrospins, its role can be extended to continuous thin films as well. Indeed, it is well established that temperature gradients produce a torque on domain walls which, as a consequence, move toward the hottest spot[58, 59]. In the presence of MCD, such gradients can emerge and were attributed by Quessab *et al.*[57] as a possible candidate in the explanation of the helicity–dependent domain wall displacement (see Sec. 2.3.2). Using the 2TM and a MCD of 2%, they computed an electronic temperature difference of 10 K between the two magnetic states. As in the Co/Pt thin film they investigated, the domain wall had a width of 10 nm, that corresponded to a thermal gradient of 1 K nm^{-1} which they estimated to have the same effect as a field of 7 mT. However, as mentioned in Sec. 2.4.3, the question of knowing if the electronic temperature is the one which is in fact "felt" by the magnetic moments is especially relevant here. Indeed, this case is providing the largest gradient of temperature, as compared to, *e.g.* the gradient of temperature in the bath of the phonons. Moreover, this work also neglected the role of hot electrons whose main contribution is, as discussed in Sec. 2.2.4, to rapidly homogenize the energy deposited by the light, and as a consequence of which the thermal gradient could be dramatically reduced.

2.4.4.2 The inverse Faraday effect

The effect of magnetized materials on the polarization of the light propagating through them has been known for nearly two centuries. Indeed, in 1845 Michael Faraday discovered the first experimental evidences of this phenomenon in a piece of glass containing traces of lead. He showed that in the presence of a magnetic field, the polarization of the light was rotated by an angle that was proportional to the field. Much more recently, the reciprocal effect, called the inverse Faraday effect (IFE) has been predicted by Pitaevskii[3] in non–dissipative mediums. Only a few years later, experimental confirmation of a static magnetization solely induced by the light was provided by Van Der Ziel *et al.*[100]. In the light of the more recent experimental results described in detail in Sec. 2.3, the IFE has naturally been invoked as a possible origin for the helicity–dependent switching. However, in this context its role is more ambiguous than in the original theory and experimental results. The objective of this section is therefore to briefly recall the theory developed by Pitaevskii[3] and Pershan[4], which has been more recently used as a basis for micromagnetic simulations. Then, we will discuss the work of Battiato *et al.*[101, 102] and Berritta *et al.*[103] concerning the formulation of an inverse Faraday effect valid in all types of medium. Finally, the capability of this phenomenon to induce the experimentally–seen helicity–dependent switching will be assessed.

In transparent mediums at thermodynamic equilibrium The inverse Faraday effect was first introduced to describe the influence of the presence of a circularly polarized light on the magnetic state of transparent and non–magnetic mediums[3, 4]. The theory was based on the existence of the potential:

$$F = \chi H(\epsilon_R \epsilon_R^* - \epsilon_L \epsilon_L^*) \tag{2.39}$$

where χ is a material–dependent constant, H is the applied external magnetic field and ϵ_L and ϵ_R are the amplitudes of the left and right circularly polarized light. Such a potential has been proved to exist for a non–absorbing isotropic or cubic material by Pershan [104] in 1963. From F, one can derive the contribution to the dielectric tensor of the left and right circularly polarized light as:

$$\begin{aligned} \Delta\epsilon_R &= -4\pi \frac{\partial^2 F}{\partial \epsilon_R \partial \epsilon_R^*} = -4\pi\chi H \\ \Delta\epsilon_L &= -4\pi \frac{\partial^2 F}{\partial \epsilon_L \partial \epsilon_L^*} = 4\pi\chi H \end{aligned} \tag{2.40}$$

from which are emerging the magneto–optical effects such as the Faraday and Kerr effects. More surprisingly, from F one can see emerging a light–induced magnetization in a zero magnetic field:

$$M_{\mathrm{IFE}} = -\frac{\partial F}{\partial H} = -\chi(\epsilon_R \epsilon_R^* - \epsilon_L \epsilon_L^*) \tag{2.41}$$

Eq. 2.41 shows that in case of a linearly polarized light, which is a superposition of a circularly left and right polarized light, $M_{\mathrm{IFE}} = 0$. Moreover, its amplitude is maximized in the case of a purely circularly polarized light, and its sign is polarization–dependent. Eq. 2.41 can equally be rewritten in the following form:

$$\boldsymbol{M}_{\mathrm{IFE}} = -\chi \boldsymbol{E} \times \boldsymbol{E}^{*} \tag{2.42}$$

Before proceeding to the next part of this thesis, it is necessary to emphasize that Eq. 2.41 is only valid in a zero magnetic field, which is not the case in magnetized materials. Finally, as seen in Eq. 2.41, the light induced magnetization is proportional to the intensity of the light and therefore vanishes with it.

In micromagnetic calculations While the potential expressed in Eq. 2.39 is only valid in non–absorbing materials and in the absence of a magnetic field or a permanent magnetization, it has been widely used to explain the origin of the AO–HDS even in dissipative and magnetized materials, notably by coupling an effective "optomagnetic field" to micromagnetic calculations. Indeed, in Sec. 2.4.3, we showed the possibility of describing the ultrafast light–induced demagnetization at different scales by using the atomistic Laudau–Lifshitz–Gilbert equation or the Laudau–Lifshitz–Bloch equation. In this framework, the most straightforward thing would be to add a magnetic field to $\boldsymbol{H}_{\mathrm{eff}}$ to account for the effect of the helicity of the light. The rationalization of this helicity–dependent magnetic field is based on Eq. 2.42: the light–induced magnetization produces a magnetic field which in turn interacts with the permanent magnetization of the medium.

Such an endeavor has been undertaken by Vahaplar *et al.*[46], as well as by Khorsand *et al.*[47] to explain the helicity–dependent single pulse switching occurring in GdFeCo. However, as reviewed in Sec. 2.3.1.2 this deterministic single pulse switching has later been attributed to a difference of absorption due to the magnetic circular dichroism.

More recently, Ellis *et al.*[97] investigated the effect of a possible light–induced optomagnetic field, as suggested by the IFE, in the switching of a granular film of FePt. They used an atomistic Laudau–Lifshitz–Gilbert equation to compute the dynamics of the magnetic moments, which they coupled to a 2TM. The form of the field is given by:

$$\mathbf{H}_{\mathrm{IFE}} = h_{\mathrm{IFE}}\mathbf{u}_z \begin{cases} e^{\left(-\frac{t-t_0}{\tau_l}\right)^2}, & t < t_0 \\ 1, & t_0 < t < t_1 \\ e^{\left(-\frac{t-t_1}{\tau_l}\right)^2}, & t > t_1 \end{cases} \tag{2.43}$$

which corresponds to two Gaussian parts accounting for both the growing of the field ($t < t_0$) as well as its decay ($t > t_1$), which are connected by a static part of variable duration ($t_0 < t < t_1$). Both the field strength, as well as the duration of the static part of the optomagnetic field were taken as parameters. As the intensity of the light–pulse was considered to be Gaussian with a width of 100 fs, the latest fact contradicts the original theory mentioned *supra*, in which the optomagnetic field would be strictly proportional to the intensity of the light, and therefore could not last after it is gone. The same value than the width of the pulse has been attributed to τ_l in Eq. 2.43. Fig. 2.32 presents the percentage of unswitched grains after one pulse. The effect of the field only appears for durations of $\approx$ 400fs and at very high fields, *i.e.* of more than 40 T. These results may indicate that the IFE is not suitable to describe such a behavior, especially because its effect has to last longer than the pulse to affect the dynamics. In Sec. 6 of this thesis, we describe a novel mechanism, whose action on the magnetization lasts even after the light is gone. As a consequence, it could be a good candidate in the description of this phenomenon.

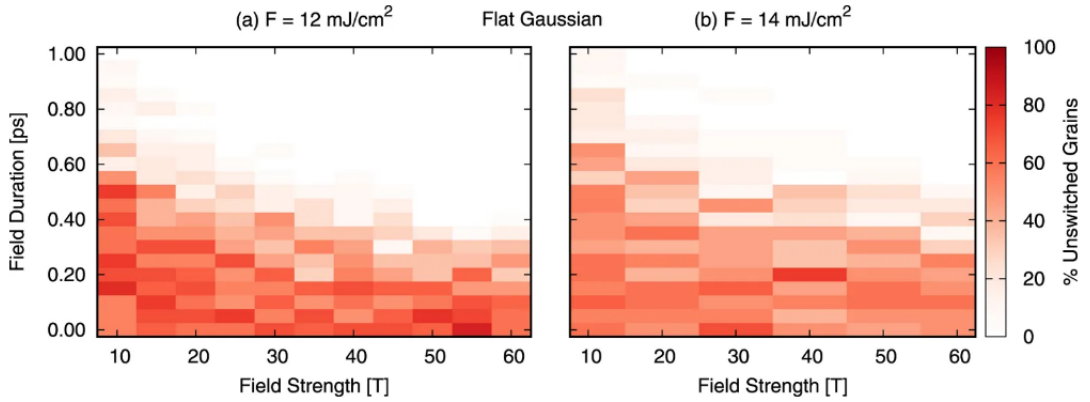


FIGURE 2.32: Percentage of unswitched grains using a laser fluence of (a) 12 mJ/cm^2 and (b) 14 mJ/cm^2 with an inverse Faraday field modeled by a flat Gaussian for varying strengths and duration. The sides of the field are Gaussian shaped with a width of τ_l = 100 fs. Image and caption extracted from Ref. [97].

Finally, it is not clear whether one should consider the IFE as an effective field acting on the magnetization, as in the aforementioned work, or as an induced magnetization as initially suggested by Eq. 2.41. Indeed, the magnetization dynamics induced in both of these cases is totally different as in the former case it is purely precessional, as given by the LLG and the LLB equation, whether in the latter case, the effect is to change the longitudinal value of the magnetization.

Quantum theory Recently, Battiato *et al.*[101, 102] computed from the Liouville–von Neumann equation the responses generated by the light up to the second order of perturbation in the density matrix. They classified these different effects by the localization of the pole of their Laplace transform in the complex plane. They found that at the first order in the density matrix, there is a first harmonic generation, as well as a transient response due to the non–adiabatic switching of the light. Fig. 2.33 lists the second order effects. There is also a transient response, accompanied by a zeroth harmonic, a second harmonic and an absorption term. While all of these contributions can be helicity–dependent, the one which they hold responsible for the presence of IFE in is the zeroth harmonic. Indeed, this contribution exhibits the same behavior as the one of Pershan *et al.*[4], *i.e.* it is strictly proportional to the intensity of the light and therefore vanishes with it.

According to Refs. [101, 102, 103], the induced magnetization due to the zeroth–harmonic generation can be written as:

$$M_{IFE} = (K_o + K_{dA} + K_{dB} + c.c.)\, E_0^2, \tag{2.44}$$

where E_0 is the electric field of the light and K_o, K_{dA} and K_{dB} are expressed as:

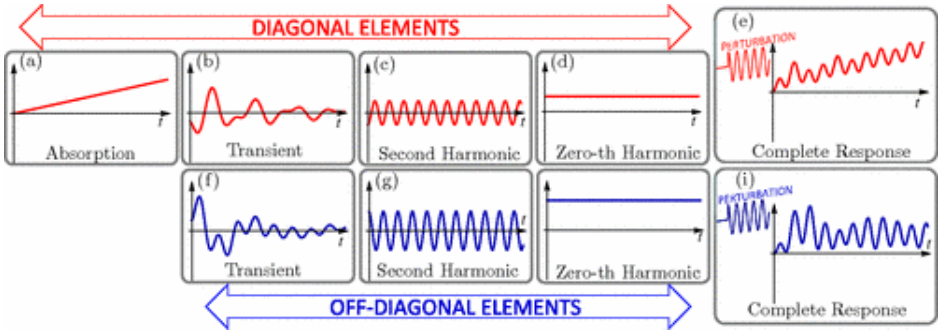


FIGURE 2.33: Second-order response for a three-level model system to the on-switching of a continuous wave external field. In the top and bottom panels, the time behaviors of a diagonal and an off-diagonal element, respectively, are displayed. The complete time behaviors are shown in panels (e) and (i) for the diagonal and off-diagonal element, respectively. The time evolutions of the density matrix elements are separated in absorption, second harmonic generation, zero-th harmonic generation, and transient behavior. Image and caption extracted from Ref. [101].

$$
\begin{aligned}
K_o &= \frac{e^2}{m^2\omega^2}\sum_{n\neq m;l} M_{mn}\frac{\frac{p^+_{nl}p^-_{lm}(f_m-f_l)}{E_n-E_l+i\hbar\Gamma_{nl}-\hbar\omega}-\frac{p^-_{nl}p^+_{lm}(f_l-f_n)}{E_l-E_m+i\hbar\Gamma_{lm}-\hbar\omega}}{E_n-E_m+i\hbar\Gamma_{nm}},\\
K_{dA} &= \frac{e^2}{m^2\omega^2}\sum_{nl} M_{nn}\left[\frac{p^+_{nl}p^-_{ln}(f_l-f_l)}{(E_l-E_n+i\Gamma_{ln}-\hbar\omega)^2}-\frac{p^-_{nl}p^+_{ln}(f_l-f_l)}{(E_n-E_l+i\hbar\Gamma_{nl}-\hbar\omega)^2}\right],\\
K_{dB} &= \frac{e^2}{m^2\omega^2}\sum_{nl}\frac{M_{nn}}{\hbar\omega}\frac{p^+_{nl}p^+_{ln}(f_n-f_l)(i\hbar\Gamma_{ln}-\hbar\omega)}{(E_l-E_n)^2+(\hbar\Gamma_{ln}+i\hbar\omega)}.
\end{aligned}
\tag{2.45}
$$

In Eq. 5.15, p_{nl} are the matrix elements of the momentum operator, where the wavevector $\boldsymbol{k}$ is implicitly included and $p^{\pm} = p_x \pm ip_y$. $f_n = f(E_n)$ are the occupation numbers provided by the Fermi distribution and Γ_{ln} are the broadenings.

Contrary to the original theory of Pitaevskii [3], the aforementioned formalism is valid in any type of material and can therefore be applied to dissipative and magnetized materials. Eq. 2.44 was later implemented by Berritta. *et al.*[103] in an augmented spherical wave *ab initio* code. Fig. 2.34 shows the orbital and spin momentum induced by a σ^+ and a σ^- polarized light in Cu, Au, Pd and Pt. These calculations included the spin–orbit coupling. All the responses are fully antisymmetrical under a change of the helicity of the light, which is in agreement with the behavior mentioned earlier in Sec. 2.4.4.2 for non–dissipative and non–magnetic materials. Moreover, a given helicity always produces an effect of the same sign in all the compounds. Interestingly, for the same helicity of the light, the sign of the light–induced orbital momentum is opposite to the induced spin momentum.

Still including the spin–orbit coupling, Fig. 2.35 shows the static induced orbital and spin magnetization in Fe, Co and Ni. As Fe, Co and Ni all present a permanent magnetization, the antisymmetry of the induced magnetization under a change of helicity is lost. Contrary to the preceding case, this behavior is in contradiction with the theory of IFE in non–dissipative and non–magnetized mediums. For both Co, Ni and Fe, the induced

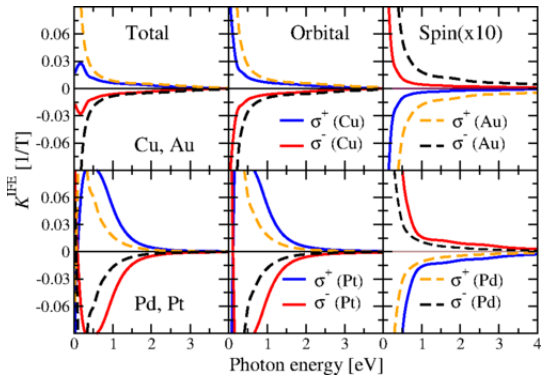


FIGURE 2.34: Calculated total, orbital, and spin IFE $K^{IFE}(\omega)$ as function of the photon energy for several nonmagnetic metals: Cu and Au (top) and Pd and Pt (bottom). The opposite circular laser polarizations are denoted with $\sigma^{\pm}$. Image and caption extracted from Ref. [103].

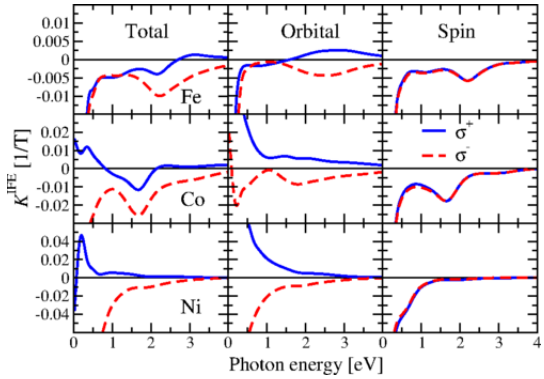


FIGURE 2.35: Calculated total, orbital, and spin inverse Faraday constant $K^{IFE}(\omega)$ as function of the photon energy and laser polarizations $\sigma^{\pm}$ for ferromagnetic bcc–Fe, hcp–Co, and fcc–Ni. Image and caption extracted from Ref. [103].

spin angular momentum is always opposed to the existing magnetization and seems to slightly depend on the helicity of the light. The antisymmetrical behavior is also lost for the light–induced orbital angular momentum, even though at most of the frequencies, the sign of the effect is opposed for opposite helicities.

Next, Berritta *et al.*[103] computed the value of the IFE in antiferromagnetic Fe. As seen at the top of Fig. 2.36, the antisymmetry of the induced magnetization is recovered as this compound is symmetric under time–reversal. Moreover, as seen at the bottom of Fig. 2.36, in the absence of spin–orbit coupling, the light–induced orbital magnetization is also antisymmetric under a change of helicity and no spin angular momentum is induced anymore. Indeed, without spin–orbit coupling, $\left[\hat{H}, \hat{\sigma}_i\right] = 0$ and the spin becomes an invariant of the motion.

Tab. 2.2 contains the calculated values for the induced magnetization at a photon energy of 1.55eV and a light intensity of 10 GW/cm^2. It shows that the induced magnetization is 3 order of magnitude lower than the existing magnetization in all the magnetized compounds. The effective magnetic field, B_{opt}, represent the field needed to induce a similar change in the value of the length of the magnetization. Its value ranges from 16 T to 420 T in magnetized materials, and from 2 T to 350 T in the other studied metals. Such

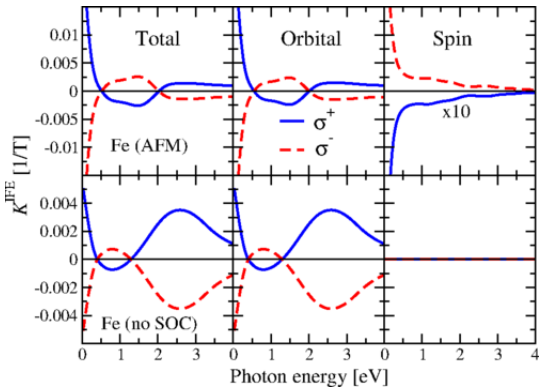


FIGURE 2.36: Calculated total, orbital, and spin IFE $K^{IFE}(\omega)$ as function of the photon energy for synthetic antiferromagnetic Fe (top panels) and for ferromagnetic Fe with zero spin-orbit coupling (bottom panels). A magnification of ten is used only for the top-right panel. Image and caption extracted from Ref. [103].

Material	M_{ind} ($^{-3}\mu_B$/at. vol.)		B_{opt} (Tesla)	
	σ^+	σ^-	σ^+	σ^-
Ni (fcc)	+1.4	-4.5	+16	-50
Fe (bcc)	-3.3	-5.5	-40	-65
Co (hcp)	-4.8	-13	-100	-260
FePt	-15	-33	-190	-420
Cu (fcc)	+2.0	-2.0	+100	-100
Pd (fcc)	+2.7	-2.7	+2	-2
Pt (fcc)	+6.5	-6.5	+28	-28
Au (fcc)	+7.5	-7.5	+350	-350

TABLE 2.2: Calculated values of the optical helicity-dependent laser-induced magnetization (in μ_B per atomic volume), for various metals, assuming a typical photon energy of 1.55 eV and intensity of 10 GW/cm^2. Also given is the computed optomagnetic field B_{opt}, *i.e.*, the Zeeman field needed to induce the same magnetization as the circularly polarized laser field. Table and caption extracted from Ref. [103].

high values raise the question of the relevance of considering the effect of this induced magnetization as a magnetic field acting on the existing magnetization, rather than simply a change in the value of the existing magnetization, as already discussed in the end of Sec. 2.4.4.2.

In the Fig. 2.34, Berritta *et al.*[103] showed that the spin part of the helicity–dependent effect is lower than the orbital part and, as a consequence they had to magnify it by a factor of 10. However, one could wonder if such a helicity–dependent effect is also present in the case of the ferromagnetic materials Ni, Co and Fe. Indeed, it seems that in these materials, the main effect of the light is to induce a component of spin opposed to the existing one. Nevertheless, looking closely at Fig. 2.35, one can see that the spin induced by a σ^+ and a σ^- polarized light do not fully overlap, hinting towards the presence of a helicity–dependence.

Furthermore, regarding the light–induced orbital magnetization which, as seen in Fig.

2.35 provides most of the helicity–dependence of M_{ind} in the ferromagnets, a note of caution is warranted. Indeed, even though the code employed by Berritta *et al.*[103] uses an augmented spherical wave basis set which provides a good framework to compute the orbital angular momentum of the localized d and f states, one may ask the relevance of such a computation when more delocalized states (such as s orbitals) are involved. In such a case, the orbital angular momentum becomes ill defined due to the periodic boundary conditions[105]. One may then question the accuracy of this contribution.

Finally, it is mandatory to mention that while the framework developed by Battiato *et al.*[101, 102] provides a general method to compute the effect of light on the matter and therefore allows to study both magnetized and absorptive compounds, the work of Berritta *et al.*[103] only accounted for the static part of the induced response. As pointed out by Battiato *et al.*[102], dissipation changes the form of this static part associated with the IFE, but it does not mean that M_{IFE} also contains the effect of absorption. Indeed, as pictured in Fig. 2.33 (a), the absorption is an entirely different part of the response which could be helicity–dependent as well. In fact, the study of this phenomenon is one of the novelties of this thesis and is reported in Chap. 6.

2.4.5 Toward the use of real–time time–dependent density functional theory

The time–dependent density functional theory (TDDFT) relies on the Runge–Gross theorem[106] which states that the time-dependent external potential is a unique functional of the time–dependent density for a given initial state. In the case of weak perturbation, where the linear regime holds, TDDFT has successfully been applied to compute the response functions (charge–charge response, the spin–spin response and charge–spin response). However, in the case of larger perturbations, the dynamics of the system can directly be calculated by propagating a Schroedinger–like equation. Indeed, in this framework, the dynamics of the Kohn-Sham spinors is given by

$$i\frac{\partial \phi_{n\mathbf{k}}(\mathbf{r},t)}{\partial t} = \Big(-\frac{1}{2}\nabla^2 - \frac{i}{c}\mathbf{A}_{ext}(t)\cdot\nabla + v_s(\mathbf{r},t) + \frac{1}{2c}\boldsymbol{\sigma}\cdot\mathbf{B}_{xc}(\mathbf{r},t) - \frac{1}{4c^2}\boldsymbol{\sigma}(\nabla v_s(\mathbf{r},t)\times i\nabla)\Big)\phi_{n\mathbf{k}}(\mathbf{r},t). \quad (2.46)$$

In this equation $\phi_{n\mathbf{k}}(\mathbf{r},t) = \langle \mathbf{r}|n\mathbf{k}(t)\rangle$ is a Bloch orbital indexed by $\boldsymbol{k}$, a vector of the first Brillouin zone and n the band index, $\mathbf{A}_{ext}$ is the vector potential of the light, $\boldsymbol{\sigma}$ are the Pauli matrices, $B_{xc}(\boldsymbol{r},t)$ is the exchange correlation magnetic field, $v_s(\boldsymbol{r},t)$ is the effective Kohn-Sham potential and is the sum of the external potential and $v_{ext}(\boldsymbol{r},t)$, the Hartree potential, $v_H(\boldsymbol{r},t)$ and the exchange correlation potential $v_{xc}(\boldsymbol{r},t)$. The last term in Eq. 2.46 is the spin–orbit coupling. Without it, $\boldsymbol{\sigma}$ would commute with the Hamiltonian and the magnetization would remain constant during the dynamics, as shown by Krieger *et al.*[107]. Using RT–TDDFT to compute the effect of a short pulse having a duration of 6 fs, a fluence of 934.8 mJ/cm^2 and for which the vector potential **A**(t) is visible at the top panel of Fig. 2.37, they studied the demagnetization of Fe, Co and Ni bulks. As seen in the middle panel, in all cases, the pulse induced a demagnetization. Surprisingly, most of the demagnetization occurred after the pulse. As explained by Krieger *et al.*, during the light–matter interaction, many localized electrons, giving rise to the magnetization,

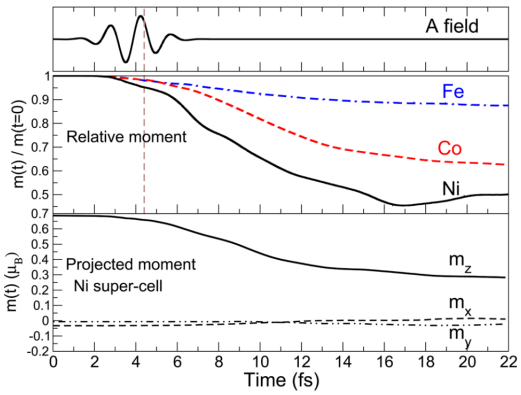


FIGURE 2.37: Top panel: **A**(t) of the laser pulse. Middle panel: relative magnetic moment. Lower panel: *x*-, *y*-, and *z*-projected magnetic moments per atom for a supercell of Ni. Image and caption extracted from Ref. [107].

were excited to more delocalized states. In this process the interstitial region, initially unpolarized, polarizes. While its polarization remains almost constant during the rest of the dynamics, the rest of the localized electrons flip their spins for $\approx 15fs$ after the pulse is gone, engendering the demagnetization.

Furthermore, as the loss of magnetization is larger in Ni than in Co, it compares well with experiments[65], however, this conclusion has to be put in perspectives. Indeed, this demagnetization occurs here in $\approx 20fs$, versus $\approx 100fs$ experimentally for the fastest demagnetizations. This may be due to both the very high fluence used ($\times 100$ what is usually used in experiments) and the very short duration of the pulse. However, one has to remind that in this framework, due to periodicity, only longitudinal change of the magnetization is allowed. As a consequence, the contribution of transversal excitations, which have been shown to be one of the major sources of ultrafast demagnetization (see Sec. 2.2.3) is nullified here. To test the possible effect of such excitations, Krieger *et al.* made a supercell and randomly applied a small tilt to the initial direction of the magnetization of each atom. They found that the interaction with light did not amplify the initial tilt and concluded that transversal excitations do not play a role. However, it might simply be that RT–TDDFT is not yet suited to account for the whole range of possible excitations, as discussed below.

Shortly after, Krieger *et al.*[108], used the same laser pump parameters as Stamm *et al.*[17] (fluence of 8.05 mJ/cm^2 and full width at half maximum of 40 fs) to be able to compare the magnetization dynamics in Ni they obtained from *ab initio* RT–TDDFT to Stamm's experiments. In their study, Krieger *et al.* compared the case of a bulk compound with an actual thin films of Ni of 5 atomic layers separated by a void of the same thickness. They observed a demagnetization of only 8% in the case of the bulk, while more than the double was obtained for the free–standing thin film. The latter was in relatively good agreement with the experimental demagnetization for the first $\approx 120fs$, while still underestimating it. However, this relatively good agreement has, once more, to be put into perspective. Indeed, Krieger *et al.*[107] overestimated the actual fluence to which the Ni film was subjected as, experimentally, a part of the pump is reflected, and the effects of absorption on the intensity profile of the light was not taken into account. Moreover, in the experiment, far from a free–standing Ni thin film of 5 atomic layers, the 15 nm thick thin film rests on an Al substrate having a thickness of 500 nm. Consequently,

as discussed at length in Sec. 2.2.4, excited carriers, or hot electrons, are able to propagate in the Al layer, leading to a totally different dynamics than what would be obtained from a freestanding Ni layer.

Later, in a joint theoretical and experimental study, Chen *et al.*[109] investigated the effect of the interface between a magnetic layer (Co) and a metal (Cu) on the magnetization dynamics. On the experimental side, they employed the second harmonic generation as a probe to selectively study the Co/Cu(001) interface pumped by 35 fs pulses having a wavelength of 800 nm. The fluence used experimentally was 4 ± 2 mJ / cm^2, while the one used in TDDFT was considerably reduced to 0.25 mJ/cm^2 in order to account for the fact that $\approx$ 94 % of the incident pump fluence was being reflected. Fig. 2.38 (left) shows both the time–dependent magnetization dynamics obtained experimentally and with RT–TDDFT. The TDDFT calculation has been performed with and without spin–orbit coupling. The purpose of the spin–orbit removal was (as the spin moment is conserved during the dynamics) to isolate the part of the demagnetization of the Co atoms which was purely due to a flow of electrons from one layer to the other. The authors found that both dynamics coincide up to $\approx 35fs$, indicating that the early stages of the demagnetization are purely due to a spin current. Interestingly, in the case where the spin–orbit coupling is activated, a total demagnetization was seen, meaning that most of the spin–flips are occurring in the Cu layer. The right side of Fig. 2.38 confirms this, as an increase of the magnetic moment in the Cu layer, simultaneous to the decrease in Co was seen. But as pointed out by the authors, it was not large enough to fully compensate the decrease in Co. While a flow of majority spins from the Co layer to the Cu layer creates this dynamics, Chen *et al.* found that it is reinforced by a current of minority spins from the Cu layer to the Co layer. This "backflow" was well explained by looking at the band structure, which, in the presence of exchange splitting, contains many minority states belonging to Co above the fermi level. Electrons are then excited from the d bands of Cu to these states, creating the aforementioned minority spin current. These results evidence the importance of interfaces in the magnetization dynamics of thin films, and the fact that purely quantum effects cannot be neglected, as it is the case in the superdiffusive model from Battiato *et al.*[34].

Very recently, RT–TDDFT proved its capacities in the description of light–induced magnetization dynamics in the study of a Ni/Pt multilayer. In their pioneering experiment, Siegrist *et al.*[110] used a near infrared pump having a duration of 4 fs to trigger the magnetization dynamics and probed it with pulses of 310 as. This unprecedented setup allowed them to study in details the dynamics occurring in the first 20 fs. Fig. 2.39 shows both the experimental and theoretical evolution of the magnetization, both in the case of Ni bulk and the Ni/Pt multilayers. While the agreement between theory and experiment was weak in the case of the bulk, the authors found a good accordance in the case of the multilayers. As in the work of Chen *et al.*[109] reviewed *supra*, the numerical dynamics was calculated with and without spin–orbit coupling in order to disentangle the contribution of spin–flip from transport in the dynamics. Indeed, previous RT–TDDFT have shown that optical excitations can induce a transfer of electrons from one atomic species to another [111, 112], phenomenon which has been coined as "optically induced spin transfer" (OISTR). With the help of TDDFT, as in Ref. [109], the authors were able to distinguish two main regimes, as indicated in Fig. 2.39. Initially, as evidenced by the overlap of the curves where TDDFT includes and does not include spin–orbit coupling, in the firsts $\approx 11fs$ the dynamics was dominated by a spin transfer from the Ni layers to

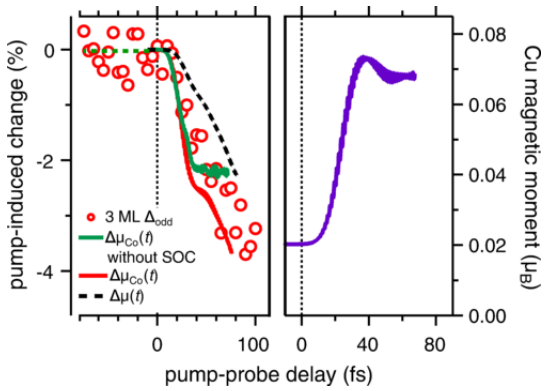


FIGURE 2.38: Left: Comparison of the time-dependent change of magnetic moment for 3 ML Co/Cu (001) as observed in experiment by using the second harmonic generation and by TDDFT calculations. The relative changes (normalized to values μ (t_i0) before excitation) of the total spin moment in Co/Cu(001) $\Delta\mu$ as well as of the Co contributions $\Delta\mu_{Co}$ with and without sin–orbit coupling are given. Right: Magnetic moment induced in Cu μ_{Cu} by spin transfer across the interface. Image and caption extracted from Ref. [109].

the Pt layers. It is only after this initial phase that spin–orbit induced spin–flips started to occur. Interestingly, in the case of Ni bulk, TDDFT strongly underestimated the demagnetization. This may be due to the fact that other mechanisms, not taken into account in TDDFT, are involved in the ultrafast demagnetization in the case of monoatomic bulk materials, as the OISTR phenomenon is not possible. Indeed, as reviewed in Sec. 2.2.3, the ultrafast generation of magnons plays a primary role in such cases. This fact could also explain that, in the work of Shokeen *et al.*[113], who was studying the demagnetization dynamics in Ni and Co films sandwiched between insulators, an average power density $10\times$ higher than the one used experimentally was required in order to reproduce the experimental light–induced demagnetization.

To conclude this section, it is necessary to acknowledge that, while RT–TDDFT is one of the most promising tools we currently have at our disposal to understand light–induced ultrafast magnetization dynamics, its current limitations are numerous. First, due to its computationally intensive nature, its application to condensed matter physics is relatively limited. Indeed, despite the fact that it can be, and has been successfully applied in periodic conditions to study crystals, accounting for interfaces which, as seen *supra* play a primary role, is a cumbersome task requiring very large cells. Moreover, even though utilizing periodic boundary conditions can help diminishing the computational load, it prevents the investigation of non–crystalline solids such as GdFeCo. Another downside of the periodicity is that it imposes constrains on the possible excitations which can possibly be triggered during the dynamics. In fact, in order to study the dynamics of phonons and magnons, one has to restrain the study to a particular mode of a given wavelength λ, commensurable to a number of primitive crystal cells, and create the supercell accordingly, and, doing so, increase the computational load. Second, dissipation processes, and their corresponding fluctuations are not accounted for. While this would impediment the *ab initio* aspect for which this method is usually praised, it would simultaneously allow for more realistic calculations. Indeed, as seen in Sec. 2.4.3, the fulfillment of the fluctuation dissipation theorem is what allowed the temperature to affect

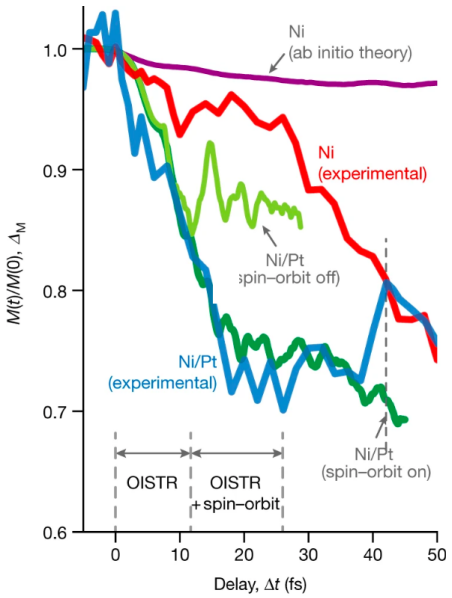


FIGURE 2.39: Comparison between the experimentally recorded attosecond MCD trace in Ni/Pt-multilayers (blue line) and pure Ni (red) with the ab initio simulation of light-field-induced spin dynamics, including spin–orbit coupling in the multilayer (dark-green line) reveals that for the first 10 fs the demagnetization of Ni layers is entirely due to flow of majority-spin current across the material interface. Theoretical calculations without the spin–orbit interaction predict saturation of the demagnetization 15 fs after the optical excitation (light-green line). This is a clear indication that beyond this time all the demagnetization is caused by spin flips, whereas at earlier times spin dynamics is governed by OISTR, which is absent in the theoretical prediction for bulk nickel (violet line; see Fig. 2). Image and caption extracted from Ref. [110].

the magnetization state. On the contrary, in RT–TDDFT, the only effect of the temperature is in the setting of the initial electronic occupation according to the Fermi distribution. As a consequence, the creation of magnons and phonons resulting from an absorption of energy is currently not possible in RT–TDDFT, and the existing modes can only be modified and will not be subjected to damping, *i.e.* they will have an infinite lifetime. However, the mere fact of defining a temperature during these ultrafast dynamics is quite troublesome and new concepts will have to emerge so that we can have a more well–rounded method of approaching such a problem.

2.4.6 Takeaways from theory

In this section, we briefly summarize the theoretical elements reviewed *supra* which contribute to the current understanding of the light–induced ultrafast magnetization dynamics, as well as their limits. Doing so allows us to clearly point out the areas where this thesis has contributed.

2.4.6.1 Ultrafast demagnetization

The spearhead of our current rationalization of the ultrafast dynamics are the two and three temperature models, which separate the degrees of freedom of the electrons, the phonons and, in the case of the 3TM, the magnons. This framework considers that the energy absorbed by the light, primarily by the electrons, is then transferred to the baths of the phonons and the magnons. As the temperature of the magnons is rising, the global magnetization is decreasing. As stated at length *supra*, this model rests upon many assumptions and approximations, which severely hinder its predicting capabilities. Notably, the specific heat of the electrons is usually computed using the Sommerfeld approximation, supposedly valid at low electronic temperature. However, in Chap. 4 of this thesis, we show large deviations from this approximation in magnetic compounds, even at low electronic temperatures.

Furthermore, the fundamental question of the conservation of angular momentum is not addressed by this model. A potential candidate for the transfer of angular momentum from the magnon bath to the phonon bath is the Elliott–Yafet spin–flip process, in which electron–phonon scattering events lead to a change of the spin state of an electron. Nevertheless, *ab initio* calculations have shown that this phenomenon can only account for a small fraction of the experimentally seen demagnetization. However, these calculations were using severe approximations regarding the nature of the excited electronic states, which plays a primary role in modifying the magnitude of this effect.

Another mechanism that could have participated to the ultrafast light–induced demagnetization was the so–called "superdiffusive" transport of majority carriers outside of the illuminated area. In this framework, the issue of the conservation of angular momentum would have been solved, as the total angular momentum of the system is not changed, but rather relocalized. However, in both this theory, and in the Elliott–Yafet scattering, the reduction of the magnetization is longitudinal rather than transversal, contradicting the experimental facts reviewed in Sec. 2.2.3.

On the other hand, the description of such a transversal dynamics can be properly achieved by an atomistic and stochastic Laudau–Lifshitz–Gilbert dynamics. However,

in this method, accounting for thermal effects still remains tarnish by many approximations. The most common one is to couple the LLG dynamics to a 2TM model, where the temperature of the electrons is taken as the instantaneous temperature to which the magnetization responds. As discussed above, this choice is rather arbitrary and rests upon the fact that it allows for the reproduction of the initial decrease and quick recovery of the magnetization, occurring in the first hundreds of femtoseconds right after the pulse. However, as discussed in Chap. 5 of this thesis, the presence of light–induced hot–electrons strongly affects the interatomic exchange, or Heisenberg exchange, from which is emerging the magnetic ordering. This phenomenon has mostly been ignored in the literature and its presence could explain the particularities of the initial magnetization dynamics, opening the way for more reasonable approximations for the coupling of the magnetization to an effective temperature. However, with this method the total energy of the electrons/magnons/phonons system is not conserved during the dynamics and the dissipation of angular momentum is fully characterized by the damping term and its microscopic origin is therefore masked.

2.4.6.2 Helicity–dependence

On top of the demagnetization, the light can also induce polarization–dependent effects from which the AO–HDS, the HD demagnetization, as well as the HD domain wall motion could originate. Sec. 2.4.4 focuses on the two main candidates currently thought of in the literature, namely the magnetic circular dichroism and the inverse Faraday effect. The former is designating an absorption depending on both the polarization of the light and magnetization state. This dependence of the absorption on the magnetization state can, in turn, stabilize and/or propagate the less absorbing magnetization state, therefore inducing a switching. On the other hand, in the IFE, a magnetization proportional to the intensity of the light is induced, as in the original work of Pitaevskii[3]. However, to be able to incorporate this effect in LLG simulations, instead of accounting for a change of the length of the magnetization, a so–called "opto–magnetic" field is usually added to the dynamics. Nevertheless, doing so leads to an entirely different type of dynamics, as in this case the switching is achieved through the precession of the magnetization around this supposedly light–induced magnetic field. However, considering the large fields obtained by Berritta *et al.*[103], one may question this approach. On the other hand, the consequence of the variation of the length of the magnetic moments has never been tested in this context, and could lead to the discovery of new types of magnetization dynamics, as suggested in Sec. 2.4.3. Furthermore, as the light–induced magnetization by the IFE disappears with the light pulse, the fact that this theory can account for the HD demagnetization, the AO–HDS and the HD domain wall motion can be questioned. Indeed, as reviewed in Sec. 2.4.4.2, the presence of the opto–magnetic field has to be extended long after the intensity of the light has vanished in order to achieve a helicity–dependent effect.

On the other hand, in Chap. 6, we show the presence of another effect, occurring during the absorption of the light, where along the absorption of energy, the system also absorbs angular momentum. As this absorbed momentum remains in the system even after the light is gone, this phenomenon is a particularly good candidate in the explanation of all the aforementioned helicity–dependent phenomena.

Chapter 3

Electronic structure calculations

A quantum mechanical system is fully characterized by its state $|\Psi\rangle$, where its representation in the position space writes as $\langle \boldsymbol{x}_1, ..., \boldsymbol{x}_n | \Psi(t) \rangle = \Psi(\boldsymbol{x}_1, ..., \boldsymbol{x}_n, t)$ with $\boldsymbol{x}_i = \boldsymbol{r}_i, \sigma_i$. $\boldsymbol{r}_i$ denotes the position of the particle i and σ_i its spin–orientation with respect to a given axis. Let us define the permutation operator, P_{ij}, such as:

$$P_{ij}\Psi\left(\boldsymbol{x}_1, ..., \boldsymbol{x}_i, ..., \boldsymbol{x}_j, ..., \boldsymbol{x}_n, t\right) = \pm\Psi\left(\boldsymbol{x}_1, ..., \boldsymbol{x}_i, ..., \boldsymbol{x}_j, ..., \boldsymbol{x}_n, t\right) \tag{3.1}$$

Where the $\pm$ respectively stands for a many–body wavefunction of Bosons and Fermions. These symmetry relations ensure the indistinguishability, as well as, in the Fermionic case, the Pauli exclusion principle.

The time–evolution of $|\Psi(t)\rangle$ is governed by the Schrödinger equation:

$$i\hbar\frac{\partial}{\partial t}|\Psi(t)\rangle = \hat{\mathcal{H}}|\Psi(t)\rangle, \tag{3.2}$$

where $\hat{\mathcal{H}}$ is the Hamiltonian of the system. In the absence of external fields, and in the case of a set of electrons and nucleus interacting together, it writes as:

$$\hat{\mathcal{H}} = \sum_i \frac{\hat{\boldsymbol{p}}_i{}^2}{2m_e} + \frac{1}{2}\sum_{i\neq j}\frac{e^2}{|\hat{\boldsymbol{r}}_i - \hat{\boldsymbol{r}}_j|} - \sum_{Ii}\frac{Z_I e^2}{|\hat{\boldsymbol{R}}_I - \hat{\boldsymbol{r}}_i|} + \sum_I \frac{\hat{\boldsymbol{P}}_I^2}{2M_I} + \frac{1}{2}\sum_{I\neq J}\frac{Z_I Z_J e^2}{|\hat{\boldsymbol{R}}_I - \hat{\boldsymbol{R}}_J|} \tag{3.3}$$

with $\hat{\boldsymbol{R}}_I$ the position operator of the nuclei I, Z_I its number of protons and M_I its mass and $\hat{\boldsymbol{p}}_i$ and $\hat{\boldsymbol{P}}_I$ respectively are the momentum operators of the electron i and the nucleus I. From left to right, the right–hand side of Eq. 3.3 accounts for the kinetic energy of the electrons, the Coulomb interaction between the electrons, the Coulomb interaction between the electrons and the nuclei, the kinetic energy of the nuclei and the Coulomb interaction between the nuclei. As this Hamiltonian does not have any explicit dependence on the time, the spatial components of $|\Psi(t)\rangle$ can be separated from the time dependent part and one is left with the static Schrödinger equation:

$$\hat{\mathcal{H}}|\Psi_n\rangle = E_n|\Psi_n\rangle \tag{3.4}$$

The solving of Eq. 3.4 is, except in the simplest cases an impossible task, even numerically, as the size of the problem increases exponentially with the number of particles. A first step towards a simplification of this problem is to consider a decoupling of the motion of the electrons from the nuclei as the mass of the latter is four orders of magnitude higher than the former. Therefore, the nuclei are considered to be at fixed positions. This is called the Born–Oppenheimer approximation. As a consequence, the two last terms of

Eq. 3.3, which do not act on the electronic degrees of freedom, are no longer necessary in the computation of the electronic states. However, the electronic wavefunction now depends parametrically on the position of the nuclei. Such a framework is the starting point, on which is built the density functional theory.

3.1 The Hohenberg-Kohn theorems

The Hohenberg–Kohn theorems[114] are foundational for density functional theory, as they state that stationary many–particle systems can be entirely characterized by the ground state density $n_0(\boldsymbol{r})$.

As mentioned *supra*, in the Born–Oppenheimer approximation, Eq. 3.3 becomes

$$\begin{aligned}\hat{\mathcal{H}} &= \sum_i \frac{\hat{\boldsymbol{p}}_i^2}{2m_e} + \frac{1}{2}\sum_{i\neq j}\frac{e^2}{|\hat{\boldsymbol{r}}_i - \hat{\boldsymbol{r}}_j|} - \sum_{Ii}\frac{Z_I e^2}{|\hat{\boldsymbol{R}}_I - \hat{\boldsymbol{r}}_i|} \\ &= \hat{T} + \hat{W} + \hat{V}_{\text{ext}}\end{aligned} \tag{3.5}$$

Indeed, due to the fact that the positions of the nuclei are fixed, the system has now been recast as a gas of interacting electrons submitted to an external static potential, $\hat{V}_{\text{ext}} = \sum_i v_i(\boldsymbol{r}_i)$ produced by the nuclei. In the process, this operator has become strictly multiplicative.

While at this point, the Hamiltonian Eq. 3.5 is non–relativistic it can, as it will be discussed later, be extended to account for relativistic effects such as the spin–orbit coupling, which plays a primary role in many light–induced effects studied in this thesis.

In the following discussion, we will consider the case where $\hat{\mathcal{H}}$ only possesses non–degenerate ground states, which is, in fact, a property of $\hat{V}_{\text{ext}}$ as both $\hat{T}$ and $\hat{W}$, the kinetic energy and the electron–electron interaction are the same for any system. While, for the sake of simplicity we will only discuss the non–degenerate case, all the results mentioned hereafter can be recovered in the degenerate case, as developed in *e.g.* [115]. The coming discussion closely follows the same reference.

As pointed out by Engel *et al.*, the Schrödinger equation can be viewed as a map between the set $\mathcal{V}$ of external potentials differing by more than a constant to the set $\mathcal{G}$ of the produced ground states where each element of $\mathcal{G}$ only corresponds to one element of $\mathcal{V}$, up to a global phase factor. These considerations are summarized by the mapping A in Fig. 3.1. A second mapping from the set of ground states $\mathcal{G}$ to the set of resulting ground state densities $\mathcal{N}$ can also be obtained, where the density writes as:

$$\begin{aligned}n_0(\boldsymbol{r}) &= \langle\Psi_0|\,\hat{n}(\boldsymbol{r})\,|\Psi_0\rangle \\ &= N\int d\boldsymbol{r}_2 d\boldsymbol{r}_3 ... d\boldsymbol{r}_N \Psi^*(\boldsymbol{r},\boldsymbol{r}_2,...,\boldsymbol{r}_n)\Psi(\boldsymbol{r},\boldsymbol{r}_2,...,\boldsymbol{r}_n)\end{aligned} \tag{3.6}$$

with

$$\hat{n} = \sum_{i=0}^{N}\delta(\boldsymbol{r}-\boldsymbol{r}_i). \tag{3.7}$$

Both the mapping A and B are surjective, as to each element of $\mathcal{G}$ is, by construction, associated at least an element of $\mathcal{V}$, and at each element from $\mathcal{N}$ is associated at least an

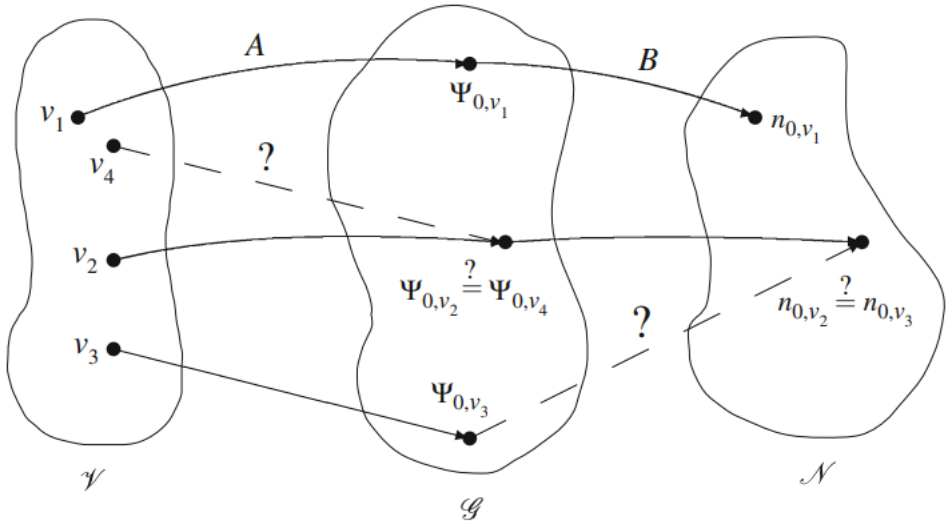


FIGURE 3.1: Correspondence between external potentials v_i, associated ground states Ψ_{0,v_i} and ground state densities n_{0,v_i} in the case of non-degenerate ground states. Image extracted from [115].

element of $\mathcal{G}$. However, until now nothing has been said about the injectivity, as highlighted by the dashed lines of Fig. 3.1. This is where the first Hohenberg–Kohn theorem comes into play:

Theorem : For any system of interacting particles in an external potential $V_{ext}(\boldsymbol{r})$, the potential $V_{ext}(\boldsymbol{r})$ is uniquely determined, except for a constant, by the ground state particle density $n_0(\boldsymbol{r})$.

The proof, which shows that the maps A and B are also injective, is based on a *reductio ad absurdum* and will not be detailed here. In other words, this theorem establishes that there is a one to one mapping between the elements $\mathcal{N}$ and the elements of $\mathcal{V}$ and, as a consequence $\hat{V}_{ext}$, $|\Psi_0\rangle$ and n_0 determine each other uniquely. As a consequence of the map B^{-1}, $|\Psi_0\rangle$ can be seen as a functional of n_0: $|\Psi[n_0]\rangle$. Thus, all the observables of the ground state are also density functionals:

$$O[n_0] = \langle \Psi[n_0] | \hat{O} | \Psi[n_0] \rangle . \tag{3.8}$$

This is especially true in the case of the energy:

$$\begin{aligned} E[n_0] &= \langle \Psi[n_0] | \hat{\mathcal{H}} | \Psi[n_0] \rangle \\ &= F[n_0] + \int d\boldsymbol{r} v_{ext}(\boldsymbol{r}) n(\boldsymbol{r}), \end{aligned} \tag{3.9}$$

where $F[n_0]$ is the aforementioned universal part of the energy writing as:

$$F[n_0] = \langle \Psi[n_0] | \hat{T} + \hat{W} | \Psi[n_0] \rangle , \tag{3.10}$$

and the last term of the right–hand side of Eq. 3.9 is derived as:

$$\begin{aligned}\langle \Psi[n_0] | \hat{V}_{\text{ext}} | \Psi[n_0] \rangle &= \sum_i \int d\boldsymbol{r}_1 ... d\boldsymbol{r}_N \Psi^*[n_0](\boldsymbol{r}_1, \boldsymbol{r}_2, ..., \boldsymbol{r}_n) v_{\text{ext}}(\boldsymbol{r}_i) \Psi[n_0](\boldsymbol{r}_1, \boldsymbol{r}_2, ..., \boldsymbol{r}_n) \\ &= N \int d\boldsymbol{r} d\boldsymbol{r}_2 d\boldsymbol{r}_3 ... d\boldsymbol{r}_N \Psi^*[n_0](\boldsymbol{r}, \boldsymbol{r}_2, ..., \boldsymbol{r}_n) v_{\text{ext}}(\boldsymbol{r}) \Psi[n_0](\boldsymbol{r}, \boldsymbol{r}_2, ..., \boldsymbol{r}_n) \\ &= \int d\boldsymbol{r} v_{\text{ext}}(\boldsymbol{r}) n_0(\boldsymbol{r})\end{aligned} \tag{3.11}$$

Eq. 3.9 gives us access to the energy of the ground state. Therefore, for densities $n_0'(\boldsymbol{r}) \neq n_0(\boldsymbol{r})$, one must have:

$$E[n_0] < E[n_0'] \tag{3.12}$$

These facts are the object of the second Hohenberg–Kohn theorem:

Theorem : A universal functional of the density $n(\boldsymbol{r})$, E[n], can be defined, valid for any external potential $v_{\text{ext}}(\boldsymbol{r})$. For any $v_{\text{ext}}(\boldsymbol{r})$ the exact ground state energy of the system is the global minimum value of this functional, and the density $n(\boldsymbol{r})$ that minimizes the functional is the exact ground state density $n_0(\boldsymbol{r})$.

3.2 The Kohn–Sham scheme

The Hohenberg–Kohn theorems provide a solid theoretical framework allowing for a great reduction of the dimensionality of the many–body interacting electron problem. Indeed, instead of solving Eq. 3.4, were the scalar fields $\Psi(\boldsymbol{x}_1, ..., \boldsymbol{x}_n, t)$ have to be evaluated on a grid, or a basis, which size increases exponentially with the number of considered electrons, one is now left with a three–dimensional scalar field representing $n_0(\boldsymbol{r})$. However, this framework does not provide any way to actually compute the universal part of the energy, $F[n_0]$ which, above else, contains all the correlation effects.

3.2.1 General framework

The Kohn–Sham approach consists in the replacement of the cumbersome interacting many–body problem by an auxiliary system which can be solved. To do so, they introduced an *ansatz* which postulates that the ground state density of the interacting system can be described by a properly built non–interacting system, therefore reducing the interacting many–body problem to a single-electron problem. To this end, each electron of the non–interacting problem must be subjected to an effective potential, v_{KS}, accurately accounting for the many–body effects and which can conveniently be local, *i.e.* acting on an electron of spin σ at $\boldsymbol{r}$. Such a Hamiltonian simply writes as:

$$\mathcal{H}_{\text{KS}} = \hat{T}_{\text{s}} + \hat{V}_{\text{KS}} \tag{3.13}$$

where $\hat{V}_{\text{KS}} = \int d\boldsymbol{r} \hat{n}(\boldsymbol{r}) v_{\text{KS}}(\boldsymbol{r})$. The ground state associated to the Hamiltonian Eq. 3.13, $|\Phi_0\rangle$, writes as a Slater determinant built from the set of orthonormalized one–electron states $|\phi_n\rangle$:

$$\begin{aligned}\langle \boldsymbol{x}_1, ..., \boldsymbol{x}_n | \Phi \rangle &= \Phi\left(\boldsymbol{x}_1, ..., \boldsymbol{x}_n\right) \\ &= \frac{1}{\sqrt{N!}} \det \begin{pmatrix} \phi_1(\boldsymbol{x}_1) & \cdots & \phi_N(\boldsymbol{x}_1) \\ \vdots & \ddots & \vdots \\ \phi_1(\boldsymbol{x}_N) & \cdots & \phi_N(\boldsymbol{x}_N) \end{pmatrix}\end{aligned} \tag{3.14}$$

and the electronic wavefunctions, $\phi_i(\boldsymbol{r}\sigma)$ are the eigenfunctions of the single–particle Schrödinger equation:

$$\left[-\frac{\hbar^2 \boldsymbol{\nabla}^2}{2m} + v_{\mathrm{KS}}(\boldsymbol{r}) \right] \phi_i(\boldsymbol{x_i}) = \varepsilon_i \phi_i(\boldsymbol{x}_i) \tag{3.15}$$

The ground state density is then simply given by summing the squared modulus of the orbitals of each spin, weighted by the occupation number, f_i:

$$n_0(\boldsymbol{r}) = \sum_{\sigma} \sum_{i} f_i \left| \phi_i(\boldsymbol{r}\boldsymbol{\sigma}) \right|^2 \tag{3.16}$$

and the independent–particle kinetic energy is expressed as:

$$\begin{aligned} T_s &= \langle \Phi[n_0] | \, \hat{T} \, | \Phi[n_0] \rangle \\ &= -\frac{\hbar^2}{2m} \sum_{\sigma} \sum_{i} \langle \phi_i | \, \hat{\boldsymbol{p}}^2 \, | \phi_i \rangle \\ &= -\frac{\hbar^2}{2m} \sum_{\sigma} \sum_{i} \int d\boldsymbol{r} \phi_i^*(\boldsymbol{r}\sigma) \boldsymbol{\nabla}^2 \phi_i(\boldsymbol{r}\sigma) \end{aligned} \tag{3.17}$$

where the first line of Eq. 3.17 recalls that, as the first Hohenberg–Kohn is valid for any many–particle systems, it also accounts for non–interacting electrons. Thus, even though T_s is not an explicit functional of the density, the dependence is implicitly given by the fact that the ground state of the system is a unique functional of the ground state density, *i.e.*: $|\Phi_0\rangle = |\Phi_0[n_0]\rangle$

Therefore, the total energy is expressed as:

$$E_{KS}[n_0] = -\frac{\hbar^2}{2m} \sum_{\sigma} \sum_{i} \int d\boldsymbol{r} \phi_i^*(\boldsymbol{r}\sigma) \boldsymbol{\nabla}^2 \phi_i(\boldsymbol{r}\sigma) + \int d\boldsymbol{r} n_0(\boldsymbol{r}) v_{\mathrm{KS}}(\boldsymbol{r}) \tag{3.18}$$

The second term of the right–hand side of Eq. 3.18 is composed of three different elements, which are all density functionals:

$$E[n] = T_s[n] + E_H[n] + E_{xc}[n] + E_{\mathrm{ext}}[n] \tag{3.19}$$

E_{ext} is the contribution to the energy coming from the interaction of the electronic density with the external potential. $E_{\mathrm{H}}[n]$ is the Hartree interaction energy of the particles of density n, writing as:

$$E_{\mathrm{H}}[n] = e^2 \frac{1}{2} \int d\boldsymbol{r} d\boldsymbol{r}' \frac{n(\boldsymbol{r}) n(\boldsymbol{r}')}{|\boldsymbol{r} - \boldsymbol{r}'|}, \tag{3.20}$$

and therefore, introduces self–interactions, *i.e.* a given electron is not only reacting and being repelled by the presence of others, but also by itself.

Finally, $E_{\mathrm{xc}}[n]$ is the exchange–correlation potential. It regroups all the many–body effects not accounted for in $T_{\mathrm{s}}[n_0]$ or in $E_{\mathrm{H}}[n_0]$ as expressed by:

$$\begin{aligned} E_{\mathrm{xc}}[n_0] &= F[n_0] - (T_{\mathrm{s}}[n_0] + E_{\mathrm{H}}[n_0]) \\ &= \langle \Psi_0 | \hat{T} | \Psi_0 \rangle - T_{\mathrm{s}}[n_0] + \langle \Psi_0 | \hat{W} | \Psi_0 \rangle - E_{\mathrm{H}}[n_0] \end{aligned} \tag{3.21}$$

where $\langle \Psi_0 | \hat{T} | \Psi_0 \rangle$ and $\langle \Psi_0 | \hat{W} | \Psi_0 \rangle$ are the true kinetic and interaction energies. Therefore, $E_{\mathrm{xc}}[n_0]$ should in principle compensate for the self–interaction present in $E_{\mathrm{H}}[n_0]$. If its exact form was known, the exact ground state energy and density could be obtained from this *ansatz*. In reality, this functional must be approximated, as mentioned hereafter.

3.2.2 Variational equations

Writing the density as Eq. 3.16, and using the variational property on the Energy, Eq. 3.9, Kohn and Sham [116] showed that the density is given by the solution of single particle Schrödinger–like equations, named the Kohn–Sham equations:

$$\left(-\frac{\hbar^2}{2m}\nabla^2 + v_{\mathrm{ext}}(\boldsymbol{r}) + v_{\mathrm{H}}[n](\boldsymbol{r}) + v_{xc}[n](\boldsymbol{r}) \right) \phi_i(\boldsymbol{r}\sigma) = \varepsilon_i \phi_i(\boldsymbol{r}\sigma) \tag{3.22}$$

where $v_{\mathrm{KS}} = v_{\mathrm{ext}}[n] + v_{\mathrm{H}}[n] + v_{xc}[n]$ and the Hartree potential writes as:

$$\begin{aligned} v_{\mathrm{H}} &= \frac{\delta E_{\mathrm{H}}}{\delta n} \\ &= e^2 \int d\boldsymbol{r}' \frac{n(\boldsymbol{r}')}{|\boldsymbol{r} - \boldsymbol{r}'|}, \end{aligned} \tag{3.23}$$

and the exchange–correlation potential is obtained from:

$$v_{xc} = \frac{\delta E_{\mathrm{xc}}[n]}{\delta n(\boldsymbol{r})} \tag{3.24}$$

However, in this framework, as the density is not known from the start and that, except $v_{\mathrm{ext}}(\boldsymbol{r})$, all the elements of the Hamiltonian are, at least implicitly, functional of the density, Eq. 3.22 has to be solved self–consistently. To this end, the Kohn–Sham states $\phi_i(\boldsymbol{r}\boldsymbol{\sigma})$ are usually expressed in a basis of functions $\psi_\alpha(\boldsymbol{r})$ as:

$$\phi_i(\boldsymbol{r}\sigma) = \sum_\alpha c_{i\alpha} \psi_\alpha(\boldsymbol{r}\sigma) \tag{3.25}$$

where the $c_{i\alpha}$ are the expansion coefficients. Given this basis of functions, these coefficients become the only unknown and have to be the ones which minimize the total energy, according to the variational principle stated by the second Hohenberg–Kohn theorem. Two types of basis, *i.e.* the plane–waves and the linear augmented plane–waves are described in Sec. 3.4.

Fig. 3.2 shows the process through which self–consistency is reached. Starting from a guess of the initial density, $n_0 = n^{in}$, which is usually based on the superposition of the densities of single atoms, the Kohn–Sham potential, v_{KS} is computed. From there, the Kohn–Sham equations, Eq. 3.22, can be solved and the Kohn–Sham eigenvalues and

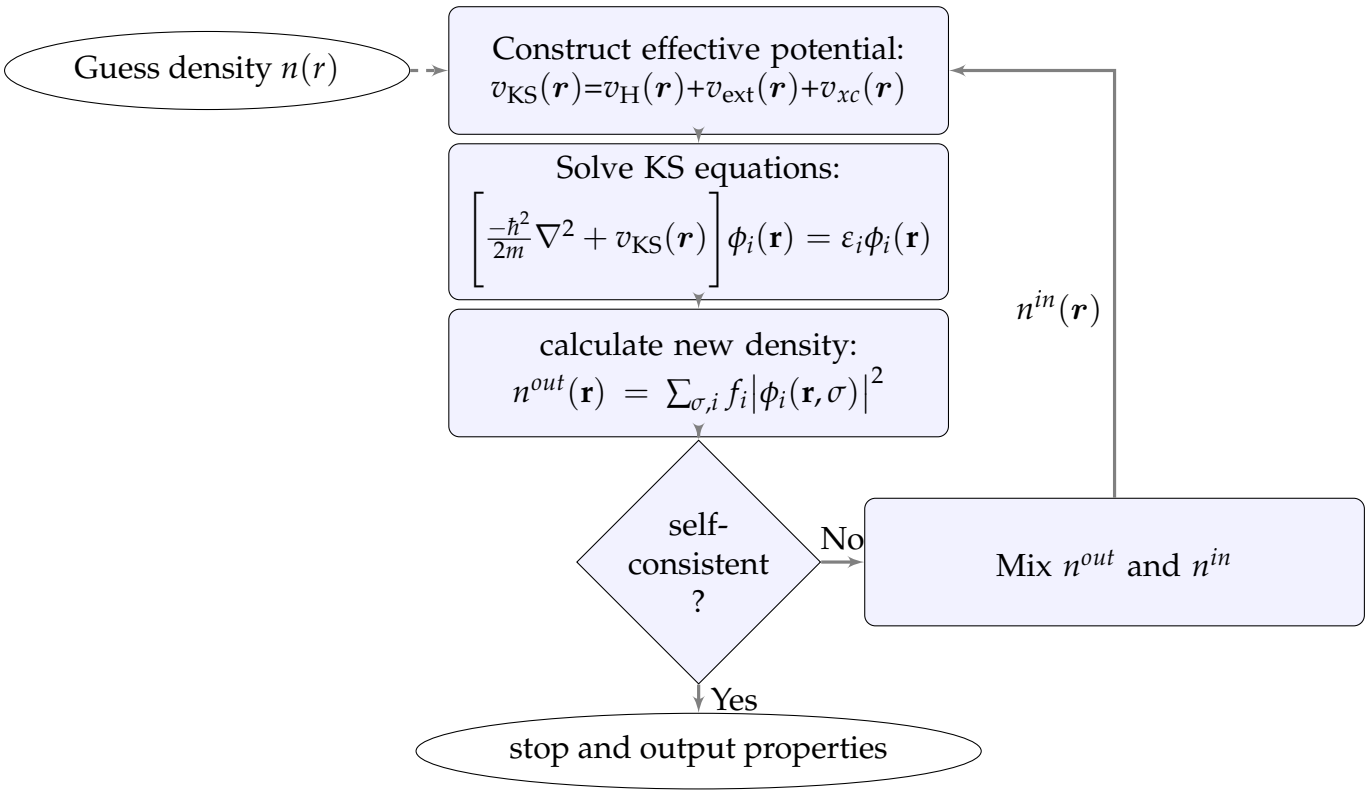


FIGURE 3.2: Schematic flow–chart for self–consistent density functional calculations.

eigenfunctions are obtained. Then, using Eq. 3.16, a new electronic density, n^{out}, is computed. n^{out} is then mixed with the input density, n^{in} to produce the input density for the next self–consistency loop. The simplest type of mixing writes as:

$$n^{in}_{i+1} = n^{in}_i + \alpha(n^{out}_i - n^{in}_i) \tag{3.26}$$

where α is the mixing parameter and the indices refer to the iteration number. This process is repeated until some convergence criteria is met.

3.2.3 Magnetism

The aforementioned formalism can be generalized to account for spin–polarization. In this framework, the electronic density, $n(\boldsymbol{r})$, becomes a 2×2 matrix and a second quantity, the magnetization $\boldsymbol{m}(\boldsymbol{r})$ appears. In general, it is a three dimensional vector field which emerges from the contribution of the functional derivative of $E_{xc}[n, \boldsymbol{m}]$ with respect to $\boldsymbol{m}(\boldsymbol{r})$:

$$\boldsymbol{b}_{xc}[n, \boldsymbol{m}](\boldsymbol{r}) = -\frac{\delta E_{xc}[n, \boldsymbol{m}]}{\delta \boldsymbol{m}(\boldsymbol{r})}, \tag{3.27}$$

acting as a magnetic field in the Kohn–Sham equation:

$$\left(-\frac{\hbar^2}{2m}\nabla^2 + v_{\text{ext}}(\boldsymbol{r}) + v_{\text{H}}[n](\boldsymbol{r}) + v_{xc}[n](\boldsymbol{r}) - \boldsymbol{b}_{xc}[n,\boldsymbol{m}]\cdot\boldsymbol{\sigma}\right)\phi_i(\boldsymbol{r}) = \varepsilon_i\phi_i(\boldsymbol{r}). \quad (3.28)$$

Here, $\phi_i(\boldsymbol{r})$ becomes a spinor:

$$\phi_i(\boldsymbol{r}) = \begin{pmatrix}\alpha_i(\boldsymbol{r})\\ \beta_i(\boldsymbol{r})\end{pmatrix}, \quad (3.29)$$

and $\boldsymbol{\sigma} = (\sigma_x, \sigma_y, \sigma_z)$ with:

$$\sigma_x = \begin{pmatrix}0 & 1\\ 1 & 0\end{pmatrix}, \qquad \sigma_y = \begin{pmatrix}0 & -i\\ i & 0\end{pmatrix}, \qquad \sigma_z = \begin{pmatrix}1 & 0\\ 0 & -1\end{pmatrix}. \quad (3.30)$$

The magnetization field is then expressed as:

$$\boldsymbol{m}(\boldsymbol{r}) = \sum f_i\phi_i^*(\boldsymbol{r})\boldsymbol{\sigma}\phi_i(\boldsymbol{r}) \quad (3.31)$$

An approximation, which allows for less computational load is to consider that the magnetization is always aligned in some arbitrarily chosen direction, in which case the spin state, σ, becomes a good quantum number to index the orbitals $\phi_i^\sigma(\boldsymbol{r})$, and $\boldsymbol{m}(\boldsymbol{r})$ reduces to a scalar field simply given by:

$$m(\boldsymbol{r}) = n_\uparrow(\boldsymbol{r}) - n_\downarrow(\boldsymbol{r}). \quad (3.32)$$

The Kohn–Sham equation writes as:

$$\left(-\frac{\hbar^2}{2m}\nabla^2 + v_{\text{ext}}(\boldsymbol{r}) + v_{\text{H}}[n](\boldsymbol{r}) + v_{xc}[n](\boldsymbol{r}) \mp b_{xc}[n,m](\boldsymbol{r})\right)\phi_i^{\uparrow/\downarrow}(\boldsymbol{r}) = \varepsilon_i\phi_i^{\uparrow/\downarrow}(\boldsymbol{r}). \quad (3.33)$$

Therefore, in the colinear case, one needs to solve a set of two uncoupled single particle equations instead of the original coupled problem. Using the convention $v_{xc,\uparrow/\downarrow} = v_{xc} \mp b_{xc}$, one can recast Eq. 3.33 in the more conventional form:

$$\left(-\frac{\hbar^2}{2m}\nabla^2 + v_{\text{ext}}(\boldsymbol{r}) + v_{\text{H}}[n](\boldsymbol{r}) + v_{xc,\uparrow/\downarrow}[n,m](\boldsymbol{r})\right)\phi_i^{\uparrow/\downarrow}(\boldsymbol{r}) = \varepsilon_i\phi_i^{\uparrow/\downarrow}(\boldsymbol{r}). \quad (3.34)$$

3.2.4 Approximation for the exchange–correlation potential

As already mentioned *supra*, in practice, the exchange–correlation energy defined by Eq. 3.21 has to be approximated. An approach which has proved itself to be quite successful is to use the exchange–correlation energy of the jellium, a system of interacting electrons placed in a uniform positive potential maintaining the overall charge neutrality. In this framework, the exchange energy of any inhomogeneous electronic density $n(\boldsymbol{r})$ can be computed as:

$$E_{xc}^{LDA}[n] = \int \epsilon_{xc}(n(\boldsymbol{r}))n(\boldsymbol{r})d\boldsymbol{r} \tag{3.35}$$

where $\epsilon_{xc}(n)$ is the exchange–correlation per electron in a Jellium of density n. Therefore, in Eq. 3.35, the exchange–correlation energy of the inhomogeneous density, $n(\boldsymbol{r})$ is approximated to be locally the exchange–correlation of the Jellium, hence the name of this approach: the local density approximation (LDA). In this framework, the Kohn–Sham equations can only provide the correct properties when the external potential is uniform. Nevertheless, using a precise assessment of the correlation energy, as obtained from Ceperley *et al.*[117], as well as a proper self–interaction correction[118], the LDA has proven to be very successful in the description of non–homogeneous densities.

The LDA can be extended to spin–polarized systems[119], and becomes the local spin density approximation (LSDA). Here, E_{xc}^{LSDA} is a functional of both the density, $n(\boldsymbol{r})$ and the magnetization, $\boldsymbol{m}(\boldsymbol{r})$. It writes as:

$$E_{xc}^{LSDA}[n, \boldsymbol{m}] = \int d\boldsymbol{r}\epsilon_{xc}(n(\boldsymbol{r}), \boldsymbol{m}(\boldsymbol{r}))n(\boldsymbol{r}), \tag{3.36}$$

where ϵ_{xc} is now a function of both the density, n, and the magnetization, $\boldsymbol{m}$. To go further than the LDA and take the effects of the inhomogeneity of the density, functionals of both the density and its gradient have been developed[120]. For an unpolarized system, they write as:

$$E_{\mathrm{XC}}^{GGA}[n] = \int d\boldsymbol{r}\epsilon_{xc}\left(n(\boldsymbol{r}), \boldsymbol{\nabla} n(\boldsymbol{r})\right) n(\boldsymbol{r}) \tag{3.37}$$

Both the GGA and the LDA approximations have been used in the work presented in this thesis.

3.2.5 Second variational inclusion of spin–orbit coupling

The Schrödinger equation, Eq. 3.4, does not contain any explicit dependence on spin. As a consequence, it does not couple the spin space with the real space. This coupling, called spin–orbit coupling emerges from the relativistic counterpart of the Schrödinger equation: the Dirac equation. It writes as:

$$\mathcal{H}_{\mathrm{SO}} = \frac{1}{2m_e^2c^2}\sum_i (\boldsymbol{\nabla} v(\boldsymbol{r}) \times -i\boldsymbol{\nabla}_i) \cdot \boldsymbol{\sigma}_i \tag{3.38}$$

From Eq. 3.38 notably arise the magneto–crystalline anisotropy or the magneto-optical effects. However, its presence complicates the solving of the Kohn–Sham equation. Indeed, without spin–orbit coupling, both spins are uncoupled and therefore Eq. 3.22 can be solved separately for both of these types of states. If one is interested in the computation of n orbitals, it means that the diagonalization of a $n \times n$ matrix is required at each k–point for both spins. However, if spin–orbit is included, one has now to diagonalize a $2n \times 2n$ matrix instead of one (or two in the case of non–spin–degenerate states) $n \times n$ matrices. As the computing cost of the diagonalization increases cubically with the size of the matrix, the inclusion of this coupling increases the computational time by a factor of 8.

The second variational approach allows for a drastic reduction of the cost of the inclusion of spin–orbit coupling by utilizing the fact that this is generally a small effect, and as a consequence does not modify the eigenstates to a great extent. Therefore, these states, called the *first variational* states, can be first computed without the inclusion of the spin–orbit coupling in the Hamiltonian. Then, the *second variational* Hamiltonian, including the spin–orbit coupling, is set up using the lowest N first variational states as basis. As a consequence, instead of the diagonalization of a $2n \times 2n$ matrix a smaller $2N \times 2N$ is handled, and the matrices at hand are only slightly non–diagonal. Furthermore, the linear augmented planewave formulation, reviewed hereafter in Sec. 3.4, provides a very convenient framework to include the spin–orbit. Indeed, considering that its contribution is negligible outside the muffin–tins, where the potential varies slowly, while inside them it can be easily computed considering that, in good approximation, the potential has a spherical symmetry, one can rewrite Eq. 3.38 as:

$$\mathcal{H}_{\mathrm{SO}} = -\frac{1}{2m_e^2c^2}\frac{1}{r}\frac{\partial v(r)}{\partial r}\sum_i \boldsymbol{l}_i \cdot \boldsymbol{\sigma}_i \tag{3.39}$$

which computation is facilitated by the fact that, in the muffin–tin, the wavefunction is described by spherical harmonics.

3.3 Time–dependent density functional theory

3.3.1 One to one mapping between the density and the potential

The time–dependent density functional theory rests upon the Runge–Gross theorem[106]:

Theorem : There is a one to one correspondence between the external time–dependent potential, $v_{ext}(\boldsymbol{r}, t)$, and the electronic density, for many–body systems evolving form a fixed initial state, $|\Psi_0\rangle$.

The proof of this theorem will not be fully detailed here, however, we will briefly describe how it proceeds. It starts from requiring the potential $v_{ext}(\boldsymbol{r}, t)$ to be time–analytic at the initial time, *i.e.* that it can be written as:

$$v_{ext}(\boldsymbol{r}, t) = \sum_{k=0}^{\infty} \frac{1}{k!}\frac{\partial^k}{\partial t^k} v_{ext}(\boldsymbol{r}, t)\bigg|_{t=0} t^k. \tag{3.40}$$

The aim is to show that if two potentials $v_{ext}(\boldsymbol{r}, t)$ and $v'_{ext}(\boldsymbol{r}, t)$ are differing by more than a time–dependent function, the time propagation starting from a same initial state, $|\Psi_0\rangle$, which does not need to be the ground state, would always lead to two different densities, $n(\boldsymbol{r}, t)$ and $n'(\boldsymbol{r}, t)$. The proof proceeds in two steps:

(1) The first part makes use of the current density operator to show that, for two potentials of the form of Eq. 3.40 differing by at least a partial derivative in the right–hand side such as:

$$\exists k \geq 0 : \frac{\partial^k}{\partial t^k}\left[v(\boldsymbol{r}, t) - v'(\boldsymbol{r}, t)\right]_{t=0} \neq \text{constant}, \tag{3.41}$$

always lead to different current densities, *i.e.* after an infinitesimally small propagation, one would verify that $\boldsymbol{j}(\boldsymbol{r},t) \neq \boldsymbol{j}'(\boldsymbol{r},t)$. This proves that $v_{ext}(\boldsymbol{r},t)$ is uniquely defined by $\boldsymbol{j}(\boldsymbol{r},t)$.

(2) The second and last part of the proof uses the continuity equation:

$$\frac{\partial n(\boldsymbol{r},t)}{\partial t} = -\boldsymbol{\nabla}\cdot\boldsymbol{j}(\boldsymbol{r},t) \tag{3.42}$$

to shows that a different current density always leads to a different density after an infinitesimal time, proving that $\boldsymbol{j}(\boldsymbol{r},t)$ is uniquely defined by $n(\boldsymbol{r},t)$.

As a consequence of the two aforementioned steps, for a given initial state, $|\Psi_0\rangle$, the time–dependent external potential $v_{ext}(\boldsymbol{r},t)$ is uniquely determined by the time–dependent electronic density $n(\boldsymbol{r},t)$. Simultaneously, because of the uniqueness of the solutions of the time–dependent Schrödinger equation, each potential $v_{ext}(\boldsymbol{r},t)$ leads a different wavefunction, which in turn leads to a different density, hence the one to one mapping:

$$|\Psi_0\rangle : v_{ext}(\boldsymbol{r},t) \leftrightarrow n(\boldsymbol{r},t) \tag{3.43}$$

In other words, if one knows the time–dependent density and the initial state of an interacting many–body problem, the external potential that produced this density is then identified. As this external potential is the only thing defining the time–dependent Hamiltonian in Eq. 3.2, it means that this equation can be solved, and all the time–dependent observables can be computed. Indeed, the wavefunction, defined up to a time–dependent phase factor coming from the aforementioned degree of freedom allowed for the potential, is in fact a functional of the time–dependent density and the initial state:

$$|\Psi(t)\rangle = e^{-i\alpha(t)}\,|\Psi[n(\boldsymbol{r},t),|\psi_0\rangle](t)\rangle\,. \tag{3.44}$$

This means that all the observables are also unique functionals of the density and initial state:

$$A[n(\boldsymbol{r},t),|\Psi_0\rangle](t) = \langle\Psi[n(\boldsymbol{r},t),|\psi_0\rangle](t)|\,\hat{A}\,|\Psi[n(\boldsymbol{r},t),|\psi_0\rangle](t)\rangle\,. \tag{3.45}$$

3.3.2 Time–dependent Kohn–Sham equations

As in the case of the ground–state theory, the unsolvable many–body problem is mapped to a non–interacting system reproducing exactly the density of the interacting system. Indeed, as the Hohenberg–Kohn theorem, the Runge–Gross theorem is valid for any type of many–particle systems, including non–interacting electrons. Therefore, using the same framework as in the static case, *i.e.* starting from a state $|\Phi_0\rangle$, which is a Slater determinant and usually the ground state, one can find a multiplicative potential, $v_{\mathrm{KS}}(\boldsymbol{r},t)$ such that the non–interacting system reproduces the time–dependent density $n(\boldsymbol{r},t)$, where $v_{\mathrm{KS}}(\boldsymbol{r},t)$ is uniquely determined by $n(\boldsymbol{r},t)$ given by:

$$n(\boldsymbol{r},t) = \sum_{\sigma}\sum_{i} f_i\,|\phi_i(\boldsymbol{r}\boldsymbol{\sigma},t)|^2\,. \tag{3.46}$$

The dynamics of the single particle orbitals, $\phi_i(\boldsymbol{x}_i,t)$, obeys the time–depend Kohn–Sham equation:

$$i\hbar\frac{\partial}{\partial t}\phi_i(\boldsymbol{x}_i,t) = \left[-\frac{\hbar^2\boldsymbol{\nabla}^2}{2m} + v_{\mathrm{KS}}(\boldsymbol{r},t)\right]\phi_i(\boldsymbol{x}_i,t) \tag{3.47}$$

where $v_{\mathrm{KS}(\boldsymbol{r},t)}$ writes as:

$$v_{\mathrm{KS}}[n](\boldsymbol{r},t) = v_{\mathrm{ext}}[n](\boldsymbol{r},t) + \int d\boldsymbol{r}'\frac{n(\boldsymbol{r}',t)}{|\boldsymbol{r}-\boldsymbol{r}'|} + v_{xc}[n](\boldsymbol{r},t) \tag{3.48}$$

where the functional dependence of the different terms is explicitly stated. As in the static case, the external potential, $v_{\mathrm{ext}}(\boldsymbol{r},t)$, is usually generated by the nuclei and in the time–dependent case, the electromagnetic field generated by, *e.g.*, a laser. This contribution is therefore fully determined by the configuration of the problem at hands and its functional dependence is not important in practice. On the other hand, $v_{xc}(\boldsymbol{r},t)$, which is defined such that the same time–dependent density than in the interacting case is recovered is a functional of $n(\boldsymbol{r},t)$. This non–locality in time introduces memory effects, which are usually ignored by using the so–called adiabatic approximation:

$$v_{xc}^{A}[n](\boldsymbol{r},t) = v_{xc}[n(t)](\boldsymbol{r}) \tag{3.49}$$

i.e. the functional dependence of $v_{xc}[n](\boldsymbol{r},t)$ on the time–dependent density is removed and v_{xc} becomes a functional of the instantaneous density. Since even in the adiabatic approximation this potential remains unknown, one usually has to resort to the use of the aforementioned LDA or GGA approximations.

In our case, Eq. 3.47 needs to be augmented to account for both the spin–orbit coupling and the presence of magnetism. The full equation implemented in the ELK code writes as:

$$\begin{aligned} i\frac{\partial\phi_i(\mathbf{r},t)}{\partial t} = \Big(&-\frac{1}{2}\boldsymbol{\nabla}^2 - \frac{i}{c}\mathbf{A}_{ext}(t)\cdot\boldsymbol{\nabla} + v_s(\mathbf{r},t) \\ &+ \frac{1}{2c}\hat{\boldsymbol{\sigma}}\cdot\mathbf{B}_S(\mathbf{r},t) - \frac{1}{4c^2}\hat{\boldsymbol{\sigma}}\cdot(\hat{\boldsymbol{\nabla}}v_s(\mathbf{r},t)\times i\boldsymbol{\nabla})\Big)\phi_i(\mathbf{r},t). \end{aligned} \tag{3.50}$$

where atomic units were used. $\boldsymbol{A}_{\mathrm{ext}}(t)$ is the vector potential of the external electromagnetic field, $v_S(\boldsymbol{r},t) = v_{\mathrm{ext}}(\boldsymbol{r},t) + v_{\mathrm{H}}(\boldsymbol{r},t) + v_{\mathrm{xc}}(\boldsymbol{r},t)$, $\boldsymbol{B}_S(\boldsymbol{r},t) = \boldsymbol{B}_{\mathrm{ext}}(\boldsymbol{r},t) + \boldsymbol{B}_{xc}(\boldsymbol{r},t)$ with $\boldsymbol{B}_{\mathrm{ext}}(\boldsymbol{r},t)$ the external magnetic field and the last term is the spin–orbit coupling.

3.3.3 Time propagation in ELK

As expressed by Dewhurst *et al.*[121], a proper time propagation algorithm is required to prevent the build–up of errors, to allow for large time steps and to be unitary in order to preserve the normalization of the wave function at each time–step. Given an initial state $|\phi_i(0)\rangle$, its time–evolution, given by Eq. 3.50, can also be expressed using the time evolution operator $\hat{U}(t_1,t_0)$ such as:

$$|\phi_i(t)\rangle = \hat{U}(t,0)\,|\phi_i(0)\rangle \tag{3.51}$$

where $\hat{U}$ is the time–evolution operator propagating the single particle orbital $|\phi_i(t)\rangle$ from $t_0 = 0$ to $t_1 = t$. As this operator satisfies:

$$\hat{U}(t,0) = \hat{U}(t,t-\Delta t)...\hat{U}(2\Delta t,\Delta t)\hat{U}(\Delta t,0) \tag{3.52}$$

allows for the division of the propagation into time–steps having a duration Δt. Furthermore, for $\Delta t \to 0$, $\hat{U}$ writes as:

$$\lim_{\Delta t\to 0} \hat{U}(t+\Delta t,t) = e^{-i\hat{h}_i\Delta t} \tag{3.53}$$

with $\hat{h}_s$ the single particle Hamiltonian. However, the exponential of an operator is cumbersome to compute. In order to bypass this problem, the strategy used in ELK is to diagonalize the Hamiltonian at each time step. Indeed, in the basis of the instantaneous eigenstates of the Hamiltonian, one gets:

$$\lim_{\Delta t\to 0} \hat{U}(t+\Delta t,t) = e^{-i\varepsilon_i\Delta t} \tag{3.54}$$

where $\varepsilon_i(t)$ is the instantaneous eigenvalue associated with the eigenstate $|\phi_i(t)\rangle$. Assuming that the time steps are sufficiently small such that $\varepsilon_i(t) \approx \varepsilon_i(t+\Delta t)$, this method provides an accurate way of propagating the time–dependent Kohn–Sham equation, given the fact that a full diagonalization can be performed at each time step. In order to efficiently perform this step, as in the case of the spin–orbit coupling described *supra*, the time–dependent states are expressed in terms of the second–variational states. In such a framework, an accurate propagation requires a high number of orbitals.

3.4 Implementations

As mentioned *supra*, the Kohn–Sham wavefunctions are usually expanded in a basis set of functions. As in this work, only periodic systems have been considered, a natural basis could be made of planewaves. Indeed, in periodic systems, the electronic wavefunctions are Bloch functions. They are writing as:

$$\phi_{n\boldsymbol{k}}(\boldsymbol{r}) = u_{n\boldsymbol{k}}(\boldsymbol{r})e^{i\boldsymbol{k}\cdot\boldsymbol{r}}, \tag{3.55}$$

where $\boldsymbol{k}$ is a vector of the first Brillouin zone, n is a band index and $u_{n\boldsymbol{k}}(\boldsymbol{r})$ is a function that possesses the same periodicity as the studied compound. It can therefore be expanded in a Fourier series such as:

$$u_{n\boldsymbol{k}}(\boldsymbol{r}) = \sum_{\boldsymbol{G}} c_{n\boldsymbol{k}}(\boldsymbol{G})e^{i\boldsymbol{G}\cdot\boldsymbol{r}} \tag{3.56}$$

where $\boldsymbol{G}$ are vectors of the reciprocal lattice and $c_{n\boldsymbol{k}}(\boldsymbol{G})$ are the coefficients of the expansion in the basis of the plane waves. While any wavefunction could theoretically be expended in planewaves, it can be numerically costly to do so. Indeed, the wavefunctions describing the core states, or the d and f states are localized in space and, due to the necessity of orthogonalization, present rapid oscillations near the nucleus. A consequence of these features in direct space is a large delocalization of the representation in reciprocal space, *i.e.* correctly describing such states would require a very large number of planewaves, which is numerically cumbersome. Indeed, even though the expansion given in Eq. 3.56 is theoretically true for any wavefunction, a cut–off is usually applied

to the energy of the planewaves, such that the size of the basis becomes finite and numerically tractable. However, such an approach is not necessarily doomed, and can even provide a very efficient way of describing the wavefunctions, as we will see in the next section.

3.4.1 Planewaves, frozen core and pseudopotentials

A first step in the reduction of the size of the problem is the so–called frozen core approximation. It relies on the fact that effectively only a few electrons, at the top of the Fermi sea, contribute to most of the properties of the materials, while the others are too localized near the nucleus to hybridize themselves and, *e.g.* generate a chemical bonding. The latter can therefore be considered as essentially fixed, or frozen, while the former, in the presence of surrounding atoms will rearrange themselves in many different ways and create the richness of the solid–state matter physics. As a consequence, these higher energy electrons, or valence electrons, are generally the only ones accounted for in the self–consistency loop, allowing for a large decrease of the computational effort.

Moreover, as a consequence of their orthogonality to the core states, the valence electrons can be regarded as evolving in an effective weaker Coulomb potential. From this fact emerges the concept of pseudopotentials, whose premises appeared in the orthogonalized plane–wave method (OPW)[122]. Reformulating the OPW, Philips and Kleinman then showed in 1959 that by expressing the valence states in terms of a pre–othogonalized basis set, one can find a pseudostate, $|\phi_{PS}\rangle$, writing as:

$$|\phi_{PS}\rangle = |\phi\rangle + \sum_{\alpha,c} \langle\psi_{\alpha,c}|\phi_{PS}\rangle\, |\psi_{\alpha,c}\rangle\,. \tag{3.57}$$

In this equation, $|\phi\rangle$ is a valence state and $|\psi_{\alpha,c}\rangle$ are the core states belonging to the nucleus α. Applying $\hat{\mathcal{H}}$ to $|\phi_{PS}\rangle$, with $\hat{\mathcal{H}}\,|\phi\rangle = \varepsilon\,|\phi\rangle$ and $\hat{\mathcal{H}}\,|\psi_{\alpha,c}\rangle = \varepsilon_{\alpha,c}\,|\psi_{\alpha,c}\rangle$, one obtains:

$$\hat{\mathcal{H}}\,|\phi_{PS}\rangle = \varepsilon\,|\phi_{PS}\rangle + \sum_{\alpha c} \langle\psi_{\alpha,c}|\phi_{PS}\rangle\,(\varepsilon_{\alpha,c} - \varepsilon)\,|\psi_{\alpha,c}\rangle \tag{3.58}$$

where ε and $\varepsilon_{\alpha,c}$ are respectively the valence and the core eigenvalues. This equation can be rewritten in the following way:

$$\left[\hat{\mathcal{H}} + \sum_{\alpha,c}(\varepsilon - \varepsilon_{\alpha,c})\,|\psi_{a,c}\rangle\,\langle\psi_{a,c}|\right]|\phi_{PS}\rangle = \varepsilon\,|\phi_{PS}\rangle\,, \tag{3.59}$$

which emphasizes the fact that $|\phi_{PS}\rangle$ satisfies a Schrödinger equation with an additional potential:

$$V_R = \sum_{\alpha,c}(\varepsilon - \varepsilon_{\alpha,c})\,|\psi_{a,c}\rangle\,\langle\psi_{a,c}|\,, \tag{3.60}$$

and nevertheless, has the same eigenvalue as $|\phi\rangle$. As depicted in Fig. 3.3, this additional contribution to the potential is only present where the core orbitals are located. This area is defined by the volume contained in a sphere of radius r_c. As the contribution of V_R is positive, it opposes to the Coulomb potential and allows for a much weaker effective potential inside the core. Moreover, $|\phi_{PS}\rangle$ has the benefit of not oscillating in the

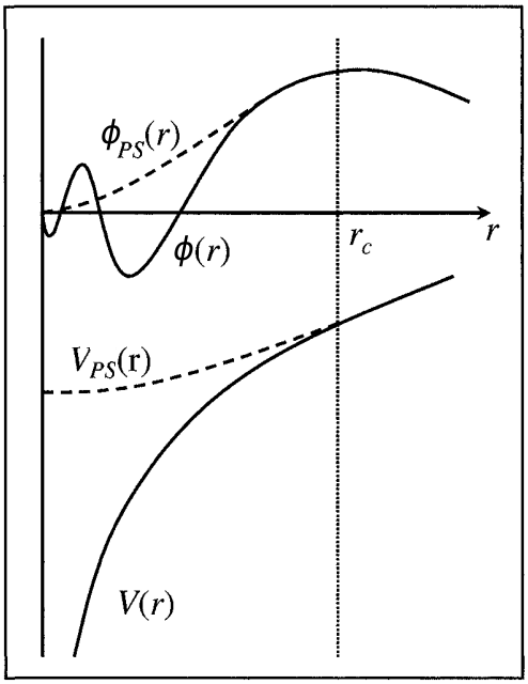


FIGURE 3.3: Schematic illustration of the replacement of the all–electron wavefunction and core potential by a pseudo wavefunction. Image adapted from [123].

core area. It can therefore be well represented by only a few planewaves, while it simultaneously satisfies $|\phi\rangle = |\phi_{PS}\rangle$ outside the core area where the potential presents weaker spatial variations and the effects of hybridization have to be properly accounted for.

Another consequence of the fact that $|\phi_{PS}\rangle$ does not present oscillations is that its kinetic energy is greatly reduced. However, as $|\phi\rangle$ and $|\phi_{PS}\rangle$ have the same eigenvalue, it means that this loss is compensated by the positive contribution brought by V_R and thus, the preorthogonalization, almost canceling the contribution of the Coulomb potential. This phenomenon is the root of the pseudopotential method.

This fruitful approach has later been taken further by Blöchl[124], and is known as the projector augmented waves–functions (PAW). As in the augmented plane–wave approach reviewed below, it is based on a judicious choice of basis to represent the part of the electronic states located near the nucleus, while using planewaves for the more delocalized part which hybridizes. This delocalized part, $|\tilde{\phi}\rangle$, is also non–zero in the augmentation sphere, however, as in the case of $\phi_{PS}(\boldsymbol{r})$ in Fig. 3.3 for the OPW, it varies smoothly. The smooth state, $|\tilde{\phi}\rangle$, is related to the all–electron valence state $|\phi\rangle$ through a linear transformation:

$$|\phi\rangle = \mathcal{T}\,|\tilde{\phi}\rangle \tag{3.61}$$

This transformation is equivalent to the identity, except inside the so–called augmentation spheres surrounding the nuclei and can therefore be written as $\mathcal{T} = \mathbf{1} + \sum_\alpha \mathcal{T}_\alpha$ where $\mathcal{T}_\alpha$ is only non–zero inside the aforementioned spheres. As a consequence, in the interstitial area, one has $|\phi\rangle = |\tilde{\phi}\rangle$.

Both $|\phi\rangle$ and $|\tilde{\phi}\rangle$ can respectively be developed in some conveniently chosen local basis $|\psi_{\alpha,c}\rangle$ and $|\tilde{\psi}_{\alpha,c}\rangle$ inside these spheres such as:

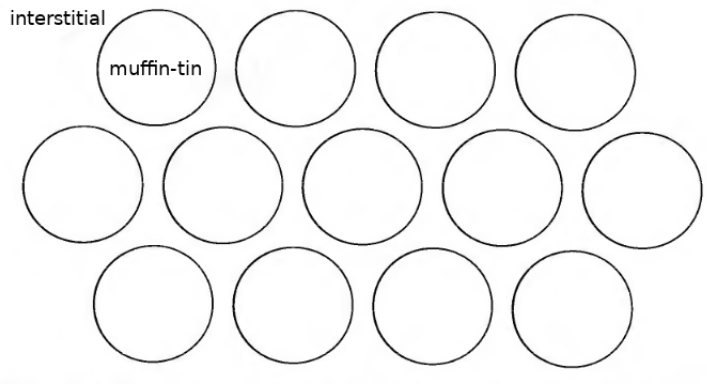


FIGURE 3.4: The "muffin–tin" division of space into intra–atomic spheres of radius R, and interstitial regions. Image adapted from [129].

$$|\tilde{\phi}\rangle = \sum_{\alpha,c} c_{\alpha,c} \, |\tilde{\psi}_{\alpha,c}\rangle \tag{3.62}$$

and

$$|\phi\rangle = \sum_{\alpha,c} c_{\alpha,c} \, |\psi_{\alpha,c}\rangle \, . \tag{3.63}$$

Therefore, the all–electron valence state writes as:

$$|\phi\rangle = |\tilde{\phi}\rangle + \sum_{\alpha,c} c_{\alpha,c} \left(|\psi_{\alpha,c}\rangle - |\tilde{\psi}_{\alpha,c}\rangle \right) \tag{3.64}$$

with $c_{\alpha,c} = \langle \tilde{p}_{\alpha,c} | \tilde{\psi} \rangle$. The projection operators $|\tilde{p}_{\alpha,c}\rangle$ are orthonormal to $|\tilde{\psi}_{\alpha,c}\rangle$, *i.e.* $\langle \tilde{p}_{\alpha,c} | \tilde{\psi}_{\alpha',c} \rangle = \delta_{\alpha\alpha'}\delta_{cc'}$. As a consequence, $|\tilde{\phi}\rangle = \sum_{\alpha,c} \langle \tilde{p}_{\alpha,c} | \tilde{\phi} \rangle \, |\tilde{\psi}_{\alpha,c}\rangle$, and the negative part of the summation in Eq. 3.64 should exactly cancel the contribution of $|\tilde{\phi}\rangle$ inside the augmentation spheres. Therefore, $\mathcal{T}$ is fully specified by the set of vectors $|\psi_{\alpha,c}\rangle$, $|\tilde{\psi}_{\alpha,c}\rangle$ and $|\tilde{p}_{\alpha,c}\rangle$ and writes as:

$$\mathcal{T} = \mathbf{1} + \sum_{\alpha,c} \left(|\psi_{\alpha,c}\rangle - |\tilde{\psi}_{\alpha,c}\rangle \right) \langle \tilde{p}_{\alpha,c}| \tag{3.65}$$

This transformation allows for the computation of the value of observables without ever having to represent the all–electron valence state:

$$\begin{aligned} a &= \langle \phi | \, \hat{A} \, | \phi \rangle \\ &= \langle \tilde{\phi} | \, \mathcal{T}^{\dagger} \hat{A} \mathcal{T} \, | \tilde{\phi} \rangle \end{aligned} \tag{3.66}$$

The PAW method[125], is *e.g.* implemented in VASP[126, 127, 128] which has been used in the work reported in Chap. 4, in combination with the use of a plane–wave basis and a frozen electrons core.

3.4.2 Linear augmented plane waves

The linear augmented plane–wave method (LAPW) finds its roots in the augmented plane–wave (APW) method originally developed by Slater[130]. He considered that the

volume of a solid can be divided into two different parts. As pictured in Fig. 3.4, he enclosed each nucleus in a sphere where the potential is similar to the one of an isolated atom, *i.e.* strongly varying and spherical. The rest of the volume, is made up from the interstitial space where the potential has less variations. Due to the strong resemblance of Fig. 3.4 with a muffin–tin, this approach is commonly designated by this name. Accordingly, the wavefunction uses two different bases in the interstitial area (I) and inside the muffin-tins (S):

$$\phi_{n\boldsymbol{k}}(\boldsymbol{r}) = \begin{cases} \frac{1}{\sqrt{\Omega}} \sum_{\boldsymbol{G}} c_{n\boldsymbol{k}}(\boldsymbol{G}) e^{i(\boldsymbol{G}+\boldsymbol{k})\cdot\boldsymbol{r}} & \boldsymbol{r} \in I \\ \sum_{lm} A_{lm} u_{\varepsilon l}(\boldsymbol{r}) Y_{lm}(\hat{\boldsymbol{r}}) & \boldsymbol{r} \in S \end{cases} \tag{3.67}$$

where the expansion coefficients are $c_{\boldsymbol{G}}$ and A_{lm}, Ω is the volume of the cell and Y_{lm} is the spherical harmonic function of degree l and order m. It reflects the fact that near the nucleus, *i.e.* inside the muffin–tin, the wavefunctions have an atomic character and are therefore easier to expand in spherical harmonics, while outside this region, due to the more delocalized nature of the states, they are more conveniently represented by planewaves. The radial part of the spherical harmonic expansion is solution of:

$$\left[\frac{\hbar^2}{2m_e}\left(-\frac{\partial^2}{\partial r^2} + \frac{l(l+1)}{r^2}\right) + V(r) - \varepsilon\right] r u_{\varepsilon l}(\boldsymbol{r}) = 0, \tag{3.68}$$

where $V(r)$ is the spherical component of the potential in the muffin–tin and ε is a parameter.

Using the fact that the wavefunctions must be continuous at the boundary between the muffin–tin and the interstitial areas, as well as the spherical harmonic expansion of planewaves, one can specify the coefficients A_{lm} as functions of the coefficients of the planewaves, $c_{n\boldsymbol{k}}(\boldsymbol{G})$:

$$A_{lm} = \frac{4\pi i^l}{\sqrt{\Omega} u_l(R)} \sum_{\boldsymbol{G}} c_{n\boldsymbol{k}}(\boldsymbol{G}) j_l\left(|\boldsymbol{k}+\boldsymbol{G}|\, R\right) Y^*_{lm}\left(\boldsymbol{k}+\boldsymbol{G}\right) \tag{3.69}$$

where R is the radius of the muffin–tins. Therefore, the variational coefficients of the APW basis are the $c_{n\boldsymbol{k}}(\boldsymbol{G})$ and ε. Indeed, if ε were not allowed to vary, the APWs would not have the variational freedom to account for changes in the wavefunctions when the band energy, $\varepsilon_{n\boldsymbol{k}}$, would differ from ε, therefore the two must be kept equal during the self–consistency. This process is quite cumbersome, as it means that the energy bands cannot be obtained from one diagonalization. In this framework, the main *raison d'être* of the LAPW basis is to remove the dependence of the basis on the band energy. To do so, Andersen[131] wrote the basis functions in the muffin–tins as linear combination of $u_{\varepsilon l}(\boldsymbol{r})$ and $\dot{u}_{\varepsilon l}(r) = \frac{\partial u_{\varepsilon l}}{\partial \varepsilon}$. The development of $\phi_{n\boldsymbol{k}}$ on the LAPW basis set writes as:

$$\phi_{n\boldsymbol{k}}(\boldsymbol{r}) = \begin{cases} \frac{1}{\sqrt{\Omega}} \sum_{\boldsymbol{G}} c_{n\boldsymbol{k}}(\boldsymbol{G}) e^{i(\boldsymbol{G}+\boldsymbol{k})\cdot\boldsymbol{r}} & \boldsymbol{r} \in I \\ \sum_{lm} \left[A_{lm} u_{\varepsilon l}(\boldsymbol{r}) + B_{lm} \dot{u}_{\varepsilon l}(r)\right] Y_{lm}(\hat{\boldsymbol{r}}) & \boldsymbol{r} \in S \end{cases} \tag{3.70}$$

with B_{lm} the expansion coefficients of $\dot{u}_{\varepsilon l}$ which are set by matching the value of the plane–wave derivative at the muffin–tin surface. This way of expressing the muffin–tin wavefunction is in fact a first order expansion of $u_{l\varepsilon}(r)$:

$$u_{l\varepsilon_{n\boldsymbol{k}}}(r) = u_{l\varepsilon}(r) + (\varepsilon_{n\boldsymbol{k}} - \varepsilon)\dot{u}_{l\varepsilon} + O\left((\varepsilon_{n\boldsymbol{k}} - \varepsilon)^2\right) \tag{3.71}$$

which allows to recover the value of $u_{l\varepsilon_{n\boldsymbol{k}}}(r)$ up to an error quadratic in the energy difference between the band and the one chosen in Eq. 3.69. This error is then quadratic of order $(\varepsilon - \varepsilon_{n\boldsymbol{k}})^4$ in the band energy. This has the benefit of allowing for a fixed value of ε and is therefore a colossal simplification over the APW method.

The LAPW method is implemented in ELK, which has been used in the work presented in Chap. 5, 6 and 7.

Chapter 4

Ab initio study of electronic temperature effects on magnetic materials properties

The content of this Chapter is nearly identical to the following published work:
Ab initio study of electronic temperature effects on magnetic materials properties
Authors: **Philippe Scheid**, Gregory Malinowski, Stéphane Mangin, and Sébastien Lebègue
Reference: Phys. Rev. B **99**, 174415 – Published 17 May 2019

4.1 Introduction

Interaction of ultrafast and intense light pulses with magnetic materials has led to the discovery of many intriguing phenomena such as ultrafast demagnetization[5] and all-optical switching[7, 8, 43]. Our understanding of these experimental facts is tightly bound to our knowledge of the properties of materials when the electronic temperature is raised far above the room temperature by the laser. Indeed, by using such femtosecond light pulses, it is possible to bring matter in previously unreachable states where the electronic temperature, T_e, can be well above the phonon temperature[132, 133]. While mechanisms involved in the ultrafast demagnetization and the all-optical switching are still heavily debated, our current rationalization of these experimental facts mostly relies on the 2-3 temperature model and, consequently, on our knowledge of the specific heat of the different baths.
To assess the electronic specific heat, the Sommerfeld approximation is usually chosen[132, 133]. However, this approximation is only meaningful at low T_e and one may ask its domain of validity. Z. Lin *et al.*[63] went beyond this approximation for a wide range of magnetic and non-magnetic compounds and found good agreement between both methods up to several thousand Kelvins, while neglecting the effect of T_e on the electronic structure.
In this work, we use *ab initio* density functional theory (DFT) to compute the static dependence on T_e of different electronic properties for fcc Ni, fcc Co, bcc Fe and FePt $L1_0$. Specifically, we self–consistently compute the dependence of the magnetization on T_e. By doing so, we define a temperature, T_S, where S refers to Stoner, at which the atomic magnetic moments completely disappear. This phenomenon has been mentioned in the literature, in particular by O. Gunnarsson[70], but its implications have never been fully explored. Therefore, we compute the electronic energy and specific heat and show the presence of a strong signature of the Stoner spin-flip process, missing from previous work[63] and from the Sommerfeld approximation.
This paper is organized as follows. In Sec. 5.2 we briefly summarize how O. Gunnarsson

computed the Stoner temperature and how we build on his results by using modern *ab initio* DFT tools. Using this framework, we explain how we compute the electronic energy and specific heat and how it contrasts with what has been done previously. In Sec. 4.3 we present and discuss our results for the Stoner temperature, the electronic energy and specific heat and compare them with previous works. Also, we discuss our results in the scope of the previously mentioned field of light-induced ultrafast dynamics. Finally, in Sec. 5.4 we present our conclusions and outlooks.

4.2 Theory

4.2.1 Self-consistent calculation of electronic dependent magnetic properties

O. Gunnarsson[70] was the first to use DFT to reproduce the experimental atomic magnetic moment of bcc-Fe, hcp-Co and fcc-Ni and to assess the behavior of magnetization when T_e changes. As spin-polarized calculations were not available at this time, he computed the magnetization by including the spin difference in the exchange correlation potential in the local spin-density approximation as a first order perturbation. By solving $I(\epsilon_F)\int_{-\infty}^{\infty}\frac{\partial f(\epsilon,\mu,T_e)}{\partial\epsilon}g(\epsilon)d\epsilon+1=0$, where $I(\epsilon)$ is the Stoner parameter, f the Fermi-Dirac distribution, μ is the chemical potential and $g(\epsilon)$ the density of states (DOS), he assessed the critical electronic temperature, T_e, at which the atomic magnetic moments would disappear and found values well above T_C, the Curie temperature of each compound. He explained this discrepancy by pointing out that even though band theory can describe the formation of atomic magnetic moments and their longitudinal temperature dependence, the Curie temperature should however be influenced by the direct or indirect exchange interactions between atomic moments, as exemplified by the Heisenberg model. As the temperature increases, so does the transversal fluctuations, and the global magnetization is in average suppressed, even though atomic moments still exist. To distinguish both effects, we define T_e, at which the atomic moments disappear as the Stoner temperature T_S.
Nowadays, spin-polarized calculations are common practice, and have shown great success in reproducing the local atomic moment values. Moreover, the possibility of performing DFT calculations at finite electronic temperature[134] allows us to build on O. Gunnarsson calculation of T_S by performing self-consistent *ab initio* computations for a wide range of T_e.

4.2.2 Self-consistent calculation of electronic energy and specific heat

In metals, changes in the electronic energy due to T_e are commonly dealt with by using the Sommerfeld approximation. In this framework the electron specific heat, C_e, depends linearly on T_e and on $g(\epsilon_F)$, the DOS at the Fermi energy, such as $C_e=\gamma T$ with $\gamma=\frac{\pi^2}{3}k_B^2g(\epsilon_F)$. However, this approximation is only valid at low electronic temperature, at which the Fermi-Dirac distribution is close to the Heaviside function. Recently, Z. Lin *et al.*[63] went beyond this approximation and fully took into account the DOS shape in their calculation. Using DFT, they computed the DOS of different compounds at low T_e, from which they accessed the temperature dependent electronic energy using:

$$E_e(T_e) = \int_{-\infty}^{\infty} f(\epsilon, \mu, T_e) \cdot g(\epsilon) \epsilon d\epsilon \tag{4.1}$$

where E_e the electronic energy and μ is accessed by solving the implicit equation:

$$N_e = \int_{-\infty}^{\infty} f(\epsilon, \mu, T_e) \cdot g(\epsilon) d\epsilon \tag{4.2}$$

where N_e is the number of electrons in the unit cell.

Finally, they obtained the electronic specific heat with:

$$C_e(T_e) = \frac{\partial E_e(T_e)}{\partial T_e} \tag{4.3}$$

In their work, Z. Lin *et al.*[63] considered the density of states to be independent of T_e. However, in the light of the work of O. Gunnarsson[70], one may ask how the existence of a Stoner temperature influences their results when dealing with magnetic materials. In contrast with Z. Lin *et al.*[63], we will compute the DOS for a wide range of T_e. Therefore, we can rewrite eq. 4.1 as:

$$E_e(T_e) = \int_{-\infty}^{\infty} f(\epsilon, \mu, T_e) \cdot g(\epsilon, T_e) \epsilon d\epsilon \tag{4.4}$$

and eq. 4.2 as:

$$N_e = \int_{-\infty}^{\infty} f(\epsilon, \mu, T_e) \cdot g(\epsilon, T_e) d\epsilon \tag{4.5}$$

4.2.3 Computational details

To solve the spin-polarized Kohn-Sham equations[114, 116], we use the VASP package[126, 127, 128] with projector augmented wave potentials[125, 135] and the generalized gradient approximation[120]. The energy cutoff of the planewave basis is set to 500 eV. Calculations are considered to be converged when the difference in energy between two electronic loops is lower than 10^{-8} eV. The Fermi-Dirac distribution is used to self-consistently compute the electronic ground state for 100 K $< T_e <$ 13000 K, sampled with 120 points. We use a k-point grid of 36x36x36 or equivalent for non–cubic geometries, except at low T_e where we increase it to 56x56x56 to ensure convergence. Then the DOS are obtained from the previous calculation using the tetrahedron method with Blöchl corrections[124].

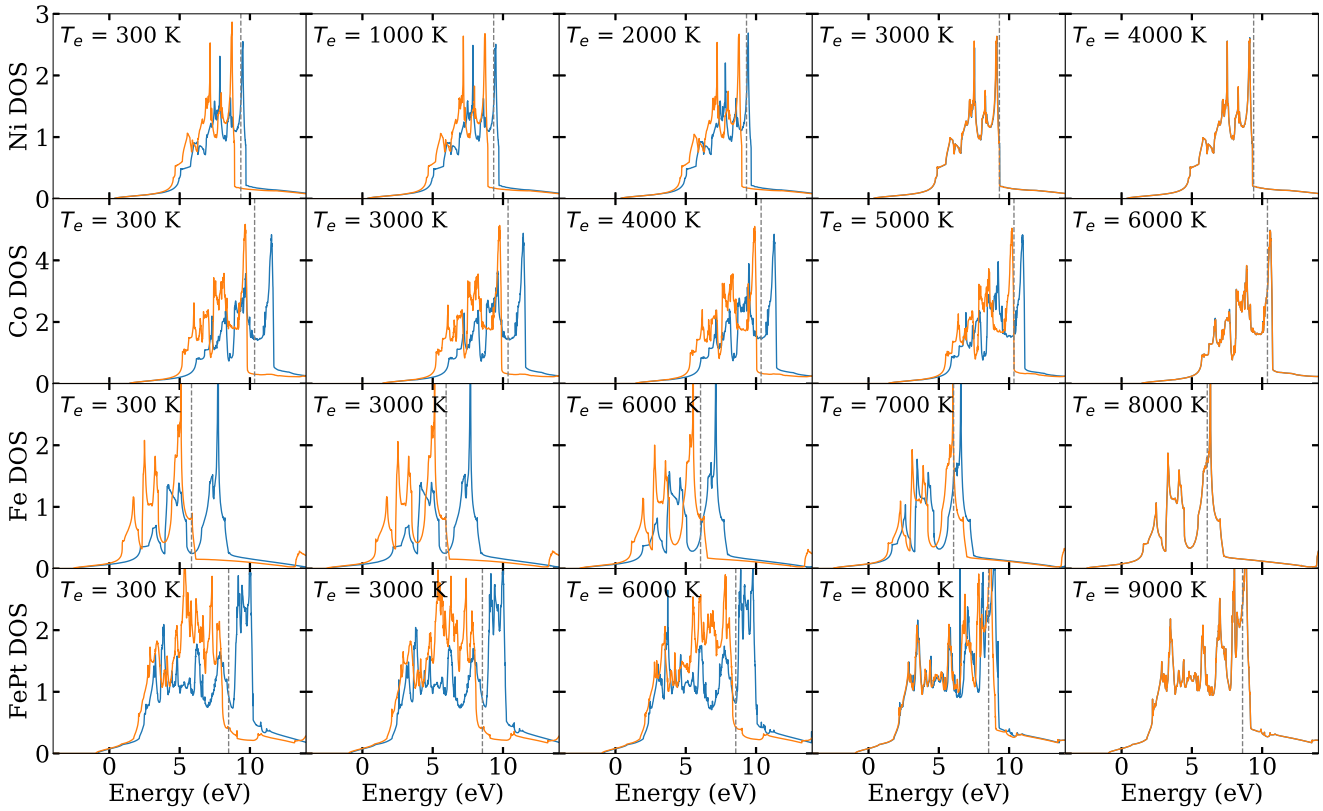


FIGURE 4.1: Spin-polarized density of states of fcc-Ni, hcp-Co, bcc-Fe and FePt $L1_0$ for different values of the electronic temperature chosen below and above the Stoner temperature. The majority (minority) spin DOS are in orange (blue) and the value of μ, the chemical potential, is indicated by a vertical dashed line.

4.3 Results and discussion

4.3.1 Dependence of the electronic structure on the electronic temperature

The T_e dependence of the electronic structure is evidenced by Fig. 4.1, showing how the self-consistently calculated spin-polarized DOS evolves with T_e. At low T_e we find that, as expected, all the compounds studied here are magnetic with 0.6 μ_B/at. for fcc-Ni, 1.6 μ_B/at. for hcp-Co, 2.2 μ_B/at. for bcc-Fe and $[3.1, 0.3]$ μ_B for [Fe, Pt] in FePt $L1_0$. As a consequence, the minority and majority-spin DOS are not identical in the lower range of T_e, and the integrated difference gives the magnetization. As T_e increases, the majority and minority-spin DOS progressively evolve until they become identical at the critical Stoner temperature, T_S. It underscores the effect of T_e on the electron eigenstates, which has been ignored so far in this context[63].

Fig. 4.2 shows the magnetization per unit cell as a function of T_e for each studied compound. The behavior is typical of a ferromagnetic-paramagnetic (as defined by Pauli) phase transition. Tab. 4.1 summarizes the Stoner temperature, ranging from 3100 K in the case of fcc-Ni up to 8100 K in the case of FePt $L1_0$, as well as the values calculated by

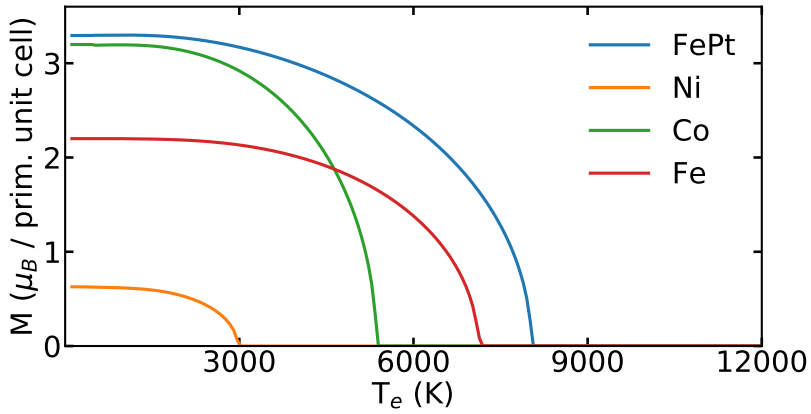


FIGURE 4.2: Magnetic moment per unit cell against the electronic temperature. In every compound, we observe a loss of the magnetization when the temperature is above T_S.

O. Gunnarsson[70] when available. Our computed values are systematically larger than the ones of [70]. This difference may be due to the assumption of the temperature independence of the Stoner parameter as well as to his first order perturbation treatment of the exchange splitting. As pointed out by Gunnarsson, T_S is not directly correlated to T_C since T_S is related to the intra-atomic exchange giving rise to atomic magnetic moments, while T_C is mainly a consequence of the inter-atomic direct and/or indirect exchange. However, as T_S is related to the local exchange, a larger atomic moment induces a larger T_S.

To explain such a behavior, one may recall that magnetism is a direct consequence of the exchange interaction between electrons, which is a quantum effect arising from the anti-symmetric nature of their wavefunctions and the Coulomb repulsion. This interaction tends to align electron spins, and by this way favors magnetic states. However, the penalty resulting from the increase of the kinetic and potential energy counteracts this magnetized state, and in most cases completely cancels it. Nevertheless, when the Fermi energy lies within a peak of the DOS, as it is the case for all the compounds studied here, the increase of the kinetic energy resulting from spin-flips is greatly reduced. These considerations are summarized by the well-known Stoner criterion: $Ig(\epsilon_F) > 1$, where I is the Stoner parameter[136, 137]. However, as T_e increases, electrons start to occupy higher energy states. When T_e becomes high enough, the smearing of the Fermi-Dirac distribution allows the minority-spin peak to start being occupied again. Consequently, the number of electrons with high kinetic energy increases. To prevent this, the compounds relax to a non-magnetic state where the minority-spin DOS shifts down in energy and the majority-spin DOS shifts up.
This strong T_e dependence of the electronic eigenstates, not taken into account in [63], raises the question of the T_e dependence of other electronic properties, such as the electronic energy and specific heat.

	M (μ_B/cell)	$M_{at.}$ (μ_B)	T_S (K)	T_S (K) from [70]	T_C (K) (exp.)
FePt $L1_0$	3.4	3.1, 0.3	8100		750
fcc-Ni	0.6	0.6	3100	2900	627
hcp-Co	3.2	1.6	5500	3300-4800	1400
bcc-Fe	2.2	2.2	7300	4400-6200	1043

TABLE 4.1: Calculated magnetic moment per unit cell and per atom and calculated Stoner temperature T_S for all the compounds studied here. For comparison, we added the results from 0. Gunnarsson[70]. In contrast with T_S, we also remind the experimental Curie temperature.

4.3.2 Consequences of the electronic temperature on the electronic specific heat

Fig. 4.3 shows the electronic energy as a function of T_e calculated with the temperature dependent DOS method (referred to as TDD), using eq. 4.4 and with the temperature independent DOS (TID), using eq. 4.1. In the latter case, we use the DOS computed with a Fermi smearing of 0.01 eV. For every compound, the temperature dependence of TDD and TID curves are significantly different. At low T_e, the calculated energies are identical for both methods, as the effect of electronic temperature is negligible. As T_e increases, the TDD electronic energies systematically become larger than the TID ones. However, the rate at which they differ as T_e increases is different. In the case of fcc-Ni, both methods give a similar result only when $T_e \to 0$ K. For hcp-Co, bcc-Fe and FePt $L1_0$, the TDD and TID energies are similar for a wider range of T_e. Another striking feature of the TDD curves is the presence of a singularity at the Stoner temperature, at which the parabolic–like behavior, characteristic of the lower temperature range, becomes quasi-linear.

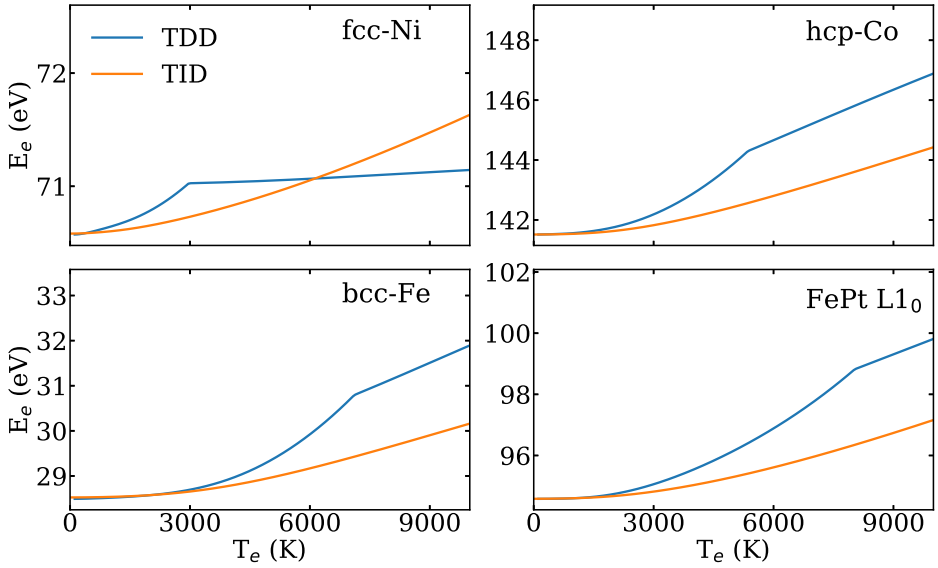


FIGURE 4.3: Electronic energy per unit cell against the electronic temperature for fcc-Ni, hcp-Co, bcc-Fe, FePt $L1_0$. The electronic energy obtained from TDD (TID) calculations is in blue (orange).

Fig. 4.4 shows the electronic specific heat calculated using eq. 4.3 and the TID and TDD approximations to compute the electronic energy. We compare our results with the specific heat obtained by using the Sommerfeld approximation, only valid at low temperature. The TID specific heat of Co reproduces the one from Z. Lin *et al.*[63]. The TID and the Sommerfeld heat capacities are always in agreement at low temperature, nevertheless it is not necessarily the case of the heat capacity calculated with the TDD method. Moreover, the TDD specific heats show a strong signature of the magnetic-paramagnetic second order phase transition, as evidenced by the increase abruptly ending at T_S. This feature strongly differentiates the TID and TDD specific heat and highlight the necessity to take explicitly the DOS temperature dependence into account.
At low T_e, in the case of bcc-Fe, T_S is high enough so the influence of Stoner spin-flip processes on the eigenstates are negligible. Therefore, below 2000 K, the TDD heat capacity matches with the Sommerfeld and the TID one. In the case of fcc-Ni, which has the lowest T_S, Stoner spin-flip processes are noticeable at any temperature below T_S, such that the TID heat capacity, as well as the Sommerfeld one, deviate from the TDD specific heat. Finally, despite the larger magnetic moment carried by Fe in FePt $L1_0$ than in bcc-Fe, its TDD heat capacity differs from the TID and the Sommerfeld one at lower temperature than in bcc-Fe. This discrepancy may be due to the presence of the Pt atom, carrying 0.3 μ_B, on which the effects of T_e are more noticeable in the lower temperature range. In Fig. 4.4 we notice that fcc-Ni not only stands out by its very low T_S but also by its very small heat capacity above T_S compared to the other compounds. Indeed, because of its d shell occupied by 9 electrons, and thus almost completely filled, the increase of T_e shifts the chemical potential above the DOS peak caused by the d shell, as seen in the fcc-Ni DOS Fig. 4.1. This significantly smaller DOS at μ results in an equally smaller specific heat. Such a behavior is not seen for the other compounds, as Co and Fe have respectively 7 and 8 electrons on their d shells. As a consequence, their chemical potentials still lie in the DOS peak when the electronic temperature is higher than T_S.

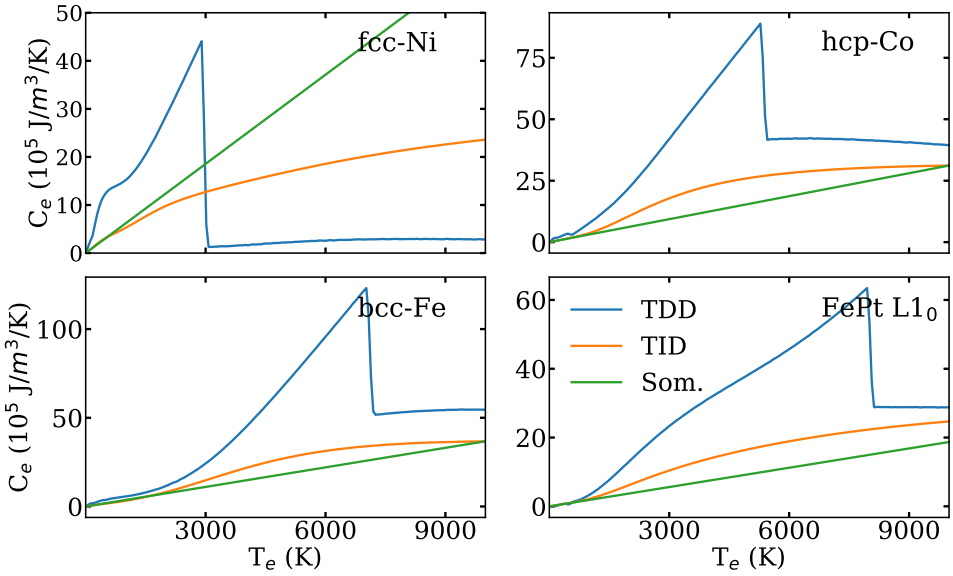


FIGURE 4.4: Electronic specific heat versus the electronic temperature for fcc-Ni, hcp-Co, bcc-Fe and FePt $L1_0$ computed with different approximations.

4.3.3 About ultrafast magnetization dynamics

Recent advances in the generation of ultrafast and intense laser pulses opened many new research fields. One of them is the study of the influence of such a light on magnetic materials. It has been shown that magnetization can be deterministically manipulated for a wide range of magnetic thin films[7, 8, 43] by using femtosecond light pulses. Moreover, the laser pulse also produces an ultrafast demagnetization happening on a 10-100 fs timescale[5, 29, 21]. The mechanisms driving such a dynamics are still heavily debated. In the case of the ultrafast demagnetization phenomenon, the two main candidates are the production of magnons reducing the average magnetization and the Stoner spin-flip processes, reducing the atomic magnetization[28, 29, 21, 107, 132].
The Stoner temperature and its connexion to the on-site exchange may provide valuable insights to the understanding of ultrafast demagnetization. Indeed, in these experiments, the laser energy is primarily absorbed by the electronic bath. Consequently, assuming that an electronic temperature can be defined shortly after the laser pulse, T_e rises from the ambient temperature, T_r, to well above T_C while the phonon bath is still at T_r. This idealized state is what we reproduce by performing *ab initio* DFT as we vary T_e while considering nucleus fixed, *i*.e. at 0 K, as in the Born-Oppenheimer approximation.
In this framework, a simple explanation of the ultrafast loss of magnetization could be that the electronic temperature exceeds T_S. Nevertheless, except in the case of fcc-Ni, reaching such temperatures would cause a melting of the compound. This failure to describe the ultrafast demagnetization is in agreement with the fact that, as reviewed in Sec. 2.2.3, the ultrafast demagnetization mainly originates from transversal excitations.
However, our results show that the electronic temperature has a strong impact on the electronic specific heat which is a key parameter in modeling the dynamics of electrons, phonons and spins within the 2-3 temperature model[133]. The electronic specific heat is usually computed using the Sommerfeld approximation. As a consequence, it is strongly underestimated as soon as the electronic temperature increases. The present work provides more precise estimates of this key quantity, which could be taken as input parameters for future investigations.

4.4 Conclusion

The static dependence of the electronic properties of fcc-Ni, hcp-Co, bcc-Fe and FePt $L1_0$ were studied with DFT for a wide range of the electronic temperature. In this framework, we were able to precisely compute the Stoner temperature, at which the intra-atomic exchange-splitting, and thus, the atomic magnetic moment disappears for all the compounds. We found values largely higher than the Curie temperatures of the different compounds. Furthermore, these values are found to be correlated with the value of the largest atomic magnetic moment in the cell.
We demonstrated that this phenomenon has a strong signature on the electronic energy, and consequently, on the specific heat. Such effects have been ignored in previous studies[63, 132] and induce large deviations from the Sommerfeld approximation and the temperature independent DOS approximation, even at a relatively low electronic temperature.

These results evidence the fact that the Sommerfeld approximation is not sufficient to obtain a correct temperature dynamics in the 2-3 the temperature model, commonly used to describe ultrafast and intense light-matter interactions. Finally, the Stoner temperatures we obtained are, except in the case of fcc-Ni, too high to be reached without destroying the compound. This is in agreement with the fact that, as reviewed in Sec. 2.2.3, the ultrafast demagnetization mainly originates from transversal excitations, *i.e.* the ultrafast generation of magnons, rather than a longitudinal decrease of each atomic magnetic moment.

Chapter 5

Effects of the electronic temperature on the magnons and ultrafast demagnetization

5.1 Introduction

Beaurepaire *et al.*[5] were the first to evidence the possibility of using a femtosecond light pulse to demagnetize a Ni film in less than a picosecond[5]. More than two decades later, this mechanism has been reproduced in many thin films differing in the heterogeneity, the magnetic ordering and the atomic species[17, 36, 39, 138, 29, 21, 20]. The nature of the magnetic excitations permitting such a dynamics has been widely discussed. According to Eich *et al.*[29] and Turgut *et al.*[28], it mostly originates from the presence of transversal excitations, which, in periodic solids are called magnons, rather than a longitudinal relation, *i.e.* Stoner excitations.

Many theories have been developed regarding the underlying mechanisms, through which these excitations are generated. One of the main candidates has been the light–induced superdiffusive currents[34, 35] delocalizing the majority spins from the illuminated area, thus causing a local demagnetization. However, even though such a spin transport has been experimentally evidenced[37], this mechanism had a relatively low contribution to the overall demagnetization[36]. Moreover, this phenomenon would lead to a longitudinal relaxation of the magnetization and is therefore not in agreement with the aforementioned experimental results. Similarly, the Elliott–Yafet spin–flip processes[73, 74] have been proposed, but this would also lead to a longitudinal reduction of the magnetization. Furthermore, according to theoretical results[75, 80, 81] this mechanism only brings a small contribution, which cannot fully account for the amplitude of the demagnetization seen experimentally. The last mechanism, and the one originally proposed by Beaurepaire *et al.*[5], is relying on a transfer of heat from the electronic bath, primarily absorbing the energy of the light to the bath of the magnons. Within this framework, as the temperature of the magnons increases the magnetization drops as in the classical Langevin theory. This phenomenon is usually described by the three temperature model[5, 132]. While such a framework is in agreement with the aforementioned experimental fact that the demagnetization is due to the presence of magnons, to this date, there is no rigorous proof that the electron–magnon coupling is large enough to heat up the magnons in such a short time–scale, as in the classical Langevin theory. To describe such a transversal dynamics, the Langevin atomistic Laudau–Lifshitz–Gilbert equation is a tool of choice, as it is perfectly able to account for transversal excitations. However,

within this framework, the temperature of the magnetic moments has to be defined and, as discussed in Sec. 2.4.3, there is no rigorous way of doing so yet. Furthermore, it is usually assumed[90, 91] that, except the temperature, all the other parameters, such as the Heisenberg exchange and the length of the magnetization, are not influenced by the laser and can be considered as time–independent.

In this work, accounting for the effect of the light by a rise of the electronic temperature, T_e, we use the frozen magnon approximation to evaluate inter–atomic Heisenberg exchange in Ni, Co and Fe. We show that an increase of T_e greatly influences the states of the magnons and consequently the interatomic exchange, from which emerges to the magnetic order. We relate our result to previous work[71, 139], in which the impact of the electronic smearing was not clearly assessed. Doing so, we show that our values of the Heisenberg exchange lead to reasonable values of the Curie temperature, T_C, which allows us to properly assess the validity of our numerical results. Finally, using the Langevin atomistic Laudau–Lifshitz–Gilbert dynamics, we show that, just as a rise of the temperature of the bath of the magnons, a reduction of the Heisenberg exchange can equally lead to an ultrafast demagnetization. In this framework, we evaluate the impact of the different parameters entering this equation on the speed and the amplitude of the demagnetization.

5.2 Theory

In this section we develop the framework we use to compute the magnon states using *ab initio* density functional theory.

5.2.1 *Ab initio* calculation of the properties of magnons

The derivations in this section closely follow the ones made by Halilov *et al.*[71] and Essenberger *et al.*[140].

5.2.1.1 Equations of motion

We interest ourselves in the motion of the expectation value of the magnetization carried by the atom i, $\left\langle \hat{\mathbf{M}}_i(t) \right\rangle = \mathbf{M}_i(t)$. As in the compounds we study here, the magnetization originating from the orbital angular momentum is quenched, we have:

$$\hat{\mathbf{M}}_i = -\frac{g\mu_B}{\hbar}\hat{\mathbf{s}}_i \tag{5.1}$$

where μ_B is the Bohr magneton and $\hat{\mathbf{s}}_i = \frac{\hbar}{2}\hat{\boldsymbol{\sigma}}_i$ with $\hat{\boldsymbol{\sigma}}_i = \left(\hat{\sigma}_{ix}, \hat{\sigma}_{iy}, \hat{\sigma}_{iz}\right)^t$.
Therefore, the magnetization of the atom i writes as:

$$\hat{\mathbf{M}}_i(t) \approx -\mu_B \sum_{\alpha,\beta=1}^{2} \int_{V_i} d^3\mathbf{r} \hat{\Psi}^{\dagger}_{\alpha}(\mathbf{r},t)\hat{\boldsymbol{\sigma}}_{\alpha\beta}\hat{\Psi}_{\beta}(\mathbf{r},t) \tag{5.2}$$

where the integral is performed on the volume V_i surrounding the atom i which contains its spin-polarized electronic density.

The motion of the magnetic moment operator, $\hat{\boldsymbol{M}}_i$ is calculated using the Heisenberg equation of motion:

$$-i\hbar\frac{d\hat{\boldsymbol{M}}_i(t)}{dt} = \left[\hat{H}_i(t), \hat{\boldsymbol{M}}_i(t)\right] \tag{5.3}$$

where $\hat{H}_i(t)$ is the Heisenberg Hamiltonian:

$$\hat{H}_i(t) = \sum_{i\neq j} J_{ij}\hat{\boldsymbol{M}}_j(t)\cdot\hat{\boldsymbol{M}}_i(t). \tag{5.4}$$

The sum in Eq. 5.4 spans over all the other atoms, *i.e.* not only the first neighbours of the atom i.

From the anti-commutation relation $\left[\hat{s}_{i\alpha}, \hat{s}_{j\beta}\right] = i\hbar\delta_{ij}\varepsilon_{\alpha\beta\gamma}\hat{s}_{i\gamma}$ at equal time, we have

$$\left[\hat{M}_{i\alpha}, \hat{M}_{j\beta}\right] = -\mathrm{i}g\mu_B\delta_{ij}\varepsilon_{\alpha\beta\gamma}\hat{M}_{i\gamma}, \tag{5.5}$$

where $\varepsilon_{\alpha\beta\gamma}$ is the Levi-Civita symbol.

Using Eq. 5.3, 5.4 and 5.5, we obtain the equation of motion of $\left\langle\hat{\boldsymbol{M}}_{\boldsymbol{i}}(t)\right\rangle$:

$$\frac{d\left\langle\hat{\boldsymbol{M}}_{\boldsymbol{i}}(t)\right\rangle}{dt} = -\frac{g\mu_B}{\hbar}\sum_{i\neq j} J_{ij}\left\langle\hat{\boldsymbol{M}}_i(t)\times\hat{\boldsymbol{M}}_j(t)\right\rangle. \tag{5.6}$$

In order to retrieve a dampingless Landau-Lifshitz equation of motion for $\boldsymbol{M}_i(t)$, we have to perform several approximations. First, we consider that spin correlations between the different atomic sites are neglectable, *i.e.* we have $\left\langle\hat{M}_{i\alpha}(t)\hat{M}_{j\beta}(t)\right\rangle = \left\langle\hat{M}_{i\alpha}(t)\right\rangle\left\langle\hat{M}_{j\beta}(t)\right\rangle$ for $i \neq j$. Secondly, we consider that the dynamics induced by the Hamiltonian Eq. 5.4 is sufficiently slow to allow for the electronic system to remain in its ground state, constrained by the directions of the magnetic moments, as in the adiabatic approximation. Consequently, we can write $\left\langle\hat{\boldsymbol{M}}_{\boldsymbol{i}}(t)\right\rangle \approx \left\langle\hat{\boldsymbol{M}}_{\boldsymbol{i}}\right\rangle(t)$. Using this framework, Eq. 5.6 rewrites as

$$\frac{d\left\langle\hat{\boldsymbol{M}}_{\boldsymbol{i}}\right\rangle(t)}{dt} \approx -\frac{g\mu_B}{\hbar}\sum_{i\neq j} J_{ij}\left\langle\hat{\boldsymbol{M}}_i\right\rangle(t)\times\left\langle\hat{\boldsymbol{M}}_j\right\rangle(t). \tag{5.7}$$

5.2.1.2 Calculation of the magnonic states and energies

Magnons are collective excitations of the magnetic moments present in a crystal lattice. On each site, the magnetic moment can be tilted away from the z axis by small angle θ_i, and its azimuthal angle is given by

$$\phi_i^{\mathbf{q}} = \mathbf{q}\cdot\mathbf{R}_i + \omega_{\mathbf{q}}t \tag{5.8}$$

such that, as seen Fig. 5.1, the moments are acting together to form a wave of wavevector $\boldsymbol{q}$ and of energy ω_q extending over the whole crystal. On each site, the magnetization is given by

$$\mathbf{M}_i^{\mathbf{q}}(t) = M_i\begin{pmatrix}\cos\left(\phi_i^{\mathbf{q}}(t)\right)\sin\left(\theta_i\right)\\ \sin\left(\phi_i^{\mathbf{q}}(t)\right)\sin\left(\theta_i\right)\\ \cos\left(\theta_i\right)\end{pmatrix} \tag{5.9}$$

and where both $\phi_i^{\mathbf{q}}$ and M_i, the magnitude of the magnetic moment on the site i, are considered to be time–independent.

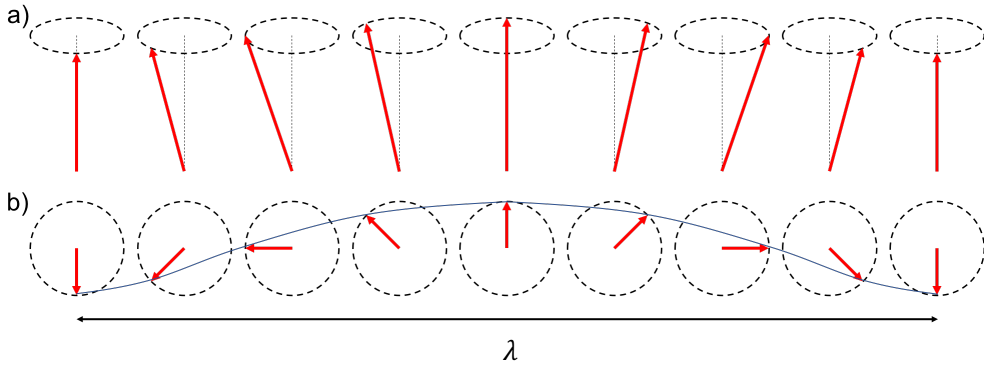


FIGURE 5.1: Side view (a)) and top view (b)) of a magnon having a wavelength λ. The red arrows represent the magnetization vectors carried by the different atomic sites.

Injecting Eq. 5.9 in Eq. 5.7, we get

$$\begin{aligned}\omega_{\mathbf{q}} \sin(\theta_j) = \frac{g\mu_B}{\hbar} \sum_{i \neq j} J_{ij} M_i \big[\sin(\theta_j) \cos(\theta_i) \\ - \cos(\theta_j) \sin(\theta_i) \cos(\mathbf{q} \cdot \mathbf{R}_j - \mathbf{q} \cdot \mathbf{R}_i) \big]\end{aligned} \tag{5.10}$$

and

$$\sum_{i \neq j} J_{ij} M_i \sin(\theta_i) \sin(\mathbf{q} \cdot \mathbf{R}_j - \mathbf{q} \cdot \mathbf{R}_i) = 0. \tag{5.11}$$

Linearizing Eq. 5.10, we obtain:

$$\omega_{\boldsymbol{q}} \theta_j = \frac{g\mu_B}{\hbar} \sum_{i \neq j} J_{ij} M_i \left[\theta_j - \theta_i Re[e^{i\boldsymbol{q} \cdot (\boldsymbol{R}_j - \boldsymbol{R}_i)}] \right] \tag{5.12}$$

In order to take advantage of the periodicity of the problem, the atomic sites are re–indexed with the following convention:

$$\boldsymbol{R}_j = \boldsymbol{R}_{n+\mu} = \boldsymbol{T}_n + \boldsymbol{\tau}_\mu \tag{5.13}$$

where n indexes the unit cell and μ the atomic site inside the unit cell. Using this notation, as well as the fact that neither θ nor M depend on the unit cell, but only on the atomic site inside the unit cell, Eq. 6.4 rewrites as:

$$\mathbf{M}^{\mathbf{q}}_{n\mu}(t) = M_\mu \begin{pmatrix} \cos\left(\phi^{\mathbf{q}}_{n\mu}(t)\right) \sin\left(\theta_\mu\right) \\ \sin\left(\phi^{\mathbf{q}}_{n\mu}(t)\right) \sin\left(\theta_\mu\right) \\ \cos\left(\theta_\mu\right) \end{pmatrix} \tag{5.14}$$

From Eq. 5.4 and Eq. 5.14, one can compute the total energy per unit cell induced by a spin spiral of wavevector $\mathbf{q}$:

$$\begin{aligned} E_{\mathbf{q}} &= -\frac{1}{2N}\sum_{\mu\nu} M_\mu M_\nu \Bigg(J^{\mathbf{0}}_{\mu\nu}\cos(\theta_\mu)\sin(\theta_\nu) \\ &+ \mathrm{Re}\left[J^{\mathbf{q}}_{\mu\nu}e^{i(\psi_\mu-\psi_\nu)}\right]\sin(\theta_\mu)\sin(\theta_\nu)\Bigg) \\ &= -\frac{1}{2N}\sum_{\mu\nu} M_\mu M_\nu \Bigg(J^{\mathbf{0}}_{\mu\nu}\left(1-\frac{\theta_\mu^2}{2}-\frac{\theta_\nu^2}{2}\right) \\ &+ \mathrm{Re}\left[J^{\mathbf{q}}_{\mu\nu}e^{i(\psi_\mu-\psi_\nu)}\right]\theta_\mu\theta_\nu\Bigg) \end{aligned} \tag{5.15}$$

where the second line is the expansion up to the second order in θ_μ and θ_ν of the first one, and $J^{\mathbf{q}}_{\mu\nu}$ is the Fourier transform of the real–space Heisenberg exchange $J_{\mu,\nu+n}$ defined as

$$J^{\mathbf{q}}_{\mu\nu} = -\sum_n (1-\delta_{0n}\delta_{\mu\nu})J_{\mu,\nu+n}e^{i\mathbf{q}(\mathbf{R}_{n+\nu}-\mathbf{R}_\mu)}. \tag{5.16}$$

As J_{ij} is symmetric under the permutation of i and j, is real, and is lattice periodic, *i.e.* $J_{\mu+n,\nu+n} = J_{\mu\nu}$, the following relations hold for $J^{\mathbf{q}}_{\mu\nu}$:

$$\begin{aligned} J^{\mathbf{q}}_{\mu\nu} &= J^{-\mathbf{q}}_{\nu\mu} \\ \mathrm{Re}J^{\mathbf{q}}_{\mu\nu} &= \mathrm{Re}J^{-\mathbf{q}}_{\mu\nu} \\ \mathrm{Im}\ J^{\mathbf{q}}_{\mu\nu} &= -\mathrm{Im}J^{-\mathbf{q}}_{\mu\nu} \end{aligned} \tag{5.17}$$

The phase factor $\psi_\mu - \psi_\nu$ in Eq. 5.15 has been added in order to allow for the computation of the real and imaginary part of the exchange $\tilde{J}^{\mathbf{q}}_{\mu\nu}$. Indeed, from the calculated energy, Eq. 5.15, one can access to the value of $\mathrm{Re}\left[\tilde{J}^{\mathbf{q}}_{\mu\nu}\right]$ by setting $\psi_\mu - \psi_\nu = 0$:

$$\begin{aligned} \mathrm{Re}\left[\tilde{J}^{\mathbf{q}}_{\mu\nu}\right] &= \mathrm{Re}\left[J^{\mathbf{q}}_{\mu\nu}\right] - \delta_{\mu\nu}\sum_\alpha \frac{M_\alpha}{M_\nu}J^{\mathbf{0}}_{\mu\alpha}\delta_{\mu\nu} \\ &= \frac{1}{M_\mu M_\nu}\frac{\partial^2 E_{\mathbf{q}}(\{\theta_\gamma\})}{\partial\theta_\mu\partial\theta_\nu}\Bigg|_{\{\theta_\gamma\}=0,\psi_\mu-\psi_\nu=0} \end{aligned} \tag{5.18}$$

as well as the value of $\mathrm{Im}\left[\tilde{J}^{\mathbf{q}}_{\mu\nu}\right]$ when $\psi_\mu - \psi_\nu = \frac{\pi}{2}$:

$$\begin{aligned} \mathrm{Im}\left[\tilde{J}^{\mathbf{q}}_{\mu\nu}\right] &= \mathrm{Im}\left[J^{\mathbf{q}}_{\mu\nu}\right] \\ &= \frac{1}{M_\mu M_\nu}\frac{\partial^2 E_{\mathbf{q}}(\{\theta_\gamma\})}{\partial\theta_\mu\partial\theta_\nu}\Bigg|_{\{\theta_\gamma\}=0,\psi_\mu-\psi_\nu=\frac{\pi}{2}}, \mu\neq\nu \end{aligned} \tag{5.19}$$

Eq. 5.12, which is giving us the dynamics of the magnetization, can, in account of Eq. 5.14 and Eq. 5.16, be written as:

$$\begin{aligned}\omega_{\boldsymbol{q}}\theta_\mu &= \frac{g\mu_B}{\hbar}\sum_{n\mu} J_{\nu+n,\mu}M_\nu\left((1-\delta_{0n}\delta_{\mu\nu})\right)\\ &\cdot\left[\theta_\mu - \theta_\nu Re[e^{i\boldsymbol{q}\cdot(\boldsymbol{R}_{n+\nu}-\boldsymbol{R}_\mu)}]\right]\\ &= \frac{g\mu_B}{\hbar}\sum_\nu M_\nu\left(\mathrm{Re}\left[J^{\mathbf{q}}_{\mu\nu}\right] - \delta_{\mu\nu}\sum_\kappa \frac{M_\kappa}{M_\mu}J^{\mathbf{0}}_{\kappa\mu}\right)\theta_\nu\end{aligned} \tag{5.20}$$

which in turn can be written as an eigenvalue problem solely involving the matrix $\tilde{J}^{\mathbf{q}}_{\mu\nu}$, which can be computed *ab initio* using Eq. 5.15 and Eq. 5.18:

$$\sqrt{M_\mu}\theta_\mu\omega_{\mathbf{q}} = \sum_\nu \frac{g\mu_B}{\hbar}\sqrt{M_\mu M_\nu}Re\left[\tilde{J}^{\mathbf{q}}_{\mu\nu}\right]\sqrt{M_\nu}\theta_\nu \tag{5.21}$$

To find the eigenenergies $\omega_{\mathbf{q}}$, we solve the secular equation:

$$\det\left(\delta_{\mu\nu}\omega_{\mathbf{q}} - \frac{g\mu_B}{\hbar}\sqrt{M_\mu M_\nu}\mathrm{Re}\left[\tilde{J}^{\mathbf{q}}_{\mu\nu}\right]\right) = 0 \tag{5.22}$$

When the crystal only contains one atom per Bravais lattice point, Eq. 5.22 simply gives:

$$\omega_{\boldsymbol{q}} = \frac{Mg\mu_B}{\hbar}\mathrm{Re}\left[\tilde{J}^{\mathbf{q}}\right] \tag{5.23}$$

In such a case, the computation of $\mathrm{Re}\left[\tilde{J}^{\mathbf{q}}\right]$ can also be greatly simplified. Indeed, the energy, Eq. 5.15, can be written as:

$$\begin{aligned}E_{\boldsymbol{q}} &= \frac{1}{2}M^2\left(J^0\cos^2\theta + \mathrm{Re}\left[J^{\boldsymbol{q}}\right]\sin^2\theta\right)\\ &= \frac{1}{2}M^2\left(J^0 + \mathrm{Re}\left[\tilde{J}^{\mathbf{q}}\right]\sin^2\theta\right)\end{aligned} \tag{5.24}$$

where the second equality is obtained by using $\tilde{J}^{\mathbf{q}} = J^{\mathbf{q}} - J^0$, which is only valid when there is a single atom per Bravais lattice point. As $\frac{1}{2}M^2J^0 = E_0$, *i.e.* the energy of the magnetic moments when they are all colinear, Eq. 5.24 can be rewritten as:

$$\mathrm{Re}\left[\tilde{J}^{\mathbf{q}}\right] = \frac{2\left(E_{\mathbf{q}} - E_0\right)}{M^2\sin^2\theta}. \tag{5.25}$$

This allows us to bypass the computation of a second derivative, as otherwise required by Eq. 5.15, and therefore, reduces the computational cost to obtain $\omega_{\boldsymbol{q}}$ using Eq. 5.23.

5.2.1.3 Computation of the Heisenberg exchange constants

From the knowledge of $\tilde{J}^{\mathbf{q}}_{\mu,n+\nu}$, one can directly compute the Heisenberg exchange between any pair of atoms respectively localized at $\boldsymbol{R}_\mu$ and at $\boldsymbol{R}_{n+\nu}$ by performing the inverse Fourier transform:

$$J_{\mu,n+\nu} = -\frac{1}{\Omega_{BZ}} \int_{BZ} d\mathbf{q} e^{-i\mathbf{q}\cdot(\mathbf{R}_\mu - \mathbf{R}_{n+\nu})} \tilde{J}^{\mathbf{q}}_{\mu,n+\nu}, \quad \mu \neq n+\nu \tag{5.26}$$

where the integration is performed over the first Brillouin zone and Ω_{BZ} is its volume.

5.2.1.4 Computation of the Curie temperature in the mean–field approximation

In the classical limit, the average magnetization modulus, $\langle M_\nu \rangle$, of a magnetic moment $\boldsymbol{M}_\nu$ in a magnetic field $\boldsymbol{B}$ and at a temperature T is given by the Langevin function:

$$\langle M_\nu \rangle = M_\nu \text{coth}\left[\frac{M_\nu B}{k_B T}\right] - \frac{k_B T}{B}, \tag{5.27}$$

and $\boldsymbol{M}_\nu$ is colinear to $\boldsymbol{B}$. In the mean field approximation, $\boldsymbol{B}$ is given by the so–called Weiss field:

$$\boldsymbol{B}^{\mu}_{\text{Weiss}} = \sum_{\mu n} (1 - \delta_{0n}\delta_{\mu\nu}) J_{\nu,\mu n} \left\langle \boldsymbol{M}_\mu \right\rangle = \sum_{\mu} J^0_{\mu\nu} \left\langle \boldsymbol{M}_\mu \right\rangle \tag{5.28}$$

which is the averaged field generated by all the other magnetic moments, $\boldsymbol{M}_\mu$, on the site ν due to their Heisenberg exchange interactions with the magnetic moment $\boldsymbol{M}_\nu$. Using Eq. 5.16 and Eq. 5.26, $J^0_{\mu\nu}$ is expressed as:

$$J^0_{\mu\nu} = -\tilde{J}^0_{\mu\nu} + \delta_{\mu\nu} \frac{1}{\Omega_{BZ}} \int_{BZ} d\mathbf{q} \tilde{J}^{\mathbf{q}}_{\mu\nu} e^{-i\mathbf{q}\cdot(\boldsymbol{\tau}_\mu - \boldsymbol{\tau}_\nu)} \tag{5.29}$$

In order to obtain T_C in this formalism, one uses the fact that at this temperature the field $\boldsymbol{B} = \boldsymbol{B}^{\mu}_{\text{Weiss}} = 0$ and Eq. 5.27 can be expanded to the first order:

$$\langle M_\nu \rangle = \frac{M_\nu^2}{3k_B T} B^{\nu}_{\text{Weiss}} = \frac{M_\nu^2}{3k_B T} \sum_{\mu} J^0_{\nu\mu} \left\langle M_\mu \right\rangle \tag{5.30}$$

The eigenvalues of this linear equation are solution of:

$$det\left(\delta_{\mu\nu} - \frac{M_\nu^2}{3k_B T_c} J^0_{\mu\nu}\right) = 0 \tag{5.31}$$

and the values of T_C obtained are the critical temperatures of the different atomic sites. When there is only one atom per Bravais lattice point, Eq. 5.31 writes as:

$$T_C = \frac{M^2 J^0}{3k_B} \tag{5.32}$$

where the label μ and ν have been removed, as there is only one atomic site, *i.e.* $J^0_{11} = J^0$. On account these facts, of Eq. 5.29 and that $\tilde{J}^0 = 0$, it is simply expressed as

$$J^0 = \frac{1}{\Omega_{BZ}} \int_{\text{BZ}} d\mathbf{q} \tilde{J}^{\mathbf{q}} \tag{5.33}$$

Using Eq. 5.25, the numerical evaluation of Eq. 5.33 is performed with:

$$T_C = \frac{2}{3k_B \sin^2\theta} \frac{1}{\Omega_{\text{BZ}}} \int_{\text{BZ}} d\mathbf{q} \left(E_{\mathbf{q}} - E_0\right) \tag{5.34}$$

5.2.2 Stochastic atomistic Laudau–Lifshitz–Gilbert dynamics

In order to study the impact of the changes in the interatomic exchange on the magnetization dynamics, we use the framework developed by Evans *et al.*[88] to solve the atomistic spin dynamics given in the most general case for a magnetic moment i by:

$$\frac{\partial \mathbf{S}_i}{\partial t} = -\frac{\gamma}{(1+\lambda^2)\mu_S}\left[\mathbf{S}_i \times \mathbf{H}^i_{\text{eff}} + \lambda \mathbf{S}_i \times \left(\mathbf{S}_i \times \mathbf{H}^i_{\text{eff}}\right)\right] \tag{5.35}$$

where $\lambda = 0.1$ is the microscopic damping, γ is the gyromagnetic ratio of the electrons, $\mathbf{S}_i$ is the unit vector associated to the magnetic moment i, μ_S is the magnitude of the magnetization vector and $\mathbf{H}^i_{\text{eff}}$ is the effective field, to which the magnetic moment i is subjected to. Note that, as $\mathbf{S}_i$ is unitless, the effective field is in unit of energy.

In our treatment, we consider a single spin in the average exchange field produced by the neighbors, up to the nearest tens. Initially, the magnetization is saturated along the z axis, which direction is given by the unit vector $\mathbf{u}_z$. Due to the cylindrical symmetry of the problem, the components of the average magnetization of the nearest ten neighbors which, due to fluctuations, would appear perpendicularly to $\mathbf{u}_z$ are neglected. Therefore, the effective field acting on the magnetic moment writes as:

$$\mathbf{H}^i(t) = -\left\langle m \right\rangle (t) \sum_j N_j J_{ij} \mathbf{u}_z + \mathbf{H}^i_{\text{th}} \tag{5.36}$$

where j indexes the neighbors by their distance to the studied magnetic moment i and N_j is the number of such neighbors, $\langle m \rangle (t)$ corresponds to the average magnetization at a time t calculated from the ensemble $n = 20000$ of simultaneously propagated dynamics, J_{ij} is the Heisenberg exchange computed from our *ab initio* calculations reported later, and $\mathbf{H}^i_{\text{th}}$ is the thermal field. The thermal field satisfies the fluctuation dissipation theorem, such that a Boltzman distribution is obtained at thermal equilibrium. Its formula is:

$$\mathbf{H}^i_{\text{th}} = \mathbf{\Gamma}(t)\sqrt{\frac{2\lambda k_B T \mu_S}{\gamma \Delta t}} \tag{5.37}$$

where $\mathbf{\Gamma}$ (t) is a Gaussian distribution in three dimensions with a mean of 0 and a standard deviation of 1, k_B is the Boltzman constant and $\Delta t = 0.33$ fs is the time step.

The numerical integration of a stochastic equation is not a straightforward task. As in [88], the propagation is done using the Heun scheme such that a convergence to the Stratonovitch solution is obtained. The first step of this method consists in computing the regular Euler integration step as:

$$\mathbf{S}'_i = \mathbf{S}_i + \Delta \mathbf{S} \Delta t, \tag{5.38}$$

where

$$\Delta \mathbf{S} = -\frac{\gamma}{(1+\lambda^2)\mu_S}\left[\mathbf{S}_i \times \mathbf{H}^i_{\text{eff}} + \lambda \mathbf{S}_i \times \left(\mathbf{S}_i \times \mathbf{H}^i_{\text{eff}}\right)\right]. \tag{5.39}$$

Using the prediction given by $\mathbf{S}'_i$, a new effective field, $\mathbf{H}^{i'}_{\text{eff}}$, is computed at the exception of the thermal field which does not change. From this, a second estimation, $\Delta \mathbf{S}'$, can be computed with:

$$\Delta \mathbf{S}' = -\frac{\gamma}{(1+\lambda^2)\mu_S}\left[\mathbf{S}_i' \times \mathbf{H}_{\text{eff}}^{i'} + \lambda \mathbf{S}_i' \times \left(\mathbf{S}_i' \times \mathbf{H}_{\text{eff}}^{i'}\right)\right]. \tag{5.40}$$

Finally the integrated value of $\mathbf{S}_i^t$, *i.e.* $\mathbf{S}_i^{t+\Delta t}$, is obtained as:

$$\mathbf{S}_i^{t+\Delta t} = \mathbf{S}_i + \frac{1}{2}\left[\Delta \mathbf{S} + \Delta \mathbf{S}'\right]\Delta t. \tag{5.41}$$

5.3 Results

5.3.1 Computational details

To compute the spin–spiral energies for any value of $\mathbf{q}$ by using only primitive cells, the following *ansatz*, as already implemented in the ELK code, is used to express the rotated Bloch states:

$$\phi_{n\mathbf{k},\mathbf{q}}(\boldsymbol{r}) = \begin{pmatrix} u^{\uparrow}_{n\mathbf{k},\mathbf{q}}(\boldsymbol{r})\mathrm{e}^{i(\mathbf{k}+\mathbf{q}/2)\cdot\boldsymbol{r}} \\ u^{\downarrow}_{n\mathbf{k},\mathbf{q}}(\boldsymbol{r})\mathrm{e}^{i(\mathbf{k}-\mathbf{q}/2)\cdot\boldsymbol{r}}, \end{pmatrix} \tag{5.42}$$

where $\phi_{n\mathbf{k},\mathbf{q}}(\boldsymbol{r})$ is the Bloch spinor state indexed by n, the band, and $\mathbf{k}$ a wavevector of the first Brillouin zone. $u^{\uparrow}_{n\mathbf{k},\mathbf{q}}(\boldsymbol{r})$ and $u^{\downarrow}_{n\mathbf{k},\mathbf{q}}(\boldsymbol{r})$ are the components of the wavefunctions which have the periodicity of the unit cell. Lastly, the factors $\mathrm{e}^{\pm\mathbf{q}\cdot\mathbf{r}/2}$ rotate the wavefunction such that the expectation value of the magnetization takes the form of Eq. 5.9.

On this basis, ground state calculations are obtained from density functional theory calculations[114, 116] using the non–colinear full potential linearized augmented planewave method and the LSDA[119] for the exchange correlation potential, as implemented in the ELK code[1]. As in Chap. 4, the electron temperature, $\mathrm{T_e}$, is accounted for by a change of the Fermi distribution. A proper assessment of Eq. 5.25 and Eq. 5.33 requires a very good convergence. As such, the APW basis is expanded on 10 spherical harmonics, $|\mathrm{k}+\mathrm{G}|_{\max} R = 8$, where R is the radius of the muffin–tin, and the Brillouin zone is sampled with a 28x28x28 mesh for all the compounds. A large grid is particularly important in order to insure the convergence at low $\mathrm{T_e}$. The self–consistence is achieved when the total energy changes by less than 10^{-8} Ha in two successive electronic loops.

We use a 14x14x14 $\mathbf{q}$–point grid to compute the density of states (DOS) of the magnons, the interatomic Heisenberg exchange and $\mathrm{T_C}$, all of which require the computation of integrals over the first Brillouin zone. We compute the density of states using a Gaussian with a smearing of 0.02 eV to replace the Dirac deltas. These computations are done in a separate, home–made, python code.

5.3.2 Softening of the magnon modes

Figures 5.2, 5.3 and 5.4 show the bands along high symmetry axis and the DOS of the magnons calculated at $\mathrm{T_e}$ = 300 K and $\mathrm{T_e}$ = 2000 K in fcc Ni, and $\mathrm{T_e}$ = 300 K and 3000 K in fcc Co and bcc Fe, as in fcc Ni the magnetization vanishes when $\mathrm{T_e}$ approaches 3000 K (see Chap. 4). The general trend is a reduction of the energy of the modes as $\mathrm{T_e}$ increases.

[1] http://elk.sourceforge.net/

In the case of fcc Ni, the top of the dispersion calculated at T_e = 300 K almost reaches 0.7 eV, as shown by the graph at the top of Figure 5.2. Increasing T_e to 2000 K induces a general flattening of the calculated dispersion by more than 33%, which makes it the most affected compound. Interestingly, using this elevated T_e allows us to be in better agreement with the computations of Halilov *et al.*[71], as well as Padja *et al.*[139]. This hints toward the fact that they used an electronic smearing, which, in fcc Ni, significantly affects the dispersion.

In fcc Co, as seen in Fig. 5.3, the top of the dispersion decreases from 0.8 eV to 0.4 eV as the electronic temperature increases from 300 K to 3000 K. In this case, both Halilov *et al.* and Padja *et al.* obtained only slightly lower frequencies when compared to our graph at T_e = 300 K. The same remark applies to bcc Fe[2]. However, as seen by comparing Fig. 5.3 and 5.4, the magnon dispersion of bcc Fe is more resilient than fcc Co upon an increase of T_e. Furthermore, bcc Fe exhibits a more complicated behavior. Indeed, as pointed out by Halilov *et al.*[71] and Padja *et al.*[139], and as seen on the upper graph of Fig. 5.4, kinks forming local minima in the dispersion are visible along the H – N and Γ – H directions. These are the consequence of anomalies predicted by Kohn[141]. They are due to a lowering of the energy of the electrons at the Fermi surface as a consequence of a periodic perturbation if the condition $\mathbf{q} = 2\mathbf{k}_F$ is met, where $\mathbf{q}$ is the wavevector of the perturbation and $\mathbf{k}_F$ is a vector of the Fermi surface. In this case, the periodic perturbation is caused by the magnetization vectors forming a spin–wave, as shown in Fig. 5.1. As evidenced by the lower graph of Fig. 5.4, contrary to the case of fcc Ni and fcc Co, in bcc Fe the effect of a change in T_e does not simply amount to a general lowering of the energy of the modes, but the anomalies are also removed. Indeed, when T_e increases and the Fermi distribution becomes smoother, the aforementioned condition cannot be satisfied anymore as it requires the sharpness of the Fermi surface[141].

To conclude this section, one may notice that the resilience of the Heisenberg exchange constant is correlated to the one of the magnetic moments carried by each atom upon the increase of T_e, as seen in Chap. 4. This is related to the fact that when the length of the atomic magnetic moments decreases, the Heisenberg exchange does so as well, and, when reaching T_S, the Heisenberg exchange becomes zero.

5.3.3 Reduction of the interatomic exchange

As it is directly related to the magnetic ordering of a compound, a key quantity in the study of the light induced demagnetization is the interatomic Heisenberg exchange. As reviewed in Sec. 2.4.3, in most of the previous work, this quantity has been considered as constant during and after the pulse. However, as seen *supra*, the modes of the magnons are greatly affected by a change in the electronic states and this should also translate in a decrease of the strength of the Heisenberg exchange coupling. To study the latter in bcc Fe, fcc Co and fcc Ni, and going up to the tenth neighbour, we use Eq. 5.26. Table 5.1 displays these values at different T_e, labeled as $J_{ij}^{T_e}$, where j is numbering the type of neighbors according to their distance to a selected atom i, and T_e is the electronic temperature.

[2] At 300 K, the dispersion presents high energy points near the edge of the Brillouin zone, while the DOS does not rise up to these energies. This is due to the fact that the sampling of the Brillouin zone is not dense enough to account for these particular points.

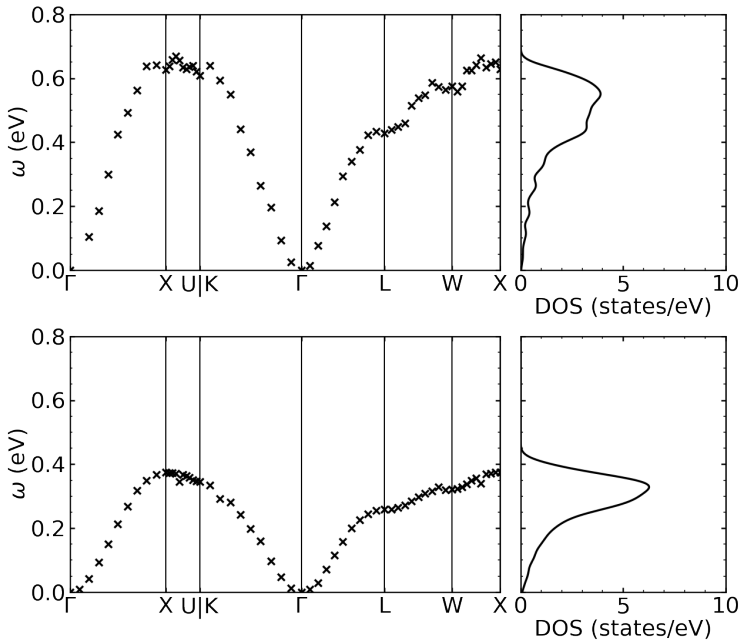


FIGURE 5.2: Band dispersion and density of states of the magnons in fcc Ni when the electronic temperature is set to 300K (top) and 2000K (bottom).

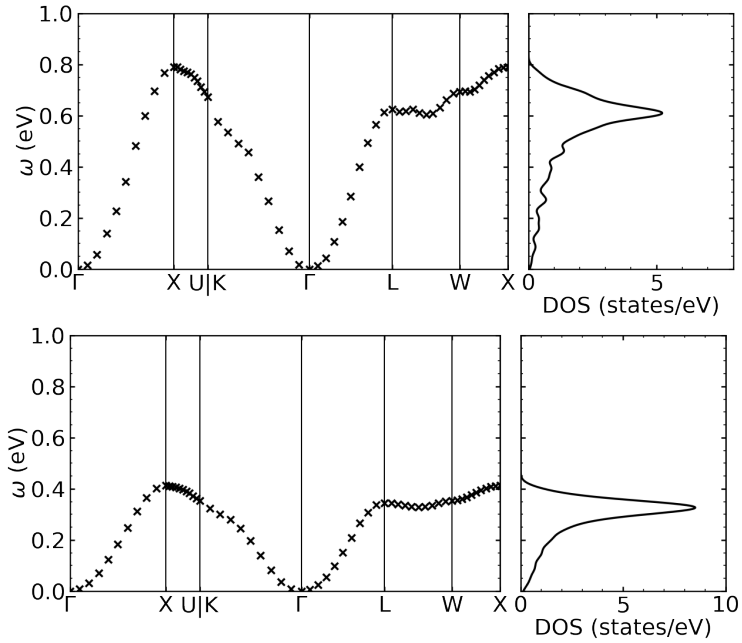


FIGURE 5.3: Band dispersion and density of states of the magnons in fcc Co when the electronic temperature is set to 300K (top) and 3000K (bottom).

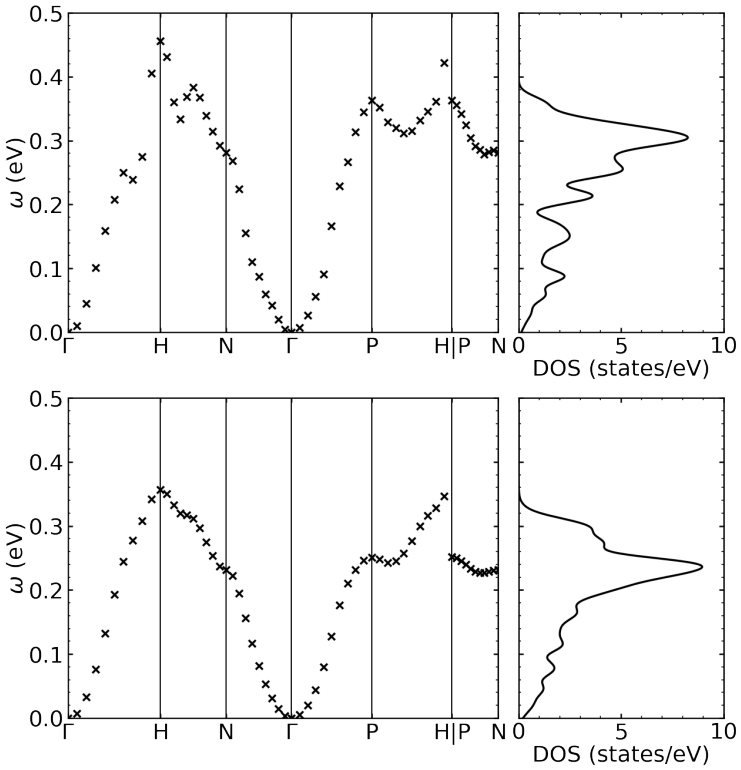


FIGURE 5.4: Band dispersion and density of states of the magnons in bcc Fe when the electronic temperature is set to 300K (top) and 3000K (bottom).

Once again, at T_e = 300 K, and even up to respectively 2000 K and 3000 K in fcc Ni and in fcc Co and bcc Fe, we obtain higher values than what is reported by Pajda *et al.*[139] for the first neighbors. Indeed, they obtained 19.48 meV for bcc Fe, 14.76 meV for fcc Co and only 2.80 meV for fcc Ni. These large discrepancies may be due to the fact that they used different computation methods, *i.e.* the tight-binding linear muffin-tin orbital and the magnetic force theorem[142] to obtain the exchange parameters, as well as their possible use of an electronic smearing to facilitate the convergence. Nevertheless, as us, they found oscillations in the sign of the coupling, *i.e.* it is alternatively changing from ferromagnetic to antiferromagnetic as the distance between the considered pairs of atoms increases. Such a behavior is typical of the Ruderman–Kittel–Kasuya–Yoshida coupling[143]. In the case of bcc Fe and fcc Ni, even though discrepancies in the magnitude of this coupling exist, the signs are in agreement with the work of Pajda *et al.*[139] and of Halilov *et al.*[71].

The T_e dependence of J_{ij} has already been assessed by Chimata *et al.*[144] in fcc Ni and fcc Co. However, in their work they only computed the contribution of the first and second neighbors, and, strangely, found a very low value for the exchange interaction ($\approx$ 13 meV) between first neighbors in bcc Fe. This is nearly half of the value found by Halilov *et al.*[71] and also well below what was found by Padja *et al.*[139]. Furthermore, contrary to our results they found that this exchange constant significantly increases with T_e up to 3500 K.

To assess the decrease of the Heisenberg exchange due to the increase of T_e, we computed $\Delta_{ij}^{T} = 100 \times \frac{J_{ij}^{Te} - J_{ij}^{300}}{J_{ij}^{300}}$. These are also shown in Tab. 5.1. As in the previous section,

fcc Ni is the most affected as a decrease of the exchange of $\approx$ 50% is seen for the first 3 neighbors when T_e is raised to 2000 K. This effect tends to increase for the pairs of atoms, which are further apart. On the other hand, at the same T_e, in fcc Co a decrease of 20% to 25% is noticed for the pairs 1, 3 and 4 and, as well, becomes more pronounced for the other pairs. Curiously though, the Heisenberg exchange between second neighbors slightly increases. Lastly, bcc Fe is clearly the less affected as the exchange between the first neighbors only decreases by 1%, even though the rest of the bounds are as much, or even more affected than in fcc Co. This trend is confirmed when increasing T_e to 3000 K, as the exchange between the first neighbors in bcc Fe only decreases by 11%, while it goes down by 57% in fcc Co.

Now, in order to assess the T_e–dependent total contribution of each type of neighbor in the magnetic ordering, we plot the quantity $N_j \times J_{ij}^{T_e}$, where N_j is the number of neighbors of type j. The bar diagram in Fig. 5.5 shows that the interactions between first neighbors are providing the most prominent contribution to the global ordering. However, due to the large number of 3rd neighbors in the fcc structure, both fcc Ni and fcc Co, these are also contributing quite significantly to the ferromagnetic ordering. Nevertheless, in the case of fcc Co, the antiferromagnetic coupling to the 4th neighbors completely cancels the benefits of the former. The same phenomenon occurs in bcc Fe, where the contribution of the 2nd and 4th neighbors are almost canceling each other for any value of T_e.

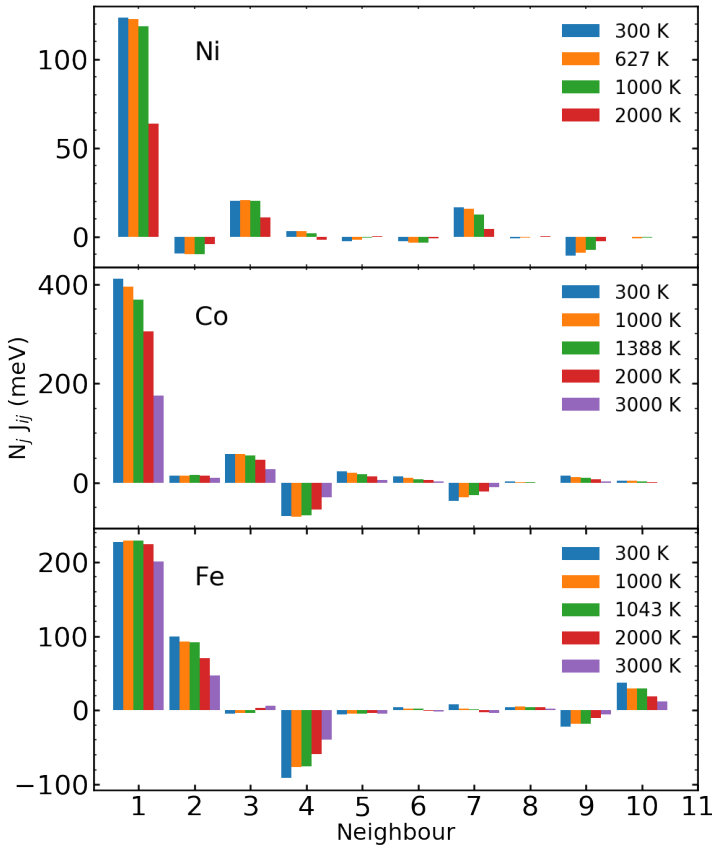


FIGURE 5.5: Bar diagram representing $N_j \times J_{ij}^{T_e}$ for j, which indexes the neighbors, in fcc Ni, fcc Co and bcc Fe. N_j is the number of neighbors of type j, *i.e.* and $J_{ij}^{T_e}$ is the Heisenberg exchange interaction between the atoms i and j.

bcc Fe	1	2	3	4	5	6	7	8	9	10
$\mathbf{R}_j$	$(\frac{1}{2}, \frac{1}{2}, \frac{1}{2})$	(1, 0, 0)	(1, 1, 0)	$(\frac{3}{2}, \frac{1}{2}, \frac{1}{2})$	(1, 1, 1)	(2, 0, 0)	$(\frac{3}{2}, \frac{3}{2}, \frac{1}{2})$	(2, 1, 0)	(2, 1, 1)	$(\frac{3}{2}, \frac{3}{2}, \frac{3}{2})$
J_{ij}^{300} (meV)	28.4103	16.5328	-0.3548	-3.8111	-0.7120	0.6210	0.3173	0.1590	-0.9390	4.6532
J_{ij}^{1000} (meV)	28.6345	15.4410	-0.3162	-3.1926	-0.6077	0.3828	0.0798	0.2132	-0.7520	3.7206
Δ_{ij}^{1000} (%)	0.7648	-7.3979	-20.1637	-17.1078	-21.0761	-42.1025	-80.1592	22.5254	-19.7937	-21.4550
J_{ij}^{1043} (meV)	28.6276	15.3098	-0.2833	-3.1591	-0.5619	0.3596	0.0630	0.1949	-0.7532	3.6549
Δ_{ij}^{1043} (%)	0.7648	-7.3979	-20.1637	-17.1078	-21.0761	-42.1025	-80.1592	22.5254	-19.7937	-21.4550
J_{ij}^{2000} (meV)	28.0623	11.7535	0.2630	-2.4775	-0.4920	-0.0746	-0.1236	0.1728	-0.4233	2.3256
Δ_{ij}^{2000} (%)	-1.2251	-28.9084	-174.1131	-34.9908	-30.8950	-112.0157	-138.9518	8.6321	-54.9261	-50.0217
J_{ij}^{3000} (meV)	25.1260	7.8009	0.4955	-1.6374	-0.5908	-0.3399	-0.1613	0.1099	-0.2495	1.4796
Δ_{ij}^{3000} (%)	-11.5603	-52.8159	-239.6449	-57.0346	-17.0176	-154.7406	-150.8414	-30.9274	-73.4295	-68.2039
fcc Co	1	2	3	4	5	6	7	8	9	10
$\mathbf{R}_j$	$(\frac{1}{2}, \frac{1}{2}, 0)$	(1, 0, 0)	$(1, \frac{1}{2}, \frac{1}{2})$	(1, 1, 0)	$(\frac{3}{2}, \frac{1}{2}, 0)$	(1, 1, 1)	$(\frac{3}{2}, 1, \frac{1}{2})$	(2, 0, 0)	$(\frac{3}{2}, \frac{3}{2}, 0)$	$(2, \frac{1}{2}, \frac{1}{2})$
J_{ij}^{300} (meV)	34.1996	2.3561	2.4441	-5.6086	0.9452	1.5597	-0.7432	0.5002	1.1598	0.1635
Jij^{1000} (meV)	32.9209	2.4315	2.3999	-5.6879	0.8582	1.2331	-0.5933	0.3359	0.9387	0.1529
Δ_{ij}^{1000} (%)	-3.7388	3.2015	-1.8076	1.4143	-9.2116	-20.9393	-20.1722	-32.8355	-19.0669	-6.4824
J_{ij}^{1388} (meV)	30.7542	2.5560	2.2808	-5.4392	0.7510	0.9857	-0.5016	0.2081	0.8324	0.1198
Δ_{ij}^{1388} (%)	-10.0742	8.4847	-6.6794	-3.0211	-20.5455	-36.8019	-32.5040	-58.3913	-28.2253	-26.7490
J_{ij}^{2000} (meV)	25.4752	2.4298	1.9167	-4.4595	0.5487	0.6639	-0.3793	0.0608	0.6158	0.0625
Δ_{ij}^{2000} (%)	-25.5101	3.1277	-21.5799	-20.4894	-41.9498	-57.4357	-48.9631	-87.8500	-46.9035	-61.8086
J_{ij}^{3000} (meV)	14.6916	1.6864	1.1457	-2.4215	0.2370	0.3148	-0.1871	0.0003	0.2439	0.0034
Δ_{ij}^{3000} (%)	-57.0415	-28.4229	-53.1218	-56.8254	-74.9244	-79.8181	-74.8209	-99.9353	-78.9738	-97.9392
fcc Ni	1	2	3	4	5	6	7	8	9	10
$\mathbf{R}_j$	$(\frac{1}{2}, \frac{1}{2}, 0)$	(1, 0, 0)	$(1, \frac{1}{2}, \frac{1}{2})$	(1, 1, 0)	$(\frac{3}{2}, \frac{1}{2}, 0)$	(1, 1, 1)	$(\frac{3}{2}, 1, \frac{1}{2})$	(2, 0, 0)	$(\frac{3}{2}, \frac{3}{2}, 0)$	$(2, \frac{1}{2}, \frac{1}{2})$
J_{ij}^{300} (meV)	10.2946	-1.5942	0.8476	0.2608	-0.0994	-0.3436	0.3489	-0.1530	-0.8765	-0.0040
J_{ij}^{627} (meV)	10.2298	-1.6564	0.8519	0.2488	-0.0693	-0.4269	0.3269	-0.0777	-0.7556	-0.0347
Δ_{ij}^{627} (%)	-0.6293	3.9057	0.5066	-4.5942	-30.2919	24.2478	-6.3189	-49.2330	-13.7905	774.9263
J_{ij}^{1000} (meV)	9.8761	-1.6344	0.8384	0.1565	-0.0226	-0.4011	0.2632	-0.0555	-0.6355	-0.0287
Δ_{ij}^{1000} (%)	-4.0651	2.5223	-1.0858	-40.0038	-77.2666	16.7551	-24.5579	-63.7064	-27.4963	622.1979
J_{ij}^{2000} (meV)	5.3016	-0.7030	0.4467	-0.1461	0.0195	-0.1338	0.0935	0.0128	-0.2222	-0.0127
Δ_{ij}^{2000} (%)	-48.5015	-55.9018	-47.2956	-156.0270	-119.6588	-61.0593	-73.1999	-108.3792	-74.6469	220.2305

TABLE 5.1: Heisenberg exchange $J_{jj}^{T_e}$ of bcc Fe, fcc Co and fcc Ni computed for the first j neighbors of a given atom i, with $j = 1...10$ at different electronic temperatures, T_e and variation of the exchange with respect to J_{ij}^{300}: $\Delta_{ij}^{T_e} = \frac{J_{ij}^{T_e} - J_{ij}^{300}}{J_{ij}^{300}}$.

	300	1000	2000	3000	$T_e = T_C$	Ref. [71]	Ref. [139]	Exp. Ref. [145]
bcc Fe	1011	1009	951	823	1007	1037	1414	1044
fcc Co	1655	1578	1225	718	1473	1250	1645	1388
fcc Ni	552	521	271		546	430	397	627

TABLE 5.2: Value of the Curie temperature, T_C, computed in the mean field approximation at different values of T_e using Eq. 5.34. For comparison, the values obtained by Halilov *et al.*[71] and by Pajda *et al.*[139] using the mean field approximation are also reported, as well as the experimental values (Exp.).

5.3.4 Remarks on the calculation of the Curie temperature

The considerations developed in this work regarding the impact of the electronic temperature on the state of the magnons were mostly ignored in the literature[71, 139]. As a consequence, not only the implementation of the DFT in these works were using more approximate methods than the FP–LAPW used in ELK, but were probably also using an electronic smearing in order to facilitate the numerical convergence without any assessment of the impact of its effect on the magnonic states. This section is therefore dedicated to a comparison of the values of T_c that we computed using the mean field approximation.

The Curie temperature is a thermodynamics quantity, *i.e.* computed at thermal equilibrium. In this particular state, the temperature of all the degrees of freedom in the material is the same. Therefore, the relevant way to compute this quantity is to set $T_e = T_C$. Tab. 5.2 shows the values of T_C we obtain in the mean field approximation and at different values of T_e, the ones obtained by Halilov *et al.*[71] and Pajda *et al.*[139] using the same approximation, as well as the experimental values. In the case of fcc Ni, as the aforementioned works, we also underestimate the value of T_C, even for $T_e = 300$ K. Nevertheless, at $T_e = T_C$, our value is, by far, closer to the experimental reality than the other authors. The impact of choosing the value of T_e correctly is better seen in the case of fcc Co, as at $T_e = 300$ K, we largely overestimate the value of T_C, whereas at $T_e = 3000$ K, we largely underestimate it. In fact, in this case choosing $T_e = T_C$ allows us to have the best agreement with the experimental reality. Finally, in the case of bcc Fe, at $T_e = 300$ K, we slightly underestimate it (by 30 K), and choosing $T_e = T_C$ does not increase too much this underestimation as the Heisenberg exchange interaction in bcc Fe is, as aforementioned, very resilient to an increase in T_e.

To conclude this section, we showed that, overall, using the mean field approximation and choosing $T_e = T_C$, we have a better agreement than previous work relying on the same approximation regarding the computation of T_C. This hints toward the fact that the ferromagnetic–paramagnetic transition in these materials is mainly due to transversal fluctuations of the magnetic moments, as opposed to a longitudinal relaxation, as discussed in Chap. 4.

5.3.5 Ultrafast reduction of the magnetization caused by a quenching of the Heisenberg exchange

In order to investigate the effect of a reduction of the Heisenberg exchange on the magnetization state, we use the Langevin atomistic LLG equation implemented as described

in Sec. 5.2.2. To isolate the contribution of this effect in the magnetization dynamics, we consider that, contrary to the rest of the literature, the temperature of the bath of the magnons, which controls the intensity of the thermal fluctuations in $\mathbf{H}^i_{\text{th}}$, remains constant during the entire dynamics and is therefore only affected by the reduction of the Heisenberg exchange.

The effect of the light–matter interaction is accounted for by a rise of the electronic energy. Then, we use the results of Chap. 4 to relate this variation of energy to a material–dependent change in temperature, which finally allows us, using the calculations of this chapter, to relate the change in electronic energy to a change in the Heisenberg exchange.

We assume that the dynamics of the variation of energy in the bath of the electrons, $\Delta E_e(t)$, obeys the equation:

$$\frac{d\Delta E_e}{dt} = -\frac{\Delta E_e}{r} + \alpha I(t). \tag{5.43}$$

Eq. 5.43 postulates that the temporal variation of energy of the electrons, $\frac{d\Delta E_e}{dt}$, is caused by the absorption of light, *i.e.* $\alpha I(t)$, where α is the absorption coefficient and $I(t)$ is the intensity of the light, and by a relaxation of the other degrees of freedom at a rate r. In the following simulations, $I(t)$ is assumed to have a temporal Gaussian profile centered at t = 500 fs with a standard deviation of 60 fs and r = 500 fs. The choice of the value of the latter is motivated by the work of You *et al.*[20], who showed that, as reviewed in Sec. 2.2.2, the dynamics of the remagnetization is governed by two timescales that are made of a quick recovery time, which they found to be 537 $\pm$ 173 fs in Ni, and a slower one. Indeed, this parameter is relevant to us as, unlike You *et al.*[20], and as discussed later in Sec. 2.2.4, we attribute the quick recovery time to the decay of the quantity of hot electrons, either due electron–phonon scattering or electronic transport. This framework is particularly robust as, unlike the use of a two–temperature model, we do not make any assumption on the electron–phonon coupling and we do not suppose that the locally deposited heat stays spatially localized, but rather, we rely on an experimental measure, which includes all these effects. However, we do make the assumption here that this decay time is also the same in bcc Fe and in fcc Co. Finally, $\alpha I(t)$ is chosen such that, for all the three compounds, the energy peaks at 0.05, 0.10, 0.15 and 0.20 eV, as shown in Fig. 5.6.

Considering that, at all time, the electronic bath is thermalized, *i.e.* obeys the Fermi distribution, we can use the results of Chap. 4 to compute T_e as a function of ΔE_e within the temperature–dependent density of states method. Fig. 5.7 shows T_e as a function of ΔE_e in fcc Ni, fcc Co and bcc Fe, as shown already in Chap. 4.

From our knowledge of $\text{T}_\text{e}\ (\Delta\text{E}_\text{e})$, as well as $\Delta\text{E}_\text{e}\ (t)$, we now compute $\text{T}_\text{e}\ (t)$ as shown in Fig. 5.8. The peaks of temperature do not rise linearly with $\Delta\text{E}_{\text{max}}$. This non–linearity is, in fact, also captured by the Sommerfeld approximation as $\Delta\text{E}_\text{e} \propto \text{T}_\text{e}^2$. Furthermore, due to their very different specific heats, for a same profile of absorbed energy, say when $\Delta\text{E}_{\text{max}}$ = 0.20 eV, the temperature rises almost twice as much in bcc Fe than in fcc Co and fcc Ni.

Then, in order to compute the non–stochastic part of the field in Eq. 5.36, which is felt by an atom i due to its Heisenberg exchange interaction with the other atoms indexed by j, writing as $\sum_j N_j J_{ij}\,(\text{T}_\text{e})$, we use the computations reported in Tab. 5.1. Fig. 5.9 shows these values for the different compounds and at different values of T_e. It reflects what has already been discussed, *i.e.* the exchange in fcc Ni is the most affected by the increase

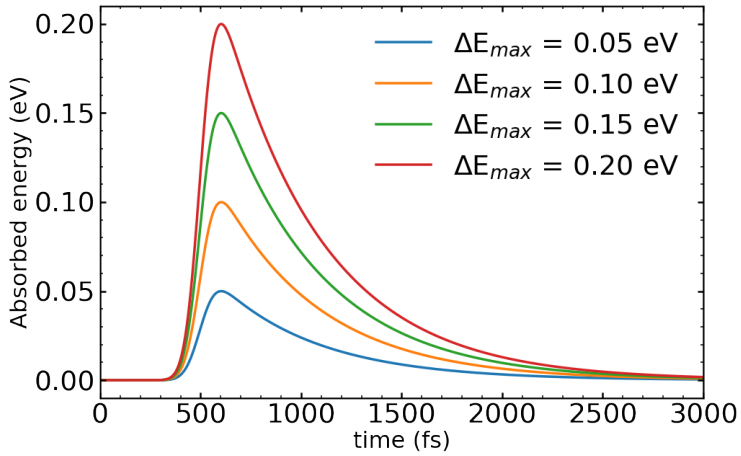


FIGURE 5.6: Variation of the electronic energy, ΔE_e, as a function of time computed using Eq. 5.43 where r = 500 fs and $I(t)$ is a Gaussian centered at 500 fs and having a standard deviation of 60 fs. $\propto I(t)$ is chosen such that ΔE_e peaks at 0.05, 0.10, 0.15 and 0.20 eV.

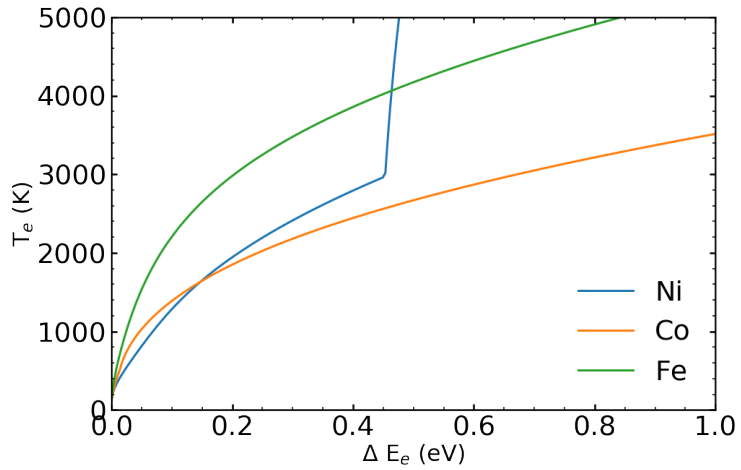


FIGURE 5.7: Electronic temperature, T_e, as a function of ΔE_e, the variation of energy in the electronic bath in fcc Ni, fcc Co and bcc Fe.

of T_e, then it is followed by fcc Co, and finally by bcc Fe, which displays an almost T_e independent value of $\sum_j N_j J_{ij}$.

Using our knowledge of $T_e(t)$ and of $\sum_j N_j J_{ij}(T_e)$, we can finally compute the time–dependent non–stochastic part of Eq. 5.36 due to the light–induced change in the interatomic Heisenberg exchange. To do so, we fit the calculated points with a third order polynomial, as shown by the dashed lines in Fig. 5.9. Fig. 5.10 shows the dynamics of $\sum_j N_j J_{ij}(t)$. When E_{max} = 0.20 eV, even though in bcc Fe, T_e reaches 3000 K, the total exchange field felt by a given atom i is only reduced by 17 %, whether a reduction of 23 % and 42 % are respectively occurring in fcc Co and fcc Ni.

Using these time–dependent exchange fields, we now use the framework developed in Sec. 5.2.2 to compute the dynamics of the magnetization. Fig. 5.11 shows the value of $M_z/M(0)$, the z component of the magnetization, as a function of time. In all the studied compounds, the effect of the reduction of the Heisenberg exchange results in a noticeable

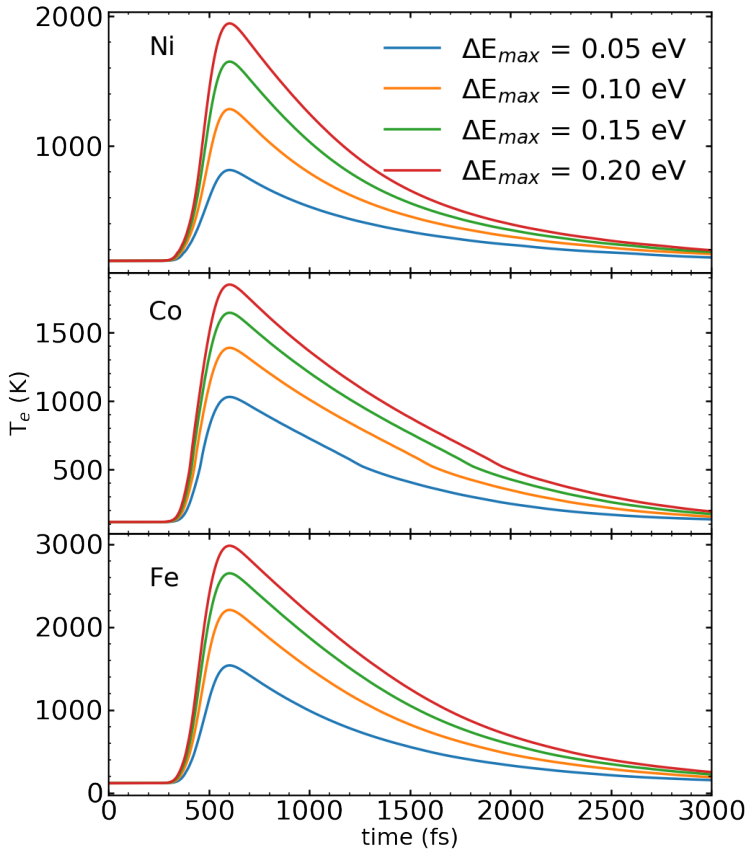


FIGURE 5.8: Electronic temperature, T_e, as a function of the time in fcc Ni, fcc Co and bcc Fe.

demagnetization. The latter is far more pronounced in fcc Ni, in which the average magnetization drops by more than 20 % when Δ E_{max} = 0.20 eV. This is due to the fact that, as seen in Fig. 5.9, it has the lowest exchange field and that it is the most sensitive to an increase of T_e. However, in the case of fcc Co and bcc Fe, whose exchange field is far more elevated, its reduction only produced demagnetization of 2 % when Δ E_{max} = 0.20 eV. Furthermore, Fig. 7.1 shows that the recovery of the magnetization closely follows the one of the Heisenberg exchange, which is due to the decay of the number of hot electrons. Indeed, as we assumed that no heat was transferred to the bath of the magnons, the magnetization goes back to its initial state in $\approx$ 700 fs. However, as argued in Sec. 2.2.4, in the case where the superdiffusive spreading of hot electrons would not be sufficient anymore to completely nullify the locally deposited heat, the recovery of the magnetization would enter a slower recovery process having a caracteristic time of $\approx$ 70 ps[20]. This could be accounted for by changing the effective temperature of the bath of the magnons.

5.4 Conclusion

Using *ab initio* calculations, we computed the magnon states in fcc Ni, fcc Co and bcc Fe at different electronic temperatures. We showed that, in all the compounds, the energy of the magnon states decreases when the electronic temperature increases, which translates in a reduction of the inter-atomic Heisenberg exchange. This phenomenon is

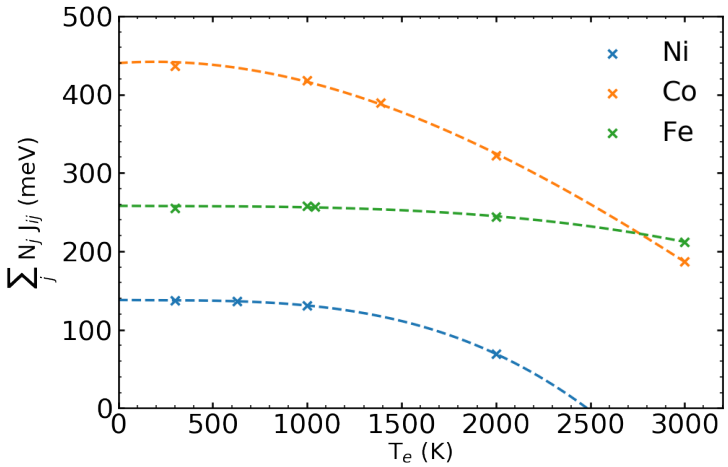


FIGURE 5.9: Value of $\sum_j N_j J_{ij}$ (T_e) in fcc Ni, fcc Co and bcc Fe as a function of the electronic temperature, where j runs over the 10 first neighbors.

the strongest in fcc Ni, then in fcc Co, and is almost absent in bcc Fe in the range of T_e studied. On this basis, we assessed the role of this reduction of exchange in the light–induced ultrafast demagnetization. To do so, we considered that the energy of the light is fully absorbed by the electrons and that no heat is then transferred to the bath of the magnons. Then, for different temporal profiles of absorbed energy, and supposing that an electronic temperature can be defined at all time, we associated this absorbed energy to a change in the interatomic Heisenberg exchange. Using Langevin atomistic Landau–Lifshitz–Gilbert calculations, we showed that this reduction of exchange can in fact lead to a large reduction of the magnetization, especially in fcc Ni.

Overall, these results challenge the usual view of the light–induced demagnetization where the reduction of the magnetization is attributed to a rise of temperature of the magnons resulting from a transfer of energy from the electrons to the former.

Further developments in this direction may involve the use of real–time time–dependent density functional theory as it allows for the computation of a real light–induced electronic state. Indeed, in this work we supposed that the electronic state was always thermalized which, for a given quantity of absorbed energy, may underestimate the effect of the reduction of exchange as compared to a light–induced electronic state. In fact, recent real–time time–dependent calculations[146] suggest that in this case the decrease in the exchange would be linear with the absorbed energy.

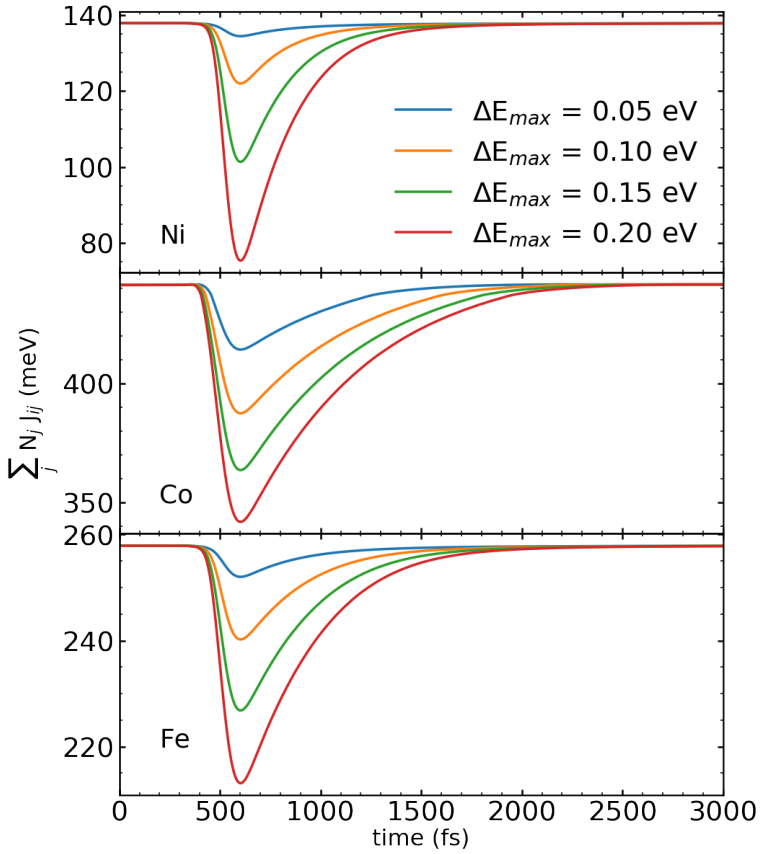


FIGURE 5.10: Dynamics of the effective mean field, $\sum_j N_j J_{ij}$ produced by the absorption

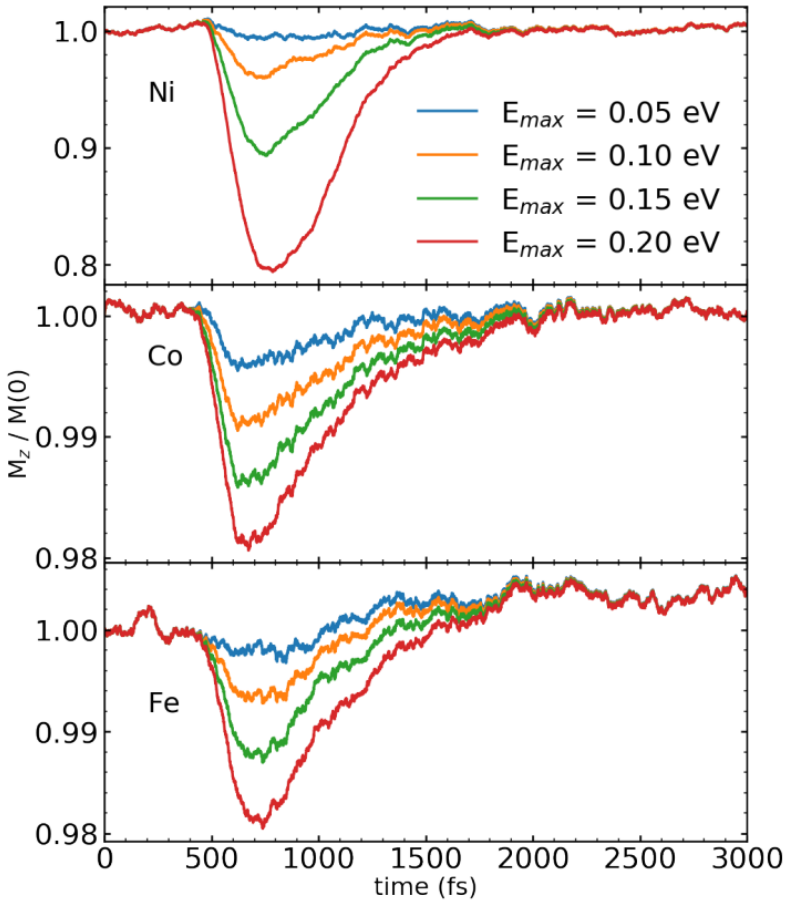


FIGURE 5.11: Dynamics of the average magnetization computed with Eq. 5.35.

Chapter 6

Ab initio theory of magnetization induced by light absorption in ferromagnets

The content of this Chapter is nearly identical to the following published work:
Ab initio theory of magnetization induced by light absorption in ferromagnets
Authors: **Philippe Scheid**, Gregory Malinowski, Stéphane Mangin, and Sébastien Lebègue
Reference: Phys. Rev. B **100**, 214402 – Published 2 December 2019

6.1 Introduction

To explain the AO–HDS, the two theoretical explanations usually invoked in the literature are the inverse Faraday effect (IFE)[6, 147, 7, 8] and a difference of absorption induced by the magnetic circular dichroism (MCD)[96, 97]. While the IFE was first introduced to describe the influence of the presence of a circularly polarized light on the magnetic state of transparent mediums[4], Battiato *et al.* showed that, without any assumption on the nature of the material, light generates a static contribution at the second order perturbation in the density matrix[101, 102], which they hold responsible for the IFE in lossy media. However, in this approach[101] the repopulation at the origin of the IFE does not grow linearly with time, as it would be the case for an absorption related phenomenon, and it fades away after the perturbation has been switched off. This fact leaves a gap between the IFE and the mechanism involved in the irreversible change of magnetization leading to the AO–HDS phenomenon[148]. Then, using this formulation and density functional theory, Berritta *et al.*[103] computed the value of this contribution for different types of materials. Conversely, the second effect, due to MCD, relies on a difference of absorption inducing a different temperature depending on the relative orientation of the magnetization and the helicity of the light. Through this thermal effect, the switching probability depends on the magnetization orientation, as shown by several parametrized models[96, 97]. Moreover, its probabilistic and absorption–based nature is in agreement with the fact that the AO–HDS phenomenon is cumulative, *i.e.* it requires multiple pulses[7], as well as a large absorptivity of the compound.

In this chapter, we demonstrate that another phenomenon occurs during the absorption of a circularly polarized light and induces a helicity–dependent magnetization in magnetic materials. Unlike the IFE which scales linearly with the intensity of the light, and therefore, fades away with it, it is a dissipative phenomenon, whose contribution grows linearly both with the intensity of the light and with time. Furthermore, as this

contribution is due to absorption, the angular momentum transferred from the light to the matter is preserved even after the light is gone, which makes it a good candidate in the explanation of the AO–HDS. Also, contrary to the statistical thermal effect discussed *supra*, this effect is purely optical.

6.2 Theory

6.2.1 Distinction between the inverse Faraday effect and the magnetization induced by light absorption

As reviewed in Sec. 2.4.4.2, in his work, Battiato *et al.*[101, 102] decomposed the first order effects induced by the light during its interaction with matter. He showed that, along with all the oscillating contributions, there is a zeroth harmonic generation, as well as an absorption–like term. The former has been attributed to the generation of the IFE, while the effect on the magnetization of the latter has, to the best of our knowledge, been left aside until this work. We name it the magnetization induced by light–absorption (MILA). To better understand the different role played by both effects, and assuming that these are the only ones inducing a magnetization in the matter, we write $M_{\text{ind}}(t)$, the magnetization induced by the light as:

$$M_{\text{ind}}(t) = \zeta_{\text{IFE}} I(t) + \zeta_{\text{MILA}} \int_0^t dt' I(t') \tag{6.1}$$

where $I(t)$ is the power of the light and ζ_{IFE} and ζ_{MILA} respectively are the magneto–optical constants characterizing the magnitude of the IFE and the MILA. As aforementioned, the contribution of the IFE is strictly proportional to the intensity, while the MILA is, as the absorbed energy, proportional to the fluence. With this simple model, we compute the time evolution of $M_{\text{ind}}(t)$ using a realistic Gaussian profile of intensity, which is shown in continuous line in Fig. 6.1 a), as well as using a gate of the same fluence, represented by the dashed line on the same figure. The latter allows for a clearer understanding of the very distinct role of the IFE and the MILA. Indeed, as pictured in Fig. 6.1 b) in dashed lines, in this case, during the period where the gate is on, the contribution of the IFE is simply a static induced magnetization, whereas the MILA, much like an absorption term, grows linearly with time. When the gate turns off, the contribution of the IFE disappears, while the dissipated magnetization remains. The continuous lines represent the IFE, the MILA, as well as the total contribution, computed with Eq. 6.1 using the Gaussian profile for the intensity. We note that, as both profiles result in the same fluence, and due to the linearity of the MILA, the resulting values of M_{HD} after the pulses are the same. Of course, both ζ_{IFE} and ζ_{MILA} depend on the material, the polarization and the direction of propagation of the light and, in case of a magnetic material, the direction of the magnetization with respect to the axis of propagation of the light. Using the framework of Battiato *et al.*, Berrita computed ζ_{IFE} using *ab initio* means. The object of the rest of this work is to compute ζ_{MILA} varying all the aforementioned parameters.

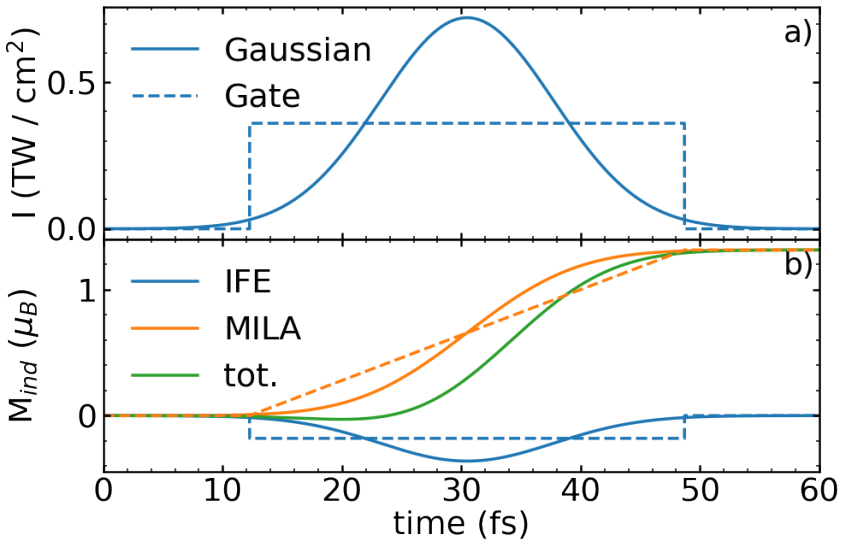


FIGURE 6.1: a) Gaussian and gate profile of the intensity. b) The continuous lines represent the contribution of IFE and the MILA to the helicity–dependent part of the magnetization dynamics, $M_{\mathrm{HD}}(t)$, as well as the total dynamics as calculated with Eq. 6.1 using $\gamma_{\mathrm{IFE}} = 0.5\mu_B/at./TWcm^2$ and $\gamma_{\mathrm{MILA}} = 0.1\mu_B/fs/at./TWcm^2$, and the Gaussian profile for the intensity of the light. The dynamics represented in dashed lines is calculated using the Gate profile for the intensity.

6.2.2 *Ab initio* computation of the absorbed magnetization

To compute the rate of transition per unit of time from the state $|\psi_{n\boldsymbol{k}}\rangle$ to $|\psi_{n'\boldsymbol{k}}\rangle$ induced by $\hat{W}$, the light–matter interaction Hamiltonian, we use the Fermi golden rule:

$$\Gamma_{n\boldsymbol{k}\to n'\boldsymbol{k}} = \frac{2\pi}{\hbar}\left|\langle\psi_{n'\boldsymbol{k}}|\,\hat{W}\,|\psi_{n\boldsymbol{k}}\rangle\right|^2 f_{n,\boldsymbol{k}}(1-f_{n',\boldsymbol{k}}) \times\left[\delta(\varepsilon_{n',\boldsymbol{k}}-\varepsilon_{n,\boldsymbol{k}}-\hbar\omega)+\delta(\varepsilon_{n',\boldsymbol{k}}-\varepsilon_{n,\boldsymbol{k}}+\hbar\omega)\right], \quad (6.2)$$

where n is the band index, $\boldsymbol{k}$ a vector of the first Brillouin zone, $f_{n\boldsymbol{k}}$ and $\varepsilon_{n\boldsymbol{k}}$ are the occupation and energy of the orbital $|\psi_{n\boldsymbol{k}}\rangle$ and ω is the pulsation of the light, where $\varepsilon_{n\boldsymbol{k}}$ and $|\psi_{n\boldsymbol{k}}\rangle$ are obtained from fully non–colinear density functional theory calculations[114, 116]. Then, the variation of the occupation number $f_{n\boldsymbol{k}}$ of the state $|\psi_{n\boldsymbol{k}}\rangle$ induced by the light writes as

$$\frac{\partial f_{n,\boldsymbol{k}}}{\partial t} = \sum_{n'}\left(\Gamma_{n'\boldsymbol{k}\to n\boldsymbol{k}} - \Gamma_{n\boldsymbol{k}\to n'\boldsymbol{k}}\right). \quad (6.3)$$

The coupling between the electrons and the electromagnetic field is expressed in the dipole approximation, *i.e.* with the Hamiltonian $\hat{W} = -\frac{q_e}{m_e}\|A\|\,\hat{\boldsymbol{p}}\cdot\boldsymbol{u}$, where $\|\boldsymbol{A}\|$ is the modulus of the potential vector of the light, $\hat{\boldsymbol{p}}$ the momentum operator acting on the wavefunctions of the electrons and $\boldsymbol{u}$ is the polarization vector of the light. We only account for vertical transition as at the considered photon energies, the wave vector of the light is small compared to the size of the Brillouin zone.

In the absence of spin–orbit coupling the Kohn–Sham orbitals are pure spin states. As $\hat{W}$ does not act on the spin part of the wavefunction, transitions between states with different spin parts are forbidden. However, $\hat{W}$ can, in the presence of spin–orbit coupling, induce transitions between electronic states having different, and even opposite magnetization. Indeed, in this case, $[\hat{H}, \hat{\sigma}_z] \neq 0$ and the Kohn–Sham orbitals are spinor states, *e.g.* they write as $\psi_{n\boldsymbol{k}}(\boldsymbol{r}) = [a_{n\boldsymbol{k}}(\boldsymbol{r}) |\uparrow\rangle + b_{n\boldsymbol{k}}(\boldsymbol{r}) |\downarrow\rangle] e^{i\boldsymbol{k}\boldsymbol{r}}$. The magnetization of such a state can be defined as $\Uparrow$ (up) when $\langle\psi_{n\boldsymbol{k}}| \uparrow\rangle \langle\uparrow |\psi_{n\boldsymbol{k}}\rangle > \langle\psi_{n\boldsymbol{k}}| \downarrow\rangle \langle\downarrow |\psi_{n\boldsymbol{k}}\rangle$ and $\Downarrow$ (down) otherwise. The coupling of two such states by $\hat{W}$ is now proportional to $\left|\langle a^{\Uparrow}_{n\boldsymbol{k}}| \boldsymbol{p}\cdot\boldsymbol{u} |a^{\Downarrow}_{n'\boldsymbol{k}}\rangle\right|^2 + \left|\langle b^{\Uparrow}_{n\boldsymbol{k}}| \boldsymbol{p}\cdot\boldsymbol{u} |b^{\Downarrow}_{n'\boldsymbol{k}}\rangle\right|^2 \geq 0$, *i.e.* transitions between $\Uparrow$ and $\Downarrow$ states are not systematically forbidden.

Assuming that the orbital magnetization is quenched, as it is the case for all of the compounds studied here; the total magnetization writes as the sum of all the electron spinor magnetization:

$$\boldsymbol{M} = \mu_B \sum_n \frac{1}{\Omega_{BZ}} \int_{BZ} \langle\psi_{n\boldsymbol{k}}| \hat{\boldsymbol{\sigma}} |\psi_{n\boldsymbol{k}}\rangle f_{n\boldsymbol{k}}\, d\boldsymbol{k}, \tag{6.4}$$

where the integral is performed over the first Brillouin zone. From Eq. 6.4, the variation of the magnetization with respect to time due to a change in occupation writes as:

$$\frac{\partial \boldsymbol{M}}{\partial t} = \mu_B \sum_n \frac{1}{\Omega_{BZ}} \int_{BZ} \langle\psi_{n\boldsymbol{k}}| \hat{\boldsymbol{\sigma}} |\psi_{n\boldsymbol{k}}\rangle \frac{\partial f_{n\boldsymbol{k}}}{\partial t}\, d\boldsymbol{k}, \tag{6.5}$$

where we neglected the time dependence of the states. The electronic eigenstates, eigenvalues and momentum matrix elements have been extracted from the full–potential, non–collinear LAPW ELK code[1]. From these, in our separate Python code we implemented the computation of all the equations presented here. A Lorentzian with a broadening of 0.27 eV has been used to smear the Dirac deltas.

6.3 Results

We now use Eq. 6.3 and 6.5 to study the magnetization induced by circularly left and right polarized light, $\sigma^+ = \frac{1}{\sqrt{2}}(1, i)^t$ and $\sigma^- = \frac{1}{\sqrt{2}}(1, -i)^t$, in the magnetic compounds fcc Ni, bcc Fe, hcp Co and FePt $L1_0$. The magnitude of the atomic magnetization is 0.6 μ_B in fcc Ni, 2.2 μ_B in bcc Fe, 1.6 μ_B in hcp Co and [3.1, 0.3] μ_B for [Fe, Pt] in FePt $L1_0$.

6.3.1 Magnetization collinear with the direction of propagation of the light

The direction of the magnetization of every atom is along the easy axis, z, and is positive for every compound, which is also set to be the direction of the propagation of the light.

Fig. 6.2 shows the calculated induced magnetization for each polarization of the light, $\frac{\partial M^{\sigma^+,\sigma^-}}{\partial t}$, as well as $\frac{\partial M^{\sigma^+}}{\partial t} - \frac{\partial M^{\sigma^-}}{\partial t}$ magnified by a factor 10. For both polarization and in each compound, the induced magnetization is opposite to the existing one. Fig. 6.2 also exhibits a dependence of the induced magnetization on the polarization of the light,

[1] Webpage: http://elk.sourceforge.net/

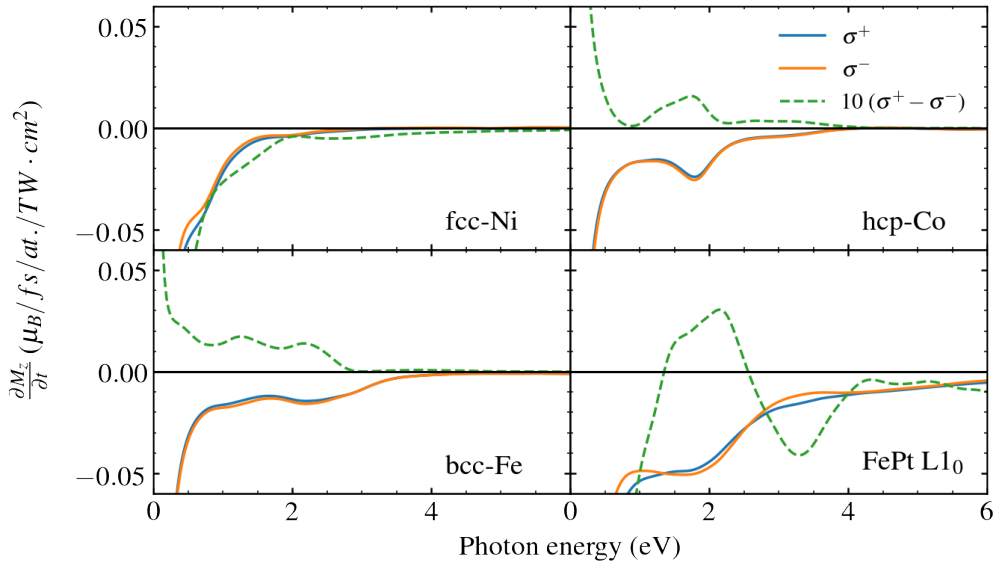


FIGURE 6.2: Continuous lines: variation of the magnetization with respect to time induced by optical transitions in fcc Ni, hcp Co, bcc Fe and FePt $L1_0$ for circularly left and right polarized light, σ^+ and σ^-. Dashed line: difference of the variation of the magnetization induced by σ^+ and σ^- polarized light with respect to time scaled by a factor 10.

which is best seen by looking at the difference of the induced magnetization by σ^+ and σ^- polarized light. Interestingly enough, for a given helicity the favored direction depends on the material, and for the same compound it can also depend on the photon energy, as evidenced in the case of FePt $L1_0$. The spin–orbit coupling also seems to play an important role in the difference of induced magnetization, as in FePt $L1_0$ it is larger than in bcc Fe. Also, this effect strongly weakens as the photon energy increases and becomes almost unnoticeable above 4 eV. This phenomenon may play a primary role in the AO–HDS, as each helicity tends to favor an opposite magnetization state.
To better understand the origin of this induced demagnetization, we define a magnetization resolved joint density of state:

$$JDOS_{\alpha'\alpha}(\omega) = \sum_n \sum_{n' \neq n} \frac{1}{\Omega_{BZ}} \int_{BZ} \Big[f_{n\boldsymbol{k}}(1 - f_{n'\boldsymbol{k}}) \times \mathcal{H}(\alpha M_{z,n\boldsymbol{k}}) \mathcal{H}(\alpha' M_{z,n'\boldsymbol{k}}) \times \left[\delta(\varepsilon_{n'\boldsymbol{k}} - \varepsilon_{n\boldsymbol{k}} - \hbar\omega) - \delta(\varepsilon_{n'\boldsymbol{k}} - \varepsilon_{n\boldsymbol{k}} + \hbar\omega) \right] \Big] \, d\boldsymbol{k}, \quad (6.6)$$

where $M_{z,n\boldsymbol{k}} = \mu_B \langle \psi_{n\boldsymbol{k}} | \hat{\sigma}_z | \psi_{n\boldsymbol{k}} \rangle$ is the value of the magnetization of a Kohn–Sham orbital $|\psi_{n\boldsymbol{k}}\rangle$, projected along the easy axis, $\mathcal{H}$ is the Heaviside distribution and α and α' can be $+$ or $-$ to select $\Uparrow$ or $\Downarrow$ states, allowing us to break down all the possible transitions into $\Uparrow$ to $\Uparrow$, $\Uparrow$ to $\Downarrow$, $\Downarrow$ to $\Uparrow$ and $\Downarrow$ to $\Downarrow$. Fig. 6.3 shows the calculated joint density of states for every compounds studied. In each case, transitions from $\Uparrow$ states to $\Downarrow$ states are dominant and the curves present a peak located at the value of the exchange splitting, which is also noticeable in Fig. 6.2. It is well explained by the fact that, as pictured in Fig. 6.4 in the case of bcc Fe, because of the exchange splitting, the states having energies below ϵ_F, the Fermi energy, are mainly $\Uparrow$, while a greater number of $\Downarrow$ states are available above ϵ_F.

For the same reason, the number of $\Uparrow$ states above ε_F is very low in comparison with the number of $\Downarrow$ states. This imbalance between the number of available transitions from $\Uparrow$ to $\Downarrow$ versus $\Downarrow$ to $\Uparrow$ and the fact that this type of excitation is made possible thanks to the presence of spin–orbit coupling, explains the systematic demagnetization.

Comparing bcc Fe with FePt $L1_0$ allows us to understand the role of the spin–mixing induced by the spin–orbit coupling. Indeed, whereas the $JDOS_{\alpha'\alpha}$ of bcc Fe and FePt $L1_0$ are similar at ≈ 2 eV, meaning that the same imbalance of available transitions from $\Uparrow$ to $\Downarrow$ states and $\Downarrow$ to $\Uparrow$ states exists, the demagnetization induced in FePt $L1_0$ is larger than in bcc Fe. This is explained by the increase of spin–orbit coupling produced by the addition of the Pt atom, which favors the spin–mixing and allows more transitions from $\Uparrow$ states to $\Downarrow$ states.

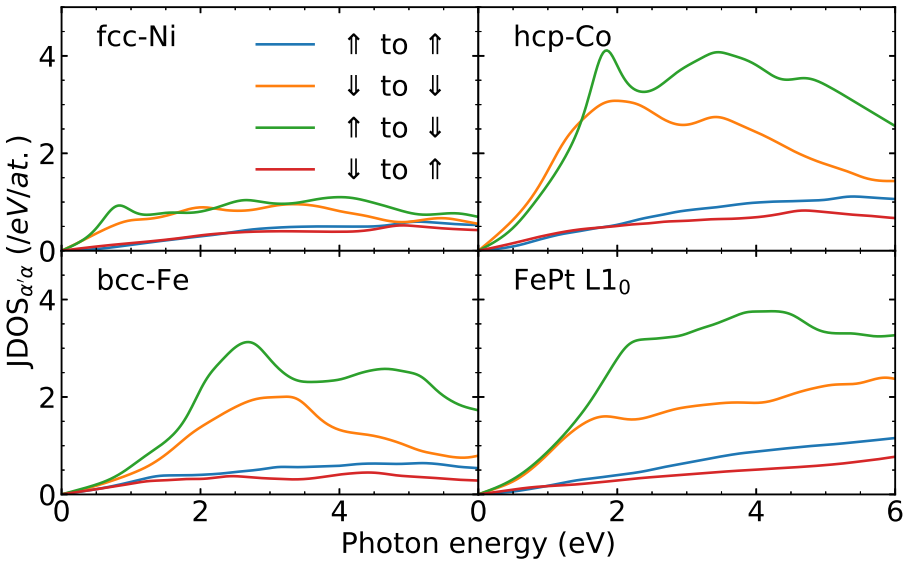


FIGURE 6.3: Joint density of states of fcc-Ni, hcp-Co, bcc-Fe and FePt $L1_0$ broken down into the different initial and final magnetic states involved, as defined in Eq. 6.6.

6.3.2 Non–collinear case

As the mechanism of AO–HDS may rely on the propagation of domain walls[57], we generalize the previous results for some directions of the magnetization, which are not collinear to the direction of propagation of the light. As sketched in Fig. 6.5, we rotate the magnetic moments of an angle θ varying from 0 to π with respect to the direction of the light propagation in the plane (1 0 0) of the conventional cells of hcp Co, bcc Fe and FePt $L1_0$ and (1 1 0) of the conventional cell of fcc Ni. For every angle, we find that $\frac{\partial \boldsymbol{M}^{\sigma^\pm}}{\partial t}$ is anti–collinear to $\boldsymbol{M}$. Therefore, the effect of the light on the magnetization can be reduced to its action on the modulus of the magnetization. These considerations are depicted in Fig. 6.5. Such a behavior strongly differs from the usual way micromagnetic simulations deal with the action of a polarized light on the magnetization, in which the induced opto–magnetic field by the IFE is along the direction of the light propagation axis[147, 97].

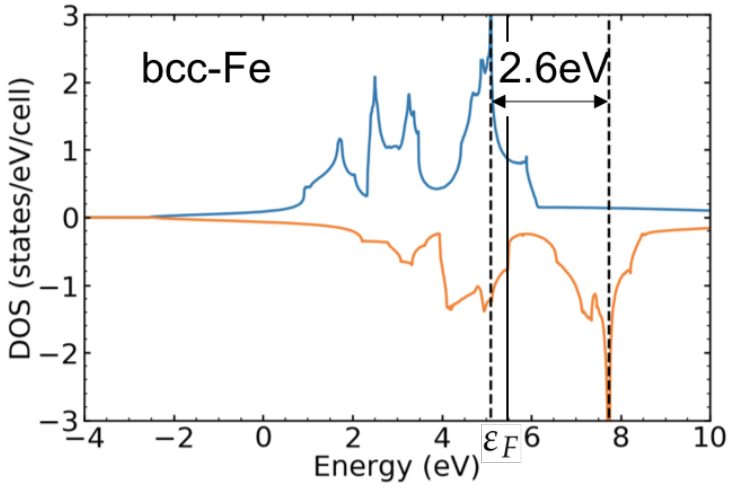


FIGURE 6.4: Majority (in blue) and minority (in orange) density of states of bcc Fe. The exchange splitting energy is represented by the vertical dashed lines.

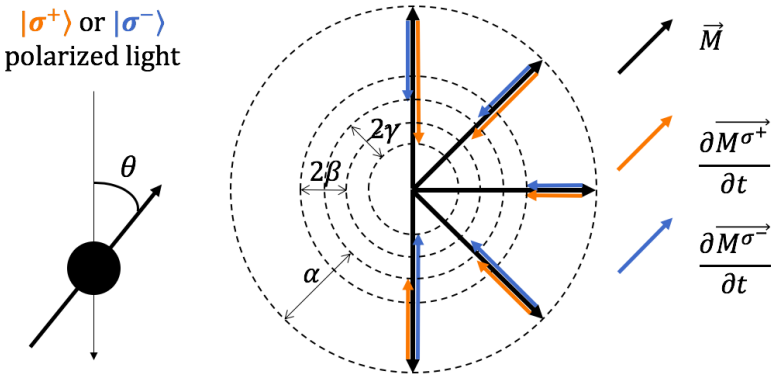


FIGURE 6.5: Sketch of the induced magnetization produced by σ^+ and σ^- polarized light per unit of time for different orientations of the magnetic moments with respect to the direction of propagation of the light. The parameters α, β and γ of the fitting law defined by Eq. 6.7 are represented.

To make our results valuable for future investigations of the AO–HDS using micromagnetic simulations[147, 97], as well as to understand the different phenomena taking place during the absorption, we fit our results with the law:

$$\frac{\partial M^{\sigma^\pm}}{\partial t} = \alpha + \beta cos(2\theta) \pm \gamma cos(\theta), \tag{6.7}$$

where $\frac{\partial M^{\sigma^\pm}}{\partial t}$ is the component of the induced magnetization per unit of time along the direction of the magnetization and α, β and γ are the fitting parameters which may be used to improve atomistic micromagnetic calculations in order to account for the light induced transition effects on the magnetization.
Each parameter has a physical meaning, allowing us to rationalize the magnetization behavior. Indeed, as evidenced in Fig. 6.6, where we fit the induced magnetization for different values of θ, the action of the light on $\boldsymbol{M}$ can, in good approximation —especially

in mono–atomic compounds—, be broken down into 3 effects. All of them are involving a different kind of angular momentum transfer induced by light. The first one, characterized by α, is helicity and angle independent. It accounts for the systematic induced demagnetization, as its sign is negative for studied compound. The second one, the magnitude and sign of which is given by β, is angle dependent, but helicity independent. It reflects the difference in the induced magnetization produced by the angle between the direction of propagation of the light and the direction of $\boldsymbol{M}$. Lastly, γ represents the amplitude and sign of the helicity–dependent part of the light–induced magnetization. It vanishes when $\theta = \frac{\pi}{2}$ and has the opposite effect when $\boldsymbol{M}$ is parallel or anti–parallel to the direction of propagation of the light.

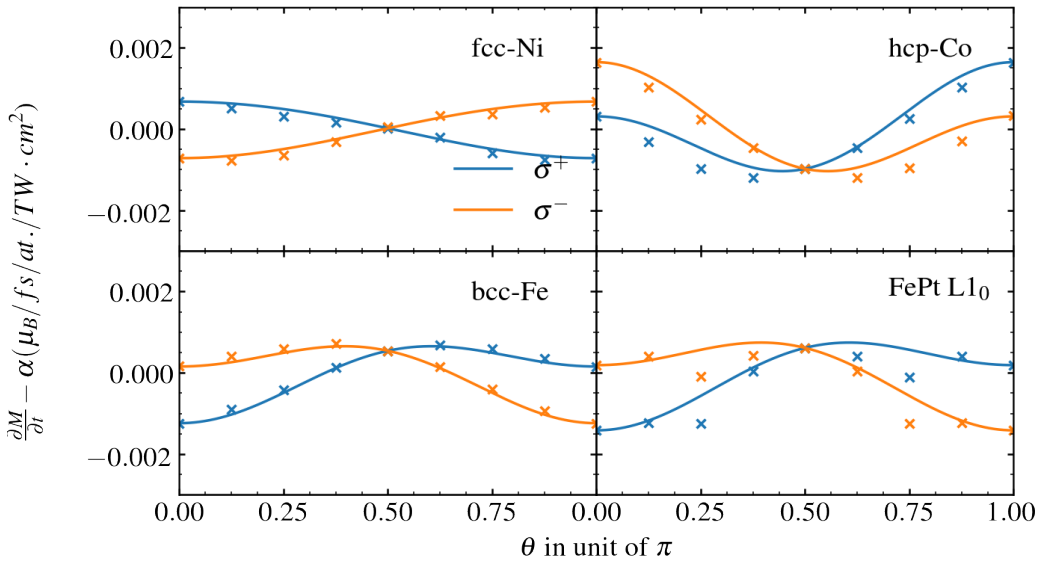


FIGURE 6.6: Markers: angle–dependent part of the magnetization induced by σ^+ and σ^- polarized photons of 1.55 eV per unit of time for different values of θ, the angle between the light propagation axis and the magnetization. Continuous lines: fit using Eq. 6.7 and the values of α, β and γ given in Tab. 6.1.

Tab. 6.1 shows the values of α, β and γ for fcc Ni, hcp Co, bcc Fe and FePt L1$_0$ calculated at a photon energy of 1.55 eV. It demonstrates that they are highly material dependent. Indeed, as previously pointed out, the values of α, characterizing the light induced demagnetization, are strongly influenced by the number of transitions from $\Uparrow$ states to $\Downarrow$ states available, as well as the presence of large spin–orbit coupling which facilitates these transitions as brought by Pt atoms in FePt L1$_0$. Furthermore, although the magnitude of the effects represented by β and γ are roughly similar, their sign depends on the compound.

(μ_B/fs/at./TW·cm^2)	α	β	γ
colrule fcc Ni	-0.00464	-0.00006	-0.00070
fcc Co	-0.02086	0.00098	0.00066
bcc Fe	-0.01233	-0.00054	0.00070
FePt $L1_0$	-0.04929	-0.00061	0.00080

TABLE 6.1: Values of the parameters α, β and γ corresponding to the law Eq. 6.7 for fcc Ni, hcp Co, bcc Fe and FePt $L1_0$ for photons of 1.55eV.

6.4 Order of magnitude of the absorbed magnetization for a realistic fluency

6.4.1 Demagnetization

Evaluating the results in Tab. 6.1 for a fluence of 5 mJ/cm^2[132] and a light propagating in the direction of the magnetization, we can compute that the induced demagnetization due to α is 3.9% of the magnetization in fcc Ni, 6.2% in hcp Co, 2.9% in bcc Fe and 15.3% in FePt $L1_0$. As this demagnetization is due to optically induced transitions only, these results may explain the early phase of the demagnetization happening during the pulse through light induced Stoner excitations. This contribution supplements the others, as *e.g.* the ultrafast generation of magnons, whose roles are still heavily debated[5, 149, 107, 28, 29, 21] in the explanation of the ultrafast light induced demagnetization. However, unlike other mechanisms where the angular momentum has to be transferred to other baths, such as phonons through Elliott–Yafet scattering[132] or the ultrafast Einstein–De Haas effect[64], these Stoner excitations are directly induced by light and no other dissipation channel is required to allow a spin–flip.

6.4.2 Helicity–dependence

We now evaluate the difference of induced magnetization between both helicities, characterized by the parameter γ in Tab. 6.1. This difference amounts to 1.0% of the magnetization in fcc Ni, 0.4% in hcp Co, 0.3% in bcc Fe and 0.5% in FePt $L1_0$. These rather small values are in agreement with the experimental fact that the AO–HDS is a cumulative effect, *i.e.* multiple pulses are needed to achieve a switching[8]. Moreover, unlike the inverse Faraday effect, the induced magnetization is preserved after the light is gone. As a consequence, much like the thermal effect induced by the MCD[97], this difference of induced magnetization can affect the dynamics on time scales longer than the pulse duration, and progressively favor one magnetic state over the other.

6.5 Conclusion

In conclusion, by considering the role of absorption, our results shine a new light on the all–optical helicity–dependent switching, as much as they raise new questions on the nature of the underlying mechanism(s). Indeed, we demonstrated that light induced transitions affect the magnetization state of the ferromagnets fcc Ni, hcp Co, bcc Fe and FePt

$L1_0$. Due to the exchange splitting and the presence of spin–orbit coupling, transition from majority spin states to minority spin states are dominant and, as a direct consequence, light always induces a demagnetization.
Furthermore, our *ab initio* calculations showed that one helicity of the light tends to demagnetize more than the other. The favored magnetic state depends on both the material and the photons energy. Extending our computation to cases where the light does not propagate along the magnetization axis, we showed that an opto–magnetic field, commonly used in micromagnetic calculation, cannot account for this effect, and we derived a set of parameters, which can be used instead. As the inverse Faraday effect and the difference of absorption due to MCD, the phenomenon described here may play an essential role in the AO–HDS[8, 7], in the HD domain wall motion[57], as well as in the HD demagnetization[60]. A further assessment of the magnitude of this effect using real–time time–dependent density functional theory[106] is planned. It will allow us to study the full response of the electronic system to a realistic circularly polarized light pulse.

Chapter 7

RT–TDDFT study of helicity dependent light–induced demagnetization: from the optical regime to the XUV

As of the 5th of July, this chapter will soon be submitted for publication.

7.1 Introduction

While the origin of the AO–HDS is still debated[96, 97], it is assumed that the dominating contribution comes from the inverse Faraday effect (IFE), originally predicted by Pitaevskii [3] in non–dissipative and non-magnetic medium. He found that circularly polarized light induces a magnetization proportional to the intensity of the light–source at any time and, as a consequence, its contribution to the magnetization dynamics vanishes with the intensity of the light. This effect was recently revisited[101, 102] and evaluated in different absorptive compounds[103] using *ab initio* means. As seen in Chap. 6, another effect, occurring simultaneously to the IFE in dissipative materials, is the magnetization induced during light absorption (MILA), whose magnitude is proportional to the fluence of the light. Consequently, and very differently from the IFE, its impact on the magnetization persist even after the presence of the light.

Recently, real–time time–dependent density functional theory (RT–TDDFT) has been successfully applied to describe the linearly-polarized laser induced demagnetization[107, 108], and predicted a new phenomenon occurring during the early dynamics based on optical intersite spin–transfer[121, 150, 112], which has later been experimentally confirmed[110, 109, 151]. Based on the success of RT-TDDFT, in the present work we investigate the dynamics of the magnetization density under the influence of circularly polarized pump pulses. The main aim of the work is to study the dependence of spin-dynamics on the helicity of the pump pulse in transition metals (TM) fcc Ni, fcc Co and bcc Fe. To this end we investigate the effect of left and right circularly polarized light of two different kind– (a) optical pulses of frequency 1.55eV and (b) XUV pulses that resonate with the $3p$ states of Fe, Co and Ni. We find that, in both cases, the induced spin–dynamics is helicity–dependent, and, that this helicity–dependence is larger when using a XUV light. The origin of this helicity–dependence is closely assessed by examining the spin–resolved time–dependent density of states. Then, we separate contribution of the IFE and the MILA in the helicity–dependent part of the magnetization dynamics and show that the latter has, especially in the XUV regime and when the light pulse vanishes, a larger impact.

7.2 Theory

The calculations are performed in two steps: first the ground state of the system is calculated using density functional theory[114, 116]. RT–TDDFT is then used to time propagate this ground-state under the influence of a pump pulse, which is treated as an external vector potential. These calculations are performed with the non–collinear full potential linearized augmented-plane-wave method[119], including spin–orbit coupling term, as implemented in the ELK code[1]. The Brillouin zone is sampled with a 20x20x20 mesh for each system and states up to 90eV above the Fermi energy are included. Within RT–TDDFT[106] the dynamics of the Kohn-Sham spinors is evaluated using:

$$i\frac{\partial \phi_{n\mathbf{k}}(\mathbf{r},t)}{\partial t} = \Big(-\frac{1}{2}\nabla^2 - \frac{i}{c}\mathbf{A}_{ext}(t)\cdot\nabla + v_s(\mathbf{r},t) + \frac{1}{2c}\boldsymbol{\sigma}\cdot\mathbf{B}_{xc}(\mathbf{r},t) - \frac{1}{4c^2}\boldsymbol{\sigma}(\nabla v_s(\mathbf{r},t)\times i\nabla)\Big)\phi_{n\mathbf{k}}(\mathbf{r},t). \quad (7.1)$$

In this equation $\phi_{n\mathbf{k}}(\mathbf{r},t) = \langle \mathbf{r}|n\mathbf{k}(t)\rangle$ is a two–component spinor Bloch orbital indexed by $\boldsymbol{k}$, a vector of the first Brillouin zone and n the band index, $\mathbf{A}_{ext}$ is the vector potential of the light, $\boldsymbol{\sigma}$ are the Pauli matrices, $\boldsymbol{B}_{xc}(\boldsymbol{r},t)$ is the exchange correlation magnetic field, $v_s(\boldsymbol{r},t)$ is the effective Kohn-Sham potential and is the sum of the external potential, $v_{ext}(\boldsymbol{r},t)$, the Hartree potential, $v_H(\boldsymbol{r},t)$, and the exchange correlation potential, $v_{xc}(\boldsymbol{r},t)$. To compute the exchange correlation potential, we use the noncollinear[152] adiabatic local spin density approximation. The magnetization, which is treated as a fully unconstrained vector field, can be evaluated using:

$$\boldsymbol{M}(t) = \mu_B \sum_n \frac{1}{\Omega_{\mathrm{BZ}}} \int_{\mathrm{BZ}} d\mathbf{k}\, \langle n\mathbf{k}(t)|\hat{\boldsymbol{\sigma}}|n\mathbf{k}(t)\rangle\, f_{n\mathbf{k}} \quad (7.2)$$

where $f_{n\boldsymbol{k}}$ is the occupation of the state $|n\mathbf{k}\rangle$ defined by the initial state of the Kohn-Sham system, μ_B is the Bohr magneton and Ω_{BZ} is the volume of the first Brillouin zone.

The last term in Eq. 7.1 is the spin–orbit coupling. Without it, $\boldsymbol{\sigma}$ would commute with the Hamiltonian and the magnetization would remain constant during the dynamics, as shown in Ref. [107]. The time propagation is done using the algorithm detailed in Ref. [121] with a time-step of 2.4 as.

7.3 Results

The dynamics of the charge and spin density of bcc Fe, fcc Co and fcc Ni are evaluated under the action of circularly polarized laser pulses having a Gaussian intensity profile of FWHM = 25 fs and an incident fluence of 13.11 mJ/cm^2. Simulations were performed with an optical pulse of frequency of 1.55 eV and and XUV pulses resonating with the lowest lying $3p$ states. The pump pulse propagates along the direction of the average magnetic moment, which we chose to be along the z-axis.

[1] http://elk.sourceforge.net/

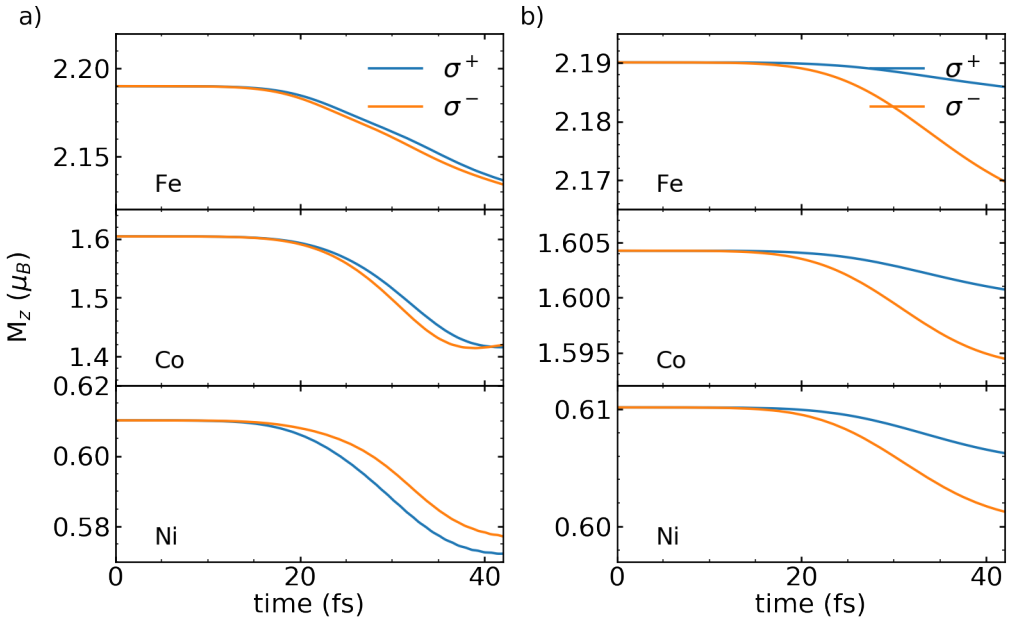


FIGURE 7.1: RT–TDDFT dynamics of the z component of the magnetization, M_z, calculated for bcc Fe, fcc Co and fcc Ni performed at 1.55 eV (a)) and in the XUV range (b)).

7.3.1 Longitudinal dynamics of the magnetization

Fig. 7.1 a) and b) show that, as linear pump pulses[107], circular pump-pulses also lead to a spin–orbit coupling mediated demagnetization as seen in Chap. 7 and in Ref. [153]. We find that for a fixed incident fluence, the demagnetization is more pronounced when using an optical pump pulse, rather than a XUV one. The helicity–dependent magnetization dynamics can also be clearly seen in Fig. 7.1; for an optical pulse, with the exception of Ni, demagnetization induced by σ^- is larger than σ^+. This particular behavior of Ni was also noted in Chap. 6. For XUV pulses, σ^- always leads to a larger demagnetization than its counterpart for all materials. As expected, the difference of demagnetization between the two helicities is much more pronounced for XUV pulses, as compared to the optical pulse.

7.3.2 Origin of the difference of dynamics induced by an optical and a XUV light

These results pose two interesting questions (i) why a larger demagnetization is produced by optical as compared to XUV pulse? and (ii) why the helicity–dependence is more pronounced for XUV pulses than for optical pulses? In order to understand this, we now proceed to the computation of the transient spin–resolved occupied density of states (oDOS) defined as[150]:

$$\text{oDOS}^{\sigma}(\varepsilon, t) = \frac{1}{\Omega_{BZ}} \sum_{n} \int_{\Omega_{BZ}} d\mathbf{k} \left[f_{n\mathbf{k}} \cdot \langle n\mathbf{k}(t)|\sigma\rangle \langle \sigma|n\mathbf{k}(t)\rangle \, \delta(\varepsilon_{n\mathbf{k}}(t) - \varepsilon) \right], \tag{7.3}$$

where ε is the energy, t is the time, $\varepsilon_{n\boldsymbol{k}}$ is the eigenvalue associated to the Bloch eigenstate $|n\boldsymbol{k}\rangle$ and σ is indexing the spin state, which, for a collinear system will be $\uparrow$ or $\downarrow$.

Fig. 7.2 a), b), c) and d) show the changes in oDOS in bcc Fe, *i.e.* $\text{oDOS}^{\sigma}(t = 32\text{fs}) - \text{oDOS}^{\sigma}(t = 0\text{fs})$, for a σ^+ and a σ^- polarization of an optical and a XUV pulse. In both cases, this quantity decreases below the ground-state Fermi level (0 eV) and increases above it, *i.e.* electrons are getting excited and start occupying empty states. Upon comparison of Fig. 7.2 a) and b) with d) and e), the question (i) immediately answers itself; the magnitude of change in the oDOS is almost 25 times larger for both helicities of the optical light, as opposed to the XUV one, *i.e.* the optical pulse is more absorbed than the XUV pulse. Consequently, and as explained in Chap. 6, this leads to a larger number of excited electrons going from the majority states to the minority states, which are preponderant above the Fermi energy, and hence lead to a larger demagnetization by the optical pulse.

In order to answer question (ii) let us first recall that dipolar coupling imposes that transitions induced by a $\sigma^{\pm}$ polarized light satisfy $\Delta j = \pm 1$ for $\sigma^{\pm}$, and $\Delta m_j = \pm 1$, where j is the total angular momentum. However, in solids, valence electrons rearrange themselves to form bonds and j is not a good quantum number anymore. Nevertheless, $3d$ states, more localized, and especially $3p$ semi–core states, do not hybridize as much and the aforementioned helicity–dependent selection rules may, at least partially, apply. To confirm this, in Fig. 7.2 c) and f) we look at the change in spin–integrated DOS produced by the two different helicities after 32 fs: $\text{oDOS}_{\Delta\text{hel.}} = \text{oDOS}_{\sigma^+}(t = 32\text{fs}) - \text{oDOS}_{\sigma^-}(t = 32\text{fs})$. In the optical range, the helicity–dependent effects are, in fact, the strongest were the DOS peaks (see the total DOS in Fig. 6.4). Indeed, these peaks reveal the presence of $3d$ states, for which the aforementioned helicity–dependent selection rules apply more. This difference is 5 times more pronounced in the XUV range, involving the $3p$ semi–core states, whose negligible dispersion is evidenced by the sharpness of the peaks they exhibit in the DOS. This answers question (ii).

7.3.3 Magnitude of the helicity–dependence

To further highlight this difference in HD dynamics from two different kinds of pulses we decompose $M_z^{\sigma^{\pm}}(t)$ in a helicity–independent and a helicity–dependent part as:

$$M_z^{\sigma^{\pm}}(t) = M_{\text{HI}}(t) \pm M_{\text{HD}}(t), \tag{7.4}$$

where $M_z^{\sigma^{\pm}}(t)$ is the z component of the time–dependent magnetization, which dynamics is triggered by a circularly left (σ^+) or right (σ^-) polarized light. The helicity–independent part writes as $M_{\text{HI}}(t) = \frac{1}{2}\left(M_z^{\sigma^+}(t) + M_z^{\sigma^-}(t)\right)$ and the helicity–dependent part as $M_{\text{HD}}(t) = \frac{1}{2}\left(M_z^{\sigma^+}(t) - M_z^{\sigma^-}(t)\right)$. Using this framework, we define:

$$\zeta(t) = \frac{|M_{\text{HD}}(t)|}{M_{\text{HI}}(0) - M_{\text{HI}}(t)}, \tag{7.5}$$

representing the relative magnitude of the HD effect over the HI one.[2]. Fig. 7.3 b) and d) are plots of ζ as a function of time for both types of pulses. They evidence that HD effects are more than twice as large in the XUV range than at 1.55 eV. Moreover, while in the optical regime ζ tends to be attenuated by the complex dynamics of the

[2]Both $M_{\text{HD}}(t)$ and $M_{\text{HI}}(t)$ have been convoluted with a Gaussian having a standard deviation of 2fs

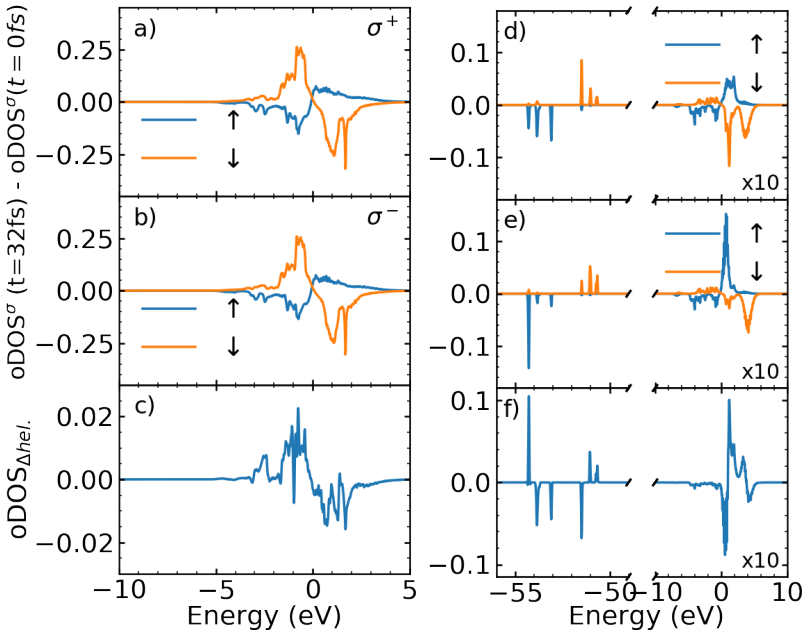


FIGURE 7.2: a), b) d), e): Variation of the spin and occupation resolved density of states, $\mathrm{oDOS}^{\sigma}(t = 32\mathrm{fs}) - \mathrm{oDOS}^{\sigma}(t = 0\mathrm{fs})$ in bcc Fe, induced by a σ^+ (a) and d)) and a σ^- (b) and e)) polarization of the light induced after 32 fs using an optical (a) and b)) and a XUV light (d) and e)). c), (f)): Difference of the total density of states induced by a σ^+ and a σ^- polarized light, $\mathrm{oDOS}_{\Delta\mathrm{hel.}} = \mathrm{oDOS}_{\sigma^+}(t = 32\mathrm{fs}) - \mathrm{oDOS}_{\sigma^-}(t = 32\mathrm{fs})$, after 32 fs computed at 1.55 eV (in the XUV range). The right side of d), e) and f) is magnified by a factor 10.

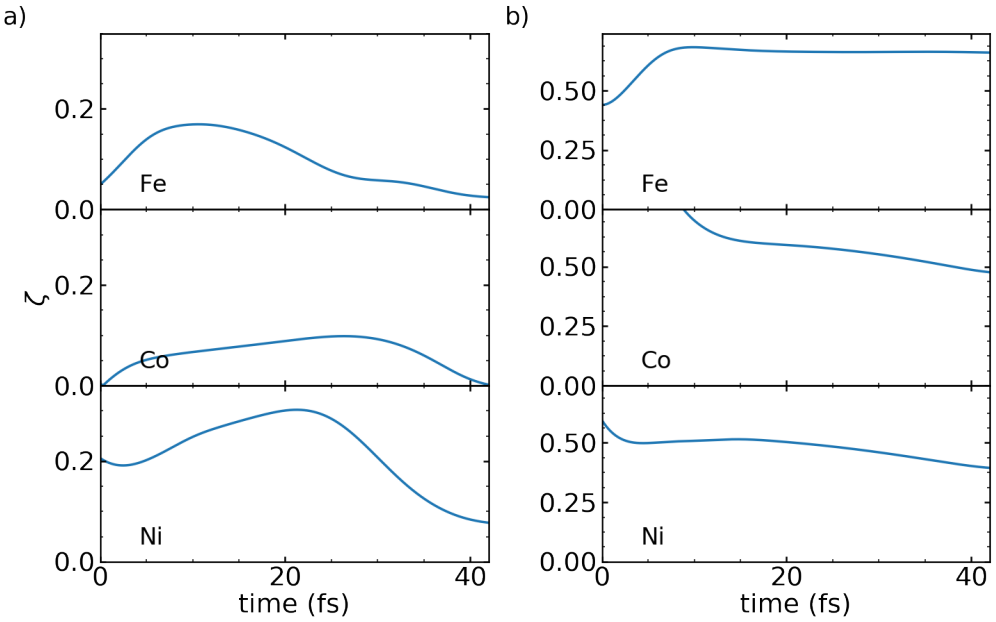


FIGURE 7.3: Magnitude of the helicity–dependent dynamics over the helicity–independent one, ζ, at 1.55 eV (a)) and in the XUV range (b))

interacting electronic density, the light–induced helicity–dependence is maintained over a longer course of time in the XUV regime.

7.3.4 Inverse Faraday effect versus magnetization induced during light absorption

In the past, there has been discussion about the factors that lead to HD dynamics. The two main candidates have been identified to be the IFE and the MILA. This analysis has been done assuming that the magnetic response of the system is dominated by linear order in perturbation. This is not the case in our work, as we demonstrated above. However, in order to comment on the relative importance of these contributions we still perform the following analysis.

Following the decomposition of Battiato *et al.*[101, 102] it can be shown that $M_{\mathrm{HD}}(t)$ is composed of a transient signal, oscillating parts, the absorptive contribution which leads to MILA, and the zeroth harmonic which leads to the IFE[3, 101, 102, 103]. To remove the oscillatory and transient contributions which together time–average to 0, we perform a convolution of M_{HD} with a Gaussian having a root mean square of 2 fs. This allows us to decompose the HD part of the magnetization dynamics into:

$$\begin{aligned} M_{\mathrm{HD}}(t) \approx & M_{\mathrm{I}}(t) + M_{\mathrm{F}}(t) \\ = & \gamma_{\mathrm{I}} I(t) + \gamma_{\mathrm{F}} \int_0^t dt' I(t') \end{aligned} \tag{7.6}$$

where $I(t)$ is the power of the light and γ_{I} and γ_{F} are respectively characterizing the magnitude of the HD effect proportional to the intensity, such as the zeroth harmonic generation, and to the fluence, such as the absorption. Within this framework, the contribution of both effects in M_{HD} is uniquely defined by:

$$\gamma_{\mathrm{I}} = \frac{\frac{\partial}{\partial t}\left(\frac{M_{\mathrm{HD}}(t)}{\int_0^t dt' I(t')}\right)}{\frac{\partial}{\partial t}\left(\frac{I(t)}{\int_0^t dt' I(t')}\right)} \tag{7.7}$$

and

$$\gamma_{\mathrm{F}} = \frac{\frac{\partial}{\partial t}\left(\frac{M_{\mathrm{HD}}(t)}{I(t)}\right)}{1 - \frac{\frac{\partial}{\partial t} I(t)}{I^2(t)} \int_0^t dt' I(t')}. \tag{7.8}$$

The individual contributions of $M_{\mathrm{I}}(t)$ and $M_{\mathrm{F}}(t)$ to the total magnetization density are shown in Fig. 7.4 for bcc Fe, fcc Co and fcc Ni. In the case of optical pump pulse, the magnitudes of both effects (MILA and IFE) are similar during the pulse.

The part of the helicity–dependent dynamics due to the absorption, M_{F}, can be compared to the previous the results obtained in Chap. 6, and, as seen in the insets of Fig. 7.4 a), we find that at the early stages of the dynamics, where the linear regime is dominant, both the signs and the magnitudes are in agreement.

In the XUV range, the dynamics is dominated by the absorption (MILA), *i.e.* $M_{\mathrm{HD}} \approx M_{\mathrm{F}}$. Consequently, the difference of magnetization length induced by the XUV light will mostly persist even after its intensity has decreased and a large ζ is obtained at all time, as compared to the optical case (see Fig. 7.3).

7.4 Conclusion

In conclusion, using real–time time–dependent density functional theory, we evidenced the presence of a helicity–dependent magnetization dynamics in fcc Ni, fcc Co and bcc Fe characterized by a difference of longitudinal relaxation. We found that this helicity–dependence is particularly strong when exciting the more localized 3p states. Indeed, by closely examining the time–dependent density of states, we found that the helicity–dependence of the dynamics is enhanced for localized states. Then, we disentangled the role of the two main first order effects which may be held responsible for the helicity–dependence, *i.e.*: the inverse Faraday effect and the magnetization induced during the absorption of the light. We found that the latter has a far greater impact than the former on the overall dynamics, especially in the XUV range and after the light is gone.

These results also have wide experimental implications and may be responsible for the helicity–dependent demagnetization evidenced by Tsema *et al.*[60] and Quessab *et al.*[61]. Furthermore, the dynamics reported here may also play a role in the AO–HDS[7, 8], as well as the helicity–dependent domain wall motion[57]. Finally, we hint toward the possibility of enhancing the efficiency of all the aforementioned phenomena by going out of the optical range and involving localized core and semi–core states, allowing for a stronger helicity–dependent dynamics due to the angular momentum absorption effect.

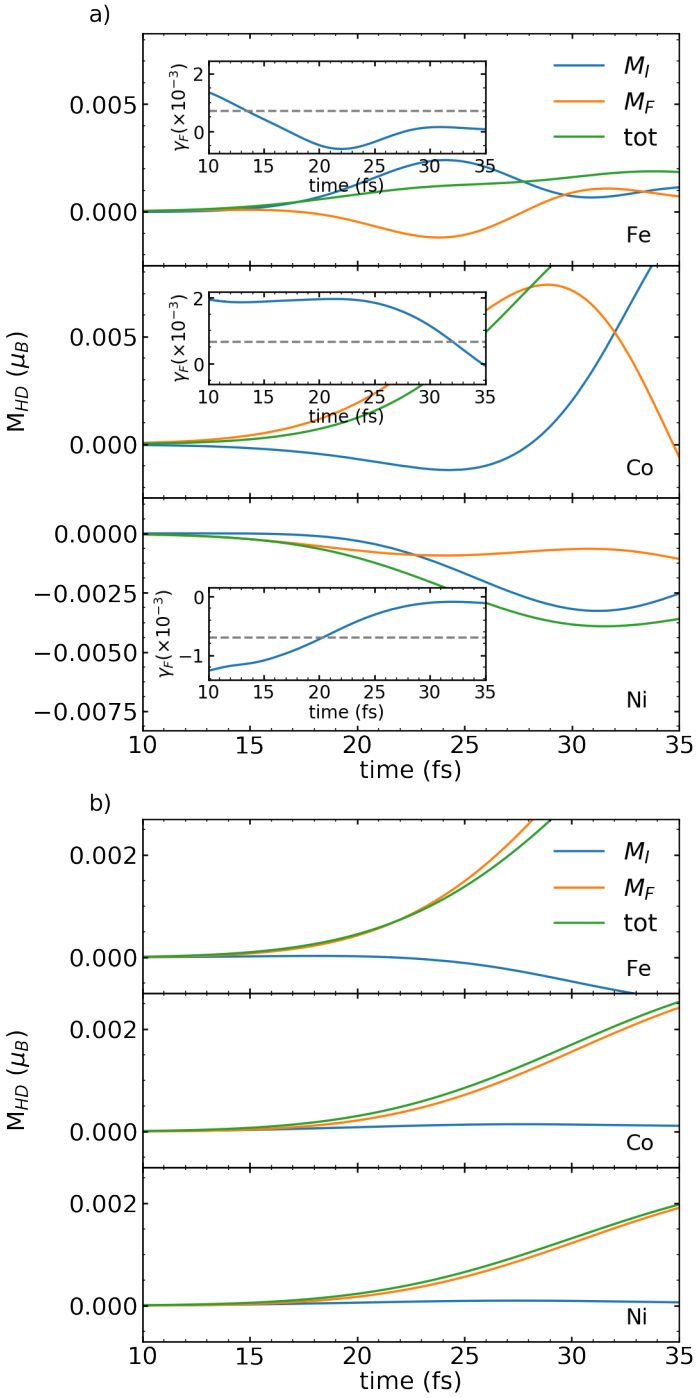


FIGURE 7.4: Zeroth harmonic (M_I) and absorption (M_F) part of the helicity–dependent dynamics calculated with Eq. 7.6, where M_{HD} is induced by a light of 1.55 eV (a)) and in the XUVs (b)). The dashed lines in a) represent the contribution to the dynamics of the angular momentum absorption effect, calculated in Chap. 6.

Chapter 8

Conclusion

This thesis has brought contributions to the theoretical understanding of both the light–induced demagnetization (Chap. 4 and 5) and the all–optical helicity–dependent switching (Chap. 6 and 7).

In Chap. 4 the electronic properties of Fe, Co, Ni and FePt $L1_0$ were studied using *ab initio* density functional theory for a wide range of the electronic temperature. We were able to compute the Stoner temperature, T_S, at which the intra–atomic exchange splitting, and thus, the atomic magnetic moment disappears for all the compounds. We found values largely higher than the Curie temperatures of the different compounds. However, this does not come as a surprise as, above T_C, the materials become Langevin paramagnets and not Stoner paramagnets, *i.e.* all the atoms are still carrying a magnetic moments, but these are randomly directed. The values of T_S are found to be correlated with the magnitude of the largest atomic magnetic moment in the cell.
Furthermore, the loss of magnetic moment carries its footprints on both the electronic energy and the specific heat. Such effects have been ignored in previous studies[63, 132] and induce large deviations from the Sommerfeld approximation and the temperature independent DOS approximation, even at relatively low electronic temperature.
These results evidence the fact that the Sommerfeld approximation is not sufficient to obtain a correct temperature dynamics in the 2–3 temperature model, commonly used to describe ultrafast and intense light-matter interactions. Finally, the Stoner temperatures we obtained are, except in the case of fcc-Ni, too high to be reached without destroying the compound. This is in agreement with the experimental fact that, the ultrafast demagnetization mainly originates from transversal excitations, *i.e.* the ultrafast generation of magnons, rather than a longitudinal decrease of each atomic magnetic moment.

In Chap. 5, using *ab initio* calculations, we computed the magnon states in fcc Ni, fcc Co and bcc Fe at different electronic temperatures. We showed that, in all the compounds, the energy of the magnon states decreases when the electronic temperature increases, which translates in a reduction of the inter-atomic Heisenberg exchange. This phenomenon is the strongest in fcc Ni, then in fcc Co, and is almost absent in bcc Fe in the range of T_e studied. On this basis, we assessed the role of this reduction of exchange in the light–induced ultrafast demagnetization. To do so, we considered that the energy of the light is fully absorbed by the electrons and that no heat is then transferred to the bath of the magnons. Different temporal profiles of absorbed energy were computed and then, supposing that an electronic temperature can be defined at all time, this absorbed energy was associated to a change in the interatomic Heisenberg exchange. Using Langevin atomistic Landau–Lifshitz–Gilbert calculations, we showed that this reduction

of exchange can in fact lead to a large reduction of the magnetization, especially in fcc Ni.

In Chap. 6, by considering the role of absorption, our results shine a new light on the all–optical helicity–dependent switching, as much as they raise new questions on the nature of the underlying mechanism(s). Indeed, we demonstrated that light induced transitions affect the magnetization state of the ferromagnets fcc Ni, hcp Co, bcc Fe and FePt $L1_0$. Due to the exchange splitting and the presence of spin–orbit coupling, transition from majority spin states to minority spin states are dominant and, as a direct consequence, light always induces a demagnetization.
Furthermore, our *ab initio* calculations showed that one helicity of the light tends to demagnetize more than the other. The favored magnetic state depends on both the material and the photons energy. Extending our computation to cases where the light does not propagate along the magnetization axis, we showed that an opto–magnetic field, commonly used in micromagnetic calculation, cannot account for this effect, and we derived a set of parameters which can be used instead. As the inverse Faraday effect and the difference of absorption due to MCD, the phenomenon described here may play an essential role in the AO–HDS[8, 7], in the HD domain wall motion[57], as well as in the HD demagnetization[60].

In Chap. 7 using real–time time–dependent density functional theory, we further evidenced the presence of a helicity–dependent magnetization dynamics in fcc Ni, fcc Co and bcc Fe characterized by a change in the magnitude of the magnetic moment carried by each atom. We found that this helicity–dependence is particularly strong when exciting the more localized 3p states. Indeed, by closely examining the time–dependent density of states, we found that the helicity–dependence of the dynamics is enhanced for localized states. Then, we disentangled the role of the two main first order effects which may be held responsible for the helicity–dependence, *i.e.*: the inverse Faraday effect and the magnetization induced during the absorption of light (Chap. 6). We found that the latter has a far greater impact than the former on the overall dynamics, especially in the XUV range and after the light is gone. These results also have wide experimental implications for the helicity–dependent demagnetization evidenced by Tsema *et al.*[60] and Quessab *et al.*[61]. Furthermore the dynamics reported here may also play a role in the AO–HDS[7, 8], as well as the helicity–dependent domain wall motion. If such is the case, we hint toward the possibility of enhancing the efficiency of all the aforementioned phenomena by going out of the optical range and involving localized core and semi–core states, allowing for a stronger helicity–dependent dynamics mainly due to the magnetization induced by light absorption evidenced in Chap. 6.

All the aforementioned results open the way to many possible developments.
For instance, in Chap. 5 we showed that a rise of the electronic temperature leads to a decrease of the interatomic Heisenberg exchange. However, this is assuming that the electronic bath remains thermalized at all time, which is obviously not the case experimentally as hot electrons originate from the excitation of the light. It is very likely that such a non–thermodynamical distribution would have a larger impact on the interatomic Heisenberg exchange. Within this framework, the demagnetization induced by a loss of

Heisenberg exchange could be far greater than what we predicted in Chap. 5. Furthermore, as seen in Chap. 6 and 7, as the electronic excitation depends on both the polarization and the frequency of the light–pulse, one may expect the same features regarding the behavior of the interatomic Heisenberg exchange. This may lead to the discovery of new phenomena as, *e.g.*, the possibility of controlling this exchange using only the polarization of the light. Real–time time–dependent density functional theory is a tool of choice to theoretically investigate this new area.
Another path of improvement regards the real–time time–dependent density functional theory itself. Indeed, the current limits of this theory are numerous. For instance, as of yet, it does not allow for a realistic simulation of the experimental reality as the electronic system is completely closed. As a consequence, if a given excitation of the electrons is produced, it will persist *ad vitam*, whether in reality the electronic bath would release energy and information to external degrees of freedom and relax back to a thermodynamic distribution. These external degrees of freedom are composed of the photons and, in periodic solids, the phonons and the magnons. The former correspond to excitations of the lattice, while the latter are transversal excitations of the magnetic moments. However, the inclusion of these new degrees of freedom is limited by the fact that the periodicity of the system restricts the possible range of excitations as, for both the magnons and the phonons, accounting for long wavelength modes would require us to work with large supercells. Furthermore, even if we had the capabilities of doing so, it is not obvious how to account for the fluctuation–dissipation theorem within such a framework. Indeed, its fulfillment is necessary in order to have thermalized degrees of freedom in the static case. Finally, while both the inverse Faraday effect and the magnetization induced during light absorption can now be theoretically assessed, evaluating their respective experimental magnitude remains impossible. This possibility is particularly interesting as the gap between the experimental and computational realities remains important, especially as the experiments use thin films with different crystalline and interface qualities. However, as both of these phenomena originate from the first order response of a material to an electromagnetic field, these quantities should be expressible in term of the dielectric tensor. Knowing the latter expression and using pump–probe experiments, one would be able to assess the experimental time–resolved–magnitude of both of the aforementioned phenomena.

Bibliography

[1] M. Fowler. *Historical Beginnings of Theories of Electricity and Magnetism*.

[2] M. Hilbert and P. López. "The world's technological capacity to store, communicate, and compute information". In: *Science* 332.6025 (2011), pp. 60–65. ISSN: 00368075.

[3] L. P. Pitaevskii. *Electric Forces in a Transparent Dispersive Medium*. Tech. rep. 5. 1961, p. 1450.

[4] P. S. Pershan, J. P. Van Der Ziel, and L. D. Malmstrom. "Theoretical discussion of the inverse faraday effect, raman scattering, and related phenomena". In: *Phys. Rev.* 143.2 (1966), pp. 574–583. ISSN: 0031899X.

[5] E. Beaurepaire, J.-C. Merle, A. Daunois, and J.-Y. Bigot. "Ultrafast spin dynamics in ferromagnetic nickel." In: *Physical review letters* 76.22 (1996), pp. 4250–4253. ISSN: 1079-7114.

[6] C. D. Stanciu et al. "All-optical magnetic recording with circularly polarized light". In: *Phys. Rev. Lett.* 99.4 (2007), p. 47601. ISSN: 00319007.

[7] S Mangin et al. "Engineered materials for all-optical helicity-dependent magnetic switching." In: *Nature materials* 13.February (2014), pp. 286–92. ISSN: 1476-1122.

[8] C. H. Lambert et al. "All-optical control of ferromagnetic thin films and nanostructures". In: *Science* 345.6202 (2014), pp. 1337–1340. ISSN: 10959203.

[9] I. Tudosa et al. "The ultimate speed of magnetic switching in granular recording media". In: *Nature* 428.6985 (2004), pp. 831–833. ISSN: 00280836.

[10] A. V. Kimel et al. "Ultrafast non-thermal control of magnetization by instantaneous photomagnetic pulses". In: *Nature* 435.7042 (2005), pp. 655–657. ISSN: 00280836.

[11] A. Kirilyuk, A. V. Kimel, and T. Rasing. "Ultrafast optical manipulation of magnetic order". In: *Rev. Mod. Phys.* 82.3 (2010), pp. 2731–2784. ISSN: 15390756.

[12] A. Kirilyuk, A. V. Kimel, and T. Rasing. "Laser-induced magnetization dynamics and reversal in ferrimagnetic alloys". In: *Reports Prog. Phys.* 76.2 (2013), p. 026501. ISSN: 00344885.

[13] B. Koopmans, M. Van Kampen, J. T. Kohlhepp, and W. J. De Jonge. "Ultrafast magneto-optics in nickel: magnetism or optics?" In: *Phys. Rev. Lett.* 85.4 (2000), pp. 844–847. ISSN: 00319007.

[14] K. Carva, P. Baláž, and I. Radu. "Laser-Induced Ultrafast Magnetic Phenomena". In: *Handb. Magn. Mater.* 26 (2017), pp. 291–463. ISSN: 15672719.

[15] A. Scholl, L. Baumgarten, R. Jacquemin, and W. Eberhardt. "Ultrafast spin dynamics of ferromagnetic thin films observed by fs spin-resolved two-photon photoemission". In: *Phys. Rev. Lett.* 79.25 (1997), pp. 5146–5149. ISSN: 10797114.

[16] J. Hohlfeld, E. Matthias, R. Knorren, and K. H. Bennemann. "Nonequilibrium Magnetization Dynamics of Nickel". In: *Phys. Rev. Lett.* 78.25 (1997), pp. 4861–4864. ISSN: 10797114.

[17] C. Stamm et al. "Femtosecond modification of electron localization and transfer of angular momentum in nickel". In: *Nat. Mater.* 6.10 (2007), pp. 740–743. ISSN: 14764660.

[18] E. Beaurepaire et al. "Coherent terahertz emission from ferromagnetic films excited by femtosecond laser pulses". In: *Appl. Phys. Lett.* 84.18 (2004), pp. 3465–3467. ISSN: 00036951.

[19] J. Y. Bigot, M. Vomir, and E. Beaurepaire. "Coherent ultrafast magnetism induced by femtosecond laser pulses". In: *Nat. Phys.* 5.7 (2009), pp. 515–520. ISSN: 17452481.

[20] W. You et al. "Revealing the Nature of the Ultrafast Magnetic Phase Transition in Ni by Correlating Extreme Ultraviolet Magneto-Optic and Photoemission Spectroscopies". In: *Phys. Rev. Lett.* 121.7 (2018). ISSN: 10797114.

[21] P. Tengdin et al. "Critical behavior within 20 fs drives the out-of-equilibrium laser-induced magnetic phase transition in nickel". In: *Science Advances* 4.3 (2018), eaap9744.

[22] P. Maldonado, K. Carva, M. Flammer, and P. M. Oppeneer. "Theory of out-of-equilibrium ultrafast relaxation dynamics in metals". In: *Physical Review B* 96.17 (2017), p. 174439.

[23] H. S. Rhie, H. A. Dürr, and W. Eberhardt. "Femtosecond Electron and Spin Dynamics in [Formula presented] Films". In: *Phys. Rev. Lett.* 90.24 (2003), p. 4. ISSN: 10797114.

[24] M. Cinchetti et al. "Spin-flip processes and ultrafast magnetization dynamics in Co: Unifying the microscopic and macroscopic view of femtosecond magnetism". In: *Phys. Rev. Lett.* 97.17 (2006). ISSN: 00319007. arXiv: `0605272 [cond-mat]`.

[25] E. Carpene et al. "Dynamics of electron-magnon interaction and ultrafast demagnetization in thin iron films". In: *Phys. Rev. B - Condens. Matter Mater. Phys.* 78.17 (2008). ISSN: 10980121.

[26] E. Carpene, H. Hedayat, F. Boschini, and C. Dallera. "Ultrafast demagnetization of metals: Collapsed exchange versus collective excitations". In: *Phys. Rev. B - Condens. Matter Mater. Phys.* 91.17 (2015), p. 174414. ISSN: 1550235X.

[27] A. B. Schmidt et al. "Ultrafast magnon generation in an Fe film on Cu(100)". In: *Phys. Rev. Lett.* 105.19 (2010). ISSN: 00319007.

[28] E. Turgut et al. "Stoner versus Heisenberg: Ultrafast exchange reduction and magnon generation during laser-induced demagnetization". In: *Physical Review B* 94.22 (2016), p. 220408. ISSN: 2469-9950.

[29] S. Eich et al. "Band structure evolution during the ultrafast ferromagnetic-paramagnetic phase transition in cobalt". In: *Science Advances* 3.3 (2017).

[30] S. D. Brorson, J. G. Fujimoto, and E. P. Ippen. "Femtosecond electronic heat-transport dynamics in thin gold films". In: *Phys. Rev. Lett.* 59.17 (1987), pp. 1962–1965. ISSN: 00319007.

[31] G. Malinowski, N. Bergeard, M. Hehn, and S. Mangin. *Hot-electron transport and ultrafast magnetization dynamics in magnetic multilayers and nanostructures following femtosecond laser pulse excitation*. 2018.

[32] N. Bergeard et al. "Hot-Electron-Induced Ultrafast Demagnetization in Co/Pt Multilayers". In: *Phys. Rev. Lett.* 117.14 (2016). ISSN: 10797114.

[33] Y. Xu et al. "Ultrafast Magnetization Manipulation Using Single Femtosecond Light and Hot-Electron Pulses". In: *Adv. Mater.* 29.42 (2017), p. 1703474. ISSN: 15214095.

[34] M. Battiato, K. Carva, and P. M. Oppeneer. "Superdiffusive spin transport as a mechanism of ultrafast demagnetization". In: *Phys. Rev. Lett.* 105.2 (2010). ISSN: 00319007. arXiv: 1106.2117.

[35] M. Battiato, K. Carva, and P. M. Oppeneer. "Theory of laser-induced ultrafast superdiffusive spin transport in layered heterostructures". In: *Phys. Rev. B - Condens. Matter Mater. Phys.* 86.2 (2012), pp. 1–16. ISSN: 10980121.

[36] A. J. Schellekens, W. Verhoeven, T. N. Vader, and B. Koopmans. "Investigating the contribution of superdiffusive transport to ultrafast demagnetization of ferromagnetic thin films". In: *Appl. Phys. Lett.* 102.25 (2013), p. 252408. ISSN: 00036951.

[37] G. Malinowski et al. "Control of speed and efficiency of ultrafast demagnetization by direct transfer of spin angular momentum". In: *Nat. Phys.* 4.11 (2008), pp. 855–858. ISSN: 17452481.

[38] A. Melnikov et al. "Ultrafast transport of laser-excited spin-polarized carriers in Au/Fe/MgO(001)". In: *Phys. Rev. Lett.* 107.7 (2011), p. 076601. ISSN: 00319007.

[39] A. Eschenlohr et al. "Ultrafast spin transport as key to femtosecond demagnetization". In: *Nat. Mater.* 12.4 (2013), pp. 332–336. ISSN: 14761122.

[40] A. R. Khorsand, M. Savoini, A. Kirilyuk, and T. Rasing. *Optical excitation of thin magnetic layers in multilayer structures*. 2014.

[41] D. Rudolf et al. "Ultrafast magnetization enhancement in metallic multilayers driven by superdiffusive spin current". In: *Nat. Commun.* 3 (2012). ISSN: 20411723.

[42] E. Turgut et al. "Controlling the competition between optically induced ultrafast spin-flip scattering and spin transport in magnetic multilayers". In: *Phys. Rev. Lett.* 110.19 (2013). ISSN: 00319007.

[43] I Radu et al. "Transient ferromagnetic-like state mediating ultrafast reversal of antiferromagnetically coupled spins." In: *Nature* 472.7342 (2011), pp. 205–8. ISSN: 1476-4687.

[44] T. A. Ostler et al. "Ultrafast heating as a sufficient stimulus for magnetization reversal in a ferrimagnet". In: *Nat. Commun.* 3 (2012), p. 666. ISSN: 20411723. arXiv: arXiv:1011.1669v3.

[45] M. L. Lalieu et al. "Deterministic all-optical switching of synthetic ferrimagnets using single femtosecond laser pulses". In: *Phys. Rev. B* 96.22 (2017), p. 220411. ISSN: 24699969.

[46] K. Vahaplar et al. "Ultrafast Path for Optical Magnetization Reversal via a Strongly Nonequilibrium State". In: *Phys. Rev. Lett.* 103.11 (2009). ISSN: 00319007.

[47] A. R. Khorsand et al. "Role of magnetic circular dichroism in all-optical magnetic recording". In: *Phys. Rev. Lett.* 108.12 (2012). ISSN: 00319007.

[48] C. Banerjee et al. "Single pulse all-optical toggle switching of magnetization without Gd: The example of Mn2RuxGa". In: (2019). arXiv: 1909.05809.

[49] S. Alebrand et al. "Light-induced magnetization reversal of high-anisotropy TbCo alloy films". In: *Appl. Phys. Lett.* 101.16 (2012), p. 162408. ISSN: 00036951.

[50] A. Hassdenteufel et al. "Thermally assisted all-optical helicity dependent magnetic switching in amorphous Fe100-xTbx alloy films". In: *Adv. Mater.* 25.22 (2013), pp. 3122–3128. ISSN: 09359648.

[51] M. S. El Hadri et al. "Domain size criterion for the observation of all-optical helicity-dependent switching in magnetic thin films". In: *Phys. Rev. B* 94.6 (2016), p. 064419. ISSN: 24699969.

[52] A. Hassdenteufel et al. "Low-remanence criterion for helicity-dependent all-optical magnetic switching in ferrimagnets". In: *Phys. Rev. B - Condens. Matter Mater. Phys.* 91.10 (2015), p. 104431. ISSN: 1550235X.

[53] J. Hohlfeld, C. D. Stanciu, and A. Rebei. "Athermal all-optical femtosecond magnetization reversal in GdFeCo". In: *Appl. Phys. Lett.* 94.15 (2009), p. 152504. ISSN: 00036951. arXiv: 0902.3800.

[54] D. Steil et al. "All-optical magnetization recording by tailoring optical excitation parameters". In: *Phys. Rev. B - Condens. Matter Mater. Phys.* 84.22 (2011), p. 224408. ISSN: 10980121.

[55] M. Ding and S. J. Poon. "Tunable perpendicular magnetic anisotropy in GdFeCo amorphous films". In: *J. Magn. Magn. Mater.* 339 (2013), pp. 51–55. ISSN: 03048853.

[56] G. Kichin et al. "From Multiple- to Single-Pulse All-Optical Helicity-Dependent Switching in Ferromagnetic Co/Pt Multilayers". In: *Phys. Rev. Appl.* 12.2 (2019). ISSN: 23317019.

[57] Y. Quessab et al. "Helicity-dependent all-optical domain wall motion in ferromagnetic thin films". In: *Phys. Rev. B* 97.5 (2018), p. 054419. ISSN: 24699969. arXiv: 1709.07645.

[58] F. Schlickeiser, U. Ritzmann, D. Hinzke, and U. Nowak. "Role of entropy in domain wall motion in thermal gradients". In: *Phys. Rev. Lett.* 113.9 (2014), pp. 1–5. ISSN: 10797114.

[59] S. Moretti, V. Raposo, E. Martinez, and L. Lopez-Diaz. "Domain wall motion by localized temperature gradients". In: *Phys. Rev. B* 95.6 (2017), p. 064419. ISSN: 24699969.

[60] Y. Tsema et al. "Helicity and field dependent magnetization dynamics of ferromagnetic Co/Pt multilayers". In: *Appl. Phys. Lett.* 109.7 (2016), p. 072405. ISSN: 00036951.

[61] Y. Quessab et al. "Resolving the role of magnetic circular dichroism in multi-shot helicity-dependent all-optical switching". In: *Phys. Rev. B* 100.2 (2019). ISSN: 24699969.

[62] S. Anisimov, B. Kapeliovich, and T. Perel'Man. "Electron emission from metal surfaces exposed to ultrashort laser pulses". In: *Sov. J. Exp. Theor. Phys.* 39 (1974), pp. 776–781. ISSN: 1063-7761.

[63] Z. Lin, L. V. Zhigilei, and V. Celli. "Electron-phonon coupling and electron heat capacity of metals under conditions of strong electron-phonon nonequilibrium". In: *Physical Review B* 77.7 (2008), p. 75133.

[64] C. Dornes et al. "The ultrafast Einstein–de Haas effect". In: *Nature* 565.7738 (2019), pp. 209–212. ISSN: 14764687.

[65] B. Koopmans et al. "Explaining the paradoxical diversity of ultrafast laser-induced demagnetization". In: *Nat. Mater.* 9.3 (2010), pp. 259–265. ISSN: 14764660.

[66] A. Y. Elezzabi, M. R. Freeman, and M. Johnson. "Direct measurement of the conduction electron spin-lattice relaxation time T1 in gold". In: *Phys. Rev. Lett.* 77.15 (1996), pp. 3220–3223. ISSN: 10797114.

[67] J. Hohlfeld et al. "Fast magnetization reversal of GdFeCo induced by femtosecond laser pulses". In: *Phys. Rev. B - Condens. Matter Mater. Phys.* 65.1 (2002), pp. 1–4. ISSN: 1550235X.

[68] T. Roth et al. "Temperature dependence of laser-induced demagnetization in Ni: A key for identifying the underlying mechanism". In: *Phys. Rev. X* 2.2 (2012). ISSN: 21603308.

[69] C. M. Schneider, P. Schuster, M. S. Hammond, and J. Kirschner. "Spin-polarized photoemission from f.C.c.-cobalt above the curie temperature: Evidence of short-range magnetic order". In: *Epl* 16.7 (1991), pp. 689–694. ISSN: 12864854.

[70] O Gunnarsson. "Band model for magnetism of transition metals in the spin-density-functional formalism". In: *Journal of Physics F: Metal Physics* 6.4 (1976), p. 587. ISSN: 0305-4608.

[71] S. Halilov, H. Eschrig, and A. Perlov. *Adiabatic spin dynamics from spin-density-functional theory: Application to Fe, Co, and Ni*. Tech. rep. 1. 1998, pp. 293–302.

[72] P. Scheid, G. Malinowski, S. Mangin, and S. Lebègue. "Ab initio study of electronic temperature effects on magnetic materials properties". In: *Phys. Rev. B* 99.17 (2019), p. 174415. ISSN: 24699969.

[73] R. J. Elliott. "Theory of the effect of spin-Orbit coupling on magnetic resonance in some semiconductors". In: *Phys. Rev.* 96.2 (1954), pp. 266–279. ISSN: 0031899X.

[74] U. Dehlinger. *Solid State Physics*. Ed. by F Seitz and D Turnbull. Vol. 9. ISSN 1-2. Elsevier Science, 1956, p. 139. ISBN: 9780080864785.

[75] S. Essert and H. C. Schneider. "Electron-phonon scattering dynamics in ferromagnetic metals and their influence on ultrafast demagnetization processes". In: *Phys. Rev. B - Condens. Matter Mater. Phys.* 84.22 (2011), p. 224405. ISSN: 10980121. arXiv: 1108.4454.

[76] A. R. Williams, J. Kübler, and C. D. Gelatt. "Cohesive properties of metallic compounds: Augmented-spherical-wave calculations". In: *Phys. Rev. B* 19.12 (1979), pp. 6094–6118. ISSN: 01631829.

[77] C. K. Sun et al. "Femtosecond investigation of electron thermalization in gold". In: *Phys. Rev. B* 48.16 (1993), pp. 12365–12368. ISSN: 01631829.

[78] N. Del Fatti et al. "Nonequilibrium electron dynamics in noble metals". In: *Phys. Rev. B - Condens. Matter Mater. Phys.* 61.24 (2000), pp. 16956–16966. ISSN: 1550235X.

[79] C. Guo, G. Rodriguez, and A. J. Taylor. "Ultrafast dynamics of electron thermalization in gold". In: *Phys. Rev. Lett.* 86.8 (2001), pp. 1638–1641. ISSN: 00319007.

[80] K. Carva, M. Battiato, and P. M. Oppeneer. "Ab initio investigation of the Elliott-Yafet electron-phonon mechanism in laser-induced ultrafast demagnetization". In: *Phys. Rev. Lett.* 107.20 (2011). ISSN: 00319007.

[81] K. Carva, M. Battiato, D. Legut, and P. M. Oppeneer. "Ab initio theory of electron-phonon mediated ultrafast spin relaxation of laser-excited hot electrons in transition-metal ferromagnets". In: *Physical Review B - Condensed Matter and Materials Physics* 87.18 (2013), p. 184425. ISSN: 10980121. arXiv: 1305.3511.

[82] F. Beuneu and P. Monod. "The Elliott relation in pure metals". In: *Phys. Rev. B* 18.6 (1978), pp. 2422–2425. ISSN: 01631829.

[83] J. Fabian and S. Das Sarma. "Spin relaxation of conduction electrons in polyvalent metals: Theory and a realistic calculation". In: *Phys. Rev. Lett.* 81.25 (1998), pp. 5624–5627. ISSN: 10797114.

[84] R. Metzler and J. Klafter. *The random walk's guide to anomalous diffusion: A fractional dynamics approach*. 2000.

[85] V. P. Zhukov, E. V. Chulkov, and P. M. Echenique. "GW+T theory of excited electron lifetimes in metals". In: *Phys. Rev. B - Condens. Matter Mater. Phys.* 72.15 (2005). ISSN: 10980121.

[86] V. P. Zhukov, E. V. Chulkov, and P. M. Echenique. "Lifetimes and inelastic mean free path of low-energy excited electrons in Fe, Ni, Pt, and Au: Ab initio GW+T calculations". In: *Phys. Rev. B - Condens. Matter Mater. Phys.* 73.12 (2006). ISSN: 10980121.

[87] M. Battiato, P. Maldonado, and P. M. Oppeneer. "Treating the effect of interface reflections on superdiffusive spin transport in multilayer samples (invited)". In: *J. Appl. Phys.* 115.17 (2014). ISSN: 10897550.

[88] R. F. Evans et al. *Atomistic spin model simulations of magnetic nanomaterials*. 2014. arXiv: 1310.6143.

[89] W. F. Brown. "Thermal fluctuations of a single-domain particle". In: *Phys. Rev.* 130.5 (1963), pp. 1677–1686. ISSN: 0031899X.

[90] N. Kazantseva et al. "Slow recovery of the magnetisation after a sub-picosecond heat pulse". In: *Epl* 81.2 (2008). ISSN: 02955075.

[91] R. F. Evans, U. Atxitia, and R. W. Chantrell. "Quantitative simulation of temperature-dependent magnetization dynamics and equilibrium properties of elemental ferromagnets". In: *Phys. Rev. B - Condens. Matter Mater. Phys.* 91.14 (2015), p. 144425. ISSN: 1550235X. arXiv: 1409.7397.

[92] O. Chubykalo-Fesenko, U. Nowak, R. W. Chantrell, and D. Garanin. "Dynamic approach for micromagnetics close to the Curie temperature". In: *Phys. Rev. B - Condens. Matter Mater. Phys.* 74.9 (2006). ISSN: 10980121. arXiv: 0604508 [cond-mat].

[93] D. Garanin. *Fokker-Planck and Landau-Lifshitz-Bloch equations for classical ferromagnets*. Tech. rep. 5. 1997, pp. 3050–3057. arXiv: 9805054 [cond-mat].

[94] R. F. Evans et al. "Stochastic form of the Landau-Lifshitz-Bloch equation". In: *Phys. Rev. B - Condens. Matter Mater. Phys.* 85.1 (2012), p. 014433. ISSN: 10980121.

[95] J. Mendil et al. "Resolving the role of femtosecond heated electrons in ultrafast spin dynamics". In: *Sci. Rep.* 4 (2014). ISSN: 20452322.

[96] J. Gorchon, Y. Yang, and J. Bokor. "Model for multishot all-thermal all-optical switching in ferromagnets". In: *Phys. Rev. B* 94.2 (2016), 20409(R). ISSN: 24699969. arXiv: 1604.06441.

[97] M. O. Ellis, E. E. Fullerton, and R. W. Chantrell. "All-optical switching in granular ferromagnets caused by magnetic circular dichroism". In: *Sci. Rep.* 6.1 (2016), p. 30522. ISSN: 20452322. arXiv: 1605.00835.

[98] G. Armelies et al. "Origin of strong intrinsic kerr effect in FePt and FePd ordered compounds". In: *IEEE Trans. Magn.* 33.5 PART 1 (1997), pp. 3220–3222. ISSN: 00189464.

[99] K. Sato et al. "Magneto-Optical Spectra of Ordered and Disordered FePt Films Prepared at Reduced Temperatures". In: *Trans. Magn. Soc. Japan* 4.4-2 (2004), pp. 297–300. ISSN: 1346-7948.

[100] J. P. Van Der Ziel, P. S. Pershan, and L. D. Malmstrom. "Optically-induced magnetization resulting from the inverse faraday effect". In: *Phys. Rev. Lett.* 15.5 (1965), pp. 190–193. ISSN: 00319007.

[101] M. Battiato, G. Barbalinardo, K. Carva, and P. M. Oppeneer. "Beyond linear response theory for intensive light-matter interactions: Order formalism and ultrafast transient dynamics". In: *Phys. Rev. B* 85.4 (2012), p. 045117. ISSN: 10980121.

[102] M. Battiato, G. Barbalinardo, and P. M. Oppeneer. "Quantum theory of the inverse Faraday effect". In: *Phys. Rev. B - Condens. Matter Mater. Phys.* 89.1 (2014), p. 014413. ISSN: 10980121.

[103] M. Berritta, R. Mondal, K. Carva, and P. M. Oppeneer. "Ab Initio Theory of Coherent Laser-Induced Magnetization in Metals". In: *Phys. Rev. Lett.* 117.13 (2016), p. 137203. ISSN: 10797114. arXiv: 1604.01188.

[104] P. S. Pershan. "Nonlinear optical properties of solids: energy considerations". In: *Phys. Rev.* 130.3 (1963), pp. 919–929. ISSN: 0031899X.

[105] D. Vanderbilt. *Berry Phases in Electronic Structure Theory*. Cambridge University Press, 2018.

[106] E. Runge and E. K. Gross. "Density-functional theory for time-dependent systems". In: *Phys. Rev. Lett.* 52.12 (1984), pp. 997–1000. ISSN: 00319007.

[107] K. Krieger et al. "Laser-Induced Demagnetization at Ultrashort Time Scales: Predictions of TDDFT". In: *Journal of Chemical Theory and Computation* 11.10 (2015), pp. 4870–4874. ISSN: 15499626.

[108] K. Krieger et al. "Ultrafast demagnetization in bulk versus thin films: An ab initio study". In: *J. Phys. Condens. Matter* 29.22 (2017). ISSN: 1361648X. arXiv: 1612.05663.

[109] J. Chen et al. "Competing Spin Transfer and Dissipation at Co/Cu (001) Interfaces on Femtosecond Timescales". In: *Phys. Rev. Lett.* 122.6 (2019). ISSN: 10797114. arXiv: 1803.03090.

[110] F. Siegrist et al. "Light-wave dynamic control of magnetism". In: *Nature* 571.7764 (2019), pp. 240–244. ISSN: 14764687.

[111] P. Elliott et al. "Optimal control of laser-induced spin-orbit mediated ultrafast demagnetization". In: *New J. Phys.* 18.1 (2016), p. 013014. ISSN: 13672630.

[112] J. K. Dewhurst et al. "Laser-induced intersite spin transfer". In: *Nano Lett.* 18.3 (2018), pp. 1842–1848. ISSN: 15306992.

[113] V. Shokeen et al. "Spin Flips versus Spin Transport in Nonthermal Electrons Excited by Ultrashort Optical Pulses in Transition Metals". In: *Phys. Rev. Lett.* 119.10 (2017). ISSN: 10797114.

[114] P. Hohenberg and W. Kohn. "Inhomogeneous electron gas". In: *Phys. Rev.* 136.3B (1964), B864–B871. ISSN: 0031899X.

[115] E. Engel and R. M. Dreizler. *Density Functional Theory: An Advanced Course*. Vol. 2011. 5. Springer Berlin Heidelberg, 2011, pp. 499–515. ISBN: 9783642140891.

[116] W. Kohn and L. J. Sham. "Self-consistent equations including exchange and correlation effects". In: *Phys. Rev.* 140.4A (1965), A1133–A1138. ISSN: 0031899X.

[117] D. M. Ceperley and B. J. Alder. "Ground State of the Electron Gas by a Stochastic Method". In: *Phys. Rev. Lett.* 45.7 (1980), pp. 566–569.

[118] J. P. Perdew and A. Zunger. "Self-interaction correction to density-functional approximations for many-electron systems". In: *Phys. Rev. B* 23.10 (1981), pp. 5048–5079.

[119] J. P. Perdew and Y. Wang. "Accurate and simple analytic representation of the electron-gas correlation energy". In: *Phys. Rev. B* 45.23 (1992), pp. 13244–13249. ISSN: 01631829.

[120] J. P. Perdew, K. Burke, and M. Ernzerhof. "Generalized gradient approximation made simple". In: *Phys. Rev. Lett.* 77.18 (1996), pp. 3865–3868. ISSN: 10797114.

[121] J. K. Dewhurst, K. Krieger, S. Sharma, and E. K. Gross. "An efficient algorithm for time propagation as applied to linearized augmented plane wave method". In: *Comput. Phys. Commun.* 209 (2016), pp. 92–95. ISSN: 00104655.

[122] C. Herring. "A New Method for Calculating Wave Functions in Crystals". In: *Phys. Rev.* 57.12 (1940), pp. 1169–1177.

[123] D. J. Singh and L. Nordstrom. *Planewaves, Pseudopotentials and the LAPW Method*. Springer {US}, 2006.

[124] P. E. Blöchl. "Projector augmented-wave method". In: *Phys. Rev. B* 50.24 (1994), pp. 17953–17979. ISSN: 01631829.

[125] G. Kresse and D. Joubert. "From ultrasoft pseudopotentials to the projector augmented-wave method". In: *Phys. Rev. B - Condens. Matter Mater. Phys.* 59.3 (1999), pp. 1758–1775. ISSN: 1550235X.

[126] G. Kresse and J. Hafner. "Ab initio molecular dynamics for liquid metals". In: *Phys. Rev. B* 47.1 (1993), pp. 558–561. ISSN: 01631829.

[127] G. Kresse and J. Furthmüller. "Efficient iterative schemes for ab initio total-energy calculations using a plane-wave basis set". In: *Phys. Rev. B - Condens. Matter Mater. Phys.* 54.16 (1996), pp. 11169–11186. ISSN: 1550235X.

[128] G. Kresse and J. Furthmüller. "Efficiency of ab-initio total energy calculations for metals and semiconductors using a plane-wave basis set". In: *Comput. Mater. Sci.* 6.1 (1996), pp. 15–50. ISSN: 09270256.

[129] R. M. Martin. *Electronic Structure: Basic Theory and Practical Methods*. Cambridge University Press, 2004.

[130] J. C. Slater. "Wave Functions in a Periodic Potential". In: *Phys. Rev.* 51.10 (1937), pp. 846–851.

[131] O. K. Andersen. "Linear methods in band theory". In: *Phys. Rev. B* 12.8 (1975), pp. 3060–3083.

[132] B Koopmans et al. "Explaining the paradoxical diversity of ultrafast laser-induced demagnetization." In: *Nature materials* 9.3 (2010), pp. 259–265. ISSN: 1476-1122.

[133] J Mendil et al. "Resolving the role of femtosecond heated electrons in ultrafast spin dynamics." In: *Scientific reports* 4.FEBRUARY (2014), p. 3980. ISSN: 2045-2322.

[134] N. D. Mermin. "Thermal Properties of the Inhomogeneous Electron Gas". In: *Physical Review* 137.5A (1965), A1441–A1443.

[135] P. E. Blöchl. "Projector augmented-wave method". In: *Physical Review B* 50.24 (1994), pp. 17953–17979.

[136] M. P. Marder. *Condensed Matter Physics*. Wiley, 2010. ISBN: 9780470949948.

[137] W Nolting and A Ramakanth. *Quantum Theory of Magnetism*. Springer Berlin Heidelberg, 2009. ISBN: 9783540854166.

[138] N. Bergeard et al. "Ultrafast angular momentum transfer in multisublattice ferrimagnets". In: *Nat. Commun.* 5 (2014). ISSN: 20411723.

[139] M Pajda et al. "Ab initio calculations of exchange interactions, spin-wave stiffness constants, and Curie temperatures of Fe, Co, and Ni". In: *Physical Review B* 64.17 (2001), p. 174402.

[140] F. Essenberger et al. "Magnon spectrum of transition-metal oxides: Calculations including long-range magnetic interactions using the LSDA+U method". In: *Physical Review B - Condensed Matter and Materials Physics* 84.17 (2011), p. 174425. ISSN: 10980121.

[141] W Kohn. "Image of the Fermi Surface in the Vibration Spectrum of a Metal". In: *Phys. Rev. Lett.* 2.9 (1959), pp. 393–394.

[142] A. I. Liechtenstein, M. I. Katsnelson, V. P. Antropov, and V. A. Gubanov. "Local spin density functional approach to the theory of exchange interactions in ferromagnetic metals and alloys". In: *Journal of Magnetism and Magnetic Materials* 67.1 (1987), pp. 65–74. ISSN: 0304-8853.

[143] M. A. Ruderman and C Kittel. "Indirect Exchange Coupling of Nuclear Magnetic Moments by Conduction Electrons". In: *Phys. Rev.* 96.1 (1954), pp. 99–102.

[144] R. Chimata et al. "Microscopic model for ultrafast remagnetization dynamics". In: *Physical Review Letters* 109.15 (2012). ISSN: 00319007. arXiv: 1210.2616.

[145] N. W. Ashcroft and N. D. Mermin. *Solid State Physics*. HRW international editions. Holt, Rinehart and Winston, 1976. ISBN: 9780030839931.

[146] N Singh, P Elliott, J. K. Dewhurst, and S Sharma. *Control of magnons via ultrafast magnetization modulation*. 2019. arXiv: 1906.12270 [cond-mat.mtrl-sci].

[147] K. Vahaplar et al. "All-optical magnetization reversal by circularly polarized laser pulses: Experiment and multiscale modeling". In: *Phys. Rev. B - Condens. Matter Mater. Phys.* 85.10 (2012), p. 104402. ISSN: 10980121.

[148] A. H. Reid et al. "Investigation of the femtosecond inverse Faraday effect using paramagnetic Dy3Al5O12". In: *Phys. Rev. B - Condens. Matter Mater. Phys.* 81.10 (2010), p. 104404. ISSN: 10980121.

[149] G. P. Zhang and W. Hübner. "Laser-induced ultrafast demagnetization in ferromagnetic metals". In: *Phys. Rev. Lett.* 85.14 (2000), pp. 3025–3028. ISSN: 00319007.

[150] P. Elliott et al. "Ultrafast laser induced local magnetization dynamics in Heusler compounds". In: *Sci. Rep.* 6 (2016). ISSN: 20452322.

[151] M. Hofherr et al. "Ultrafast optically induced spin transfer in ferromagnetic alloys". In: *Science Advances* 6.3 (2020), pp. 1–8. ISSN: 23752548.

[152] J. Kubler, K. H.hock, J. Sticht, and A. R. Williams. "Density functional theory of non-collinear magnetism". In: *Journal of Physics F: Metal Physics* 18.3 (1988), pp. 469–483. ISSN: 03054608.

[153] P Elliott et al. "The microscopic origin of spin-orbit mediated spin-flips". In: *Journal of Magnetism and Magnetic Materials* 502 (2020), p. 166473. ISSN: 0304-8853.

Résumé

Le magnétisme s'est, au cours de notre histoire, forgé une place prépondérante de par les applications technologiques qu'il rend possible. En effet, depuis l'invention de la boussole au 12ème siècle qui permit d'améliorer la navigation, jusqu'aux technologies de stockage de l'information aujourd'hui, l'utilisation du magnétisme continue d'augmenter à un rythme toujours plus rapide. Cet état de fait est particulièrement bien illustré par l'évolution de la manière dont est stockée l'information. En effet, alors qu'à la fin des années 1980, 99 % de l'information était encodée sur des supports analogiques, cette tendance se renversa radicalement puisqu'en 2007, 97 % de celle–ci était stocké digitalement.



FIGURE 1: Boussole magnétique aimantée.
Sous licence Creative Commons Attribution-Share Alike 3.0 Unported license.

Plus que son omniprésence dans le domaine technologique, le magnétisme a présenté un terrain tout aussi fertile en physique, notamment dans le domaine de l'interaction lumière-matière. L'effet des matériaux aimantés sur la polarisation de la lumière qui s'y propage est connu depuis près de deux siècles. En effet, en 1845, Michael Faraday a découvert les premières preuves expérimentales de ce phénomène dans un morceau de verre contenant des traces de plomb. Il a montré qu'en présence d'un champ magnétique, la polarisation de la lumière était tournée d'un angle proportionnel à l'intensité de ce champ. En 1961, l'effet réciproque, appelé effet Faraday inverse, fut prédit par Pitaevskii[3] dans des milieux non dissipatifs. Quelques années plus tard, la confirmation expérimentale d'une aimantation statique induite uniquement par la lumière fut donnée[4]. Ces dernières années, grâce à l'arrivée de sources de lumière ultrarapides à haute intensité, de nouveaux régimes d'interaction lumière-matière, dans lesquels la matière est éloignée de l'équilibre thermodynamique, ont été atteints. Dans ce cadre, Beaurepaire *et al.*[5] a découvert en 1996 que de telles impulsions lumineuses pouvaient désaimanter un film mince de nickel en moins de 1 ps, ce qui à ce jour reste le moyen le plus rapide d'influencer l'état de l'aimantation de la matière . Cette découverte fut suivie d'une intense recherche, à la fois théorique et expérimentale, sur l'origine de ce phénomène. Ce domaine d'étude s'est encore plus étendu après la découverte du retournement tout optique dépendant de l'hélicité, c'est-à-dire de la possibilité de manipuler l'état magnétique de couches minces métalliques aimantées à base de gadolinium, de fer et de cobalt en utilisant uniquement des impulsions lumineuses[6]. Quelques années plus tard, Mangin *et al.*[7] ont découvert la présence du retournement tout optique dépendant de l'hélicité dans une grande variété de couches minces, où l'ordre magnétique, l'hétérogénéité, ainsi que le type d'atomes ont été variés sans en affecter sa présence. Notamment, le retournement tout optique dépendant de l'hélicité peut être obtenu même sans la présence

d'atomes de terres rares, et plus précisément dans un milieu granulaire de fer et de platine qui, en raison de sa grande anisotropie magnétique, est un bon candidat pour les futures technologies de stockage d'informations[8].

Néanmoins, pour exploiter pleinement les possibilités technologiques que nous offrent les phénomènes susmentionnés, leur compréhension est nécessaire, et la présente thèse s'inscrit dans ce cadre. En nous appuyant principalement sur la théorie de la fonctionnelle de la densité, ainsi que sur son extension permettant la propagation temporelle, nous étudions théoriquement plusieurs aspects de la désaimantation ultrarapide induite par la lumière, ainsi que le retournement tout optique dépendant de l'hélicité. Nous verrons que la physique impliquée dans leur description est très étendue, puisqu'elle regroupe des aspects de la théorie de l'interaction lumière-matière, de la physique hors équilibre et, bien sûr, du magnétisme.

Le chapitre 2 est consacré à l'état de l'art expérimental et théorique des principaux domaines de contribution de cette thèse que sont la démagnétisation ultrarapide induite par des impulsions lumineuses de quelques dizaines de femtosecondes et le retournement tout optique dépendant de l'hélicité. En effet, comme souvent en physique, les expériences et la théorie se sont guidées l'une l'autre et, par conséquent, la compréhension d'un de ces domaines nécessite la compréhension de l'autre. Nous commençons cette section en mentionnant les premiers résultats expérimentaux rapportant la désaimantation ultrarapide induite par la lumière. Ceci est suivi d'une revue des différentes investigations expérimentales de son origine. Ensuite, nous aborderons la thématique du retournement tout optique dépendant de l'hélicité. Dans cette section, nous soutiendrons que la compréhension de cette dernière ne peut être entreprise sans une connaissance des mécanismes de la désaimantation induite par la lumière, étant donné que les deux phénomènes se produisent simultanément. Une attention particulière sera accordée au retournement tout optique dépendant de l'hélicité qui, comme mentionné ci-dessus, se produit dans une large gamme de couches minces magnétiques, et constitue l'un des objets d'étude de cette thèse. Celui-ci est à distinguer du retournement tout optique indépendant de l'hélicité, dont l'occurrence est beaucoup plus restreinte et n'est pas examiné dans ce manuscrit. La deuxième partie de cet état de l'art développera les traitements théoriques des phénomènes précités. Après avoir discuté des modèles phénoménologiques à 2 et 3 températures, qui ont été parmi les plus utilisés dans la littérature afin de rationaliser à la fois la désaimantation ultrarapide et le retournement tout optique dépendant de l'hélicité, nous détaillerons les possibles origines microscopiques de la réduction de l'aimantation. Celles-ci peuvent être divisées en effets qui induisent une diminution du vecteur de moment magnétique porté par chaque atome, et en effets qui génèrent une inclinaison aléatoire de ces vecteurs, réduisant ainsi l'aimantation moyenne. Ensuite, nous passerons en revue les éventuels effets dépendant de l'hélicité, qui, s'ajoutant à ceux mentionnés ci-dessus, peuvent éventuellement conduire au retournement tout optique dépendant de l'hélicité ainsi qu'à d'autres effets connexes. Ce chapitre se termine par un résumé des éléments théoriques actuels permettant de rationaliser les résultats expérimentaux. Ce faisant, nous mettons en évidence leurs lacunes et les domaines de contribution de cette thèse.

Le chapitre 3 présente au lecteur la théorie sur laquelle s'appuie la plupart des travaux

de cette thèse, *i.e.* la théorie de la fonctionnelle de la densité. Celle-ci fournit un cadre rigoureux permettant une grande simplification de la résolution de l'équation de Schrodinger à plusieurs corps sans, en principe, nécessiter l'utilisation d'approximation. Ainsi, cette théorie nous permet de trouver la densité électronique de l'état fondamental de matériaux réels, ainsi que leurs observables quantiques, qui peuvent être exprimés en fonction de la densité électronique. Néanmoins, dans la pratique, il faut s'appuyer sur des approximations pour que cette théorie soit d'une quelconque utilité pratique. Celles-ci, ainsi que la méthode numérique utilisée dans ce travail sont passées en revue, et l'application de la théorie de la fonctionnelle de la densité aux matériaux magnétiques, auxquels cette thèse s'intéresse, est détaillée. L'extension de cette théorie au domaine temporel, utilisée dans le chapitre 7 pour calculer l'effet de vraies impulsions de lumière polarisée circulairement, est ensuite passée en revue.

Les chapitres 4, 5, 6 et 7 rendent compte des contributions de cette thèse. Les deux premiers se concentrent sur le comportement de l'aimantation lorsque la température électronique est élevée. En effet, comme détaillé dans le chapitre 2, la lumière est principalement absorbée par les électrons, qui sont alors considérés comme "chauds" par rapport aux autres degrés de liberté du matériau n'interagissant pas avec la lumière. Dans le cadre de la théorie de la fonctionnelle de la densité, cela peut être pris en compte par un changement de la température électronique. Ce faisant, dans le chapitre 4, nous avons constaté que lors d'une augmentation de cette dernière, une réduction de la longueur du moment magnétique se produit sur chaque atome, jusqu'à la température dite de Stoner, variant de 3100 K à 8100 K, où les moments disparaissent complètement. Cependant, pour certains composés, les conséquences de ce phénomène sont perceptibles sur l'énergie électronique et la chaleur spécifique, même à basse température électronique. Par conséquent, de grands écarts par rapport à l'approximation de Sommerfeld et à certains travaux antérieurs qui ne prenaient pas explicitement en compte la dépendance de la structure électronique vis à vis de la température électronique sont mis en évidence. Ces résultats sont particulièrement pertinents pour le domaine de la dynamique de l'aimantation ultrarapide induite par laser, car ils fournissent une estimation plus précise de la chaleur spécifique électronique qui entre dans le modèle à trois températures susmentionné, et montrent qu'une relaxation longitudinale de l'aimantation uniquement due à une une augmentation de la température électronique est peu probable. Dans le chapitre 5, nous utilisons la théorie de la fonctionnelle de la densité pour étudier l'effet d'une élévation de la température électronique sur les états des magnons, qui sont des excitations magnétiques transversales dans les solides périodiques. Nous constatons qu'un tel changement de la température électronique entraîne une diminution des valeurs propres des magnons, ce qui, à son tour, se traduit par une diminution de l'échange interatomique d'Heisenberg. Ensuite, en utilisant cette dernière et l'équation de Landau-Lifshitz-Gilbert atomistique, nous calculons la dynamique des moments magnétiques atomiques induite par une impulsion de lumière. Nous montrons que l'augmentation de la température électronique peut, en effet, représenter une partie importante de la démagnétisation, car elle abaisse l'ordre magnétique sans que le bain des magnons ne monte en température, comme le suppose traditionnellement le modèle à trois températures[5].

Les chapitres 6 et 7 examinent l'effet de la lumière polarisée circulairement sur l'aimantation. Dans le chapitre 6, nous utilisons la théorie de la fonctionnelle de la densité et la règle d'or de Fermi pour calculer quantitativement l'effet de l'absorption optique

de la lumière dans les matériaux ferromagnétiques. Dans une première partie, nous différencions cet effet de l'effet Faraday inverse qui est traditionnellement invoqué dans la littérature comme étant responsable du retournement tout optique dépendant de l'hélicité. En effet, à la différence de ce dernier, ce mécanisme est dû à l'absorption et reste donc présent dans le matériau même après la disparition de la lumière. Ensuite, nous montrons qu'en conséquence du couplage spin-orbite, les transitions optiquement induites ne conservent pas l'aimantation et engendrent systématiquement une désaimantation, dont l'amplitude dépend à la fois de l'hélicité de la lumière et de la direction de l'aimantation. Avant de conclure, dans le chapitre 7, nous utilisons la théorie de la fonctionnelle de la densité dépendante du temps pour étudier l'effet des impulsions femtosecondes polarisées circulairement dans le régime optique et XUV sur la dynamique de l'aimantation des matériaux ferromagnétiques. Nous montrons que la lumière induit toujours une réduction de la longueur de l'aimantation, et que cette réduction dépend de l'hélicité. Dans le régime XUV, où les états 3p de semi-coeur sont impliqués, nous constatons une plus grande dépendance à l'hélicité, qui persiste même après la disparition de la lumière. Ensuite, nous procédons à la séparation de la partie de la dynamique dépendante de l'hélicité due à l'absorption de celle due à l'effet Faraday inverse. Ce faisant, nous montrons que le premier a, dans l'ensemble, un impact plus important sur l'aimantation que le second, en particulier lorsque la lumière disparaît et dans le régime XUV.

Enfin, dans le chapitre 8, nous concluons en résumant nos principales conclusions et nous discutons des nombreux développements possibles qui pourraient suivre cette thèse.

Tous les résultats susmentionnés ouvrent la voie à de nombreux développements possibles.
Par exemple, au chapitre. 5 nous avons montré qu'une augmentation de la température électronique entraîne une diminution de l'échange interatomique d'Heisenberg. Cependant, cela suppose que le bain électronique reste thermalisé à tout moment, ce qui n'est évidemment pas le cas expérimentalement car les électrons chauds proviennent de l'excitation de la lumière. Il est très probable qu'une telle distribution non thermodynamique ait un impact plus important sur l'échange interatomique de Heisenberg. Dans ce cadre, la désaimantation induite par une perte d'échange de Heisenberg pourrait être bien plus importante que ce que nous avons prédit au chapitre 5. De plus, comme nous l'avons vu au chapitre 6 et 7, étant donné que l'excitation électronique dépend à la fois de la polarisation et de la fréquence de l'impulsion lumineuse, les mêmes caractéristiques peuvent être attendues concernant le comportement de l'échange interatomique de Heisenberg. Cela pourrait conduire à la découverte de nouveaux phénomènes comme, par exemple, la possibilité de contrôler cet échange en utilisant uniquement la polarisation de la lumière. La théorie de la fonctionnelle de la densité dépendante du temps est un outil de choix pour étudier théoriquement ce nouveau domaine.
Une autre voie d'amélioration concerne la théorie de la fonctionnelle de la densité dépendante du temps elle-même. En effet, les limites actuelles de cette théorie sont nombreuses. Par exemple, pour l'instant, elle ne permet pas une simulation réaliste de la réalité expérimentale car le système électronique est complètement fermé. Par conséquent, si une excitation électronique est produite, elle persistera *ad vitam*, alors qu'en réalité, le bain électronique libère de l'énergie et de l'information aux degrés de liberté externes et,

se faisant relaxe vers une distribution thermodynamique. Ces degrés de liberté externes sont composés des photons et, dans les solides périodiques, des phonons et des magnons. Les premiers correspondent à des excitations du réseau, tandis que les seconds sont des excitations transversales des moments magnétiques. Cependant, l'inclusion de ces nouveaux degrés de liberté est limitée par le fait que la périodicité du système restreint la gamme possible d'excitations car, pour les magnons et les phonons, la prise en compte des modes de grande longueur d'onde nous obligerait à utiliser de grandes supercellules . De plus, même si nous en avions les capacités, il n'est pas évident de savoir comment tenir compte du théorème de fluctuation-dissipation dans un tel cadre. En effet, sa réalisation est nécessaire pour avoir des degrés de liberté thermalisés dans le cas statique.
Enfin, alors que l'effet Faraday inverse et l'aimantation induite pendant l'absorption de la lumière peuvent maintenant être évalués théoriquement, l'évaluation de leur valeur expérimentale respective reste impossible. Cependant, ceci serait particulièrement intéressant étant donné que l'écart entre les réalités expérimentales et informatiques reste important, notamment parce que les expériences utilisent des films minces avec différentes qualités cristallines et d'interface. Néanmoins, comme ces deux phénomènes proviennent de la réponse du premier ordre d'un matériau à un champ électromagnétique, leur intensité doit être exprimable en termes du tenseur diélectrique. Connaissant cette expression et utilisant des expériences pompe-sonde, nous serions alors en mesure d'évaluer l'amplitude expérimentale résolue en temps des deux phénomènes susmentionnés.